

On the trail of the
Ebola virus p. 120

A winning strategy for two-
handed poker pp. 122 & 145

China's aquaculture threat
to global fisheries p. 133

Science

\$10
9 JANUARY 2015
sciencemag.org

AAAS



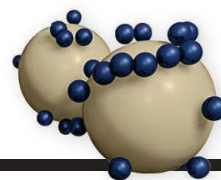
Popping into the third dimension

Time sequence
of buckling silicon
microwires

pp. 130 & 154

CONTENTS

9 JANUARY 2015 • VOLUME 347 • ISSUE 6218



131 & 149

An inside look at battery operation

NEWS

IN BRIEF

108 Roundup of the week's news

IN DEPTH

111 LASER FUSION, WITH A DIFFERENCE

Europe's Laser Mégajoule project blazes its own trail toward nuclear ignition
By D. Clery

113 U.S. PATENT OFFICE REWORKS UNPOPULAR POLICY

New guidelines lower the barrier for patenting products derived from nature, quelling some biotech fears *By K. Service*

114 A SOFT APPROACH KICK-STARTS CYBERNETIC IMPLANTS

Mimicking real tissue, novel materials lead to flexible electrode implants that help paralyzed animals walk again
By R. F. Service
► REPORT P. 159

115 AIR FORCE TURNS A KEEN EYE ON SPACE JUNK

Flood of data from new "space fence" radar may overwhelm some satellite operators *By I. Loomis*

116 BEYOND THE TURING TEST

Concluding that there is no one test for machine intelligence, AI researchers develop a battery of research challenges
By J. You

FEATURES

117 SALVAGING SCIENCE

Underwater archaeologist Charles Beeker works to preserve famous wrecks as museums *By M. Barwaya*

120 ON THE TRAIL OF CONTAGION

One team's quest to find a potential Ebola case in Liberia reveals how difficult it will be to end the epidemic
By K. Kupferschmidt

INSIGHTS

PERSPECTIVES

122 SOLVING IMPERFECT-INFORMATION GAMES

The smallest common poker game, two-player limit Texas Hold'em, is essentially solved *By T. Sandholm*
► RESEARCH ARTICLE P. 145

124 PRESCRIBING SPLICING

A model predicts the impact of variations in the human genome on RNA splicing and disease
By R. Guigó and J. Valcárcel
► RESEARCH ARTICLE P. 144

125 COPING WITH OXIDATIVE STRESS

A crystal structure helps to explain how cells detoxify *By U. Krengel and S. Törnroth-Horsefield*
► REPORT P. 178

127 DYNAMICS OF A COLD QUANTUM GAS

A cloud of cold atoms provides a route to understanding complex phase transitions *By G. Ferrari*
► REPORT P. 167

128 MAKING SENSE OF AMINO ACID SENSING

Biochemically and spatially diverse intracellular mechanisms couple the activity of a cell growth regulatory complex to the availability of amino acids *By R. T. Abraham*
► REPORTS PP. 188 & 194

130 DESIGNING TWO-DIMENSIONAL MATERIALS THAT SPRING RAPIDLY INTO THREE-DIMENSIONAL SHAPES

Buckling of sheets can be engineered to rapidly create complex shapes
By C. Ye and V. V. Tsukruk
► REPORT P. 154

131 USING ALL ENERGY IN A BATTERY

Controlled electrode structure improves energy utilization *By N. J. Dudney and J. Li*
► REPORT P. 149

133 CHINA'S AQUACULTURE AND THE WORLD'S WILD FISHERIES

Curbing demand for wild fish in aquafeeds is critical *By L. Cao et al.*

BOOKS ET AL.

136 CHRONIC DISEASE IN THE TWENTIETH CENTURY

By G. Weisz, reviewed by P. Weindling

137 THE MEANING OF HUMAN EXISTENCE

By E. O. Wilson, reviewed by S. R. Wolf

138 THE PERIPHERAL

By W. Gibson, reviewed by G. Riddihough

LETTERS

139 RETRACTION

By M. Loretz et al.

139 PROTECTING COFFEE FROM INTENSIFICATION

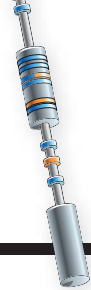
By R. Aerts et al.



111

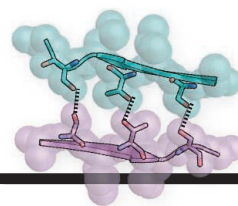
Published by AAAS

Science Staff	106
New Products	199
Science Careers	200



124 & 144

Mutations that misregulate splicing cause disease



185

A new player in DNA repair

139 MEASURING MERIT: TAKE THE RISK

By K. Selvarajoo

140 MOVING TOWARD DATA ON SOIL CHANGE

By D. A. Robinson

RESEARCH

IN BRIEF

141 From *Science* and other journals

RESEARCH ARTICLES

144 RNA SPLICING

The human splicing code reveals new insights into the genetic determinants of disease *H. Y. Xiong et al.*

RESEARCH ARTICLE SUMMARY; FOR FULL TEXT: [dx.doi.org/10.1126/science.1254806](https://doi.org/10.1126/science.1254806)

► PERSPECTIVE P. 124

145 COMPUTER SCIENCE

Heads-up limit hold'em poker is solved *M. Bowling et al.*

► PERSPECTIVE P. 122

REPORTS

149 BATTERIES

In situ visualization of $\text{Li}/\text{Ag}_2\text{VP}_2\text{O}_8$ batteries revealing rate-dependent discharge mechanism *K. Kirshenbaum et al.*

► PERSPECTIVE P. 131

154 MATERIALS SCIENCE

Assembly of micro/nanomaterials into complex, three-dimensional architectures by compressive buckling *S. Xu et al.*

► PERSPECTIVE P. 130

159 BIOMATERIALS

Electronic dura mater for long-term multimodal neural interfaces *I. R. Mineev et al.*

► NEWS STORY P. 114



122 & 145

164 ULTRAFAST DYNAMICS

Four-dimensional imaging of carrier interface dynamics in p-n junctions *E. Najafi et al.*

167 QUANTUM GASES

Critical dynamics of spontaneous symmetry breaking in a homogeneous Bose gas *N. Navon et al.*

► PERSPECTIVE P. 127

170 GUT MICROBIOTA

Antimicrobial peptide resistance mediates resilience of prominent gut commensals during inflammation *T. W. Cullen et al.*

175 EPIDEMIOLOGY

Opposite effects of anthelmintic treatment on microbial infection at individual versus population scales *V. O. Ezenwa and A. E. Jolles*

► PODCAST

178 STRUCTURAL BIOLOGY

Division of labor in transhydrogenase by alternating proton translocation and hydride transfer *J. H. Leung et al.*

► PERSPECTIVE P. 125

182 EARTH HISTORY

U-Pb geochronology of the Deccan Traps and relation to the end-Cretaceous mass extinction *B. Schoene et al.*

185 DNA REPAIR

PAXX, a paralog of XRCC4 and XLF, interacts with Ku to promote DNA double-strand break repair *T. Ochi et al.*

METABOLISM

188 Lysosomal amino acid transporter SLC38A9 signals arginine sufficiency to mTORC1 *S. Wang et al.*

194 Differential regulation of mTORC1 by leucine and glutamine *J. L. Jewell et al.*

► PERSPECTIVE P. 128

DEPARTMENTS

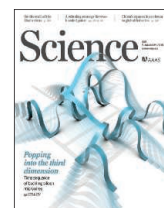
107 EDITORIAL

Judging synthetic biology risks *By Rainer Breitling et al.*

206 WORKING LIFE

My metamorphosis *By Elizabeth A. Marchio*

ON THE COVER



Computational results for the dynamic transformation of a planar, two-dimensional structure into an extended, three-dimensional open framework. Controlled buckling follows from

compressive forces that act at precise locations across the structure upon release of prestrain in an elastomeric substrate. This example uses microscale ribbons of silicon, with potential applications in electronic circuits, battery anodes, photodetectors, and other semiconductor devices. See pages 130 and 154 and see scim.ag/6218_vid for a related video. *Illustration: John Rogers, Yihui Zhang, and C. Bickel/Science*

SCIENCE (ISSN 0036-8075) is published weekly on Friday, except the last week in December, by the American Association for the Advancement of Science, 1200 New York Avenue, NW, Washington, DC 20005. Periodicals mail postage (publication No. 484460) paid at Washington, DC, and additional mailing offices. Copyright © 2015 by the American Association for the Advancement of Science. The title SCIENCE is a registered trademark of the AAAS. Domestic individual membership and subscription (51 issues): \$153 (\$74 allocated to subscription). Domestic institutional subscription (51 issues): \$1282. Foreign postage extra: Mexico, Caribbean (surface mail) \$55; other countries (air assist delivery) \$85. First class, airmail, student, and emeritus rates on request. Canadian rates with GST available upon request. GST #R1254 88122. Publications Mail Agreement Number 1069624. Printed in the U.S.A. **Change of address:** Allow 4 weeks, giving old and new addresses and 8-digit account number. **Postmaster:** Send change of address to AAAS, P.O. Box 96178, Washington, DC 20090-6178. **Single-copy sales:** \$10.00 current issue, \$15.00 back issue prepaid includes surface postage; bulk rates on request. **Authorization to photocopy** material for internal or personal use under circumstances not falling within the fair use provisions of the Copyright Act is granted by AAAS to libraries and other users registered with the Copyright Clearance Center (CCC) Transactional Reporting Service, provided that \$30.00 per article is paid directly to CCC, 222 Rosewood Drive, Danvers, MA 01923. The identification code for Science is 0036-8075. Science is indexed in the Reader's Guide to Periodical Literature and in several specialized indexes.

Editor-in-Chief Marcia McNutt

Executive Editor Monica M. Bradford **News Editor** Tim Appenzeller

Managing Editor, Research Journals Katrina L. Kelner

Deputy Editors Barbara R. Jasny, Andrew M. Sugden(UK), Valda J. Vinson, Jake S. Yeston

Research and Insights

SR. EDITORS Caroline Ash(UK), Gilbert J. Chin, Lisa D. Chong, Maria Cruz(UK), Julia Fahrenkamp-Uppenbrink(UK), Pamela J. Hines, Stella M. Hurtley(UK), Paula A. Kiberstis, Marc S. Lavine(Canada), Kristen L. Mueller, Ian S. Osborne(UK), Beverly A. Purnell, L. Bryan Ray, Guy Riddihough, H. Jesse Smith, Jelena Stajic, Peter Stern(UK), Phillip D. Szurmi, Brad Wible, Nicholas S. Wigginton, Laura M. Zahn **ASSOCIATE EDITORS** Brent Grocholski, Melissa R. McCartney, Margaret M. Moerchen, Sacha Vignieri **ASSOCIATE BOOK REVIEW EDITOR** Valerie B. Thompson **ASSOCIATE LETTERS EDITOR** Jennifer Sills **CHIEF CONTENT PRODUCTION EDITOR** Cara Tate **SR. CONTENT PRODUCTION EDITORS** Harry Jach, Trista Wagoner **CONTENT PRODUCTION EDITORS** Jeffrey E. Cook, Chris Filiatreau, Cynthia Howe, Lauren Kmec, Barbara P. Ordway **SR. EDITORIAL COORDINATORS** Carolyn Kyle, Beverly Shields **EDITORIAL COORDINATORS** Ramatoulaye Diop, Joi S. Granger, Lisa Johnson, Anita Wynn **PUBLICATIONS ASSISTANTS** Aneera Dobbins, Jeffrey Hearn, Dona Mathieu, Le-Toya Mayne Flood, Shannon McMahon, Scott Miller, Jerry Richardson, Rachel Roberts(UK), Alice Whaley(UK), Brian White **EXECUTIVE ASSISTANT** Anna Bashkirova **ADMINISTRATIVE SUPPORT** Janet Clements(UK), Michael Crabtree(UK, Intern), Lizanne Newton(UK), Maryrose Madrid, John Wood(UK)

News

NEWS MANAGING EDITOR John Travis **INTERNATIONAL EDITOR** Richard Stone **DEPUTY NEWS EDITORS** Daniel Clery(UK), Robert Coontz, Elizabeth Culotta, David Grimm, David Malakoff, Leslie Roberts **CONTRIBUTING EDITORS** Martin Enserink(Europe), Mara Hvistendahl (Asia) **SR. CORRESPONDENTS** Jeffrey Mervis, Elizabeth Pennisi **NEWS WRITERS** Adrian Cho, Jon Cohen, Jennifer Couzin-Frankel, Carolyn Gramling, Eric Hand, Jocelyn Kaiser, Kerli Servick, Robert F. Service, Erik Stokstad, Emily Underwood **INTERNS** David Shultz, Jia You **CONTRIBUTING CORRESPONDENTS** Pallava Bagla(South Asia), Michael Balter(Paris), John Bohannon, Ann Gibbons, Sam Kean, Richard A. Kerr, Eli Kintisch, Kai Kupferschmidt(Berlin), Andrew Lawler, Christina Larson(Beijing), Mitch Leslie, Charles C. Mann, Eliot Marshall, Virginia Morell, Dennis Normile(Tokyo), Heather Pringle, Lana Rabesandratana(Brussels), Gretchen Vogel(Berlin), Lizzie Wade(Mexico City) **CAREERS** Jim Austin(Editor), Donisha Adams **COPY EDITORS** Kara Estelle, Nora Kelly, Jennifer Levin **ADMINISTRATIVE SUPPORT** Scherraine Mack

Executive Publisher Alan I. Leshner

Publisher Kent R. Anderson **Chief Digital Media Officer** Rob Covey

BUSINESS OPERATIONS AND ADMINISTRATION DIRECTOR Deborah Rivera-Wienhold **BUSINESS SYSTEMS AND FINANCIAL ANALYSIS DIRECTOR** Randy Yi **MANAGER OF FULFILLMENT SYSTEMS** Neal Hawkins **SYSTEMS ANALYST** Nicole Mehmedovich **ASSISTANT DIRECTOR, BUSINESS OPERATIONS** Eric Knott **MANAGER, BUSINESS OPERATIONS** Jessica Tierney **BUSINESS ANALYSTS** Cory Lipman, Cooper Tilton, Celeste Troxler **FINANCIAL ANALYST** Jeremy Clay **RIGHTS AND PERMISSIONS ASSISTANT DIRECTOR** Emilie David **PERMISSIONS ASSOCIATE** Elizabeth Sandler **RIGHTS, CONTRACTS, AND LICENSING ASSOCIATE** Lili Kiser

MARKETING DIRECTOR Ian King **MARKETING MANAGER** Julianne Wielga **MARKETING ASSOCIATE** Elizabeth Sattler **SR. MARKETING EXECUTIVE** Jennifer Reeves **SR. ART ASSOCIATE, PROJECT MANAGER** Izeitel Sorrosa **ART ASSOCIATE** Seil Lee **ASSISTANT COMMERCIAL EDITOR** Selby Frame **MARKETING PROJECT MANAGER** Angelissa McArthur **SR. WRITER** Bill Zimmer **PROGRAM DIRECTOR, AAAS MEMBER CENTRAL** Peggy Mihelich **FULFILLMENT SYSTEMS AND OPERATIONS** membership@aaas.org **MANAGER, MEMBER SERVICES** Pat Butler **SPECIALISTS** LaToya Casteel, Javia Flemmings, Latasha Russell **OPERATIONS, DATA ENTRY** Maggie Napoleoni **DATA ENTRY SPECIALISTS** JJ Regan, Jaimee Wise, Fiona Giblin

DIRECTOR, SITE LICENSING Tom Ryan **DIRECTOR, CORPORATE RELATIONS** Eileen Bernadette Moran **SR. PUBLISHER RELATIONS SPECIALIST** Kiki Forsythe **PUBLISHER RELATIONS MANAGER** Catherine Holland **PUBLISHER RELATIONS, EASTERN REGION** Keith Layson **PUBLISHER RELATIONS, WESTERN REGION** Ryan Rexroth **MANAGER, SITE LICENSE OPERATIONS** Iquo Edim **FULFILLMENT ANALYST** Lana Guz **ASSOCIATE DIRECTOR, MARKETING** Christina Schlecht **MARKETING ASSOCIATES** Thomas Landreth, Minah Kim

DIRECTOR OF WEB TECHNOLOGIES Ahmed Khadr **SR. DEVELOPER** Chris Coleman **DEVELOPERS** Dan Berger, Jimmy Marks **SR. PROJECT MANAGER** Trista Smith **SYSTEMS ENGINEER** Luke Johnson **PRODUCT MANAGER** Walter Jones

CREATIVE DIRECTOR, MULTIMEDIA Martyn Green **DIRECTOR OF ANALYTICS** Enrique Gonzales **SR. WEB PRODUCER** Sarah Crespi **WEB PRODUCER** Alison Crawford **VIDEO PRODUCER** Nguyen Nguyen **SOCIAL MEDIA PRODUCER** Meghna Sachdev

DIRECTOR OF OPERATIONS PRINT AND ONLINE Elizabeth Harman **DIGITAL/PRINT STRATEGY MANAGER** Jason Hillman **QUALITY TECHNICAL MANAGER** Marcus Spiegel **DIGITAL PRODUCTION MANAGER** Lisa Stanford **ASSISTANT MANAGER DIGITAL/PRINT** Rebecca Doshi **DIGITAL MEDIA SPECIALIST** Tara Kelly **SENIOR CONTENT SPECIALISTS** Steve Forrester, Antoinette Hodal, Lori Murphy, Anthony Rosen **CONTENT SPECIALISTS** Jacob Hedrick, Kimberley Oster

DESIGN DIRECTOR Beth Rakouskas **DESIGN EDITOR** Marcy Atarod **SENIOR SCIENTIFIC ILLUSTRATORS** Chris Bickel, Katharine Sutliff **SCIENTIFIC ILLUSTRATOR** Valerie Altounian **SENIOR ART ASSOCIATES** Holly Bishop, Preston Huey **SENIOR DESIGNER** Garvin Grullón **DESIGNER** Chrystal Smith **SENIOR PHOTO EDITOR** William Douthitt **PHOTO EDITOR** Leslie Blizard

DIRECTOR, GLOBAL COLLABORATION, CUSTOM PUBLICATIONS, ADVERTISING Bill Moran **EDITOR, CUSTOM PUBLISHING** Sean Sanders: 202-326-6430 **ASSISTANT EDITOR, CUSTOM PUBLISHING** Tianna Hicklin: 202-326-6463 **ADVERTISING MARKETING MANAGER** Justin Sawyers: 202-326-7061 **science_advertising@aaas.org** **ADVERTISING MARKETING ASSOCIATE** Javia Flemmings **ADVERTISING SUPPORT MANAGER** Karen Foote: 202-326-6740 **ADVERTISING PRODUCTION OPERATIONS MANAGER** Deborah Tompkins **SR. PRODUCTION SPECIALIST/GRAPHIC DESIGNER** Amy Hardcastle **PRODUCTION SPECIALIST** Yuse Lajiminmuhup **SR. TRAFFIC ASSOCIATE** Christine Hall **SALES COORDINATOR** Shirley Young **ASSOCIATE DIRECTOR, COLLABORATION, CUSTOM PUBLICATIONS/CHINA/TAIWAN/KOREA/SINGAPORE** Ruolei Wu: +86-186 0822 9345, rwu@aaas.org **COLLABORATION/CUSTOM PUBLICATIONS/JAPAN** Adarsh Sandhu + 81532-81-5142 asandhu@aaas.org **EAST COAST/E. CANADA** Laurie Faraday: 508-747-9395, FAX 617-507-8189 **WEST COAST/W. CANADA** Lynne Stickrod: 415-931-9782, FAX 415-520-6940 **MIDWEST** Jeffrey Dembski: 847-498-4520 x3005, Steven Loerch: 847-498-4520 x3006 **UK EUROPE/ASIA** Roger Goncalves: TEL/FAX +41 43 243 1358 **JAPAN** Katsuyoshi Fukamizu(Tokyo): +81-3-3219-5777 kfukamizu@aaas.org **CHINA/TAIWAN** Ruolei Wu: +186-0082-9345

WORLDWIDE ASSOCIATE DIRECTOR OF SCIENCE CAREERS Tracy Holmes: +44 (0) 1223 326625, FAX +44 (0) 1223 326532 tholmes@science-int.co.uk **CLASSIFIED advertise@sciencereaders.org** **U.S. SALES** Tina Burks: 202-326-6577 **Nancy Toema**: 202-326-6578 **SALES ADMINISTRATOR** Marci Gallun **EUROPE/ROW SALES** Axel Gesatzki, Sarah Lelange **SALES ASSISTANT** Kelly Grace **Japan** Hiroyuki Mashiki(Kyoto): +81-75-823-1109 hymashiki@aaas.org **CHINA/TAIWAN** Ruolei Wu: +86-186 0082 9345 rwu@aaas.org **MARKETING MANAGER** Allison Pritchard **MARKETING ASSOCIATE** Aimee Aponte

AAAS BOARD OF DIRECTORS **RETIRING PRESIDENT, CHAIR** Phillip A. Sharp **PRESIDENT** Gerald R. Fink **PRESIDENT-ELECT** Geraldine (Geri) Richmond **TREASURER** David Evans **SHAW CHIEF EXECUTIVE OFFICER** Alan I. Leshner **BOARD** Bonnie L. Bassler, May R. Berenbaum, Carlos J. Bustamante, Claire M. Fraser, Laura H. Greene, Elizabeth Loftus, Raymond Orbach, Inder M. Verma

SUBSCRIPTION SERVICES For change of address, missing issues, new orders and renewals, and payment questions: 866-434-AAAS (2227) or 202-326-6417, FAX 202-842-1065. Mailing addresses: AAAS, P.O. Box 96178, Washington, DC 20090-6178 or AAAS Member Services, 1200 New York Avenue, NW, Washington, DC 20005

INSTITUTIONAL SITE LICENSES 202-326-6755 **REPRINTS**: Author Inquiries 800-635-7181 **COMMERCIAL INQUIRIES** 803-359-4578 **PERMISSIONS** 202-326-6765, permissions@aaas.org **AAAS Member Services** 202-326-6417 or <http://membercentral.aaas.org/discouints>

Science serves as a forum for discussion of important issues related to the advancement of science by publishing material on which a consensus has been reached as well as including the presentation of minority of conflicting points of view. Accordingly, all articles published in Science—including editorials, news and comment, and books reviews—are signed and reflect the individual views of the authors and not official points of view adopted by AAAS or the institutions with which the authors are affiliated.

INFORMATION FOR AUTHORS See pages 680 and 681 of the 7 February 2014 issue or access www.sciencemag.org/about/authors

SENIOR EDITORIAL BOARD

A. Paul Alivisatos, Lawrence Berkeley Nat'l Laboratory, Ernst Fehr, U. of Zürich
Susan M. Rosenberg, Baylor College of Medicine, Michael S. Turner, U. of Chicago

BOARD OF REVIEWING EDITORS (Statistics board members indicated with \$)

Adriano Aguzzi, U. Hospital Zürich
Takuzo Aida, U. of Tokyo
Leslie Aiello, Wenner-Gren Foundation
Judith Allen, U. of Edinburgh
Sonia Altizer, U. of Georgia
Virginia Armbrust, U. of Washington
Sebastian Amigorena, Institut Curie
Kathryn Anderson, Memorial Sloan-Kettering Cancer Center
Peter Andolfatto, Princeton U.
Meinrat O. Andreae, Max-Planck Inst. Mainz
Paola Ariotti, Harvard U.
Johan Auwerx, EPFL
David Awschalom, U. of Chicago
Jordi Bascompte, Estación Biológica de Doñana CSIC
Facundo Batista, London Research Inst.
Ray H. Baughman, U. of Texas, Dallas
David Baum, U. of Wisconsin
Kamran Behnia, ESPCI-ParisTech
Yasmine Belkaid, NIAID, NIH
Philip Benfey, Duke U.
Stephen J. Benkovic, Penn State U.
Carlo Beenakker, Leiden U.
Gabriele Bergers, U. of California, San Francisco
Christophe Bernard, Aix-Marseille U.
Bradley Bernstein, Massachusetts General Hospital
Peer Bork, EMBL
Bernard Bourdon, Ecole Normale Supérieure de Lyon
Chris Bowler, Ecole Normale Supérieure
Ian Boyd, U. of St. Andrews
Emily Brodsky, U. of California, Santa Cruz
Ron Brookmeyer, U. of California Los Angeles (\$) **Christian Büchel**, U. Hamburg-Eppendorf
Joseph A. Burns, Cornell U.
Gyorgy Buzsaki, New York U. School of Medicine
Blanche Capel, Duke U.
Mats Carlsson, U. of Oslo
David Clapham, Children's Hospital Boston
David Clary, U. of Oxford
Joel Cohen, Rockefeller U., Columbia U.
Jonathan D. Cohen, Princeton U.
James Collins, Boston U.
Robert Cook-Deegan, Duke U.
Alan Cowman, Walter & Eliza Hall Inst.
Robert H. Crabtree, Yale U.
Roberta Croce, Vrije Universiteit
Janet Currie, Princeton U.
Jeff L. Dangl, U. of North Carolina
Tom Daniel, U. of Washington
Frans de Waal, Emory U.
Stanislas Dehaene, Collège de France
Robert Desimone, MIT
Claude Desplan, New York U.
Ap Dijksterhuis, Radboud U. of Nijmegen
Dennis Discher, U. of Pennsylvania
Gerald W. Dorn II, Washington U. School of Medicine
Jennifer A. Doudna, U. of California, Berkeley
Bruce Dunn, U. of California, Los Angeles
Christopher Dye, WHO
Todd Ehlers, U. of Tuebingen
David Ehrhardt, Carnegie Inst. of Washington
Tim Elston, U. of North Carolina at Chapel Hill
Gerhard Ertl, Fritz-Haber-Institut, Berlin
Barry Everitt, U. of Cambridge
Ernst Fehr, U. of Zurich
Michael E. Ferguson-Smith, U. of Cambridge
Michael Feuer, The George Washington U.
Kate Fitzgerald, U. of Massachusetts
Peter Fratzl, Max-Planck Inst.
Elaine Fuchs, Rockefeller U.
Daniel Geschwind, UCLA
Andrew Gewirth, U. of Illinois
Karl-Heinz Glassmeier, TU Braunschweig
Ramon Gonzalez, Rice U.
Julia R. Greer, Caltech
Elizabeth Grove, U. of Chicago
Kip Guy, St. Jude's Children's Research Hospital
Taekjip Ha, U. of Illinois at Urbana-Champaign
Christian Haass, Ludwig Maximilians U.
Steven Hahn, Fred Hutchinson Cancer Research Center
Michael Hasselmo, Boston U.
Martin Heimann, Max-Planck Inst. Jena
Yka Helariutta, U. of Cambridge
James A. Hendler, Rensselaer Polytechnic Inst.
Janet G. Hering, Swiss Fed. Inst. of Aquatic Science & Technology
Michael E. Himmel, National Renewable Energy Lab.
Kai-Uwe Hinrichs, U. of Bremen
Kei Hirose, Tokyo Inst. of Technology
David Hodell, U. of Cambridge
David Holden, Imperial College
Lora Hooper, UT Southwestern Medical Ctr. at Dallas
Raymond Huey, U. of Washington
Steven Jacobsen, U. of California, Los Angeles
Kai Johnsson, EPFL Lausanne
Peter Jonas, Inst. of Science & Technology (IST) Austria
Matt Kaeblerlein, U. of Washington
William Kaelin Jr., Dana-Farber Cancer Inst.
Daniel Kahne, Harvard U.
Daniel Kammen, U. of California, Berkeley
Masashi Kawasaki, U. of Tokyo
Joel Kingsolver, U. of North Carolina at Chapel Hill
Robert Kingston, Harvard Medical School
Eitonne Koechlin, Ecole Normale Supérieure
Alexander Koldin, Johns Hopkins U.
Roberto Kolter, Harvard Medical School
Alberto R. Kornblihtt, U. of Buenos Aires
Leonid Kruglyak, UCLA
Thomas Langer, U. of Cologne
Mitchell A. Lazar, U. of Pennsylvania
David Lazer, Harvard U.
Thomas Lecuit, IBDM
Virginia Lee, U. of Pennsylvania
Stanley Lemon, U. of North Carolina at Chapel Hill
Ottoline Leyser, Cambridge U.
Marcia C. Linn, U. of California, Berkeley
Jiangui Lu, Michigan State U.
Luis Liz-Marzan, CIC biomaGUNE
Jonathan Losos, Harvard U.
Ke Lu, Chinese Acad. of Sciences
Christian Lüscher, U. of Geneva
Laura Machesky, CRUK Beatson Inst. for Cancer Research
Anne Magurran, U. of St. Andrews
Oscar Marin, CSIC & U. Miguel Hernández
Charles Marshall, U. of California, Berkeley
C. Robertson McClung, Dartmouth College
Graham Medley, U. of Warwick
Yasushi Miyashita, U. of Tokyo
Richard Morris, U. of Edinburgh
Alison Møntsgaard-Reif, NC State U. (\$) **Sean Munro**, MRC Lab. of Molecular Biology
Thomas Murray, The Hastings Center
James Nelson, Stanford U. School of Med.
Karen Nelson, J. Craig Venter Institute
Daniel Neumark, U. of California, Berkeley
Timothy W. Nilsen, Case Western Reserve U.
Pär Nordlund, Karolinska Inst.
Helga Nowotny, European Research Advisory Board
Ben Olken, MIT
Joe Orenstein, U. of California
Berkeley & Lawrence Berkeley National Lab
Harry Orr, U. of Minnesota
Andrew Oswald, U. of Warwick
Steve Palumbi, Stanford U.
Jane Parker, Max-Planck Inst. of Plant Breeding Research
Giovanni Parmigiani, Dana-Farber Cancer Inst. (\$) **Donald R. Paul**, U. of Texas, Austin
John H. J. Petrini, Memorial Sloan-Kettering Cancer Center
Joshua Plotkin, U. of Pennsylvania
Albert Polman, FOM Institute AMOLF
Philippe Poulin, CNRS
David Randall, Colorado State U.
Colin Renfrew, U. of Cambridge
Felix Rey, Institut Pasteur
Trevor Robbins, U. of Cambridge
Jim Roberts, Fred Hutchinson Cancer Research Ctr.
Barbara A. Romanowicz, U. of California, Berkeley
Jens Rostrop-Nielsen, Haldor Tøpsee
Mike Ryan, U. of Texas, Austin
Mitinori Saitou, Kyoto U.
Shimon Sakaguchi, Kyoto U.
Miguel Salmeron, Lawrence Berkeley National Lab
Jürgen Sandkühler, Medical U. of Vienna
Alexander Schlier, Harvard U.
Randy Seeley, U. of Cincinnati
Vladimir Shalaev, Purdue U.
Robert Siliciano, Johns Hopkins School of Medicine
Joseph Silk, Institut d'Astrophysique de Paris
Denis Simon, Arizona State U.
Alison Smith, John Innes Centre
Richard Smith, U. of North Carolina (\$) **John Speakman**, U. of Aberdeen
Allan C. Spradling, Carnegie Institution of Washington
Jonathan Sprent, Garvan Inst. of Medical Research
Eric Steig, U. of Washington
Paula Stephan, Georgia State U. and National Bureau of Economic Research
Molly Stevens, Imperial College London
V. S. Subrahmanian, U. of Maryland
Ira Tabas, Columbia U.
Sarah Teichmann, Cambridge U.
John Thomas, North Carolina State U.
Shubha Tole, Tata Institute of Fundamental Research
Christopher Tyler-Smith, The Wellcome Trust Sanger Inst.
Herbert Virgin, Washington U.
Berth Vogelstein, Johns Hopkins U.
Cynthia Volkert, U. of Göttingen
Douglas Wallace, Dalhousie U.
David Wallace, Weizmann Inst. of Science
Ian Walsmsley, U. of Oxford
David A. Wardle, Swedish U. of Agric. Sciences
David Waxman, Fudan U.
Jonathan Weissman, U. of California, San Francisco
Chris Wilke, U. of Missouri (\$) **Ian A. Wilson**, The Scripps Res. Inst. (\$) **Timothy D. Wilson**, U. of Virginia
Rosemary Wyse, Johns Hopkins U.
Jan Zaenen, Leiden U.
Kenneth Zaret, U. of Pennsylvania School of Medicine
Jonathan Zehr, U. of California, Santa Cruz
Len Zon, Children's Hospital Boston
Maria Zuber, MIT

BOOK REVIEW BOARD

David Bloom, Harvard U. Samuel Bowring, MIT, Angela Creager, Princeton U., Richard Sweder, U. of Chicago, Ed Wasserman, DuPont

Judging synthetic biology risks

Last month, the European Commission (EC) Scientific Committees issued a draft opinion on whether existing risk assessment methods are adequate for synthetic biology. This opinion, which was written by a Working Group of 20 experts from Europe and the United States,* could have a substantial impact on shaping European and global synthetic biology policy for years to come. It is open for public comment through 3 February 2015.†

Synthetic biology already has delivered transformative products to market, from gene therapies that obliterate leukemia to biodegradable plastics synthesized from sugar. Yet since its beginnings at the turn of the century, synthetic biology has been steeped in controversy regarding its potential for societal benefit or harm. In response, the EC requested a scientific opinion on the definition of synthetic biology, the adequacy of risk assessment methods, and research priorities on risk assessment from a joint panel of its Scientific Committees on Consumer Safety, on Emerging and Newly Identified Health Risks, and on Health and Environmental Risks.

Part I was adopted on 25 September 2014 and defined synthetic biology as “the application of science, technology and engineering to facilitate and accelerate the design, manufacture and/or modification of genetic materials in living organisms.” Already, this specification has influenced discussions at the United Nations Convention on Biological Diversity and is making its way into various scientific forums. This definition is important for several reasons. It avoids the traditional focus on conceptual aspects such as “modularity” in favor of a testable definition; it emphasizes that synthetic biology and genetic modification are fundamentally the same and yet continuously evolving fields; and it recognizes that existing regulations and guidelines for biological and genetically modified materials apply to synthetic biology materials. The definition includes the relatively new research areas of genetic parts libraries, designer

cell chassis, DNA synthesis, genome editing, and xenobiology (engineering with noncanonical alternatives to DNA and RNA), but excludes research areas (such as bionanoscience and protocell research) that do not presently generate living organisms.

In Part II (draft released on 19 December 2014), the Committees evaluated whether existing methods are adequate to assess the potential risks associated with synthetic biology research and whether “safety locks” can be built into products of synthetic biology. The group wrestled with a broad set of questions. Will the continual acceleration of genetic modification technologies overburden current risk assessment procedures? What are appropriate comparators for synthetic biology organisms if they diverge substantially from the natural organisms? Will current methods ensure safe practices in nontraditional research realms, such as the do-it-yourself biology movements? The Committees balanced a forecast of major technological developments in the next decade, and the long-term scientific

ambitions of the field. The resulting recommendations encourage standardization and streamlining of the submission of genetic engineering information to risk assessors, suggest the use of genetically modified organisms with a proven safety record as comparator organisms, and call for research to improve the ability to predict the behavior of complex engineered organisms. Moreover, existing genetic safety locks were considered insufficient as a primary strategy to contain the risks of synthetic biology. The development of additional approaches, including genetic firewalls based on noncanonical genetic material, was recommended.

Given the economic weight and thought leadership of the European Union, this opinion on synthetic biology will have substantial global impact. We encourage the scientific community and general public to comment on the draft opinion before the Committees issue the final opinion in spring 2015.

– Rainer Breitling, Eriko Takano, Timothy S. Gardner



“... this opinion on synthetic biology will have substantial global impact.”

Rainer Breitling is a Professor of Systems Biology at the University of Manchester, Manchester, UK, and an external expert to the European Commission Scientific Committees. E-mail: rainer.breitling@manchester.ac.uk

Eriko Takano is a Professor of Synthetic Biology and Co-Director of the Manchester Centre for Synthetic Biology of Fine and Speciality Chemicals (SYNBIOCHEM), University of Manchester, Manchester, UK, and an external expert to the European Commission Scientific Committees. E-mail: eriko.takano@manchester.ac.uk

Timothy S. Gardner is Chief Executive Officer of Riffyn, Inc., in Oakland, CA, USA, and an external expert to the European Commission Scientific Committees. E-mail: tg@riffyn.com

*http://ec.europa.eu/health/scientific_committees/emerging/members_wg/index_en.htm#.

†http://ec.europa.eu/health/consultations/index_en.htm.

“This is a decisive event on the hard road to commercializing transgenic technology in China.”

Statement on **Agrogene.cn**, a website set up by Chinese scientists, after the government this week renewed permits allowing scientists to grow three genetically modified crops.

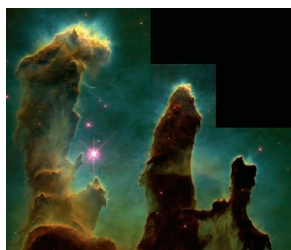
IN BRIEF



Hubble's high-definition update to the iconic Eagle Nebula image.

A fresh look at the 'Pillars of Creation'

In honor of the 25th anniversary of the launch of the Hubble Space Telescope in April, astronomers have taken another snapshot of one of the images that made Hubble famous: the “Pillars of Creation” in the Eagle Nebula. “It’s a new image of an old friend,” said Paul Scowen of Arizona State University, Tempe, presenting the images at a meeting of the American Astronomical Society in Seattle this week. “You can see how far Hubble has come in the past 25 years serving the astronomical community.” Hubble’s instruments have been upgraded since the original image was snapped 19 years ago (inset), so astronomers are able to see more detail and gather



more data than previously. The image shows a region of gas and dust where stars are being born, but much of the material is in the process of being blown away by ultraviolet light from massive young stars elsewhere in the nebula. At the top of each pillar is a denser region that is shadowing material below from light coming in from above, producing the pillar effect.

AROUND THE WORLD

Lawmakers scrutinize monkey lab

WASHINGTON, D.C. | Four members of Congress have asked the National Institutes of Health (NIH) to investigate psychological experiments on monkeys being carried out at an NIH lab in Poolesville, Maryland. The letter, which comes in response to an aggressive campaign by the animal rights group People for the Ethical Treatment of Animals, claims that for more than 30 years researchers at the Eunice Kennedy Shriver National Institute of Child Health and Human Development have been “removing [macaques] from their mothers at birth and subjecting them to distressful and sometimes painful procedures that measure their anxiety and depression.” NIH says it will respond directly to Congress, and that its director will address the letter in detail. http://scim.ag/_monkeylab

Lab animal welfare questioned

WASHINGTON, D.C. | The agency responsible for overseeing lab animal welfare in the United States is not performing as well as it should, according to an audit released in December by the U.S. Department of Agriculture’s (USDA’s) Office of Inspector General. The report claims that USDA’s Animal and Plant Health Inspection Service (APHIS) has been wasting resources inspecting facilities that don’t house animals and that it has been too lax in punishing institutions that don’t comply with animal welfare guidelines. APHIS says it welcomes the report and has already begun working on solutions. <http://scim.ag/labanim>

Push for open access in India

NEW DELHI | Two of India’s major science funding agencies are joining the push to make the results of the research they fund freely available to the public. India’s Ministry of Science & Technology on 12 December announced it will require researchers who receive funding from its biotechnology and science and technology departments to deposit copies of their papers in publicly accessible depositories.



The ant, the plant, and the bear

Black bears inhabiting a mountain meadow in Colorado wield an unexpected influence over a part of the ecosystem—by eating ants, the bears indirectly helped a key plant species called rabbitbrush thrive. Over 4 years, a team of ecologists found, bears damaged or destroyed 26% to 86% of ant nests in the subalpine meadow—and plants lacking ants grew better and produced more seeds. The scientists performed a series of controlled experiments to better understand the complex relationship between bears, ants, and rabbitbrush, including removing all ants from some plants, allowing a few ants on others, and leaving the ants alone on still others. In other tests, they manipulated the number of insect predators on the plants. Although the ants themselves don't directly harm the plants, they scare off predatory insects, allowing treehoppers and other plant-munching insects to take a serious toll on plant growth, the team reported online ahead of print in *Ecology Letters*. <http://scim.ag/antplantbear>

Insect-tending ants can compromise plant growth.

Researchers must post the papers within 2 weeks of acceptance by a peer-reviewed journal, although journals can ask for a 6- to 12-month delay to protect subscription revenue. India's policy, which tracks similar policies adopted by other funding agencies around the world, applies to all research funded since the 2012 to 2013 fiscal year. Institutions will also have to hold annual "Open Access Day" activities that promote the free sharing of results, the policy states. <http://scim.ag/IndiaOA>

STAP cells likely contaminated

TOKYO | Tying up a loose end in a long-running research fiasco, an investigation by Japan's RIKEN research institute has concluded that stem cells created through a supposedly breakthrough process were actually the product of cultures contaminated with regular embryonic stem cells. The breakthrough cells—so-called stimulus-triggered acquisition of pluripotency (STAP) stem cells—were the subject of two *Nature* papers published in January 2014. But the contamination finding "refutes all of the main conclusions of the two papers," a RIKEN panel reported on 26 December, adding that it "suspected that the contamination may have occurred artificially." The committee also found that Haruko Obokata, the lead author of both

papers, was responsible for doctoring two images appearing in one article. Obokata resigned from RIKEN earlier last month. <http://scim.ag/STAPcontam>

Seed banks pay off

SAN DIEGO, CALIFORNIA | Gene banks may soon cease to serve primarily as warehouses of stored plant seeds and begin exploiting the 7 million seed deposits held in repositories all over the world. A new initiative, dubbed DivSeek (for Diversity Seek), will hold its first assembly on 9 January at the annual International Plant & Animal Genome conference in

San Diego. DivSeek aims to mine the often hidden biodiversity in those gene-banked seeds. By systematically characterizing the genetic, physical, and biochemical makeup of banked crop seeds, researchers will track down traits—such as drought tolerance and pest resistance—crucial for future food security. The international consortium of 69 public sector partners, including the Mexico-based International Maize and Wheat Improvement Center and the Philippines-based International Rice Research Institute, will coordinate and prioritize characterization efforts for a host of crops to speed up the creation of new varieties. <http://scim.ag/DivSeek>



A seed bank at Iowa State University in Ames, one of 69 partners in DivSeek.

Antarctic balloon flight cut short

MCURDO STATION, ANTARCTICA | A leak has foiled NASA's record-setting attempt for long-duration scientific ballooning. On 30 December, NASA scientists in Antarctica brought down a gamma ray telescope, called the Compton Spectrometer and Imager (COSI), that had dangled for 2 days beneath a helium balloon 115 meters in diameter. Carried by gentle counterclockwise winds in the stratosphere, COSI was to make circles above Antarctica for 100 days or more. The previous record for a balloon mission, set in 2013, was 55 days. COSI's balloon was equipped with special tendons to allow it to resist changes in volume and avoid fluctuations in altitude. But a leak in the balloon ended the mission early; scientists hope to retrieve the instrument, which landed several hundred kilometers from McMurdo, and the data it collected.

Logging law's impact unclear

WASHINGTON, D.C. | A 2008 law aimed at reducing U.S. imports of products from



Timber from Kalimantan in Indonesia, a major source of tropical timber.

illegal logging appears to be working, concludes an analysis published this month in *Forest Policy and Economics*—but it may not be helping protect the world's forests. The Lacey Act was first passed in 1900 to penalize imports of poached wildlife (helping curb markets for feathers and hides); it was amended in 2008 to cover plant products such as wood, paper, or pulp to discourage illegal logging. The analysis shows that the Lacey Act does appear to be reducing U.S. imports of problematic timber—but the authors note that that

doesn't mean the illegal logging problem is solved, as shady exporters may instead take their products to other nations with laxer regulation. <http://scim.ag/Laceylogging>

How to make a habitable planet

SEATTLE, WASHINGTON | Earth-like exoplanets—with a rocky surface, iron core, and a dash of water—are also likely to be similar in size to Earth, suggests research presented here this week at the American Astronomical Society's annual meeting. The scientists used a spectrograph called HARPS-North, attached to Italy's Galileo National Telescope in the Canary Islands, to measure the mass of 10 smallish exoplanets; the five smallest (no more than 1.6 times Earth's mass) lay on a curve typical of a rocky planet with an iron core (also where Earth and Venus sit), suggesting they “have the same recipe as Earth,” said lead author Courtney Dressing, an astronomer at the Harvard-Smithsonian Center for Astrophysics in Cambridge, Massachusetts, in a press conference. <http://scim.ag/habitarecipe>



The “Jawzall,” consisting of shark teeth mounted onto sawing blades.

A shark-toothed chainsaw

First there was the Sawzall, a reciprocating saw that is the go-to tool for cutting up unwanted material. Now there's the “Jawzall.” Sharks shake their heads as they chomp, ripping prey's flesh; to assess how deadly different shark bites can be, a Cornell University undergraduate and her colleagues mounted four to 10 teeth from four different sharks onto separate sawing blades, then videotaped how well the teeth sliced through a dead salmon after six saws. Tooth performance matched a shark's lifestyle, the researchers reported this week at the annual meeting of the Society for Integrative and Comparative Biology. The tiger shark, which eats crunchy turtles and crustaceans, had the deadliest teeth, breaking the salmon's spine in six cuts, while the large, coarsely serrated ivories of the carrion-eating sixgill shark performed the poorest. After 12 saws, the team found that the teeth dulled quickly—which may limit how often sharks can eat. <http://scim.ag/sharkchainsaw>

BY THE NUMBERS

51,840

Area, in square kilometers, of China's glaciers, according to the Second Glacier Inventory of China—a decrease of 13% compared with the last inventory in 2002.

74%

Orangutan habitat in Borneo lost by 2080, according to models of climate change and deforestation published in *Global Change Biology* this week.

41

Number of new drug approvals by the U.S. Food and Drug Administration in 2014, the fastest pace in the past 18 years.



Positioning a target in the reaction chamber of Laser Mégajoule, France's new €3 billion laser fusion laboratory.

PHYSICS

Laser fusion, with a difference

Europe's Laser Mégajoule project blazes its own trail toward nuclear ignition

By Daniel Clery, in Le Barp, Aquitaine, France

To anyone familiar with laser fusion research, a visit to Laser Mégajoule (LMJ), a €3 billion research facility completed late last year near France's Atlantic coast, triggers instant déjà vu. The site is a dead ringer for the world's leading lab, the National Ignition Facility (NIF) in California. LMJ has the same stadium-sized building, the same shiny white metal framework, the same square beam tubes and 10-meter-wide reaction chamber. The coffee is richer than NIF's, the security less obtrusive, the visitors' area larger and more informative. Overall, however, walking through LMJ's doors is like stepping into a parallel universe in which Lawrence Livermore National Laboratory, the U.S. nuclear weapons laboratory that runs NIF, has somehow come under French control.

The similarities are no coincidence. Both sites were designed for the same purpose—to train scores of powerful laser beams on a single target, subjecting it, for an instant, to outlandish extremes of temperature and pressure. The two labs have collaborated extensively, and the primary mission of each is military: replicating nuclear explosions in miniature so that weapons scientists can ensure their bombs will detonate

if needed without having to test them. The French facility, like its U.S. counterpart, will also pursue a sideline in inertial fusion energy (IFE) research: crushing capsules of hydrogen isotopes with laser pulses so that the isotopes fuse into helium, releasing vast stores of energy that might one day be harnessed in a power plant.

But in a major departure from NIF's initial approach, LMJ is putting top-secret weapons research first. Once NIF was com-

plete in 2009, Livermore researchers immediately embarked on a crash program to achieve ignition—generating a self-sustaining fusion reaction that produces as much energy as went into triggering it. They failed to reach that goal and have since changed their approach (*Science*, 21 September 2012, p. 1444).

"The target of ignition drives the design of the machine."

Pierre Vivini, LMJ project leader

plete in 2009, Livermore researchers immediately embarked on a crash program to achieve ignition—generating a self-sustaining fusion reaction that produces as much energy as went into triggering it. They failed to reach that goal and have since changed their approach (*Science*, 21 September 2012, p. 1444).

France's Alternative Energy and Atomic Energy Commission (CEA), which built LMJ, also wants to achieve ignition, because it's key to both weapons research and energy. "The target of ignition drives the design of the machine," says Pierre Vivini,

LMJ's project leader. But generating power from laser fusion will be left to outside academic researchers, and they won't get their hands on the machine for another 2 years. When they do, some key design differences may give LMJ a better chance of triggering ignition than NIF has. At their core, the two facilities are near-twins. Just as at NIF, LMJ researchers use a fiber laser to produce a pulse of infrared light that lasts a few billionths of a second, with just billionths of a joule of energy. This weak pulse then passes into preamplifiers, slabs of neodymium-doped glass that are pumped full of energy by xenon flash lamps just before the pulse comes through. They dump that energy into the beam, boosting it to about a joule, before the light is split into many parallel beams and sent to the main amplifiers (the same neodymium glass and flash lamps, only bigger).

LMJ has 22 main amplifier chains, arranged in four vast halls around the building, and each amplifier accommodates eight parallel beams at a time. During a laser shot, the eight beams are bounced back and forth through the amplifier four times to multiply their energy by a factor of 20,000. An elaborate array of mirrors will direct the 176 beams around all sides of the spherical reaction chamber; then a final set

of optics will convert the beams from infrared to ultraviolet (UV) light and focus them to a needle-sharp point at the center of the chamber. Recombining all the beams delivers 1.5 megajoules of energy into the target at the center of the chamber—roughly the same as the kinetic energy of a 2-tonne truck traveling at 140 kilometers per hour. NIF's laser delivers 1.8 megajoules.

Because of funding constraints, only one main amplifier chain is now online. But that is enough to get started on nuclear weapons research, says François Geleznikoff, director of nuclear weapons at CEA: "With eight beams we can do good physics. We don't need all the beams to study weapons." The facility will add at least another two chains (16 beams) each year until it reaches full capacity sometime in the next 10 years. Well before then, academic IFE researchers from across Europe have been promised at least 20% of the machine's time. "With 50 shots per year we can really develop a serious program," says plasma physicist Dimitri Batani of the University of Bordeaux in France.

Their game plan includes some significant deviations from NIF's strategy. For example, they've won funding for a separate laser to be installed at LMJ, providing pulses much shorter and more powerful than anything NIF can match. The PETawatt Aquitaine Laser (PETAL) will generate pulses with a relatively modest 3.5 kilojoules of energy, but that energy will be crammed into a trillionth of a second, producing a power of more than a thousand trillion watts—a hundred times that of LMJ's pulses. PETAL's pulses won't be split and delivered from all directions; they'll come from a single direction timed to coincide with a pulse from the main laser. In experiments, they could provide a sudden intense kick of power or could be used like a strobe light to take snapshots of what's going on.

Experiments combining PETAL and LMJ will mimic the conditions in the interiors of stars and other astrophysical objects. Researchers will also use the powerful laser jolts to accelerate protons—an approach that could yield compact accelerators for cancer therapy. But what excites laser fusion researchers is the prospect that the short, sharp blasts from PETAL could act as a spark plug for fusion reactions.

The hope is that using PETAL in this way will allow IFE researchers to avoid some of the pitfalls that have hobbled NIF. The key element of any IFE scheme is the fuel capsule, a plastic sphere about the size of a peppercorn containing frozen deuterium and tritium—isotopes of hydrogen that are the fuel of fusion. Placed at the center of the reaction chamber, the plastic of the capsule is vaporized by the intense heating from the laser pulse, causing an implosion that crushes the fuel to 100 times the density of lead and heats it to 100 million K—which should be sufficient for fusion to ignite.

At NIF and in the weapons research experiments at LMJ, researchers trigger the implosion indirectly by enclosing the capsule in a metal can that is heated by the laser and in turn bombards the capsule with x-rays. That approach offers some

advantages—it smoothes out imperfections in the laser beam, and x-rays are better than UV light at driving the implosion—but it makes the target complex and expensive, not what you want for energy generation. NIF researchers have struggled to make this approach work: Energy is lost in the process of converting light into x-rays, and the implosions do not progress smoothly.

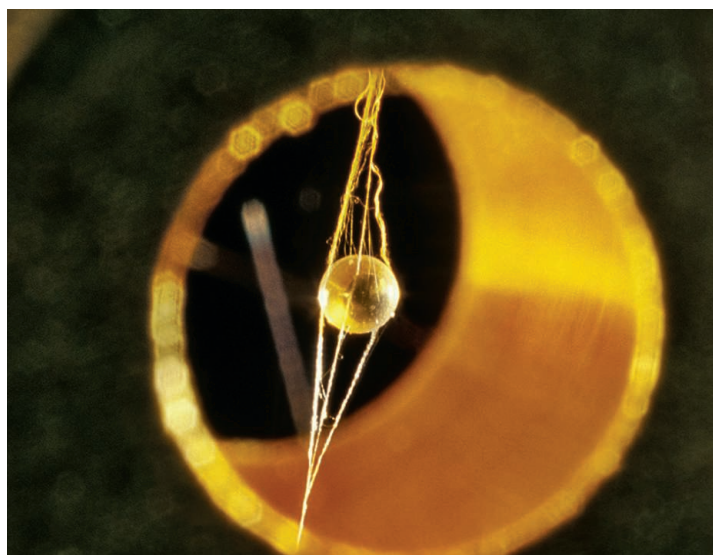
Recent experiments on lower powered machines have suggested that PETAL might not pack enough punch to trigger fast ignition. But another alternative approach, pioneered at the University of Rochester in New York, might save the day. The technique, known as shock ignition, compresses the fuel capsule with a laser pulse from the main laser as in other techniques. But at the end of the pulse, the laser adds

a sudden spike of power to produce a shock wave converging on the center of the fuel. When the shock hits the center, the sudden hike in pressure sparks the reaction. "Experiments at Omega [Rochester's laser] and elsewhere are encouraging, and the laser requirements [for shock ignition] look rather more benign than fast ignition at this stage," says Chris Edwards, a fusion researcher at the Central Laser Facility at the United Kingdom's Rutherford Appleton Laboratory and one of the leaders of HiPER.

In their quest for fusion energy with LMJ-PETAL, researchers face sociological and political challenges, too. The European IFE community is small and is not used to work-

ing with such a huge machine or with weapons lab levels of security. "LMJ alone is like a cathedral in the desert," Batani says. "Researchers are interested, but suspicious. Many are not convinced it is a good tool for research." CEA also needs to overcome its reluctance to share simulation codes with academic researchers for fear of helping rogue nations develop thermonuclear weapons, Batani says: "We need reliable simulations, but there is no open code." And Europe has traditionally focused on a different approach, magnetic confinement fusion, which has its own cathedral not far away: the multibillion-euro ITER, under construction in Cadarache, France.

"If shock ignition on LMJ works, politicians could become more positive," Batani says. And Europe—always an also-ran in this branch of fusion energy—might just gain some boasting rights. ■

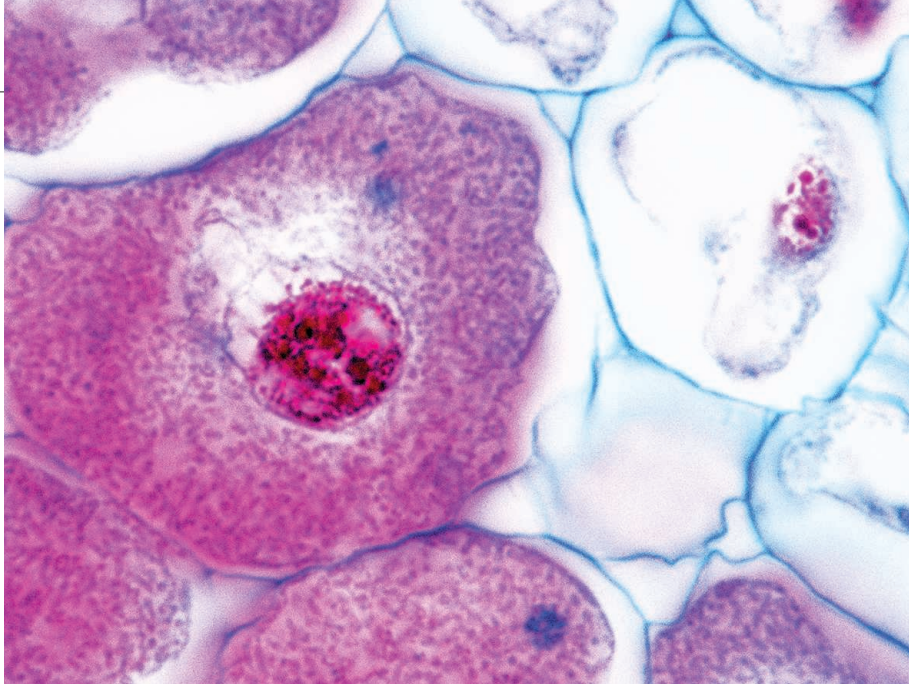


A peppercorn-sized fusion fuel capsule suspended inside its metal can.

advantages—it smoothes out imperfections in the laser beam, and x-rays are better than UV light at driving the implosion—but it makes the target complex and expensive, not what you want for energy generation. NIF researchers have struggled to make this approach work: Energy is lost in the process of converting light into x-rays, and the implosions do not progress smoothly.

IFE researchers outside the weapons labs want to do things differently. By getting rid of the can and targeting beams directly on the capsule, they can avoid the complications and energy loss of converting UV light to x-rays. To get a smooth, symmetrical implosion, many advocate driving it more slowly. But then the compressed fuel won't get hot enough to start reacting on its own; it will need an extra spark to start it off.

One possible solution, known as fast igni-



New U.S. patent office rules explain that a company couldn't patent soil-enriching rhizobium bacteria (within a plant root nodule, left), but could patent a mixture of two bacterial strains if it takes on whole new properties.

says Raul Tamayo, a USPTO senior legal adviser. "Are further tweaks necessary? That's basically what we're looking for."

Many patent experts see the document as an improvement. The agency did "kind of a heroic job" reconciling existing court decisions, says Robert Hardy, director of contracts and intellectual property management for the Council on Governmental Relations, a Washington, D.C.-based association of research universities. Particularly appealing, he says, is that it gives an examiner multiple criteria for deciding whether a product is sufficiently different from its natural counterpart: "structure, function, and/or other properties." He suspects that language could lead to fewer eligibility-based rejections.

The guidance also gives a pass to applications that involve a natural product or process but don't prevent others from using that same product or process in a different way, says Hans Sauer, intellectual property counsel for the Biotechnology Industry Organization in Washington, D.C. "In practice, that could make a big difference," Sauer says, by letting some biotech claims dodge the perilous eligibility test altogether.

Still, Sauer says it is hard to predict what patent evaluators will consider a meaningful difference from nature. Researchers might purify an antibiotic from an organism and alter it to create a medicine without changing its essential bacteria-killing abilities, he says. Does that count as a functional difference? "It seems to me that under PTO guidance the answer is probably no." And demonstrating a functional difference gets even harder, Sauer notes, if a molecule's original "function" in nature is unknown.

Another persistent concern is how evaluators will deal with patents on diagnostic processes or technologies related to personalized medicine, which some fear will be deemed too reliant on unpatentable laws of nature, despite any innovative use. It's not clear, for example, if companies will be able to get a patent on the process of analyzing gene expression from a tumor biopsy to decide on a course of treatment. "Personalized medicine companies ... keep expressing a lot of frustration," Sauer says.

Patent officials are accepting written comments on the guidance until 16 March. Meanwhile, they're keeping an eye on several upcoming court decisions, which could clarify the legal background ... or add another layer of complexity. ■

INTELLECTUAL PROPERTY

U.S. patent office reworks unpopular policy

New guidelines lower the barrier for patenting products derived from nature, quelling some biotech fears

By Kelly Servick

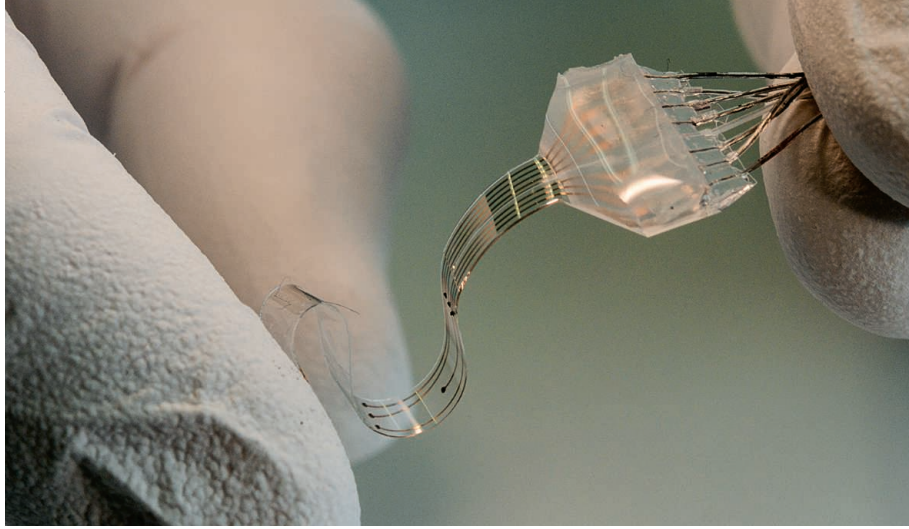
Under pressure from university groups and the biotech industry, the U.S. Patent and Trademark Office (USPTO) is again changing how it evaluates inventions derived from nature. Recent Supreme Court decisions, including a 2013 ruling that struck down patents on human genes, forced the agency to tighten its rules about what is eligible for patent protection. But its attempt to set a new standard last March raised a stink (*Science*, 4 July 2014, p. 14). Now, USPTO is seeking feedback on a revised set of guidelines, released last month, which patent experts suspect will be more favorable to patent filers.

Critics of the March 2014 guidelines claimed they went further than the court's ruling on DNA intended. The guidelines required that other naturally derived products—such as chemical compounds, vaccines, seeds, and antibodies—show structural differences from anything found in nature in order to be considered for a patent. Amid claims that such rules would chill investment and render new therapies and diagnostics unpatentable, the agency vowed to rethink them.

In doing so, USPTO had to respect not only the 2013 Supreme Court decision

(*Association for Molecular Pathology v. Myriad Genetics Inc.*) but also other, murky directions handed down by federal judges, notes Dan Burk, a law professor at the University of California, Irvine. One case, however, offered a way through the legal thicket: the Supreme Court's June 2014 ruling in *Alice Corp. v. CLS Bank International*. There, the justices ruled that financial analysis software is an unpatentable "abstract idea." That may not seem relevant to biotech, but the ruling laid out a two-step test for deciding patent eligibility: If a claim describes "a law of nature, a natural phenomenon, or an abstract idea" (step 1), it must amount to "significantly more" than what's found in nature (step 2) in order to be considered for a patent.

That test forms the backbone of the new USPTO guidance released 16 December, which officials call an "interim" measure, subject to change after new court decisions and stakeholder suggestions. "I have really never seen final guidance at the PTO," says Drew Hirshfeld, deputy commissioner for patent examination policy, who helped draft both the March and December documents. The next round of changes will depend in part on feedback from a 21 January forum at USPTO headquarters in Alexandria, Virginia. The agency wants more input on how to interpret recent cases, including *Alice*,



This flexible, soft electronic implant overcame spinal cord damage in rats.

with the same softness and flexibility as dura mater, the thick protective sheath that surrounds the brain and spinal cord. They started with a 120-micron-thick sheet of rubbery silicone, then used a combination of printing, stamping, and other materials deposition techniques to add seven highly pliable platinum-silicon electrodes and gold interconnects. For example, the gold was riddled with microcracks, a byproduct of the thermal evaporation deposition technique, which helped increase the metal's ability to stretch. They also added a network of microscopic channels to deliver drugs.

Lacour's team first tested the long-term viability of the implants on rats. The researchers inserted the electrode array in the region below the natural dura mater, enabling the electrodes to sit in intimate contact with nerves. Rats in one control group received electrode arrays made from stiffer materials, while a second "sham" group had their dura exposed but weren't given the electrode array. Despite 6 weeks of postsurgery recovery and training, the animals with the stiff implants had severe disruptions in their gait and their ability to walk on their hind legs. But the animals with the soft implants performed as well as the sham-operated controls. Furthermore, the stiff implants were surrounded by astrocytes and microglial cells, while the soft implants lacked these common signs of immune rejection.

In a separate study, Lacour's team implanted the soft electrodes along the spinal cords of rats with paralyzed hindlimbs due to damage to that nerve bundle. The researchers delivered drugs known to promote nerve firing through the channels

and showed the animals regained their ability to walk. They had equally promising results with soft electronic arrays implanted in the brains of mice along the motor cortex, where the electrodes tracked brain activity associated with movement.

Giving implants the suppleness of actual tissue is just a first step toward devices that the body readily accepts. The implants Lacour's team created still have to be wired to the outside world to operate, but she and her colleagues are designing wireless versions of the technology. Watch out, Hollywood, reality is catching up. ■



A CT scan shows a rat spine with implant (red).

BIOELECTRONICS

A soft approach kick-starts cybernetic implants

Mimicking real tissue, novel materials lead to flexible electrode implants that help paralyzed animals walk again

By Robert F. Service

Soft, flexible nerves connected to unyielding silicon and metal—the combination has spawned many a Hollywood cyborg. But in actual cybernetic implants, which aim to restore sensation or movement by marrying electronics with biology, matching hard electronic materials with tissue can be a recipe for failure. On page 159, an international team of researchers reports that a soft touch works better. They created ultrasoft, flexible electronics modeled on real tissue that when implanted along the spinal cord of paralyzed rats restore their ability to walk.

Suppleness had an added benefit, helping the implants avoid triggering rejection by immune system for as long as 6 weeks. "This is fantastic," says John Rogers, a bioelectronics materials expert at the University of Illinois, Urbana-Champaign. "It moves the ball a significant way forward" to creating long-term electronic implants that could, for example, restore a person's mobility or treat neurological ailments such as Parkinson's disease and Tourette syndrome.

Researchers have tested electronic implants in animals for years. But chemical and mechanical mismatches between natural and synthetic materials can spark powerful immune responses that can kill their hosts. In animals that survive, tissue growth around the implant can cut it off electronically, or the rigid implant can detach from the neural tissue it is supposed to manipulate. A 6-week life span for an electrical im-

plant may not seem impressive, but "this is by far the longest" an animal with such a device has lived normally, says Sigurd Wagner, a bioelectronics engineer at Princeton University.

Scientists and engineers such as Rogers and Wagner have long sought to improve implant performance by using flexible plastic substrates or metal electrodes thin enough to bend. In many cases, however, these newer materials still trigger dangerous immune responses, and they aren't as flexible as native muscle and nerve tissues.

So Stéphanie Lacour, a bioelectronics expert at the Swiss Federal Institute of Technology in Lausanne, along with colleagues in Switzerland and the United States, conducted a systematic analysis of how the mechanical properties of different materials correlate with the success of implants. They found that not only do implants need to be flexible to move with bodily tissues, but they must also be soft. The reason, Lacour says, is that even though many plastics are flexible on the millimeter to centimeter scale, they're still too rigid on the microscopic scale, at which the material meets a bundle of nerves.

Lacour's team aimed to make an electronic implant

SPACE SCIENCE

Air Force turns a keen eye on space junk

Flood of data from new “space fence” radar may overwhelm some satellite operators

By Ilima Loomis

Sometimes you'd rather not know the bad news. An estimated 500,000 pieces of space junk—old satellites, rocket parts, debris from collisions—swarm in orbit around Earth. Much of it is potentially deadly: NASA officials say anything larger than 1 centimeter in diameter poses a threat to the International Space Station (ISS). But current tracking systems can generally only watch objects 10 cm or larger, and the U.S. government now follows less than 5% of space hazards—just 23,000 objects.

That should change with the addition of a powerful new Air Force radar system, scheduled to break ground this month on Kwajalein Atoll in the Marshall Islands. When it comes online in 2019, Space Fence is expected to find and track as many as 150,000 additional humanmade objects, some as small as a golf ball, says Dana Whalley, Space Fence program manager, who is stationed at Hanscom Air Force Base in Massachusetts. In addition to enabling the Air Force to better protect Defense Department satellites from collisions, the new system will improve the military's ability to observe and track foreign satellite activity, especially in the busy Asia-Pacific region.

The flood of information passed along to nonmilitary spacecraft operators will bring reassurance—but also some wrenching choices about which hazards to ignore. “It's a bit of a two-edged sword,” says William Lark Howorth, trajectory operations officer for the ISS at NASA. “The whole community is really going to have to start coming up with answers about how do you deal with all the new data you're going to be receiving.”

Being built under a \$914.7 million contract with Lockheed Martin, the new radar will replace an older Space Fence radar on the U.S. mainland that was decommissioned in 2013. The two systems are “like comparing apples to automobiles,” Whalley says. “Their levels of performance are orders of magnitude apart.”

Space Fence gets its name from the beam pattern it will create. Rather than focusing its beam on a particular object of interest, Whalley says, it will “create many little beams,” fanning out to form a picket fence that will intercept objects in low Earth orbit and up to an altitude of 3000 km. Space Fence will also be able to power up a “pencil

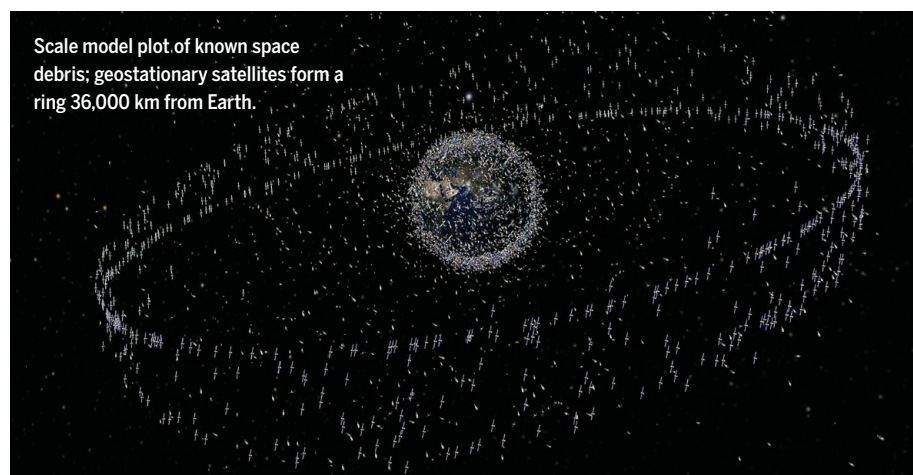
beam” that can track objects in higher orbits or a “minifan” for tracking objects flying lower on the horizon, he says. The beams can track debris more accurately than the earlier Space Fence could. They can also detect smaller objects and reveal the altitude of orbital debris.

These improvements will deliver an unprecedented flood of data about space hazards. Existing Air Force computer systems will be unable to keep up, a 2013 report from Congress's Government Accountability Office (GAO) predicted. A major upgrade of hardware and software at the Joint Space Operations Center, or JSpOC, is now under way, in part to accommodate Space Fence.

Many civilian satellite operators find the coming data deluge from Space Fence as

costs have led the military to downsize earlier, more ambitious plans. Although the original Space Fence design called for Kwajalein to be the first of three radar fences strategically placed around the globe, the Air Force is now planning only a tentative second fence, to be built in western Australia. The second location would generate more accurate predictions by allowing the Air Force to track objects for longer periods throughout their orbits. It would also catch a significant number of objects that can't be observed outside the Southern Hemisphere. Even so, the costs are approaching \$2.1 billion, according to the 2013 GAO report.

One of the biggest impacts of Space Fence might be on space policy, says Brian Weeden, a technical adviser for the Secure



daunting as it is promising. Most collision warnings, they note, turn out to be low risk or false alarms; historically, the ISS has executed avoidance maneuvers only once or twice a year, even though it receives about 12 to 15 warnings a month from JSpOC. Space Fence will increase the number of warnings by as many as 10 times, Howorth says. His office may be forced to significantly increase the time and resources it spends on data analysis, or it may simply ignore some warnings and hope for the best.

Whalley downplays those concerns. With the more accurate tracking data from Space Fence, “we are going to significantly reduce the number of false alarms,” he says. “I think the satellite owners are going to quickly realize that.”

The massive project is already several years behind schedule, and ballooning

World Foundation in Washington, D.C. Weeden notes that Space Fence and other technological advances are drawing new attention to broad questions about how to handle orbital debris and who should decide when, where, and how satellites should maneuver to avoid colliding with one another. Although the role of tracking space traffic has been largely filled by the U.S. military to date, that might change as space becomes increasingly commercial and international.

“It raises interesting questions about what does it make sense for government to do, and what does it make sense for the private sector to do,” Weeden says. “It's no longer just the military that uses space—we all do.” ■

Ilima Loomis is a freelance journalist based in Hawaii.

COMPUTER SCIENCE

Beyond the Turing Test

Concluding that there is no one test for machine intelligence, AI researchers develop a battery of research challenges

By Jia You

As the movie *The Imitation Game* celebrates British mathematician Alan Turing's contributions to the Allied victory in World War II, the artificial intelligence (AI) community is rethinking another of his legacies: the Turing Test.

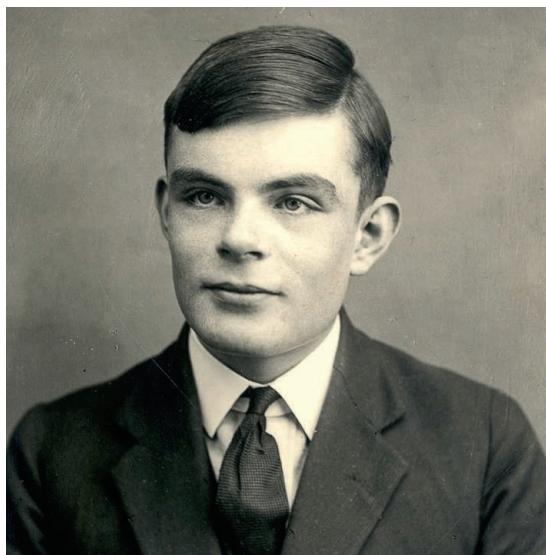
In 1950, Turing laid out an appealingly simple test for whether a machine possesses human-level intelligence: Will a person conversing with it in text mistake it for another human being? But more than 60 years later, it's time for new criteria, says computer scientist Leora Morgenstern of Leidos Inc. in Reston, Virginia. "We now know a lot about AI and what's needed to make progress. It's a big leap from Turing's time."

At a 25 January workshop at the 29th Association for the Advancement of Artificial Intelligence conference in Austin, Morgenstern and other researchers will discuss proposals for a new Turing Championship. In contrast with Turing's single litmus test, the proposed challenges acknowledge that intelligence has multiple dimensions—from language comprehension to social awareness—that are best tackled piece by piece.

Over the years, Turing's original idea has grown into a small industry while drawing increasing criticism. Competitions such as the long-running Loebner Prize ask human judges to text chat with either a person or a computer program for less than 30 minutes and then determine the converser's identity. In June, a computer program named Eugene Goostman, which adopts the persona of a 13-year-old Ukrainian boy, was declared to have passed a Turing Test organized by the University of Reading in the United Kingdom after fooling a third of the judges in 5-minute conversations. Yet researchers such as cognitive scientist Gary Marcus of New York University in New York City argue that such competitions put a premium on stock answers and other ruses. "It's a parlor trick," Marcus says. "There's no sense in which that program is genuinely intelligent." The new Turing Championship

would motivate researchers to develop machines with a deeper understanding of the world, argues Marcus, who is co-organizing the workshop.

One set of proposed challenges focuses on common-sense reasoning, which remains a tall order for machines yet is crucial for comprehending language. Take the sentence, "The trophy would not fit in the



"We can only see a short distance ahead, but we can see plenty there that needs to be done."

Alan Turing, 1950

brown suitcase because it was too big." Deducing that "it" refers to the trophy, not the suitcase, requires general knowledge that is second nature for a person but difficult to program into a machine. Next fall, in what could be the first of the new Turing challenges, the industry-sponsored Winograd Schema Challenge will test machines' comprehension of such grammatically ambiguous sentences.

A second set of proposed challenges centers on machine vision. With new machine-learning techniques that train computers to discern objects, researchers at places such as Google and Facebook are developing algorithms that can guide a self-driving car or automatically identify any face in any

photograph. But AI researchers want machines to understand and reason with what they see, says computer scientist Fei-Fei Li of Stanford University in Palo Alto, California. The challenge Li will propose would ask machines to tell stories from pictures—not only identifying an object such as a coffee mug, for example, but also noting that it sits half-empty on a table because someone drank from it. Such machines might one day interpret what she calls the "dark matter of the digital age": images and videos, which today's search engines and bots can hardly make sense of.

For machines to truly assist people in their daily lives, physical movement smoothly integrated with language and perceptual skills has to be part of the mix, says computer scientist Charles Ortiz of the Nuance Natural Language and AI Laboratory in Sunnyvale, California. His proposed challenge would ask both a machine and a human to manipulate a robotic arm in order to, say, play with a toy. At the same time, they would carry on a conversation about their actions. As in Turing's original test, a judge would evaluate the "humanness" of the computer's performance.

Intelligence has one more dimension, says computer scientist Barbara Grosz of Harvard University: teamwork. To effectively collaborate with humans, machines will need to understand their teammates' preferences, share information appropriately, and handle uncertain environments. Grosz's challenge would pair computers with people in group activities, such as formulating health care plans, to test whether people overlook that their partners aren't human.

Many more research challenges will be debated at the workshop, aimed at capabilities from long-term learning to creativity. The goal, Marcus says, is to winnow the proposals down to three to five competitions. A balance of ambition and realism is key, says computer scientist Stuart Shieber of Harvard. "You want to design competitions that are qualitatively beyond the current level of AI, but not so far that ... it would be like setting an X prize for space flight in da Vinci's era," he says.

Although it's unlikely that consensus will emerge in January, the discussion will continue at another AI conference in July, says co-organizer Manuela Veloso of Carnegie Mellon University in Pittsburgh, Pennsylvania. By early 2016, the organizers hope to stage a set of trial competitions that will be revised and repeated regularly. "If we don't move fast, it won't happen," Veloso says. "People will lose momentum." ■

FEATURES

By Michael Bawaya

One day during fieldwork in March 2010, Charles Beeker was having a drink with his dean and several colleagues at his favorite restaurant in Santo Domingo. Noticing their Indiana University (IU) shirts, an inebriated American staggered over and asked if they were the archaeologists who stole the Captain Kidd shipwreck. The man was an investor in a treasure-hunting operation that had searched for months for the remains of Kidd's ship, the *Quedagh Merchant*, which famously sank off the southeast coast of the Dominican Republic in 1699. But it was Beeker who had identified the wreck and won international press attention.

The investor "started getting a little rowdy," Beeker recalls. There was pushing and shoving, overturned tables and broken glass. "The guy had spent his savings and lost his marriage, and I guess he blamed me."

Such is life for Beeker, the founder and director of the Underwater Science Program at IU Bloomington. "I've been working for years to put treasure hunters out of business," he says. The treasure hunters, for their part, would like to do the same to him. In addition to the occasional fisticuffs, Beeker has been sued (he won), slandered, and harassed by treasure hunters who oppose his efforts to find, protect, and research historic shipwrecks.

To archaeologists such as Beeker, wrecks offer a bounty of information from a single moment in time. But researchers are waging increasingly bitter battles over access to this sunken scientific booty (*Science*, 17 May 2013, p. 802). Treasure hunters are often supported by investors who hope to profit by selling items from the shipwreck, Beeker says; they offer a portion of the take to governments in exchange for diving and salvage permits. Archaeologists can have a hard time competing because we're "selling history, not artifacts," he says.

Beeker, 61, claims some success in this battle, uncovering key information for science and preserving historic wrecks. A big man with a no-nonsense demeanor that can border on gruffness, he is a workaholic who has investigated more than 200 shipwrecks and visited thousands more. Last May, he made the news for evaluating a wreck off the north coast of Haiti that he thinks could be Christopher Columbus's flagship, the *Santa Maria*. Other experts disagree, but Beeker

SALVAGING SCIENCE

Underwater archaeologist Charles Beeker works to preserve famous wrecks as museums

PHOTO: INDIANA UNIVERSITY



Beeker focuses mostly on historic shipwrecks and their diagnostic artifacts, such as a cannon from Kidd's ship (left), but he has also studied a submerged cavern in the Dominican Republic that yielded the skull of a tiny prehistoric primate as well as artifacts left by prehistoric Native Americans.

isn't backing down, and this week he presented his case at the Society for Historical Archaeology meeting in Seattle.

As satisfying as his discoveries have been, Beeker considers his work helping preserve wrecks as dive museums to be his greatest achievement. "Beyond the sustainable tourism value of living museums, we consider the sites living laboratories" for many scientific disciplines, he says.

Establishing underwater museums "is not unique to Charlie," says James Delgado, the National Oceanic and Atmospheric Administration's (NOAA's) director of maritime heritage, who's based in Silver Spring, Maryland, and has known Beeker since the 1980s. But "he is a leading advocate and has done tremendous work ... in the theory and practice of in situ preservation of shipwreck sites and public outreach with them."

BEEKER STARTED DIVING at age 11 and was a scuba instructor by 1974. While working in a paleobotany lab and taking graduate classes at IU, he started a scuba training center and came to realize that his real passion was shipwrecks. By 1984, he was teaching academic scuba diving at IU. His dives have uncovered exquisitely preserved mammal fossils and prehistoric Taíno Indian sites, but his focus has been shipwrecks.

Back in the 1960s and 1970s, historic shipwrecks had no value beyond exploration and plunder. Dive magazines glamorized the looting of wrecks. In the 1980s, Beeker helped change that, serving on a federal advisory committee that helped draft the Abandoned Shipwreck Act of 1987. The act acknowledged the archaeological impor-

tance of historic wrecks and clarified their ownership and management on federal, state, and tribal submerged lands.

At the time, most people thought that the best way to preserve historic shipwrecks was to raise them for display in museums. Beeker and a number of other archaeologists stood that concept on its head, bringing the museum to the wreck rather than the reverse. In 1989, he helped create the San Pedro Underwater Archaeological Preserve State Park in Florida, which features the remains of the *San Pedro*, a Dutch-built ship that sank in 1733. It was plundered by treasure hunters in the 1960s, but divers and snorkelers can still examine ballast stones, seven replica cannons, and an anchor.

Beeker went on to help create 11 more underwater shipwreck parks in Florida and California. By 2000, he and other archaeologists, most with government agencies, had formed a national system of marine protected areas to preserve wrecks. Beeker "is one of the few in the academic field" to push for these museums, Delgado says.

During the past 20 years, Beeker has joined with the government of the Dominican Republic to establish three underwater museums, including the *Quedagh Merchant* site. That's progress, given that a number of treasure hunters, thwarted by preservation laws in the United States, had moved east to the Caribbean, where laws are lax and wrecks plentiful. If a shipwreck isn't in a national park, the Dominican Republic allows treasure hunters to haul up artifacts and sell them, as long as the government gets half the take. "I tell my students we're in the Dominican Republic because we

need to be there," Beeker says.

To wean officials from treasure-hunting revenue, Beeker offered an alternative: Protect wrecks and earn tourism revenue by creating museums in the sea. "You can only sell [a shipwreck] once as a treasure hunt," he told them. "I can sell it forever" as an underwater museum.

The government has bought into the idea. "Beeker has provided [the] Dominican Republic the 'Living Museums in the Sea' model, which preserves shipwrecks as part of our marine environment," says Francis Soto, technical director of the underwater patrimony program of the country's Ministry of Culture, which oversees shipwrecks. "Rather than allow important shipwrecks to be excavated for profit, instead they are preserved for future generations."

Shipwreck museums contain mooring buoys for boats, historic marker buoys, artifacts, and underwater plaques with interpretative information. One, the 1724 Guadalupe Underwater Archaeological Preserve, "is one of the most dived shipwrecks in the Dominican Republic," Soto says, explored by up to 300 people a day, according to Beeker.

The museums are free, but divers bring in revenue by buying equipment, food, lodging, and more. Beeker adds that underwater traffic tends to inhibit rather than promote vandalism, as people tend to be better behaved when observed. The museums also protect the ecosystem that has formed around the wreck. Large artifacts like anchors and cannons offer habitat for hard and soft coral and many kinds of fish, "turning an archaeological project into an envi-

PHOTOS: (LEFT TO RIGHT) INDIANA UNIVERSITY; CHRIS MEYER/INDIANA UNIVERSITY

ronmental project,” Beeker says.

Beeker has “helped to establish the [Dominican Republic’s] conservation capabilities, as well as educating them on archaeological methods and conservation of the sites,” says Steven James, an underwater archaeologist with Panamerican Consultants Inc. in Memphis, Tennessee, who has worked extensively with Beeker. “Not many people can lay claim to that.”

BACK IN 1699, just before he traveled to New York in hopes of acquitting himself of piracy charges, the infamous Kidd abandoned his vessel, and it was sunk off the coast of the Dominican Republic. For more than 3 centuries, the *Quedagh Merchant* rested peacefully in shallow water, somehow eluding treasure hunters, until a snorkeler noticed part of the wreck and alerted government officials. They told Beeker, who visited the site in 2007, then led an investigation that discovered part of the lower hull, 26 guns, a ballast stone, and other artifacts.

To confirm the authenticity of the ship, his team identified the composition of the ballast stone and traced it to western India outside the city of Surat. They also determined that the hull was made of teak and featured rabbet joint construction, in which one piece of wood is notched in order to accept another, a method used in western India, according to Beeker.

These findings all fit with Kidd’s accounts of the ship: The pirate mentioned the Indian construction of his ship in his testimony in New York. “There are thousands of shipwrecks in the Dominican Republic, but this one is the *Quedagh Merchant*,” Beeker says. James concurs: “From what I have seen, everything points to it being correctly identified.”

Kidd’s testimony didn’t save him: He was hanged for piracy on 23 May 1701. On the 310th anniversary of his death, the wreck of his ship was dedicated as a museum.

To further research the wreck, Beeker visited India and found that rabbet joint construction is still used to make teak ship hulls in remote areas outside of Surat. The *Quedagh Merchant* “represents one of the only archaeological examples” of this unique construction, he says.

Beeker’s latest target is even higher profile: the *Santa Maria*. According to historical accounts, the 40-man ship ran aground off the coast of what is now northern Haiti some 500 years ago. Last year, underwater explorer Barry Clifford of Provincetown, Massachusetts, who had a permit to work in Haiti, invited Beeker to examine a wreck there.

Some archaeologists decline any contact with such explorers. “My opinion is that working with treasure hunters sends the

wrong message. I’ve never worked with a treasure hunter,” Delgado says. In contrast, Beeker decided that archaeologists must “be willing to talk with all stakeholders.” He agreed to join forces with Clifford, but only after the pair had some “fairly heated discussions.” Beeker told Clifford he couldn’t “own” the *Santa Maria*, and Clifford agreed that the site and artifacts would be preserved as a museum. “I modified a treasure hunt and turned it into something good for Haiti,” Beeker claims.

He investigated the site in the spring for 4 days and concluded that, although more investigation is required, the wreck could be the *Santa Maria*. International media reported the possible discovery.

But the “find” was short-lived: Last October, a team of experts assembled by the United Nations Educational, Scientific and Cultural Organization (UNESCO) examined

15th century origin for the ship. He saw no copper sheathing and notes that UNESCO hasn’t analyzed the wreck’s wood, ballast, or datable ceramics. He argues that UNESCO’s study offers “no real proof” that the wreck is not the *Santa Maria*. In his talk at the meeting, he revealed that he was able to sample the ballast stone. Its composition included the mineral pigeonite, which is not native to the Caribbean; more analysis is needed to determine if it could have come from Spain.

Ulrike Guérin, a Paris-based program specialist for UNESCO’s Secretariat of the 2001 Convention on the Protection of the Underwater Cultural Heritage, says that their investigation was run by top experts, and Delgado and Roger Smith, the state of Florida’s underwater archaeologist who’s based in Tallahassee, agree. “Everybody wants to make this a controversy,” Smith

Where wrecks rest easy

Charles Beeker has helped establish a number of dive museums that preserve shipwrecks off the coasts of Florida and the Dominican Republic, and he is working to set up more.



the wreck at the request of Haiti’s government. The team determined that the wreck was too far from shore to be the famous vessel and that artifacts in it, such as bronze or copper fasteners, were used in 17th and 18th century shipbuilding, long after Columbus’s time. UNESCO announced that the shipwreck was not the *Santa Maria*, and Haiti’s government rejected IU’s proposal for a detailed investigation.

Although Beeker admits that bronze fasteners are unusual for Columbus’s time, he argues that they alone don’t rule out a

“but to my mind it’s not a controversy; it’s simple archaeology.”

Whatever comes of the *Santa Maria* hunt, Beeker intends to carry on with his work in the Dominican Republic, persuading the public that historic shipwrecks should be preserved. “I’ve seen a lot of people in your government come and go,” Beeker tells residents. But he promises that he’s there to stay. ■

Michael Bawaya is the editor of American Archaeology magazine.



on the trail of **CONTAGION**

One team's quest to find a potential Ebola case in Liberia reveals how difficult it will be to end the epidemic

By Kai Kupferschmidt, in Bong County, Liberia

The only map we have to guide us in our hunt for the Ebola virus looks like a child's drawing, with a simple hospital sketched in the middle and paths snaking away in all directions. It is taped to a wall in the hospital itself, in Fanutoli, a small city in Bong County, in the heart of Liberia. Our team drove here this morning from the regional town of Gbarnga: 90 minutes on pavement, then another hour on a red dirt road. We have come in search of a woman.

Her last name may be Washington or Moses. She may be pregnant. She may be ill. The only thing the search team knows for sure is that she has been in contact with two people who recently died of Ebola. We

need to find her, explains Arthur Mutaawe Lubogo, an epidemiologist from Uganda, and bring her to the county holding center where she can be monitored for 21 days.

The woman's story isn't unusual. She came to the hospital seeking medical care, but when the doctors called an ambulance to take her to a treatment unit to be tested for Ebola, she disappeared into the jungle. County surveillance officer Emmanuel Dweh, who leads the search team, has heard that she fled to a village called Fenemetaa, at the very end of one winding path on the little map. We can only get there on foot, about 2.5 hours through the jungle, a young nurse tells us.

Our party gathers: Dweh; Lubogo and another epidemiologist from the African Union; two people from Doctors Without

Borders (MSF); and a handful of journalists. We pack some water and set off.

TRACING CONTACTS IS CRUCIAL for stopping an Ebola outbreak. You need to find every patient, identify everyone they have interacted with, and monitor them during Ebola's 21-day incubation period. Anyone who starts showing symptoms has to be isolated before he or she infects anyone else. Liberia's official goal is to find each and every contact, but at the height of the epidemic, when tens of thousands of people had been in contact with patients, the task was impossible. Now that the number of cases has declined sharply (*Science*, 28 November 2014, p. 1039), following contacts is much easier, which should make it possible to end the epidemic.

Liberian epidemiologist Emmanuel Dweh at the start of a contact tracing mission to find a woman who has fled to a remote village.

But at a late November meeting in the ministry of health in Liberia's capital, Monrovia, contact tracers talked about the huge difficulties they still faced. They were supposed to tell contacts living in Monrovia not to leave their homes, but there was no system in place to provide people in quarantine with food. There were no thermometers to check them for fever.

And then there's the fact that many people are as afraid of the contact tracers as they are of the disease. They often run away into the jungle for fear of being taken to a treatment unit. Instead they seek help or solace from traditional healers, which puts new people at risk. "This is a new phenomenon and a very worrying one," says Mosoka Fallah, who heads the contact tracing effort in Monrovia. Early prevention messages were counterproductive, says Almudena Marí Sáez, an anthropologist who has worked in Guinea and Liberia, because they emphasized that Ebola is deadly and incurable. "People said, 'Well if you cannot help us, why should we come to you at all?'"

We had seen the consequences that morning on the way to Fenutoli. In a quarantined town named Telata, the empty stalls of a normally bustling market lined the road. Earlier that month, a man from the village had taken in the children of his sister, who had died of Ebola in the capital. When the kids started dying, the man declared that someone who wished him ill had transformed his own spirit into a leopard, which attacked the children—traditional understandings of infection remain common here. The man finally fell sick himself and went to the Bong County treatment unit, where the beds around him soon filled up with other family members, friends, and neighbors. In a cruel irony, he was one of the few to survive.

AS WE SET OFF INTO THE JUNGLE to find the missing woman, thickets of bamboo tower over us. The air smells of wet earth and, strangely, cooked rice. We cross streams and swamps, often bridged by no more than a few logs. Once I lose my balance and fall into a small stream. There are no helping hands as I clamber out, my boots soaking

wet. "We have a no touching policy," I'm told.

The villages along the way are mostly deserted, only a shadow glimpsed behind a hut or a flicker of movement in the trees hinting at any life. In one village, a pot is simmering on an open fire, abandoned. A village elder, a thin man with a weathered face and a small gray beard, appears at a window but does not come out. Dweh asks him if he knows about Ebola. Yes, he says, but no one in the village has symptoms, and he has not heard of the woman we're seeking.

In another village, we find a man called Leopold Glepoli. Dweh has heard that he is a traditional healer who treated the woman. We need to take him to Fenutoli, Dweh tells him, so he can be taken by ambulance to a holding center for Ebola contacts—a couple of tents in a stadium in Gbarnga, where contacts can await the end of the incubation period. If a contact falls ill in one of the

of water, and the sun will set in just a few hours. We turn back.

ON THE WAY BACK, we pick up Glepoli. He is still angry but says he wants to prove his "innocence." Darkness filters slowly into the jungle, the path fades, and the bridges are even more harrowing. Fortunately, Glepoli knows the way. Morten Rostrup, a Norwegian physician working for MSF, tells the story of a multiday trek through the Liberian jungle 15 years ago, during the second civil war. Rostrup and a colleague had heard that a mysterious fever was killing many people in a remote village. "We thought even then that it could be Ebola," he says. But when they arrived at the village, there were no more patients, only graves.

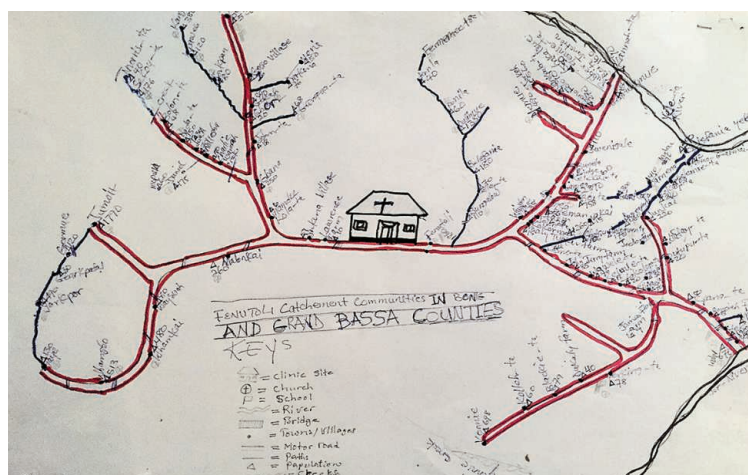
The hours go by and we grow thirsty, hungry, and exhausted. Fran Miller, the other

MSF worker, offers me her last sip of water. "Don't touch the bottle with your mouth," she says. "Pour it into your mouth." When it gets completely dark, we use flashlights, iPhones, whatever we have, to light the way ahead. Then we see other lights approaching through the thicket. It's a search party from Fenutoli, sent out by the drivers, who expected us back hours ago.

After another 30 minutes, we reach the top of a small hill and see Fenutoli below us. It's about 7 p.m. The whole village has come out to meet us. There is applause as we stumble out

of the jungle, dirty and exhausted. Surrounded by the villagers, Glepoli insists that he hasn't been in contact with sick people. A huge cloud flashes with lightning in the distance and Glepoli is working up a rage again, shouting that he doesn't want to go to the holding center. But there is no way to get him there anyway: The ambulance isn't coming today. The villagers don't want him to stay either, so he slips back into the jungle to return to his village.

Glepoli did not get sick. And the woman named Washington or Moses was later found. She "surrendered to the Bong County Health Team," Dweh writes me in an e-mail a few weeks later. Her 21 days passed without her getting sick. In an epidemic that is filled with heartbreak and sad stories, it was the best outcome anyone could hope for. But that night, a happy end seemed as elusive as the fireflies flickering in the depths of the forest. ■



This simple, hand-drawn map helped guide an Ebola team during a 9-hour trek through the Liberian jungle.

remote villages, it becomes almost impossible to get them to a treatment unit. Glepoli, a small man, denies having had any contact with a sick person and angrily rejects the plan. It's already past 1 p.m., and the team decides to push on.

The map proves by and large correct, but Fenemetaa is much farther than the nurse told us. When we arrive after 4.5 hours of strenuous walking, we don't find bodies, sick people—or anyone at all, except for four young men, lounging about in T-shirts, shorts, and sandals. Dweh asks them about the woman and tells them about Ebola. He calls the virus a dangerous poison that she may be carrying inside her.

It's not clear if the men understand. But they say the woman hasn't been in the village. Later, they tell Dweh that she was there but has left. "They are lying," Dweh says, his head low, his eyes sad. "I can see it in their faces." But it is late, we're almost out



PERSPECTIVES



Playing at a normal human pace, one can't beat a computer program for limit Texas Hold'em with statistical significance in a lifetime.

COMPUTER SCIENCE

Solving imperfect-information games

The smallest common poker game, two-player limit Texas Hold'em, is essentially solved

By **Tuomas Sandholm**

Imperfect-information games model settings where players have private information. Tremendous progress has been made in solving such games over the past 20 years, especially since the Annual Computer Poker Competition was established in 2006, where programs play each other. This progress can fuel the operationalization of seminal game-theoretic solution concepts into detailed game models, powering a host of applications in business (e.g., auctions and negotiations), medicine (e.g., making sophisticated sequential plans

against diseases), (cyber)security, and other domains. On page 145 of this issue, Bowling *et al.* (1) report on having computed a strategy for two-player limit Texas Hold'em poker that is so close to optimal that, at the pace a human plays poker, it cannot be beaten with statistical significance in a lifetime. While strong strategies have been computed for larger imperfect-information games as well (2–6), this is, to my knowledge, the largest imperfect-information game essentially solved to date, and the first one competitively played by humans that has now been essentially solved.

The general leading approach for solving imperfect-information games is shown in the figure; for a review, see (7). First, the game is abstracted to generate a smaller but

strategically similar game, reducing it to a size that can be tackled with an equilibrium-finding algorithm. Then, the abstract game is solved for equilibrium or near-equilibrium. A Nash equilibrium defines a notion of rational play. It is a profile of strategies, one per player, such that no player can increase her expected payoff by switching to a different strategy. A strategy for a player states for each information set where it is the player's turn, the probability with which the player should select each of her available actions. An information set is a collection of game states that cannot be distinguished by the player whose turn it is because of private information of the other players. Finally, the strategies from the abstract game are mapped back to the original game.

Carnegie Mellon University, Computer Science Department, Pittsburgh, PA, USA. E-mail: sandholm@cs.cmu.edu

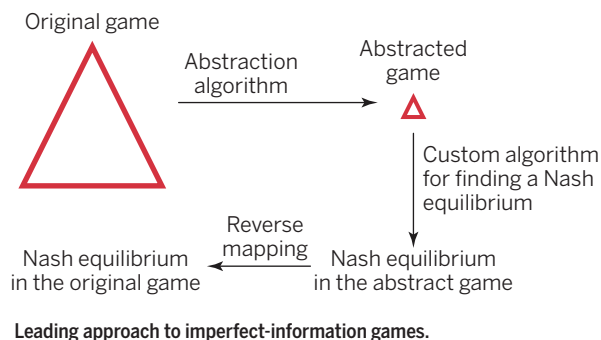
Two main kinds of abstraction are used. One is information abstraction, where it is assumed in the abstract game that a player does not know some information that she knows—that is, information sets are bundled. Lossless abstraction algorithms (8) yield an abstract game from which each equilibrium is also an equilibrium in the original game, and typically reduce the size of poker games by one-to-two orders of magnitude. My group (8) first used them to solve Rhode Island Hold'em, a benchmark introduced in 2001. Bowling *et al.* used lossless abstraction in the form of encoding the game in a way that avoids card suit symmetries. This reduced the number of information sets from 3.19×10^{14} to 1.38×10^{13} . Their scalable equilibrium-finding algorithm enabled them to essentially solve this lossless abstract game. For many larger games, the losslessly abstracted game would still be prohibitively large. Lossy abstraction algorithms (2, 3, 8–10) are used to create a smaller, coarser abstract game. An optimal strategy from such a game is typically not optimal for the original game.

The second method, action abstraction (2, 4, 5, 9), removes some actions from consideration in the game model, and is useful when the number of actions that a player can choose is large. For example, in two-player no-limit Texas Hold'em—a more popular game with 6.38×10^{61} information sets—a player can bet a variable number of chips, unlike in limit Texas Hold'em, where the bet size is fixed. Sophisticated techniques are then needed to map any action that the opponent plays that is not included in the abstract game to an action in the abstract game (6), because the opponent may try to manipulate the action abstraction—by clever bet-sizing in the case of poker.

Empirically, in Texas Hold'em, as a finer-grained abstraction is used, the quality of the strategy improves even when evaluated in the original game. Unfortunately, this is not always the case. Unlike in single-player settings, using a finer-grained abstraction can cause the computed strategy to be worse (more exploitable) in the original game. Despite this, some recent frameworks for lossy abstraction yield bounds on solution quality (5, 9). For a review of abstraction, see (10).

The second step of the game-solving process is finding an equilibrium in the abstract game (as shown in the figure). Before 2006, general-purpose linear programming solvers and the sequence-form representation

were used to solve small variants of poker or coarse abstractions of two-player limit Texas Hold'em. Since then, two families of dramatically more scalable equilibrium-finding algorithms and problem representations have been developed for two-player zero-sum games. One family is based on smoothed gradient descent algorithms and a decomposed problem representation (11, 12). The other family, counterfactual regret minimization (CFR) (13), is based on a form of self-play



using no-regret learning, adapted cleverly so that regret updates can be computed at each information set separately, instead of the naïve approach that would require regrets to be updated for entire game strategies. The best available guarantees for CFR require $\sim 1/\epsilon^2$ iterations over the game tree to reach an ϵ -equilibrium, that is, strategies for the players such that no player can be exploited by more than ϵ by any strategy. The gradient-based algorithms require only $\sim 1/\epsilon$ (11) or $\sim \log(1/\epsilon)$ iterations (12). The latter approach matches the optimal number of iterations required (previously only achievable by interior-point methods that have prohibitive memory requirements). On the other hand, more effective sampling techniques have been developed for CFR than for the gradient-based algorithms, so quick approximate iterations can be used.

The key contribution of Bowling *et al.* is a scalable equilibrium-finding algorithm. It uses full CFR iterations rather than sampling. It distributes the computation across computers by dividing the game into disjoint pieces based on publicly observable information—public cards and past moves of the players—akin to related CFR work (6, 7). The numeric resolution of probabilities was reduced to save memory, with the drawback of slightly reducing solution quality. Careful compression techniques were used to store the game pieces on local disks and to bring them back into memory for updates. To empirically enhance speed, their algorithm never lets the regrets decrease below zero and uses the most recent computed strategies as the solution—instead of average strategies as in CFR convergence proofs.

Bowling *et al.* lower the bar for “solving” the game from finding an exact equilibrium or one within machine precision to requiring that at human playing speed, an adversary could not win with statistical significance in a lifetime. For many applications, this guarantee will be strong enough.

Much work is still required on tackling larger imperfect-information games (2–6). Another key direction is opponent exploitation—taking advantage of suboptimal play. Solely using machine learning for this typically opens oneself up to considerable exploitation in return, and one also typically accrues substantial losses during the learning process. Interesting recent approaches hybridize the game-theoretic approach and opponent exploitation in various ways (14, 15). It is even possible to exploit an opponent’s weaknesses more than any equilibrium strategy would, without opening oneself to any exploitation! This can be accomplished by—and only by—risking in one’s exploitation attempts winnings obtained so far via the opponent’s mistakes rather than luck (16).

Games with more than two players and that are not zero sum also deserve further attention. Most of the abstraction techniques apply here, but these equilibrium-finding problems are in a complexity class for which no polynomial-time algorithm is known. It is not even clear that finding a Nash equilibrium is the right goal in such games. Different equilibria can have different values to the players. If the opponents fail to play an equilibrium strategy, it may not be safe for us to play an equilibrium strategy. Finally, opponents may collude. ■

REFERENCES

1. M. Bowling *et al.*, *Science* **347**, 145 (2015).
2. E. Jackson, *Workshop on Computer Poker and Imperfect Information* (AAAI, Palo Alto, 2013), pp. 35–38.
3. N. Brown, S. Ganzfried, T. Sandholm, in *AAAI Workshop on Computer Poker and Imperfect Information* (AAAI, Palo Alto, 2015); www.cs.cmu.edu/~sandholm/2014champion.pdf
4. J. Hawkin, R. Holte, D. Szafron, in *Proc. 26th AAAI Conf. Artif. Intell.* (AAAI, Palo Alto, 2012), pp. 1924–1930.
5. N. Brown, T. Sandholm, in *Proc. 28th AAAI Conf. Artif. Intell.* (AAAI, Palo Alto, 2014), pp. 594–601.
6. S. Ganzfried, T. Sandholm, in *Proc. 23rd Int. Joint Conf. Artif. Intell.* (AAAI, Palo Alto, 2013), pp. 120–128.
7. T. Sandholm, *AI Mag.* **31**, 13 (2010).
8. A. Gilpin, T. Sandholm, *J. ACM* **54**, 25, es (2007).
9. C. Kroer, T. Sandholm, in *Proc. 15th ACM Conf. Econ. Comput.* (ACM, New York, 2014), pp. 621–638.
10. T. Sandholm, in *Proc. AAAI Conf. Artif. Intell.* (AAAI, Palo Alto, 2015); www.cs.cmu.edu/~sandholm/abstraction.pdf
11. S. Hoda *et al.*, *Math. Oper. Res.* **35**, 494 (2010).
12. A. Gilpin *et al.*, *Math. Program.* **133**, 279 (2012).
13. M. Zinkevich, M. Johanson, M. Bowling, C. Piccione, *Adv. Neural Inf. Process. Syst.* **20**, 905 (2008).
14. O. S. Ganzfried, T. Sandholm, in *Proc. 10th Int. Conf. Autonomous Agents Multiagent Syst.* (IFAAMAS, Richland, SC, 2011), pp. 781–788.
15. N. Bard *et al.*, in *Proc. 12th Int. Conf. Autonomous Agents and Multiagent Systems* (IFAAMAS, Richland, SC, 2013), pp. 255–262.
16. S. Ganzfried, T. Sandholm, in *Proc. 13th Conf. on Electronic Commerce* (ACM, New York, 2012), pp. 587–604.

10.1126/science.aaa4614

RNA

Prescribing splicing

A model predicts the impact of variations in the human genome on RNA splicing and disease

By Roderic Guigó^{1,2} and Juan Valcárcel^{1,2,3}

The unfolding of the instructions encoded in the genome is triggered by the transcription of a gene's DNA sequence into RNA, and the subsequent processing of the primary RNA transcript to generate functional messenger RNAs (mRNAs), which in turn are translated into proteins. DNA sequence variation can influence every step along this pathway, often in association with disease, but the impact of specific sequence variants is difficult to predict. On page 144 of this issue, Xiong *et al.* (1) provide remarkably accurate in silico predictions of the effects of sequence variants on pre-mRNA splicing, a key RNA processing step, including their impact on various human pathologies.

Splicing is the process by which intervening sequences in the primary transcript (introns) are excised and the remaining sequences (exons) concatenated together to form the mRNA sequence (see the figure). It is often invoked as the mechanism by which the human genome (and other genomes) can generate a larger number of RNAs and proteins from a limited repertoire of genes. Indeed, through the alternative combination of exons, multiple mRNA species are usually encoded in a gene's sequence. Although the global importance of alternative splicing regulation in defining cell type specificity is still unknown, many examples document the potential of this process to influence biological outcomes such as sex determination, neural differentiation, synapse formation, or programmed cell death (2). Not surprisingly, alterations in the machinery of the splicing process cause diseases such as spinal muscular atrophy, and an imbalance of alternatively spliced products can contribute to cancer progression as well as muscular and neurodegenerative pathologies (3).

The regulation of transcription is relatively well understood, and as a consequence, mathematical models exist that can predict cell type-specific transcriptional levels of genes with great accuracy (4, 5). By contrast, the mechanisms involved in alter-

native splicing regulation are only partially characterized. The splice sites (relatively conserved short sequences), together with a plethora of other more transcript-specific regulatory motifs, play a role in defining intron-exon boundaries and regulating splice site selection (6). Although advances have been made in predicting differential alternative splice site choices between broad tissue types (7, 8), the algebra relating par-

“...a new era of personalized medicine when individual genomic sequences will be used to predict variations in splicing patterns associated with the onset or progression of pathological conditions.”

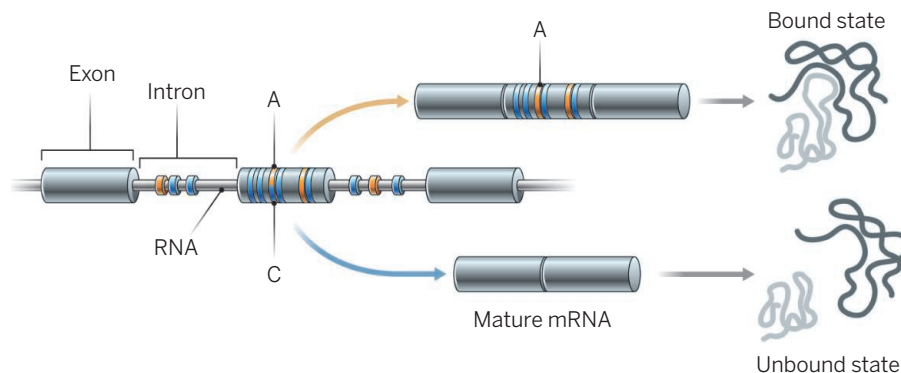
ticular combinations of regulatory motifs to splice site selection in a cell type-specific manner has remained elusive.

Now, Xiong *et al.* have made a successful crack at this algebra. Using sophisticated machine-learning approaches, they built a mathematical model that predicts with substantial accuracy the absolute amounts of exon inclusion in different tissues. The model—a reflection of the complexity of alternative splicing regulation—depends

on nearly 1400 features in the exons and neighboring introns, which often influence exon inclusion in opposite directions depending on the broader sequence context or the specific cell type in which the feature is functional. The features include splice site signals and regulatory motifs, but also exon and intron lengths, mono-, di-, and trinucleotide frequencies, and RNA secondary structures, among others. Xiong *et al.* show that the model successfully integrates this seemingly diverse set of features and predicts the individual as well as the collective effect of RNA binding proteins—the proteins that recognize the splicing regulatory motifs—in the regulation of exon inclusion.

As a demonstration of the general validity of their code, Xiong *et al.* show that the model can predict with substantial precision interindividual variation in exon inclusion elicited by nucleotide changes at single positions (single-nucleotide variants, SNVs) in the sequence of the splicing features. The model provides an unprecedented view of the impact of SNVs on splicing regulation by identifying more than 20,000 unique SNVs likely to affect splicing. These include synonymous changes within protein-coding sequences, generally assumed to be functionally neutral, as well as missense or nonsense changes whose effects on protein expression may be more dramatic than anticipated because of their impact on the splicing process.

This wealth of information has important medical implications. Xiong *et al.*'s model predicts that intronic mutations associated with disease alter splicing 9 times as often as common variants, and the authors argue that their approach is more sensitive than standard genome-wide association studies for capturing splicing-related disease SNVs. Furthermore, they benchmark their method by correctly predicting the outcome of nearly 100 muta-



Alternative splicing. The splicing process removes introns from primary RNA and concatenates exons to generate mature mRNAs. Exons can be included or skipped, thus generating alternatively spliced products that encode different proteins (light gray). The example shows how spliced products could differ by the presence or absence of a domain that interacts with another protein (dark gray). Regulatory sequences in the exons or introns promote (orange) or prevent (blue) inclusion of the alternative exon. Nucleotide differences (e.g., A or C) can alter the function of the regulatory sequences and therefore change the balance between alternatively spliced mRNAs.

¹Center for Genomic Regulation, 08003 Barcelona, Spain.

²Universitat Pompeu Fabra, 08003 Barcelona, Spain.

³Institució Catalana de Recerca i Estudis Avançats, 08010 Barcelona, Spain. E-mail: roderic.guigo@crg.cat

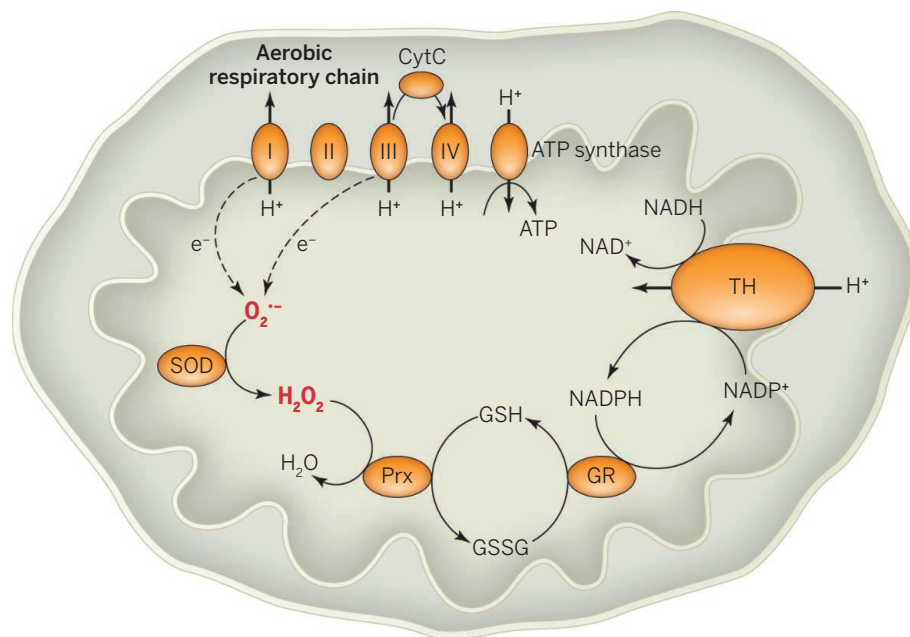
tions in an exon of the *SMN2* gene, whose level of inclusion is the target of emerging therapies for spinal muscular atrophy. In addition, their model explains disease penetrance of silent mutations in hereditary colorectal cancer, and provides interesting candidates for splicing alterations that may play a role in autism. These examples may herald a new era of personalized medicine when individual genomic sequences will be used to predict variations in splicing patterns associated with the onset or progression of pathological conditions.

As is often the case, the past is only the prologue. Although the work of Xiong *et al.* is indeed an important step toward understanding the complex code underlying splicing regulation, a long way remains for it to be fully deciphered. A number of features contributing to the model may reflect the effect of other steps in RNA metabolism not directly involved in splice site selection (e.g., RNA stability or translatability), thus complicating the mechanistic interpretation of the model. Also, there is emerging evidence that splicing occurs mostly cotranscriptionally (9) and that splice site selection can be influenced by the transcriptional machinery, nucleosome positioning (10, 11), epigenetic modifications (12), and possibly three-dimensional chromatin conformation. None of these features are currently captured in the model, but they could certainly be included in future developments. It is also important to remember that the truly functional unit is not the exon but the full mRNA sequence, often composed of many exons and harboring different combinations of sequence variants that affect both coding and regulatory regions. Developments in sequencing technologies and bioinformatic methods should soon make it possible to accurately quantify the cellular abundance of full mRNA species. Understanding and modeling this RNA dynamics in different cell types and along temporal processes is essential to understand how the cells work to form functional tissues and organisms—a goal toward which the study of Xiong *et al.* is a solid step forward. ■

REFERENCES

1. H.Y. Xiong *et al.*, *Science* **347**, 1254806 (2015).
2. T.W. Nilsen, B.R. Graveley, *Nature* **463**, 457 (2010).
3. T.A. Cooper, L. Wan, G. Dreyfuss, *Cell* **136**, 777 (2009).
4. R. Karlič, H.R. Chung, J. Lasserre, K. Vlahovicek, M. Vingron, *Proc. Natl. Acad. Sci. U.S.A.* **107**, 2926 (2010).
5. X. Dong *et al.*, *Genome Biol.* **13**, R53 (2012).
6. Z. Wang, C.B. Burge, *RNA* **14**, 802 (2008).
7. Y. Barash *et al.*, *Nature* **465**, 53 (2010).
8. C. Zhang *et al.*, *Science* **329**, 439 (2010).
9. A.R. Kornblith *et al.*, *Mol. Cell. Biol.* **14**, 153 (2013).
10. H. Tilgner *et al.*, *Nat. Struct. Mol. Biol.* **16**, 996 (2009).
11. S. Schwartz, E. Meshorer, G. Ast, *Nat. Struct. Mol. Biol.* **16**, 990 (2009).
12. R.F. Lucio *et al.*, *Science* **327**, 996 (2010).

10.1126/science.aaa4864



Mitochondrial ROS defense. Transhydrogenase (TH) contributes to mitochondrial ROS defense by producing NADPH. During aerobic respiration, electrons leak to molecular oxygen, primarily from complexes I and III. This results in “superoxide anions” $O_2^{\cdot -}$, which is converted to H_2O_2 by mitochondrial superoxide dismutase (SOD) and finally to water by peroxidases (Prx), using reduced glutathione (GSH). GSH levels are maintained by glutathione reductase (GR), which uses NADPH formed by TH to reduce glutathione (GSSG).

BIOCHEMISTRY

Coping with oxidative stress

A crystal structure helps to explain how cells detoxify

By Ute Krenkel¹ and
Susanna Törnroth-Horsefield²

Ever since living systems began to use molecular oxygen for efficient energy generation, they have had to deal with its detrimental by-products. Reactive oxygen species (ROS), which are mainly formed in the mitochondria, cause oxidative damage to cellular components and have been implicated in several pathological conditions, including cancer, diabetes, and Alzheimer's and Parkinson's diseases, as well as in cell death and aging (1). To minimize oxidative stress, cells have developed defense machineries that can neutralize ROS. On page 178 of this issue, Leung *et al.* (2) report the crystal structure of nicotinamide nucleotide transhydrogenase (TH), a key enzyme in this defense machinery.

The mitochondrial ROS defense system transforms reactive superoxide anions ($O_2^{\cdot -}$), formed by electrons leaking to molecular oxygen during aerobic respiration, to hydrogen peroxide (H_2O_2) (see the first figure). Hydrogen peroxide is detoxified to water by peroxidases that use reduced glutathione (GSH) as

a substrate. High GSH levels are maintained by reduced nicotinamide adenine dinucleotide phosphate (NADPH)-dependent glutathione reductase, and this is where TH (a key contributor of mitochondrial NADPH) comes into the story. TH is present in the inner membrane of animal mitochondria and the cytoplasmic membrane of many bacteria. Under normal physiological conditions, it couples the hydride transfer between reduced NAD (NADH) and NAD phosphate ($NADP^+$) to proton translocation across the membrane (see the first figure). NADPH production by TH is thus directly coupled to the rate of aerobic respiration, and hence ROS production (3).

Ever since TH was discovered more than 40 years ago, its main physiological role has been assumed to be mitochondrial NADPH production (4). In 2005, Arkblad *et al.* reported direct evidence that the enzyme is indeed involved in ROS defense, showing that a TH knockout mutant of the worm

¹Department of Chemistry, University of Oslo, NO-0315 Oslo, Norway. ²Department of Biochemistry and Structural Biology, University of Lund, SE-22100 Lund, Sweden. E-mail: ute.krenkel@kjemi.uio.no; susanna.horsefield@biochemistry.lu.se

Caenorhabditis elegans was much more sensitive to oxidative stress than the wild type (5). At about the same time, Toye *et al.* reported a link between TH and diabetes, showing that the glucose intolerance and impaired insulin secretion of a particular mouse strain, C57BL/6J, mainly results from reduced expression of TH (6).

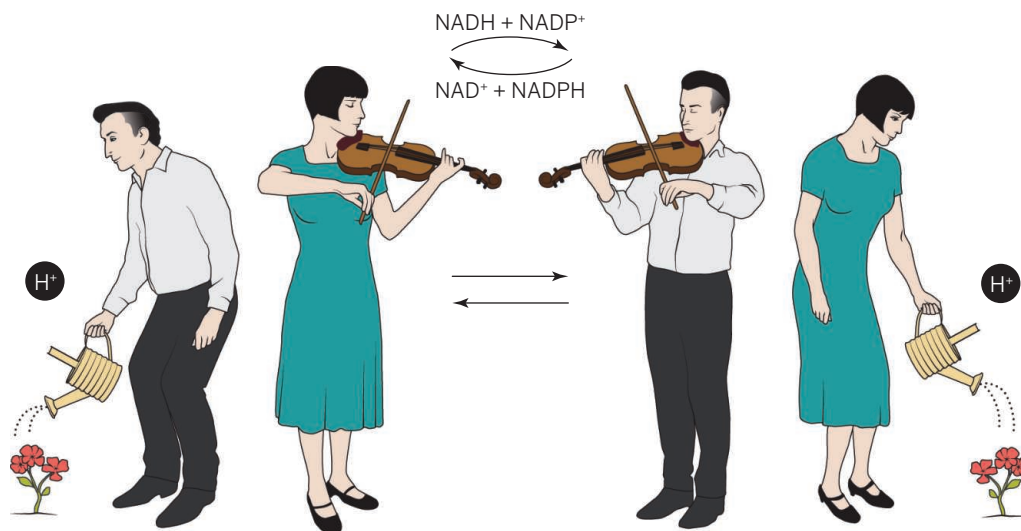
The TH enzyme forms a homodimer, with each half consisting of three domains: one integral membrane domain (dII) and two soluble domains (dI and dIII) that protrude into the mitochondrial matrix (animals) or

with cysteine cross-linking studies. The results allow a glimpse into the workings of the intact enzyme.

The complete structure of TH reveals a highly asymmetric dimer. The main surprise is the upside-down orientation of the second dIII domain relative to its counterpart in the other half of the enzyme; this orientation positions the NADP(H) binding site of dIII close to the exit of the proton channel. Judging from the cryo-EM data, this domain is highly mobile. Although the exact coupling mechanism remains to be elucidated, it is

protein function but do not involve rotatory movement. Instead, conformational changes of transmembrane helices form the basis of the “alternating-access” model, in which a substrate binding site switches between being accessible from one side of the membrane to the other (11).

Curiously, TH, with its 180° rotation of dIII and shuttling between proton pumping and hydride transfer (see the second figure), combines features of both the rotation and alternating-access models. With respect to its conformational coupling of proton pump-



Sharing the load. The TH mechanism is analogous to a couple sharing their load by alternating between two mutually exclusive tasks. In a free interpretation, the legs represent the membrane domain dII, the head domain dI, and the body domain dIII, which displays the largest movements, with the arms rotating 180°. Through this rotation, dIII has access to either the dII or the dI domains, thus coupling proton pumping by TH efficiently with hydride transfer and lowering cellular stress.

cytosol (bacteria). The two soluble domains bind NAD(H) (dI) and NADP(H) (dIII), respectively. Crystal structures of these domains have allowed the hydride transfer mechanism between the dI and dIII domains to be elucidated (7), but the complete mechanism has remained elusive in the absence of a crystal structure of the dII domain. In particular, it has been unclear how hydride transfer is coupled to proton translocation through the membrane. Moreover, it has been difficult to envisage how the second dIII domain could be accommodated in the dimer without steric clashes.

Leung *et al.* now address all of these shortcomings. The authors report the crystal structures of the complete TH enzyme (to 6.9 Å resolution), the sought-after dII domain (2.8 Å), the dI dimer (1.8 Å), and the asymmetric complex between two dI domains and one dIII domain (2.4 Å), all from the same organism, *Thermus thermophilus*. They further investigated the structure of TH by cryo-electron microscopy (cryo-EM; 18 Å) and supported their structural data

clear that dIII shuttles between two highly different structural states, related to each other by a 180° rotation. In one of these states, the NADP(H) binding site is solvent-accessible and close to the proton exit site; in the other, the binding site is occluded and in close contact with NAD(H) in dI, allowing hydride transfer. The two states cannot exist simultaneously in the assembled dimer, promoting alternation and coupling of the two events.

It is interesting to compare TH with another conformationally coupled proton pump, the well-characterized adenosine triphosphate (ATP) synthase (8). Both enzymes use the proton-motive force to power perpendicular rotations, leading to the synthesis of important biomolecules. Furthermore, both enzymes use binding-change mechanisms that rely on protein asymmetry (9, 10). Some secondary transporters, such as proton-driven carbohydrate transporters of the major facilitator superfamily, also depend on the proton-motive force. Here, conformational changes again lie at the heart of

protein function but do not involve rotatory movement. Instead, conformational changes of transmembrane helices form the basis of the “alternating-access” model, in which a substrate binding site switches between being accessible from one side of the membrane to the other (11).

The complete structure of TH, resolved 40 years after its original discovery, adds to the portrait gallery of important cellular machines, allowing yet another fascinating molecular mechanism to be explored. TH elegantly uses the proton-driven rotation of a soluble domain (dIII) to provide alternating access to the two other domains, hence switching between proton pumping and

hydride transfer. It achieves this by dividing the labor equally between the two protein halves, taking turns at the job (see the second figure). A lesson to be learned is that to efficiently manage stress, whether oxidative or not, we would do well to share the workload with our (better) halves. ■

REFERENCES

1. T.R. Figueira *et al.*, *Antioxid. Redox Signal.* **18**, 2029 (2013).
2. J.H. Leung *et al.*, *Science* **347**, 178 (2015).
3. J. Rydstrom, *Trends Biochem. Sci.* **31**, 355 (2006).
4. N.O. Kaplan, S.P. Colowick, E.F. Neufeld, *J. Biol. Chem.* **195**, 107 (1952).
5. E.L. Arkblad *et al.*, *Free Radic. Biol. Med.* **38**, 1518 (2005).
6. A.A. Toye *et al.*, *Diabetologia* **48**, 675 (2005).
7. V. Sundaresan, J. Chartron, M. Yamaguchi, C.D. Stout, *J. Mol. Biol.* **346**, 617 (2005).
8. A.G. Stewart, E.M. Laming, M. Sobti, D. Stock, *Curr. Opin. Struct. Biol.* **25**, 40 (2014).
9. D.D. Hackney, G. Rosen, P.D. Boyer, *Proc. Natl. Acad. Sci. U.S.A.* **76**, 3646 (1979).
10. J.B. Jackson, *Biochim. Biophys. Acta* **1817**, 1839 (2012).
11. P.J. Henderson, S.A. Baldwin, *Nat. Struct. Mol. Biol.* **20**, 654 (2013).
12. R. Baradaran, J.M. Berrisford, G.S. Minhas, L.A. Sazanov, *Nature* **494**, 443 (2013).

10.1126/science.aaa3602

Dynamics of a cold quantum gas

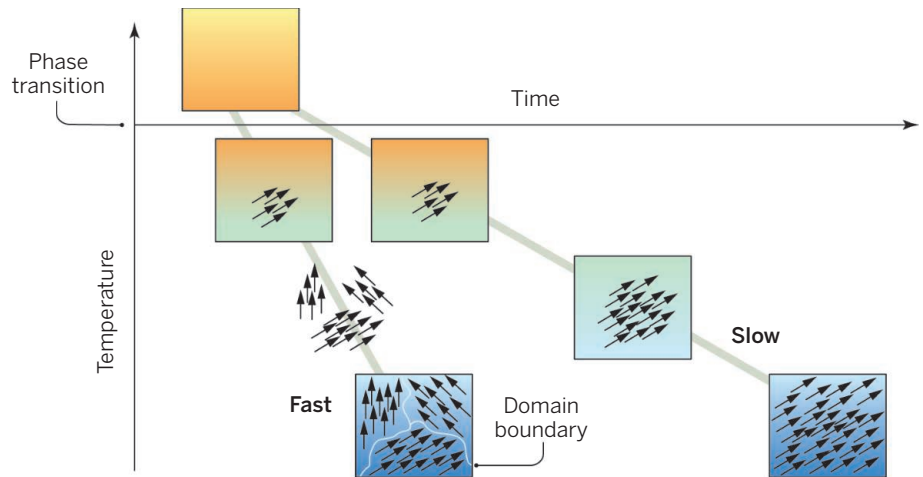
A cloud of cold atoms provides a route to understanding complex phase transitions

By **Gabriele Ferrari**

All physical systems evolve in response to changes in their internal parameters and modifications of the environment in which they are embedded. Water vapor in cold air, for example, forms crystals, and this crystallization produces snowflakes, the size and shape of which are determined by parameters such as the rate of cooling, the humidity of the air, and the number of ice nuclei present. Similar complex dynamics can be found in any system, classical or quantum, crossing a phase transition in a dynamical process out of equilibrium. On page 167 of this issue, Navon *et al.* (1) reveal the dynamics of a transition crossing by following the evolution of a system of cold atoms at the transition from the thermal to the Bose-condensed phase.

Phase transitions are ubiquitous in nature. One reason for their attractiveness is the fact that, in many cases, they imply the breaking of one or more symmetries of the Hamiltonian describing the system, with the appearance of an order parameter. At the transition point, the system spontaneously picks one of the many equivalent choices for the newborn order parameter. If the process is faster than the typical time scale for equilibration, different parts of the system may acquire different order parameters, thus creating spatially independent domains. These domains then grow and eventually approach one another, giving rise to domain boundaries or defects (see the figure).

An elegant theoretical framework for understanding such nonequilibrium processes is provided by the Kibble-Zurek (KZ) theory (2, 3). The key prediction of the theory is a power-law dependence of the density of defects on the quench time; that is, the time scale over which the phase transition is crossed. This power-law involves the static and dynamic critical exponents, usually designated as ν and z , that determine the divergent behavior of the correlation length and the relaxation time of the system close to the transition. The KZ mechanism is expected to be universal. It was first introduced in the context of cosmological models and then extended to condensed-matter systems.



Making a transition. Cooling a Bose gas across a transition toward the condensed phase. At faster cooling rates, the gas condenses without “knowing” what is happening in neighboring regions. Hence, after crossing the critical temperature, the condensate’s wave function grows homogeneously, or forms grains with independent phases, depending on the rate at which the gas is cooled.

Navon *et al.* report on a very clean measure of the KZ scaling law in a homogeneous Bose gas. They study the spatial correlation properties of a dilute ultracold gas of rubidium atoms rapidly cooled across the critical temperature for Bose-Einstein condensation.

With dilute Bose gases, the effects of the KZ mechanism were already observed in the spontaneous generation of quantized vortices in harmonically trapped Bose-Einstein condensates (BECs) (4, 5). The power-law scaling of the number of defects with the quench time has been also verified for defects created in an elongated BEC (6). However, the extraction of useful information about the critical exponents from the experimental data is a challenging task, and first indications were obtained in a system at reduced dimensions (7).

Navon *et al.* developed an ingenious approach in which the experimental setting, with clever use of a boxlike trapping potential, allows for a clear comparison between the experimental data and the theoretical predictions. Conflicts between different theoretical predictions can be directly settled, hence providing new insight on the critical exponents ν (8) and z , the latter having not been measured so far.

The approach developed by Navon *et al.* has the potential to be a trailblazer for a whole new family of experiments on critical phenomena relying on ultracold

gases and on the wonderful experimental tools they offer. For instance, consider the role of interactions at thermodynamic critical points, a topic debated at length over the last decades. Experiments based on naturally occurring condensed-matter systems, such as liquid helium at the normal-to-superfluid transition, or superconductors, could not provide evidence to discriminate among different theories: In these systems, most of the parameters are set by nature, leaving us with few options to get the right answer.

However, atomic physicists know how to vary the thermodynamic properties of ultracold gases, and to tailor interactions among atoms (9). Now, they have the means to vary both of them, to shed new light on one of the most challenging problems in modern physics. ■

REFERENCES

1. N. Navon, A. L. Gaunt, R. P. Smith, Z. Hadzibabic, *Science* **347**, 167 (2015).
2. T. Kibble, *J. Phys. Math. Gen.* **9**, 1387 (1976).
3. W. H. Zurek, *Nature* **317**, 505 (1985).
4. L. E. Sadler, J. M. Higbie, S. R. Leslie, M. Vengalattore, D. M. Stamper-Kurn, *Nature* **443**, 312 (2006).
5. C. N. Weiler *et al.*, *Nature* **455**, 948 (2008).
6. G. Lamporesi, S. Donadello, S. Serafini, F. Dalfovo, G. Ferrari, *Nat. Phys.* **9**, 656 (2013).
7. L. Corman *et al.*, *Phys. Rev. Lett.* **113**, 135302 (2014).
8. T. Donner *et al.*, *Science* **315**, 1556 (2007).
9. C. Chin, R. Grimm, P. Julienne, E. Tiesinga, *Rev. Mod. Phys.* **82**, 1225 (2010).

Istituto Nazionale di Ottica-Consiglio Nazionale delle Ricerche, BEC Center and Dipartimento di Fisica, Università di Trento, 38123 Povo, Italy. E-mail: ferrari@science.unitn.it

CELL BIOLOGY

Making sense of amino acid sensing

Biochemically and spatially diverse intracellular mechanisms couple the activity of a cell growth regulatory complex to the availability of amino acids

By Robert T. Abraham

Mammalian cells integrate nutrient and growth factor availability with anabolic responses to support cell growth and proliferation. A key signaling hub in this process is the mechanistic target of rapamycin complex 1 (mTORC1) (1, 2). Growth factor receptors deliver activating signals to mTORC1 primarily through the phosphoinositide 3-kinase (PI3K)–AKT signaling cascade. However, amino acid sufficiency activates mTORC1 through a family of guanosine triphosphatases (GTPases) called Rags (3, 4). The lysosome is now recognized as a key intracellular organelle involved in mTORC1 activation by amino acids and growth factors (5). A candidate amino acid sensor for lysosome-based activation of mTORC1 has now been identified by Wang *et al.* (6) on page 188 of this issue, and by Rebsamen *et al.* (7). However, studies by Thomas *et al.* (8), and by Jewell *et al.* (9) on page 194 of this issue, demonstrate that amino acid sensing is not the sole domain of either the lysosome or its associated Rag GTPases. These four studies advance substantially our understanding of the amino acid-sensing machinery in mammalian cells.

Mammalian cells express four Rag GTPases that assemble into heterodimers containing RagA or RagB partnered with RagC or RagD (2, 10). Functionally active heterodimers contain guanosine 5'-triphosphate (GTP)-loaded RagA/B bound to guanosine 5'-diphosphate (GDP)-loaded RagC/D. The accumulation of active Rag heterodimers on the cytoplasmic surface of the lysosome is promoted by an amino acid-responsive supercomplex that includes the pentameric Ragulator complex and the multisubunit vacuolar ATPase (vATPase) complex. In the active configuration, the Rag heterodimer recruits mTORC1 to the lysosomal membrane, thereby initiating the process of mTORC1 activation. A distinct small GTPase called Rheb is also anchored to the lysosomal membrane, and its mTORC1-activating function is pro-

moted by the mitogen-stimulated PI3K pathway. Thus, the lysosomal membrane represents the site at which the amino acid- and growth factor-sensing machineries converge to stimulate mTORC1 (10). A logical, though as yet unproven, extension of this model is that the lumen of the lysosome harbors a pool of amino acids that is monitored by the mTORC1-activating machinery. The identification of a membrane protein that links luminal amino acids to the mTORC1-activating machinery on the lysosomal membrane would provide strong support for this prediction. Now, Wang *et al.* and Rebsamen *et al.* report that a mem-

“The lysosome is now recognized as a key intracellular organelle involved in mTORC1 activation by amino acids and growth factors.”

ber of the solute carrier (SLC) family of proteins, SLC38A9, is a strong candidate for a proximate amino acid sensor in such a pathway.

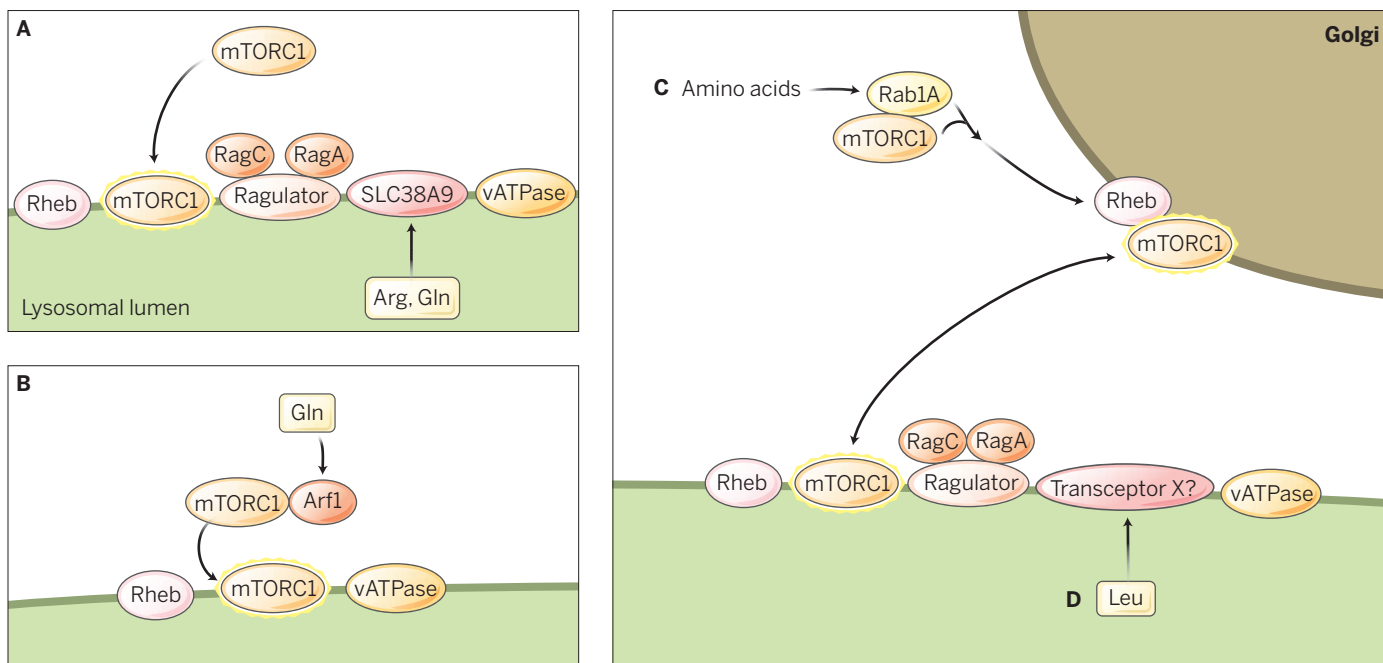
The solute carriers constitute the second largest family of transmembrane proteins (second only to the heterotrimeric GTP-binding proteins), with ~400 genes encoding these carriers in humans (11). Collectively, they mediate the flow of biomolecules, ions, and xenobiotics across plasma membranes, typically using ionic gradients as the driving force for solute transport. The SLC38 subfamily contains 11 members that function as sodium-coupled amino acid transporters. Wang *et al.* used an immunoproteomic approach to identify a specific isoform of SLC38A9 (SLC38A9.1), as a transmembrane protein associated with the lysosomal Rag-Ragulator complex. Rebsamen *et al.* zeroed in on SLC38A9 by mining databases for ubiquitously expressed, lysosomally localized amino acid transporters of unknown function. SLC38A9 contains 11 predicted transmembrane domains and an N-terminal domain that protrudes into the cytoplasm. The N-terminal domain

is necessary and sufficient to bind the Rag-Ragulator complex. A reduction in SLC38A9 expression by RNA interference blunted the increase in mTORC1 signaling induced by amino acids, whereas overexpression of the solute carrier rendered mTORC1 signaling insensitive to amino acid depletion.

Several amino acids, including leucine, arginine, and glutamine, have been identified as effective activators of mTORC1 (8). Consequently, both Wang *et al.* and Rebsamen *et al.* examined the amino acid transport functions of recombinant SLC38A9 embedded in liposomal vesicles. Wang *et al.* characterized SLC38A9 as a low-affinity arginine transporter and showed that disruption of the gene encoding SLC38A9 suppressed mTORC1 activation by arginine, but not leucine. Rebsamen *et al.* report that SLC38A9 transports glutamine as well as arginine, and demonstrate that SLC38A9-mediated glutamine efflux from proteoliposomes. Amino acid efflux activity is consistent with the proposed role of SLC38A9 as a sensor of luminal amino acid content in lysosomes. Both studies also show that SLC38A9's interaction with the Rag-Ragulator complex is modulated by amino acids, suggesting that this solute carrier is an upstream regulator of Rag-Ragulator and, in turn, mTORC1 activation in mammalian cells (see the figure). Collectively, these results suggest that SLC38A9 is a “transceptor” whose primary function is to initiate signaling through the Rag-Ragulator complex, rather than to mediate bulk amino acid transport.

The discovery of the SLC38A9 transceptor supports the Rag-Ragulator-based model of mTORC1 activation by amino acids (5, 12). Both Wang *et al.* and Rebsamen *et al.* acknowledge that other amino acid sensors will likely be uncovered in mammalian cells. Indeed, Jewell *et al.* and Thomas *et al.* show that amino acids can stimulate mTORC1 independently of the Rag-Ragulator complex. Jewell *et al.* demonstrate that mTORC1 is responsive to amino acids in cells lacking both RagA and RagB. Interestingly, the authors found that RagA/B-deficient cells could not activate mTORC1 in response to leucine stimulation, but were competent to respond to glutamine. Stimulation of mTORC1 by glu-

Oncology Research Unit, Pfizer Worldwide Research and Development, 10646/CB4 Science Center Drive, San Diego, CA 92121, USA. E-mail: robert.abraham@pfizer.com



Amino acid sensing. (A) The lysosome harbors amino acids [such as arginine (Arg), and possibly glutamine (Gln)] that are monitored by the membrane transceptor SLC38A9. This sensor couples amino acid transport to activation of the Rag-Ragulator complex, and, in turn, mTORC1. (B) Gln is also sensed by Arf1, which recruits mTORC1 to the lysosome where it is activated in a vATPase-dependent, but Rag-Ragulator-independent, mechanism. The location of this Gln pool is unclear. (C) mTORC1 also is activated by amino acids on Golgi membranes. Rab1A recruits mTORC1 to this organelle, where it is activated by Rheb. Potential interactions of endomembrane and vesicular structures may propagate amino acid-dependent signals to mTORC1 at multiple subcellular locations. (D) Lysome-associated leucine (Leu) is postulated to be sensed by an unidentified transceptor (Transceptor X) linked to the vATPase and RAG protein complexes.

tamine was dependent on the lysosome and the activity of the vATPase. Moreover, Jewell *et al.* show that the mTORC1 regulation by glutamine is strongly dependent on the small GTPase Arf1 in RagA/B-deficient cells. Treatment of these cells with brefeldin A, an Arf1 inhibitor, blocked both the lysosomal localization and activation of mTORC1 through a mechanism unrelated to the inhibitory effects of brefeldin A on vesicular transport from the endoplasmic reticulum to the Golgi apparatus. Whether the responses to glutamine observed by Jewell *et al.* are attributable directly to this amino acid or to a product(s) of glutamine metabolism remains unclear.

Thomas *et al.* uncover another, at least partially, Rag-independent mechanism of mTORC1 activation, initially through analyses of amino acid responsiveness in budding yeast cells lacking orthologs of the mammalian Rag GTPases. The yeast studies identified yet another small GTPase, the paralog of mammalian Rab1A, as an essential mediator of signaling from amino acids to TORC1. Subsequent experiments in mammalian cells confirmed these results and implicate the Golgi apparatus as the membrane structure on which Rab1A tethers mTORC1 for activation. This occurs in part through close apposition to Rheb, which is found in the Golgi as well as on lysosomal membranes. Thomas *et al.* ob-

served that Rab1A is overexpressed in most colorectal cancers and that high-level overexpression correlates with aggressive disease, hyperactivation of mTORC1 signaling, and rapamycin sensitivity.

In addition to the need for a full definition of the number, individual components, and interdependencies of these sensing pathways, several pivotal, physiological questions remain to be answered. Foremost is how the amino acid-sensing mechanisms that converge on mTORC1 regulate mTORC1 activity in vivo. The standard protocol to study amino acid starvation and stimulation responses in cultured cells involves complete removal of amino acids from the culture medium, followed by the addition of single amino acids or amino acid mixtures. Although this protocol has helped to delineate the biochemistry of amino acid sensing and response, cells residing in bodily tissues are normally bathed in nutrients, including more than one mTORC1-activating amino acid. Perhaps growth factor abundance regulates intracellular amounts of amino acids by governing the expression of amino acid transporters in the plasma membrane. In addition, a considerably more detailed understanding of the composition of lysosomal amino acid pools in nutrient-starved and -replete cells is needed to fully comprehend the regula-

tion of mTORC1 by this organelle. Additional research is also required to define the mechanism of amino acid sensing by Golgi-associated mTORC1. Given the established functions of Rab and Arf GTPases in vesicular transport, the proposal that amino acids regulate the vesicular trafficking of lysosome-associated mTORC1 to the Golgi and other endomembrane structures merits further evaluation (13). The results presented by Rebsamen *et al.*, Wang *et al.*, Jewell *et al.*, and Thomas *et al.* almost certainly foreshadow the complexity yet to be uncovered regarding amino acid sensing by mTORC1. ■

REFERENCES

1. R. Zoncu, A. Efeyan, D. M. Sabatini, *Nat. Rev. Mol. Cell Biol.* **12**, 21 (2011).
2. J. L. Jewell, R. C. Russell, K. L. Guan, *Nat. Rev. Mol. Cell Biol.* **14**, 133 (2013).
3. Y. Sancak *et al.*, *Science* **320**, 1496 (2008).
4. E. Kim, P. Goraksha-Hicks, L. Li, T. P. Neufeld, K. L. Guan, *Nat. Cell Biol.* **10**, 935 (2008).
5. R. Zoncu *et al.*, *Science* **334**, 678 (2011).
6. S. Wang *et al.*, *Science* **347**, 188 (2015).
7. M. Rebsamen *et al.*, *Nature* **10.1038/nature14107** (2015).
8. J. D. Thomas *et al.*, *Cancer Cell* **26**, 754 (2014).
9. J. L. Jewell, *Science* **347**, 194 (2015).
10. C. C. Dibble, B. D. Manning, *Nat. Cell Biol.* **15**, 555 (2013).
11. P. J. Höglund, K. J. Nordström, H. B. Schiöth, R. Fredriksson, *Mol. Biol. Evol.* **28**, 1531 (2011).
12. Y. Sancak *et al.*, *Cell* **141**, 290 (2010).
13. J. Sanchez-Gurmaches, D. A. Guertin, *Cancer Cell* **26**, 601 (2014).

10.1126/science.aaa4570

MATERIALS ASSEMBLY

Designing two-dimensional materials that spring rapidly into three-dimensional shapes

Buckling of sheets can be engineered to rapidly create complex shapes

By **Chunhong Ye** and **Vladimir V. Tsukruk**

One of the hallmarks of living organisms, including humans, is the ability to actively respond and adapt to stress. Even plants, which lack a nervous system, react to different stimuli by changing their shape. Some well-known examples are the wrinkled edges of leaves as a response to compression during growth, wrinkles of skin to accommodate flexing and bending movements or age-drying stresses, or the mimosa's rapid folding of its leaves via propagating waves of osmotic pressure when touched. Similar phenomena have been used in engineered artificial two-dimensional (2D) materials that can respond to external stimuli, but these applications typically are simple, slow, and work only along one dimension. On page 154 of this issue, Xu *et al.* (1) demonstrate a new paradigm of designing functional materials that can quickly snap into complex 3D architectures via localized buckling.

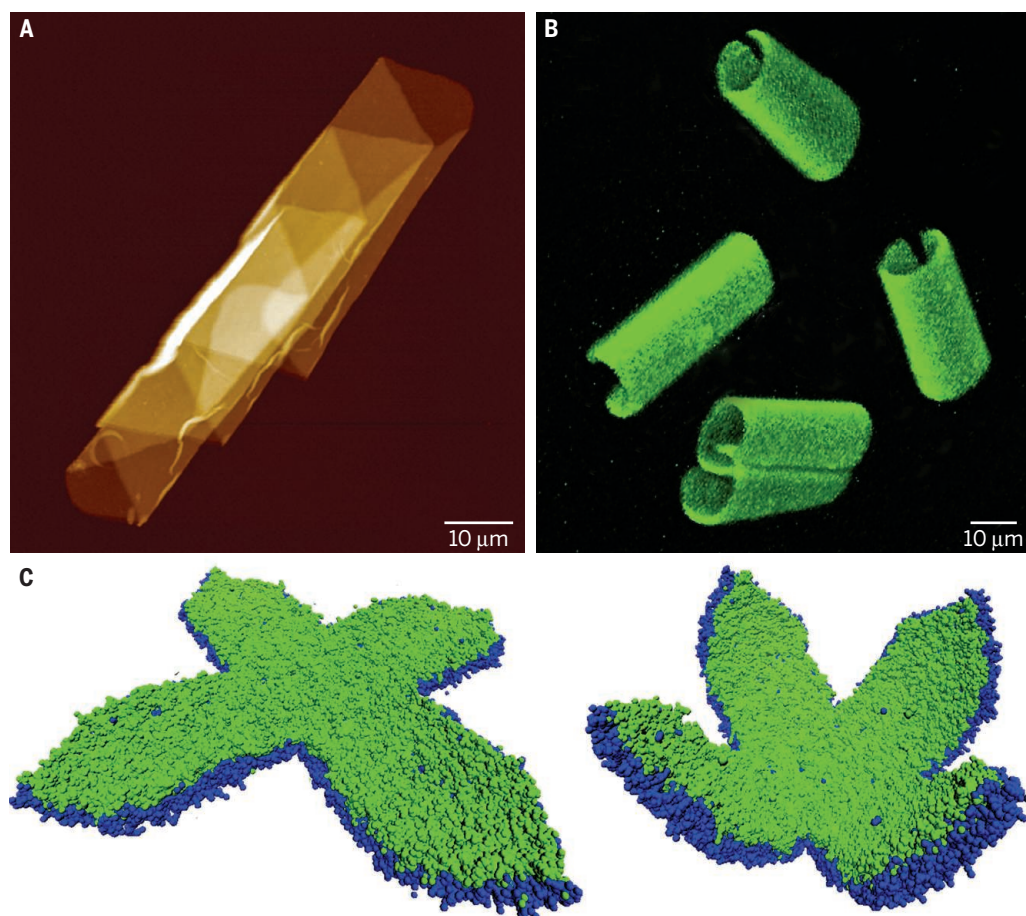
Buckling phenomena have been widely explored as a means for measuring elastic properties of ultrathin polymer films (2), as periodic templates for organized nanoparticle assemblies (3), as a complex patterning approach for metal-polymeric sandwiched films (4), for bistable patterning of nanoparticle-polymer multilayers (5), and for chiral patterning of periodic porous materials (6). The underlying physics of wrinkle formation is well understood and arises from the mechanical instability that develops in compressed thin films (7). However, all of these phenomena have an essentially 2D nature, with "penetration" into the third dimension being extremely limited. Furthermore, attempts to overstress the mate-

rials result in irregular large-scale folding and crumpling.

Thus, efforts to break through into the realm of 3D shapes now exploit controlled interfacial stresses. Among them are multistep folding of polymer bilayer films into 3D pyramids and "flowers" (8), chemomechanical mediation of a gel-embedded high-aspect ratio nanorod array (9), self-rolling of helical microtubes from laterally patterned hydrogel sheets (10), and self-rolling of bilayer gel sheets with different shapes into helical and smooth tubules (11) (see the figure, panels A and B). Complex shapes can also be induced by thermal control of out-of-plane transformation of gels with halftone-patterned cross-linking (12). These

transformations and the resulting 3D shapes are predicted by either analytical considerations for simple shapes (7, 8) or finite-element analysis for complex shapes (9).

In the case of nanoscale materials, more sophisticated computer modeling is required to predict corresponding transformations (see the figure, panel C). Moreover, tuning composition, thickness, and mechanical properties with fine resolution can be a very challenging feat of materials engineering. Even if some astonishing examples of shape transformations have been demonstrated, these materials are usually slow to respond (on a time scale of minutes), frequently require controlled environment (e.g., swollen hydrogels need liquid water or humidity),



Getting into shape. (A) An atomic force microscopy image shows a silk self-rolling helical microtube. (B) Confocal microscopy image of pH-stimulated self-rolling microtubes created from silk bilayer sheets. (C) Coarse-grain computer models of Janus flowers shown in relaxed and stress-responsive conditions.

School of Materials Science and Engineering,
Georgia Institute of Technology, Atlanta,
GA 30332, USA. E-mail: vladimir@mse.
gatech.edu

and are often limited to fairly simple shapes and transformation paths.

New design principles for materials with fast-snapping microstructures suggested by Xu *et al.* cleverly combine conventional uniform compressive stresses with multiple preprogrammed “weak” points that allow buckling to occur in a hierarchical fashion. Compressive stresses initiate a cascade of buckling events that spring the initial surface-confined planar architectures into 3D complex structures. In this way, various metal and silicon serpentes and ribbons are converted into a collection of microscopic tents, tables, baskets, flowers, boxes, stars, and many other shapes. An amazing variety of conveniently separated “first floor” and “second floor” buckled microstructures are demonstrated as well.

Although the prospective applications of this technique are astounding in breadth and impact, there are more intriguing questions to address. How can the extremely tedious planar processing of large-scale microfabrication be improved or replaced by more facile approaches, such as directed assembly, with similar outcomes? Can these architectures be “unbuckled”—for example, can an open box be closed? Can these structures eventually be sustainable in their 3D shape as stand-alone structures after release from supporting substrates? How does snapping into a 3D architecture affect the global functions of nanostructured constructs, such as electronic, optical, or magnetic properties? Can structures that mimic the mimosa, in which a highly localized stimulus with a pinpoint compression results in a rapid cascade of 3D shape transformations, be made on much larger scale? And finally, what are the limits of scale? Perhaps one day, if you order a house complete with furnishings and a white picket fence, you may just receive a box with a label that reads, “Compress to unfold.” ■

REFERENCES AND NOTES

1. S. Xu *et al.*, *Science* **347**, 154 (2015).
2. C. M. Stafford *et al.*, *Nat. Mater.* **3**, 545 (2004).
3. A. Schweikart, N. Pazos-Pérez, R. A. Alvarez-Puebla, A. Fery, *Soft Matter* **7**, 4093 (2011).
4. N. Bowden *et al.*, *Nature* **393**, 146 (1998).
5. C. Jiang, S. Singamaneni, E. Merrick, V. V. Tsukruk, *Nano Lett.* **6**, 2254 (2006).
6. J. Shim *et al.*, *Soft Matter* **9**, 8198 (2013).
7. J. Genzer, J. Groenewold *et al.*, *Soft Matter* **2**, 310 (2006).
8. G. Stoychev *et al.*, *Adv. Funct. Mater.* **23**, 2295 (2013).
9. A. Grinthal, J. Aizenberg, *Chem. Soc. Rev.* **42**, 7072 (2013).
10. Z. L. Wu *et al.*, *Nat. Commun.* **4**, 1586 (2013).
11. C. Ye *et al.*, *Adv. Funct. Mater.* **24**, 4364 (2014).
12. J. Kim *et al.*, *Science* **335**, 1201 (2012).

ACKNOWLEDGMENTS

We thank A. Alexeev for computer simulation images and R. Geryak for assistance. Supported by Air Force Office of Scientific Research grant FA9550-14-1-0269 and NSF grants DMR-1002810 and CBET-1402712.

10.1126/science.aaa2643

MATERIALS SCIENCE

Using all energy in a battery

Controlled electrode structure improves energy utilization

By Nancy J. Dudney and Juchuan Li

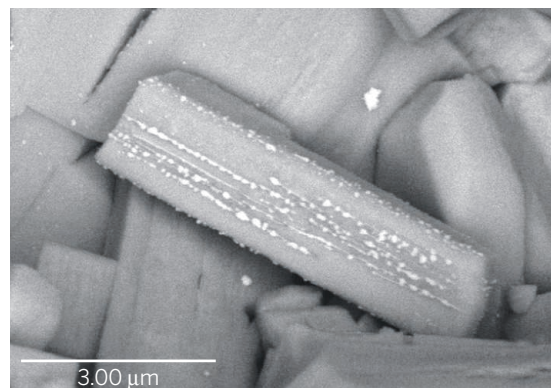
It is not easy to pull all the energy from a battery. For a battery to discharge, electrons and ions have to reach the same place in the active electrode material at the same moment. To reach the entire volume of the battery and maximize energy use, internal pathways for both electrons and ions must be low-resistance and continuous, connecting all regions of the battery electrode. Traditional batteries consist of a randomly distributed mixture of conductive phases within the active battery material. In these materials, bottlenecks and poor contacts may impede effective access to parts of the battery. On page 149 of this issue, Kirshenbaum *et al.* (1) explore a different approach, in which silver electronic pathways form on internal surfaces as the battery is discharged. The electronic pathways are well distributed throughout the electrode, improving battery performance.

Commercial battery electrodes (anodes and cathodes) are typically created by casting a porous powder composite (a mixture of the active material, a small amount of polymer binder, and a conductive additive such as carbon) onto a metal foil current collector. Electrons are conducted via chains of particles through the composite to the current collector. In contrast, ions move through the liquid or solid electrolyte that fills the pores of the composite. Optimization of both pathways is critical for battery performance. Although this slurry-cast electrode structure works very well, better control of the three-dimensional (3D) architecture would enhance the energy per unit mass and volume of the electrode. Cobb and Blanco recently reported an important step in this direction by creating a cathode consisting of alternating low- and high-density stripes. The low-density stripes provide higher porosity and better access for ions traveling through the liquid electrolyte into the cathode (2).

Kirshenbaum *et al.* now report the fabrication and performance of a silver vanadium phosphate cathode with a well-defined 3D architecture. The cathode

consists of relatively dense thick pellets without binder or conductive additives. When Li^+ ions and electrons move into the silver vanadium phosphate particles, V^{4+} is reduced to V^{3+} and Ag^+ is reduced to metallic silver; the latter remains at the surface of the active material particles as small silver particles, presumably electrically connected by a thin layer of Ag (see the image for a micrograph following such a reaction). Under the right conditions, the silver forms an effective electronic path throughout the electrode, enhancing the insertion of Li^+ into the cathode lattice and hence increasing the amount of accessible energy in the battery.

Such reduction displacement reactions, also known as conversion reactions, occur upon Li^+ reaction with a wide range of binary and bimetallic oxide, fluoride, and sul-



Silver particles grow on the surface. Scanning electron micrograph of a silver vanadium phosphate cathode after reduction with Li (15). The composition of the material is similar but not identical to that studied by Kirshenbaum *et al.*

fide compounds (3). These materials have potentially very high energy densities that may yield rechargeable and low-cost battery materials. The biggest challenge for practical use of such reversible conversion electrodes is the voltage penalty, where the voltage of the battery during discharge (conversion) is much less than the voltage needed for recharge of the battery (reconversion). It remains unclear how much of this voltage penalty is intrinsic and how much of it is a result of kinetic limitations that could in principle be minimized (4, 5).

Material Science and Technology Division, Oak Ridge National Laboratory, Post Office Box 2008, MS 6124, Oak Ridge, TN 37831, USA. E-mail: dudney@ornl.gov

Many studies have shown the advantages of intimate “wiring” of the active battery electrode particles with the electronic conducting component. Robust physical or chemical bonds formed during cosynthesis or annealing of the active particles with conductive fibers (see the second figure, panel B) give superior performance during charge-discharge cycling compared with traditional electrodes (see the second figure, panel A) (6–8). However, fibrous or templated 3D structures are generally difficult to form as a dense body. Conversion electrodes such as those reported by Kirshenbaum *et al.* (see the figure, panel C) provide improved density by forming an internal conductive network through electrochemical reaction. Bonding of the conversion particles (as in the second figure, panel C) to a conductive carbon fiber scaffold through high-temperature processing (as in the second figure, panel B) not only prevents capacity loss but also reduces the voltage penalty to recharge the battery (9).

Kirshenbaum *et al.* analyze the distribution of discharge products for their model cathode materials in an extraordinary level of detail. They use energy dispersive x-ray diffraction (EDXRD) to probe the intact battery. Although not noted by the authors, the results indicate a slight accumulation of metallic Ag at both faces of the electrode. This distribution is similar to that in at least one other study of a thick electrode, where the distribution was attributed to the relative transport rates of reactants from opposing directions (10).

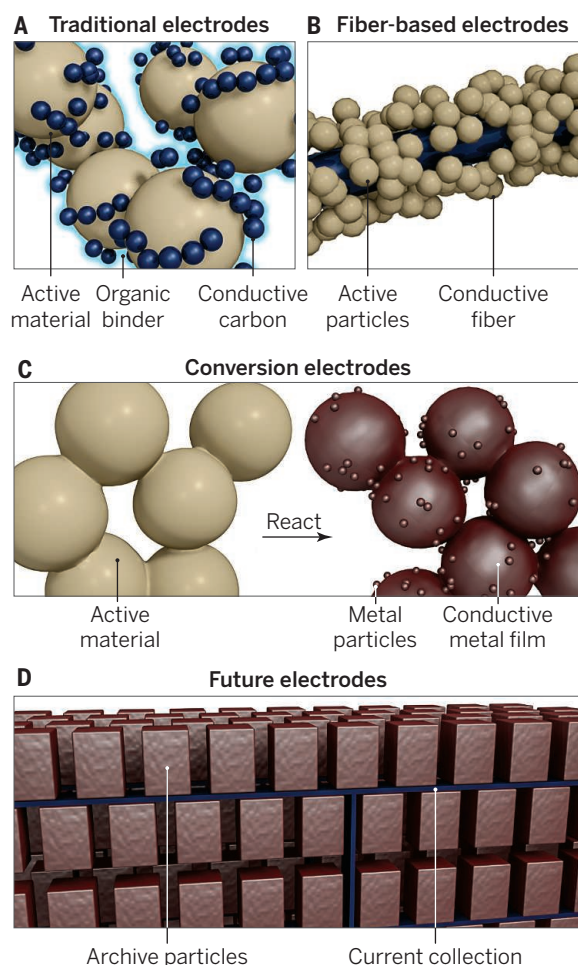
Kirshenbaum *et al.* focus instead on the equally intriguing result that the silver metal distribution and discharge performance is very sensitive to the discharge rate: When the current drawn early in the discharge is reduced by a factor of 3, the metallic silver is distributed more uniformly and capacity utilization is higher. The authors attribute this sensitivity to the tendency for the active particles to crack upon rapid lithium addition, which creates more internal surface

and nucleation sites for the silver clusters. Support for this idea comes from Woodford *et al.* (11), who have predicted a critical discharge rate based on particle size and the diffusion-induced stress above which brittle battery particles are likely to fracture.

Other advanced in situ methods are also helping researchers to visualize the complex chemical and structural changes during charge-discharge reactions. Transmission neutron diffraction analysis has revealed strong changes in the active electrode material located close to the edges of a large battery electrode sheet after substantial cy-

cling (12). This method cannot resolve any gradients across the thickness of the battery electrodes, but can map lateral inhomogeneities along the battery area from edge to edge. Synchrotron radiation x-ray tomographic microscopy provides dramatic maps of changes in both electrode structure and chemical content with cycling. Ebner *et al.* recently used this method to study Li addition into SnO particles in a carbon matrix, revealing swelling and crack formation in 20- μm particles (13). Yang *et al.* used transmission x-ray microscopy combined with x-ray absorption near-edge structure to reveal much more subtle changes in a cycled intercalation electrode, reporting not only a distortion in the particle shape, but also a redistribution of Mn, Ni, and Co transition metals and formation of a new phase (14).

Kirshenbaum *et al.*'s study is an exciting step toward understanding how optimized battery electrode architectures can maximize the energy per unit volume and weight (see the second figure, panel D). Silver compounds may be too expensive for applications other than medical ones, but bimetallic polyanionic materials (crystalline or amorphous) containing Cu or Fe have promise as active electrode materials with widespread application. To further improve access to full capacity, future, thicker electrodes could also include gradients in morphology spanning the thickness of the electrode and the distance from the electrode terminal. Using the battery chemistry itself to drive the formation of the electrode structure, as shown by Kirshenbaum *et al.*, is an elegant approach toward such an optimized structure. ■



Fabricating Li-ion battery electrodes. (A) Traditional electrodes rely on a random arrangement of contacts and may result in parts of the battery not being accessible. (B) Electrodes with physical or chemical bonds connecting the active particles to a conductive fiber perform better, but are difficult to make into a dense structure. (C) In Kirshenbaum *et al.*'s study, the electrode starts as a porous monolith. Upon reaction via lithium addition, a conductive metal such as silver moves to the particle surface as a thin conductive coating and small nodules. The metal coating and nodules provide a conductive pathway for electrons along all interior surfaces. If well formed, it should penetrate the entire volume of the electrode for full access of the stored energy. (D) In a conceptual, completely optimized battery electrode, every active particle is perfectly shaped, sized, and wired to the current collector and to the solid or liquid electrolyte (not shown).

REFERENCES AND NOTES

1. K. Kirshenbaum *et al.*, *Science* **347**, 149 (2015).
2. C. L. Cobb, M. Blanco, *J. Power Sources* **249**, 357 (2014).
3. J. Cabana, L. Monconduit, D. Larcher, M. R. Palacin, *Adv. Mater.* **22**, E170 (2010).
4. J. K. Ko *et al.*, *ACS Appl. Mater. Interfaces* **6**, 10858 (2014).
5. F. Wang *et al.*, *Nat. Commun.* **3**, 1201 (2012).
6. S. K. Martha, J. O. Kiggans, J. Nanda, N. J. Dudney, *J. Electrochem. Soc.* **158**, A1060 (2011).
7. A. Marschilok, C. Y. Lee, A. Subramanian, K. J. Takeuchi, E. S. Takeuchi, *Environ. Sci.* **4**, 2943 (2011).
8. C. Banet *et al.*, *Adv. Mater.* **22**, E145 (2010).
9. S. K. Martha *et al.*, *RSC Adv.* **4**, 6730 (2014).
10. J. Nanda *et al.*, *J. Phys. Chem. C* **116**, 8401 (2012).
11. W. H. Woodford, Y. M. Chiang, W. C. Carter, *J. Mech. Phys. Solids* **70**, 71 (2014).
12. L. Cai, K. An, Z. L. Feng, C. D. Liang, S. J. Harris, *J. Power Sources* **236**, 163 (2013).
13. M. Ebner, F. Marone, M. Stampanoni, V. Wood, *Science* **342**, 716 (2013).
14. F. Yang *et al.*, *Nano Lett.* **14**, 4334 (2014).
15. E. S. Takeuchi *et al.*, *Chem. Mater.* **21**, 4934–4939 (2009).

ACKNOWLEDGMENTS

Work by N.J.D. is supported by the Center for Mesoscale Transport Properties, an Energy Frontier Research Center funded by the U.S. Department of Energy (DOE), Office of Science, Basic Energy Sciences (BES). Work by J.L. is supported by the U.S. DOE, Office of Science, BES, Materials Sciences and Engineering Division. We thank A. Sproles (ORNL) for help with graphics.

10.1126/science.aaa2870



GLOBAL FOOD SUPPLY

China's aquaculture and the world's wild fisheries

Curbing demand for wild fish in aquafeeds is critical

By **Ling Cao**¹, **Rosamond Naylor**^{1*}, **Patrik Henriksson**², **Duncan Leadbitter**³, **Marc Metian**⁴, **Max Troell**^{4,5}, **Wenbo Zhang**^{6,7}

China is the world's largest producer, consumer, processor, and exporter of finfish and shellfish (defined here as "fish"), and its fish imports are steadily rising (1–3). China produces more than one-third of the global fish supply, largely from its ever-expanding aquaculture sector, as most of its domestic fisheries are overexploited (3–6). Aquaculture accounts for ~72% of its reported domestic fish production, and China alone contributes >60% of global aquaculture volume and roughly half of global aquaculture value (1, 3).

How China develops its aquaculture sector—and whether such development can relieve pressure on wild fisheries—are key questions for the future of the oceans. China's wild fisheries, used partially for aquaculture feeds, are both targeted and nontargeted (multiple species of fish captured indiscriminately at one time, including low-valued fish for direct human consumption and fish unfit for direct consumption, a.k.a. "trash fish") (see the photo) [supplementary materials (SM)]. The country's nonspecific and often erroneous reporting of fish production and

trade (7, 8) makes it especially difficult to assess the impact of China's aquaculture and aquafeed use on ocean fisheries. For example, roughly 300,000 tons of marine fish "nei" (not elsewhere included or unidentified species) are cultivated annually in China's aquaculture systems, and nei represent 31% of China's marine capture, surpassing the reported catch of any individual species in its ocean fisheries (6).

Here, we characterize and quantify the connections between China's aquaculture production and wild fisheries. We estimate fishmeal demand and trade, and document, to the greatest extent possible, the species and stock status of fish used for aquafeeds. We also assess the potential use of fish-processing wastes for aquafeeds as a means to reduce China's dependence on capture fisheries while increasing net fish supplies.

AQUACULTURE EXPANSION. China's total production of capture and farmed fish tripled during the past two decades (2, 3). Virtually all of this increase came from aquaculture, the country's fastest growing food sector (5 to 6% annual growth in volume from 2000 to 2012) (1, 3). China's aquaculture output reached 40 million metric tons (mmt; including shell weight, excluding algae) in 2012, four times the production volume in 1990, and the area devoted to fish farming doubled to 8 million hectares (1). China accounts for one-quarter of global fish demand, and despite rapid aquaculture growth, trends in domestic consumption portend a major shift in its trade position, from the world's leading fish exporter to a net importer in coming

Fish feed for aquaculture. Unidentified species of finfish, mollusks, crustaceans, and cnidaria from the trash fish component of nontargeted fisheries packaged and frozen for delivery for a fishmeal factory in Maoming, Guangdong province, China.

decades (SM). Aquaculture systems throughout the country are intensifying as producers seek higher returns on scarce land, water, and coastal zone resources (2). Intensification is reflected in higher stocking densities, greater reliance on commercial feeds, and more frequent water exchange and aeration (9, 10). The sector is transitioning from low-input, multitrophic systems (e.g., traditional carp polycultures that do not require formulated feeds) to monocultures or polycultures containing high-valued species dependent on feeds (2, 11).

Fish farming remains a highly diverse industry in China and is influenced by a variety of government directives and policies (SM). More than 100 freshwater and 60 marine fish species are raised in habitats and infrastructures that include ponds, cages in lakes and coastal waters, and raft and bottom-sowing systems in shallow seas and mud flats (2, 3). Carps in polyculture, tilapia in monoculture and polyculture, and penaeid shrimp in monoculture are three of the largest subsectors, constituting over half of China's total aquaculture production by volume (see the table). In 2012, China produced >90% of the world's carp, 50% of global penaeid shrimp, and 40% of global tilapia (3).

All of these species, with the exception of filter-feeding carps, rely on formulated feeds. Fishmeal inclusion rates in feeds average 27% for shrimp, 6% for tilapia, and 3.2% for carp, whereas fish oil inclusion is minimal. Given the scale of carp and tilapia production in China, even small rates of fishmeal inclusion sum to a large demand for fishmeal (11). The efficiency of feeding practices and nutrient uptake by the fish, represented by the average feed conversion ratio (FCR), also determine the overall demand for fishmeal and, hence, fish inputs in aquafeeds. The average FCR for Chinese systems that use feeds is 1.7 for carp, 1.6 for tilapia, and 1.2 for penaeid shrimp. The relatively high FCR for carp reflects the use of poor-quality fishmeal and the integration of various high-value fish species into carp polyculture, which often results in poor feed targeting and inefficient feed practices (11). The use of trash fish to supplement or substitute for commercial feeds via direct feeding of higher-valued species is also common and contributes to poor FCRs.

DEPENDENCE ON WILD FISH. China is the world's largest importer of fishmeal, accounting for about one-third of the global fishmeal

¹Stanford University, Stanford, CA 94035, USA. ²Leiden University, 2333 CC Leiden, the Netherlands. ³University of Wollongong, Wollongong NSW 2522, Australia. ⁴Stockholm University, 106 91 Stockholm, Sweden. ⁵The Royal Swedish Academy of Sciences, 104 05 Stockholm, Sweden. ⁶University of Stirling, FK9 4LA, UK. ⁷Shanghai Ocean University, Shanghai 201306, PR China. *E-mail: roz@stanford.edu

trade in any given year (SM). The country's entire aquaculture sector consumed an estimated 1.4 mmt of fishmeal in 2012 (12), equivalent to ~6.7 mmt of live-weight forage fish (e.g., anchovy, sardine, herring, menhaden) destined for reduction. More than one-quarter of the global fish catch (targeted and nontargeted) is composed of forage fish that are reduced into fishmeal and fish oil (3, 13). Although these small pelagic fish reproduce rapidly, they are equally, if not more, vulnerable to collapse than larger predatory fish because of poor management, overfishing, and climatic fluctuations (14). Many forage fisheries are fully- or overexploited.

Assessing sustainability of fish inputs used for aquaculture feeds in China requires a focus well beyond targeted reduction fisheries

higher in protein and price, is commonly reserved for high-value farmed species in China. In an effort to secure future supplies of high-quality fishmeal, Chinese companies and state subsidiaries have purchased fishing rights in foreign countries, including quotas for the Peruvian anchovy fishery (SM). As China commands an increasing global share of high-quality fishmeal, feed companies in other parts of the world are likely to move into the lower-quality fishmeal market, raising demand for trash fish. China also sources fishmeal from other Asian countries that is derived from nontargeted fisheries including trash fish (6).

Given the decline in marine catches in much of China's exclusive economic zone (EEZ) and its demand for fishmeal, the price

feeds has gained attention (3, 21, 23). Recent estimates indicate that ~40% of China's domestically produced fishmeal (~0.25 mmt) is derived from processing wastes, with wide year-to-year variation (24).

From 2003 to 2012, the country's seafood-processing industry grew at an annual rate at 10.7%, twice that of its aquaculture sector (1). Although the reexport market is shrinking in China with rising domestic fish consumption, the volume of processing wastes remains large, especially when wastes from its expanding aquaculture sector are included. Use of aquaculture wastes provides an important opportunity for meeting domestic fishmeal and oil demands, reducing use of trash fish in feeds, and minimizing waste discharges and pollution from processing plants.

Feed efficiencies and wild fish inputs in feed for farmed species

SPECIES	TOTAL PRODUCTION (MMT)	PRODUCTION WITH FEEDS (MMT)	AVERAGE FCR	AVERAGE FM IN FEED (%)	AVERAGE FO IN FEED (%)	TOTAL FM USED (MMT)	FORAGE FISH EQUIVALENT (MMT)
I. Carps							
Grass carp	4.8	2.6	1.7	1.5	0	0.07	0.32
Silver carp*	3.7	0	0	0	0	0	0
Bighead carp*	2.9	0	0	0	0	0	0
Common carp	2.9	1.6	1.7	6	0	0.16	0.77
Crucian carp	2.5	1.3	1.7	8	0	0.18	0.87
Bream	0.7	0.4	1.7	2.6	0	0.02	0.08
Black carp	0.5	0.3	1.7	2.6	0	0.01	0.06
II. Tilapia	1.6	1.3	1.6	6	0.5	0.13	0.60
III. Penaeid shrimp	1.6	1.5	1.2	27	2	0.50	2.36
Total	21	9.1	—	—	—	1.06	5.07

Feed efficiencies and wild fish inputs in feed for nine leading farmed species in China. Total production data in 2012 for each species from (I). Production with feeds was estimated based on (28). All other data were estimated from primary field surveys. Average economic FCR = total feed fed/total biomass increase. FM, fishmeal; FO, fish oil. An average reduction ratio of 21% for fishmeal and 5% for fish oil obtained from our field surveys were used to estimate wet weight equivalent of forage fish. *Filter-feeding species are not fed; they graze planktons proliferated through fertilization and the leftover feeds in the polyculture system.

(SM, table S1). Processing wastes from China's domestic fisheries and its fish reexport industry are used in feed production, and the wild fisheries contributing to these processing wastes are all fully- or overexploited or depleted. Large amounts of trash fish are also used for fishmeal production (6, 15), and China's high-valued marine aquaculture uses around 3 mmt of trash fish each year for direct feeding (16, 17). China's trash fish consist mainly of juveniles of commercially important species (~32 to 50%), small benthic and mesopelagic fish (e.g., sand lance, lanternfish), crustaceans, and cephalopods (18) (SM). Domestically produced fishmeal from trash fish and local processing by-products usually has a lower protein content (38 to 50%) and a high ash content (over 20%), and thus can be purchased at a relatively cheap price to supplement feeds of low-valued aquaculture species (11, 19).

Our surveys indicate that imported fishmeal from the eastern Pacific (e.g., Peru, Chile, U.S.A.) and Russia, which tends to be

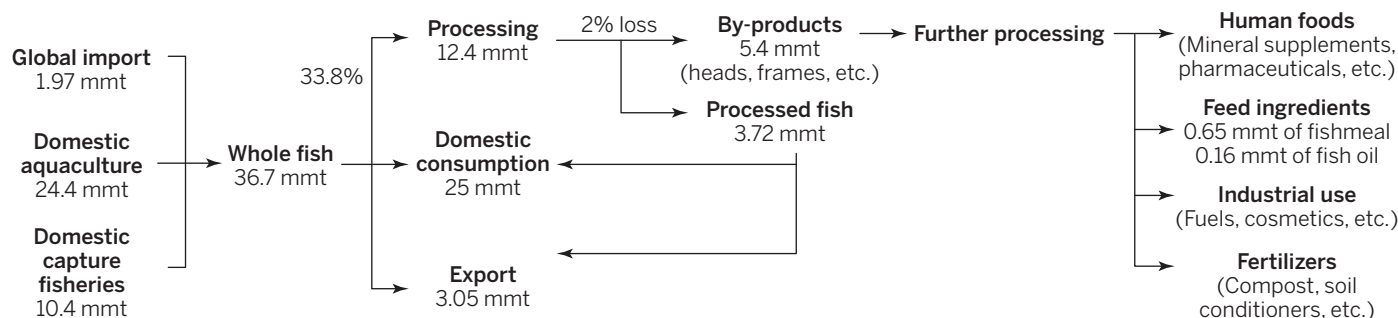
of trash fish is expected to rise in China and elsewhere in Asia where nontargeted fisheries are common. As its value increases, so too will concerns over the impacts of nontargeted fishing on marine resources and ocean ecosystems (6, 17). Unfortunately, the species composition of trash fish varies highly and is poorly recorded. We identified 71 trash fish species caught in China and used as feed inputs for aquaculture (table S2). Relatively few trash fish species have been assessed for their stock status, and of those that have, most are classified as overfished or fully-fished.

WASTE AS FEED. Recovery of feed ingredients from fish-processing wastes provides an important avenue for reducing aquaculture's dependence on targeted and nontargeted fisheries. Between 30 and 70% of the volume of processed fish biomass ends up as wastes depending on the type of fish and processing level (20–22). Because fish-processing wastes can be high in protein, minerals, and energy, their use in aquaculture

Our analysis shows that 0.65 mmt of fishmeal (± 0.26 mmt, 95% confidence interval (CI)) and 0.16 mmt of fish oil (± 0.07 mmt, 95% CI) could be produced from China's fish-processing industry (see the figure) (SM and table S3). These results suggest that fish-processing wastes could meet almost half (based on the average value), and potentially two-thirds (based on the upper 95% confidence limit), of China's current demand for fishmeal in aquafeeds. A more conservative estimate, based only on processing of fish for export (versus domestic consumption), indicates 0.42 mmt of fishmeal and 0.1 mmt of fish oil could be produced from processing wastes (table S4).

Serious constraints exist, however, on utilization of fish-processing wastes for aquafeeds in China. First, nutritional quality of fishmeal from processing wastes tends to be inferior to fishmeal produced from wild fish (23). Conventional fishmeal made from wild forage fish often has a crude protein content between 67% and 90%, whereas fish-

Potential of fishmeal and oil production



Estimated potential of fishmeal and oil production from China's fish-processing industry. The 95% CIs are (0.39, 0.92) for fishmeal and (0.09, 0.22) for fish oil. Authors' calculations based on 2012 data from (1, 27). Details in SM.

meal derived from processing wastes usually contains between 57% and 80% crude protein (25). Nutritional deficiencies caused by using offal-based fishmeal can be overcome with alternative feedstuffs; e.g., plant-based products such as algae and ethanol yeast developed through the biofuels industry (26). Alternatives to fishmeal must have comparable nutritional values, ready availability, digestibility, and reasonable palatability at competitive cost (23).

Second, use of fish-processing wastes in aquafeeds presents food safety risks related to bioaccumulation of contaminants, cross-species transmission of pathogens, and, possibly, prions (21, 23). To avoid disease transmission, the Europe Union forbids the use of farmed fish by-products in finfish feeds but allows them to be used in crustacean diets or vice versa (21). Although China has no such food safety regulations, there is increasing awareness on traceability and quality in aquafeed inputs (SM). China is examining a new national standard for regulating dioxins and usage of multiple species in fishmeal and oil. Development may be hindered however by the predominance of small-scale processing plants with outdated equipment and by inefficient or costly collection of raw materials along the supply chain. Overcoming these constraints is not insurmountable but will require substantial investments in research and development, and strict enforcement of advanced food safety regulations.

Strategic design of an aquafeed sector based on processing wastes from aquaculture makes perfect sense for China, especially if food safety risks can be monitored. China's massive aquaculture sector yields a steady and consistent stream of processing wastes. If processing facilities are colocated with fishmeal and feed plants, the problems of perishability, transportation costs, and sup-

ply chain barriers can be minimized. Such a strategy would require improving facilities to meet environmental standards. Colocation would then support China's current Five-Year Plan (2011–2015), which aims to promote energy and water efficiency and to minimize waste discharges and pollution (SM).

ADDING OR DEPLETING? The scale and complexity of China's aquaculture sector places it in a precarious position between adding and depleting global seafood availability. The diversity and low-trophic-level base of China's aquaculture sector provides substantial opportunity for positive change, but the use of feeds containing fishmeal remains profitable in most systems. If China is to increase its net production of fish protein, its aquaculture industry will need to reduce FCRs and the inclusion of fish ingredients in feeds and to improve fishmeal quality. Fish-processing wastes have potential to substitute increasingly for imported fishmeal in China's aquaculture sector if appropriate technology and supply chains are developed, if nutritional qualities can be improved, and if food safety can be guaranteed.

Even if fish-processing wastes are recycled as feeds, China's aquaculture industry will continue to strain wild fisheries unless the country commits to stricter enforcement of regulations on targeted and nontargeted fishing within and outside of its EEZ and to responsible sourcing of fishmeal and/or oil (SM). Using fishmeal derived from by-catch or by-products of wild fisheries as a means of reducing pressure on wild fisheries remains controversial and should be monitored (23). Without such measures, China's aquaculture sector is destined to diminish wild fish stocks worldwide. ■

REFERENCES AND NOTES

1. Fishery Bureau, Ministry of Agriculture, People's Republic of China, *China Fisheries Yearbook 2013* (China Agriculture Press, Beijing, 2013).
2. Project Team for Research into the Sustainable Development Strategy of China's Cultivation Industry, *Study on the Sustainable Development Strategy of China's Cultivation Industry—Aquaculture* (China Agricultural Press, Beijing, 2013).

3. Food and Agriculture Organization of the United Nations, "The state of world fisheries and aquaculture" (FAO, Rome, 2014).
4. T. G. Mallory, *Mar. Policy* **38**, 99 (2013).
5. S. Villasante *et al.*, *Ambio* **42**, 923 (2013).
6. S. Funge-Smith, M. Briggs, W. Miao, "Regional overview of fisheries and aquaculture in Asia and the Pacific 2012" (Asia-Pacific Fishery Commission, FAO, Rome, 2013).
7. D. Pauly *et al.*, *Fish Fisheries* **15**, 474 (2014).
8. R. Blomeyer *et al.*, "The role of China in world fisheries" (European Parliament, Directorate General for Internal Policies, Brussels, 2012).
9. L. Cao *et al.*, *Environ. Sci. Technol.* **45**, 6531 (2011).
10. B. Xie *et al.*, *Aquaculture* **414–415**, 243 (2013).
11. A. Chiu *et al.*, *Aquaculture* **414–415**, 127 (2013).
12. C. X. Ai, Q. Y. Tao, *Feed Industry* **34**, 1 (2013).
13. J. Alder, B. Campbell, V. Karpouzi, K. Kaschner, D. Pauly, *Annu. Rev. Environ. Resour.* **33**, 153 (2008).
14. M. L. Pinsky, O. P. Jensen, D. Ricard, S. R. Palumbi, *Proc. Natl. Acad. Sci. U.S.A.* **108**, 8317 (2011).
15. M. R. Hasan, M. Halwart, "Fish as feed inputs for aquaculture: practices, sustainability and implications" (FAO, Rome, 2009).
16. S. Funge-Smith, E. Lindebo, D. Staples, "Asian fisheries today: The production and use of low value/trash fish from marine fisheries in the Asia-Pacific region" (Asia-Pacific Fishery Commission, FAO, Rome, 2005).
17. S. S. De Silva, G. M. Turchini, "Use of wild fish and other aquatic organisms as feed in aquaculture—a review of practices and implications in the Asia-Pacific" (FAO, Rome, 2009).
18. R. Grainger, Y. Xie, S. Li, Z. Guo, "Production and utilization of trash fish in selected Chinese ports" (Asia-Pacific Fishery Commission, FAO, Rome, 2005).
19. Y. Kong, *Chinese J. Anim. Sci.* **49**, 7 (2013).
20. A. E. Ghaly *et al.*, *J. Microb. Biochem. Technol.* **5**, 107 (2013).
21. R. Newton *et al.*, *Crit. Rev. Food Sci. Nutr.* **54**, 495 (2014).
22. R. L. Olsen *et al.*, *Trends Food Sci. Technol.* **36**, 144 (2014).
23. R. L. Naylor *et al.*, *Proc. Natl. Acad. Sci. U.S.A.* **106**, 15103 (2009).
24. FAO, FishstatJ—software for fishery statistical time series (2014); www.fao.org/fishery/statistics/software/fishstatj/en.
25. F. Y. Ayadi, K. A. Rosentrater, K. Muthukumarappan, *J. Aquacult. Feed Sci. Nutr.* **4**, 1 (2012).
26. D. Klinger, R. Naylor, *Annu. Rev. Environ. Resour.* **37**, 247 (2012).
27. UN, UN Comtrade Statistics Database (2014); <http://comtrade.un.org/>.
28. A. G. J. Tacon, M. Metian, *Aquaculture* **285**, 146 (2008).

ACKNOWLEDGMENTS

We thank W. Falcon, D. Little, S. L. Dong, Y. Chen, Y. S. Qiu, A. Chiu, C. Fedor, and L. Seaman for input on the manuscript. We thank the China Fund of the Freeman Spogli Institute for International Studies at Stanford University and the Lenfest Ocean Program of the Pew Charitable Trusts for financial support, and the EU-FP7 Sustaining Ethical Aquaculture Trade (SEAT) project and the David and Lucile Packard Foundation for support of our field surveys in China.

SUPPLEMENTARY MATERIALS

www.sciencemag.org/content/347/6218/133/suppl/DC1

10.1126/science.1260149



HEALTH POLICY

Defining disease

Paul Weindling welcomes a historical approach to the concept of chronic illness

There is consensus that the transition from infectious to chronic disease was a necessary rite of passage to modernity. Yet as this thoughtful book makes clear, the concept of chronic disease has long been elastic and fluid, making the term a cultural concept rather than a self-evident clinical entity or epidemiological category. This account, then, is not one of epidemiological statistics on death and disease incidence, but a cultural history about a key medical and policy-related category. Although the focus of this book is firmly on the United States, author George Weisz recognizes that chronic disease has had a long history throughout the world.

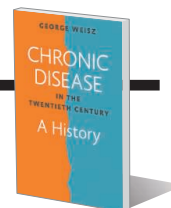
Weisz begins by examining the concept of “national vitality,” which emerged in the early 20th century and touted the idea of prevention and care of all illnesses, as opposed to only infectious diseases. According to Weisz, the crucial turning point in the acceptance of the chronic disease construct was the period between the late 1910s and the 1950s, when innovative organizations including the National Health Council of 1919–1920 and the New York Committee on Health Examinations began to advocate for periodic preventive health examinations.

If there is a hero in this story, it is the statistician and later scientific director of the Milbank Memorial Fund, Edgar Sydenstricker, who conducted meticulous epide-

Chronic Disease in the Twentieth Century A History

George Weisz

Johns Hopkins University Press, 2014. 325 pp.



miological research on public health in the United States and Europe between 1915 and 1935. Sydenstricker was a proponent of the use of statistics in the study of morbidity and was among the first to consider factors such as occupation and social status in his reports on the topic. The best known of these studies, The Hagerstown Morbidity Survey, is regarded as a precursor to the U.S. National Health Survey.

The reform of urban health care and the emergence of chronic care policies occurred simultaneously, with foundations such as the Milbank Fund and the Rockefeller Foundation playing a central role. Unfortunately, Weisz does not engage with the richly innovative literature on foundation-funded health care studies, which could have potentially informed his analysis.

With the initiation of a National Health Survey and then a National Health Assembly came a transition from local health management programs to national policies. Despite the growing involvement of the federal government, organizations such as the American Medical Association were quick to advocate that the role of government programs should be to strengthen the relationship of physician and patient but not to supplant the physician altogether.

Weisz argues that there was a “chronic disease movement” in the United States, beginning in the middle of the 20th century, that originated in specific institutions and clinics and spread throughout the country with the support of federal programs. Pilot programs in home-based care developed at Montefiore Hospital in New York City, for example, were replicated on a national basis when Medicaid began providing new funds for homecare in the 1960s.

This certainly contrasted with the priorities of the British National Health Service at the time. Weisz maintains that until the late 1950s, the United Kingdom focused on defined illness and infections, as opposed to chronic long-term diseases. “Social medicine”—the idea that health status and social conditions are linked and that a social science perspective could improve both—did not emerge until the 1960s and found advocates in epidemiologists Thomas McKeown and Jerry Morris, who were concerned with demonstrating how chronic diseases are preventable. Similarly, France had less of a chronic disease movement than a movement for public assistance for the elderly, which became a national priority in the 1960s. Weisz justifies comparing the public health priorities of the United States with those of the United Kingdom and France during these periods as a way to demonstrate what was distinctive and innovative about the American system. The differences are not only cultural but also sociopolitical.

Although the book does not delve into nefarious incidents in chronic disease experimentation, such as the Tuskegee Syphilis Study, Weisz is alert to the sociocultural significance of the shift from hospital-centered care to “surveillance medicine,” which is characterized as treating and preventing disease states through “ever-more pervasive and sophisticated forms of monitoring and screening.” He also acknowledges how the notion of prevention can be used to cloak agendas of power.

There are wider implications for this type of discourse that have to do with how we define different disease entities. The difference between infectious and chronic illness becomes unclear, for example, when considering tuberculosis or venereal disease. Certain lung diseases, including mesothelioma, muddy the waters further.

This book is brave and insightful and succeeds in raising the intriguing possibility that cultural histories of health must acknowledge the distinct vocabulary and sociocultural definitions that are inherent to specific disease states. It is full of potential leads and insights, references, and analysis that will be consulted time and time again.

10.1126/science.1261701

The reviewer is at the Centre for Medical Humanities,
Department of History, Philosophy and Religion, Oxford
Brookes University, Oxford OX3 0BP, UK.
E-mail: pjweindling@brookes.ac.uk

PHILOSOPHY

Science and the search for meaning

Susan R. Wolf considers an ambitious attempt to employ scientific and philosophical reasoning to understand our place in the cosmos

In my part of the world, if someone asks why the sky is blue, he will be told that it is because God is a Tarheel (that is, a supporter of the University of North Carolina, whose colors are white and a beautiful light blue). If the questioner is a child, that answer will be at least somewhat satisfying. If one gives the child an answer having to do with the wavelengths of light that are absorbed by gas molecules in the atmosphere, the child may find that satisfying, too. On the other hand, his eyes might glaze over—it is possible that this is not the sort of answer he was looking for.

Similarly, if a person asks why humans exist, he may be asking for a purpose or a point to our existence, or he may be asking for a causal explanation of how the species came to be. If he asks for the meaning of human existence, I would have surmised that he is interested in the first sort of question. But in his new book, *The Meaning of Human Existence*, biologist E. O. Wilson seems to understand this as a question of the second sort. According to him, “the meaning of human existence [is] the epic of the species, begun in biological evolution and prehistory, passed into recorded history, and ... also what we will choose to become.”

Even if the title is misleading, as I think it is, the epic of the species is certainly an ambitious enough topic for a 200-page book. In a remarkably short space, Wilson gives an account of how our species evolved; of how it is similar to and different from other species; of the sources of our creativity and of some of our most recalcitrant tendencies; and of

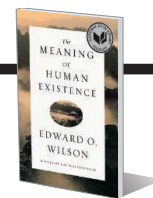
how we are apt to be similar to any possible extraterrestrial species with a level of intelligence comparable to or greater than ours. In other words, he puts the existence of our species in both global and cosmic perspective. Much of what he says is fascinating food for thought.

There is, however, another strand running through the book that I find puzzling, regarding the unification of knowledge. Wilson repeatedly rants against the “archaic misconception” that the sciences and the humanities are intellectually independent

The Meaning of Human Existence

Edward O. Wilson

Liveright, 2014. 208 pp.



and should remain so. Noting the explosive growth of scientific knowledge over the past few decades, he asks what this has to do with the humanities and answers “Everything.” Thanks to science, he says, “It is within the power of the humanities and

the serious creative arts within them to express our existence in ways that begin at last to realize the dreams of the Enlightenment.” This theme of the consilience of science and the humanities will be familiar to readers of Wilson’s earlier work (*I*), and although in this book he frequently takes pains to refer to the humanities as “all-important” and as one of the “two great branches of learning,” I cannot help but hear an echo of the Victorian gentleman who claims to find “the gentler sex” superior to his own, putting her on a pedestal while denying her the right to own property or vote.

What Wilson understands the humanities to be is not so clear. When he writes, near the end of the book, that “the humanities address in fine detail all the ways human beings relate to one another and to the environment, [whereas] science addresses everything else,” it sounds as though not just history and literature but economics, sociology, and political science are part of the humanities. When, on the other hand, he remarks, “I don’t believe it too harsh to say that the history of philosophy when boiled down consists mostly of failed models of the brain,”



Insights from science and the humanities are woven throughout this existential treatise.

The reviewer is in the Department of Philosophy at the University of North Carolina at Chapel Hill, Chapel Hill, NC 27599, USA. E-mail: susanw@unc.edu

he appears to regard philosophy not as part of the humanities but as an incompetent attempt at science.

It is also hard to see what Wilson wants the humanities to do other than present the findings of science in engaging prose. At one point, he suggests that the reason the view from his friend's penthouse overlooking Central Park is beautiful may be found in our prehuman ancestors' origins in the savannas of Africa. This is an admittedly fascinating suggestion, but I hope it is not offered as a model for what the study and appreciation of art should become.

A wonderful documentary called *Tim's Vermeer* vividly presents the possibility that the Dutch painter Johannes Vermeer used a camera obscura and other mechanical devices to create his paintings (2). It is an unsettling idea. But if it were true, it would not establish that "the meaning" of Vermeer's paintings consisted in his having created them by these means. For the art historian, the art critic, and the philosopher of art, the question of how to understand Vermeer's achievement if the hypothesis were true begins rather than ends here. Similarly, one might argue that understanding the way that humans evolved and what they share and don't share with other species does not give us the meaning of human existence, so much as sets the parameters within which that question must be addressed.

There is another, more salutary lesson supporters and practitioners of the humanities may take away from this book, however. In keeping with the book's grand perspective, Wilson encourages us to reflect on the path of our species from prehistory into the future. He brings up and weighs in on what he (somewhat puzzlingly) calls "the greatest moral dilemma since God stayed the hand of Abraham"—namely, how much to use genetic engineering to direct our own evolution. He also urges us to overcome tribalism in order to achieve the unity of the human race. These are indeed enormously important and pressing concerns that address the future not just of our friends and compatriots but of humanity itself.

To meet such challenges, we can only benefit from a scientific understanding of the history and nature of our species. If Wilson's book encourages more humanists to take up these issues as their own—informed by science but not defined by it—it will be an accomplishment for which we all have reason to be grateful.

REFERENCES AND NOTES

1. E. O. Wilson, *Consilience: The Unity of Knowledge* (Knopf, New York, 1998).
2. P. Jillette, Teller, *Tim's Vermeer* (Sony Pictures Classics, New York, 2013).

10.1126/science.aaa0328

SCIENCE FICTION

Lessons from the future

A futuristic time travel tale resonates today, finds Guy Riddihough

William Gibson both coined the term "cyberspace" and vividly brought it to life in his award-winning 1984 book, *Neuromancer*. In his latest science fiction novel, he fashions an intricate portrayal of the future that touches on a range of social and ethical issues. The result is an often satirical meditation on the science and politics of today.

The plot revolves around two time points in the future: one a couple of decades from now and the other a century hence. The two futures exist on either side of the "jackpot," a global disaster that has decimated most of the world's population—a disaster that might yet be prevented.

The nearer future is set in a corner of small-town America that is a sharply observed extrapolation of the present-day United States: Strip malls are

The Peripheral

William Gibson
Putnam, 2014.
496 pp.



dominated by warehouse supermarkets and 3D printing outlets, a chronically depressed economy has fostered a thriving black market for illicit synthetic drugs, computer gaming has become a form of employment for the young, and Homeland Security waits and watches in the background. We see this world through the eyes of Flynne Fisher, a pragmatic and unflappable young woman who gets more than she bargained for when she accepts an opportunity to earn much-needed cash in exchange for beta-testing what she is told is a new virtual game.

The "postjackpot" future is set in the early 22nd century and is mostly based in London, now a form of city-state run by

The reviewer is on staff at Science Magazine, AAAS, Washington, DC 20005, USA. E-mail: griddiho@aaas.org



Engaging characters and a cyberpunk slant bring the future to life in William Gibson's *The Peripheral*.

powerful guilds. This part of the book is told from the perspective of Wilf Nether-ton, a hapless publicist and failed celebrity-handler whose patent ineptitude is in many ways the comedic antithesis of Flynne's level-headed practicality.

Gibson lets his imagination range freely in this farther future, as illustrated most strikingly in a massive floating island formed from the agglomeration of plastic waste in the Great Pacific Garbage Patch, which is inhabited by a community of genetically engineered grotesques. We encounter one of Wilf's clients here, an artist who repeatedly tattoos and then flays her skin for exhibition, and discover a boutique body-rental industry, where people can rent and virtually control fully organic human and nonhuman bodies—the "peripherals" of the title.

For all of the stylistic parallels, Gibson's vision of the future is not as single-mindedly focused as it was in *Neuromancer*, and the themes are more obviously derivative of the genre. Additionally, some of the major plot points were less clearly defined than I would have hoped, and we never really learn the "why" behind the book's climax, visceral though it is. Still, *The Peripheral* succeeds in creating a menagerie of compelling characters—from Flynn and Wilf to Ainsley Lowbeer, a cool and calculating detective; Daedra West, the "epidermal artist"; and Conner Penske, a traumatized war veteran—and provides a wry and oddly disturbing view of the future.

10.1126/science.aaa0604

Edited by Jennifer Sills

Retraction

OUR REPORT “Single-proton spin detection by diamond magnetometry” (1) presents measurements on near-surface nitrogen-vacancy centers in diamond. In these measurements, we observed signals that showed all the characteristics expected from single-proton nuclei. This interpretation was based on the three criteria of the Zeeman effect, quantum-coherent coupling, and (in one occasion) on a before/after-type control experiment.

We have discovered a potentially serious issue with the main conclusion in the paper, namely the “detection of a single-proton spin.” Specifically, we have recognized that resident carbon-13 nuclei within the diamond can mimic single-proton behavior, challenging our interpretation. Carbon-13 can produce quantum-coherent signals at the proton nuclear magnetic resonance frequency, and the scaling of frequency with magnetic field is indistinguishable from that of single protons within the measurement error. This behavior is due to an unrecognized effect that occurs with the dynamical decoupling sequence used for signal detection. We provide a detailed description of this behavior in a separate article (2).

Our *Science Express* Report claims single-proton spin detection in three instances. We find that two of these instances are ambiguous and can be explained by either single proton or single carbon-13, whereas the third instance can only be explained by single proton. Because this is only a single data point, we are not confident that it provides sufficient basis to support our claim of

“single-proton spin detection.” We therefore retract the Report.

M. Loretz,¹ T. Rosskopf,¹ J. M. Boss,¹ S. Pezzagna,² J. Meijer,² C. L. Degen^{1*}

¹Department of Physics, ETH Zurich, Otto Stern Weg 1, 8093 Zurich, Switzerland. ²Institute for Experimental Physics II, Department of Nuclear Solid State Physics, Universität Leipzig, Linnéstrasse 5, D-04103 Leipzig, Germany.

*Corresponding author. E-mail: degenc@ethz.ch

REFERENCES

1. M. Loretz et al., *Science* **10.1126/science.1259464** (2014); published online 16 October 2014.
2. M. Loretz et al., “Spurious harmonic response of multipulse quantum sensing sequences,” arXiv:1412.5768 (2014).

Protecting coffee from intensification

SUSTAINABLE AGRICULTURAL intensification is one approach to meet food security and biodiversity conservation goals simultaneously (1, 2). The yield increases required to achieve these goals can be facilitated by using improved crops (3, 4). Pest-resistant or high-yielding crops may deliver higher returns than unimproved crops and thus alleviate pressures on remaining natural habitats. However, because higher yields increase household income, such improved crops may also incentivize farmers to expand cropland, which negatively affects biodiversity and ecosystem services. Arabica coffee, which is one of the most valuable agricultural commodities in the world, exemplifies this problem.

Wild *Coffea arabica* is a shrub native to the understory of the moist evergreen Afromontane forest of Ethiopia and is the ancestor of all commercial Arabica cultivars worldwide. In its region of origin, arabica coffee was originally harvested from wild populations, but over time, shade trees and coffee shrubs have been increasingly managed by farmers to increase coffee yields (5).

Increased coffee yields improve local livelihood, but unfortunately the intensification of coffee agriculture is also degrading forest and causing severe biodiversity losses (6, 7). Even more important, excessive forest management and the use of locally improved arabica coffee cultivars are threatening the mating system and the genetic resources of wild *Coffea arabica*. Past and ongoing conversion of natural moist evergreen forest to heavily managed forest has already resulted in decreased pollen dispersal and increased self-pollination in wild arabica stands (8), and the original coffee gene pool already shows signs of admixture with cultivars (9). To date, three forests with wild *Coffea arabica* populations have been designated as UNESCO Biosphere Reserves in Ethiopia and a few others are proposed as reserves, but there are currently no guarantees that the genetic integrity of any of these populations will be maintained.

If the worldwide coffee industry plans to use the genetic diversity of the Ethiopian wild coffee to adapt arabica coffee to climate change and emerging pests and diseases (10, 11), more conservation efforts in the Ethiopian coffee forests are urgently needed. The ongoing conversion of the last remaining wild coffee populations to managed agroforests must be halted to conserve wild coffee and its pollinators, and the use of improved cultivars in the immediate vicinity of these populations must be discouraged to avoid introgression of cultivar genes into the wild arabica gene pool.

Raf Aerts,^{1*} Gezahegn Berecha,^{1,2} Olivier Honnay¹

¹Plant Conservation and Population Biology, University of Leuven, Kasteelpark Arenberg 31-2435, BE-3001 Leuven, Belgium. ²Department of Horticulture and Plant Science, Jimma University, Jimma, Ethiopia.

*Corresponding author. E-mail: raf.aerts@bio.kuleuven.be

REFERENCES

1. B. Phalan et al., *Science* **333**, 1289 (2011).
2. T. Garnett et al., *Science* **341**, 33 (2013).
3. M. Tester, P. Langridge, *Science* **327**, 818 (2010).
4. E. C. Brummer et al., *Front. Ecol. Environ.* **9**, 561 (2011).
5. R. Aerts et al., *For. Ecol. Manag.* **261**, 1034 (2011).
6. K. Hundera et al., *Biol. Conserv.* **159**, 285 (2013).
7. K. Hundera et al., *Environ. Manag.* **51**, 801 (2013).
8. G. Berecha et al., *Biol. J. Linn. Soc.* **112**, 76 (2014).
9. R. Aerts et al., *Evol. Appl.* **6**, 243 (2013).
10. M. Gross, *Curr. Biol.* **24**, R503 (2014).
11. D. Zamir, *Science* **345**, 1124 (2014).

Measuring merit: Take the risk

I AGREE WITH M. McNutt that young scientists should be evaluated on the basis of their willingness to take risks



Coffee beans

PHOTO: TONY QUILLAS/ISTOCKPHOTO.COM

(Editorial, “The measure of research merit,” 5 December 2014, p. 1155). I believe most scientists do recognize that the current approach of using bibliometrics to gauge achievement is misleading, not just for young scientists but for scientists of all ages.

This system is especially damaging to scientists coming from the developing or underdeveloped countries, where the training and facilities may not match those of the developed world. For scientists in these countries, the open-access cost or publication fees of high-impact factor journals may not be affordable.

Furthermore, a young scientist enrolling with a highly accomplished research group may find it easier to publish research articles compared with one who pursues original ideas in a newly formed lab. During my time as a Ph.D., it was very common to see fellow students striving to join the most productive or established groups for postdoctoral training, even if their interests did not match. This trend continues today, mainly because of the current evaluation process.

How do we encourage youngsters to pursue their passion and dreams, which may not materialize in the short time frame of a

Ph.D. or postdoc period? McNutt’s proposal should be seriously investigated by universities and funding agencies.

Kumar Selvarajoo

Institute for Advanced Biosciences, Keio University,
Tsuruoka, Japan and Systems Biology Program,
Graduate School of Media and Governance,
Keio University, Fujisawa, Japan.
E-mail: kumar@ttck.keio.ac.jp

Moving toward data on soil change

IN THE NEWS FEATURE “Rare earth” (7 November 2014, p. 692), M. Tennesen reports that soil scientists are focused on documenting and preserving soil diversity. However, the central challenge is not simply identifying endangered soils, but understanding, documenting, and responding to all soil change. The U.N. Intergovernmental Technical Panel on Soils’ forthcoming report (1), mentioned in Tennesen’s article, aims to document global soil change and its impact on soil and ecosystem function and service delivery. This effort is challenging, given the lack of data documenting decadal soil

change. A single survey identifying endangered soils is of intellectual and scientific interest, but focusing resources on delineating rare soil boundaries, at increasing resolution, could be a distraction when we lack data on regional and global soil change resulting from climate and land use.

We need new monitoring approaches like the ecosystem approach implemented in the United Kingdom’s Countryside Survey (2, 3). Similar monitoring, such as LUCAS in the European Union (4), provides vital data on the state and change of soils in an ecosystem context that can inform policy at national levels.

David A. Robinson

Centre for Ecology and Hydrology, ECW Bangor,
Bangor, Gwynedd, LL57 2UW, UK.
E-mail: David.Robinson@ceh.ac.uk

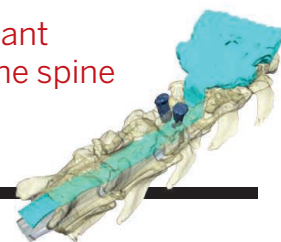
REFERENCES

1. Global Soil Partnership, Intergovernmental Technical Panel on Soils (www.fao.org/globalsoilpartnership/intergovernmental-technical-panel-on-soils/en/).
2. B. Reynolds *et al.*, *Vadose Zone J.* **12**, 2 (2013).
3. B. A. Emmett *et al.*, “Countryside Survey: Soils report from 2007” (Centre for Ecology and Hydrology, Wallingford, Oxon, UK, 2010).
4. G. Tóth, A. Jones, L. Montanarella, Eds., “LUCAS topsoil survey” (European Commission Joint Research Centre, Institute for Environment and Sustainability, Ispra, Italy, 2013).

RESEARCH

A neural implant
suitable for the spine

Minev et al., p. 159



IN SCIENCE JOURNALS

Edited by **Melissa McCartney** and **Margaret Moerchen**

EPIDEMIOLOGY

Co-infection complicates treatment

Infections rarely occur in isolation, and treating one pathogen may have unpredictable effects on another. Ezenwa and Jolles, working on wild African buffaloes, expected that because deworming relieves immune suppression, such treatment would lead to a drop in tuberculosis because the animals would clear the second infection without further intervention. Not so. Deworming did improve the lot of parasite-infested individuals, but it also increased the spread of tuberculosis among the population. What apparently happened is that the worm-free buffalo lived longer but stayed infected with tuberculosis and had longer to spread the infection among the herd. — CA

Science, this issue p. 175



Water buffalo show that
curing one infection does not
stop the spread of another

EARTH HISTORY

Dating the influence of Deccan Traps eruptions

The Deccan Traps flood basalts in India represent over a million cubic kilometers of erupted lava. These massive eruptions occurred around the same time as the end-Cretaceous mass extinction some 65 million years ago, which famously wiped out all nonavian dinosaurs. Schoene

et al. determined the precise timing and duration of the main phase of the eruptions, which lasted over 750,000 years and occurred just 250,000 years before the Cretaceous-Paleogene boundary. The relative contribution of these eruptions and of the Chicxulub impact in Mexico to the mass extinction remains unclear, but both provide potential kill mechanisms. — NW

Science, this issue p. 182



Gases released in these lava flows in India may have aided an extinction event

CANCER

Going BATty to fight prostate cancer

Although many early cases of prostate cancer can be treated by blocking the activity of male hormones, the tumor often develops resistance and regrows. Standard hormone-based treatments, which all involve androgen deprivation, are ineffective at this stage of the disease. Now, Schweizer *et al.* describe an approach based on evidence that cancer cells adapted to low-androgen conditions may not tolerate high concentrations of testosterone. A clinical trial of BAT (bipolar androgen therapy), in which very high and very low concentrations of testosterone alternate in the patients' blood, showed that the regimen was well tolerated. In addition to direct anticancer effects, intermittent testosterone treatment also

restored the tumors' sensitivity to anti-androgen agents, further expanding patients' treatment options. — YN

Sci. Transl. Med. **7**, 269ra2 (2015).

QUANTUM GASES

Breaking the symmetry in an atomic gas

Cooling a physical system through a phase transition typically makes it less symmetrical. If the cooling is done very slowly, this symmetry change is uniform throughout the system. For a faster cooling process, the system breaks up into domains: The faster the cooling, the smaller the domains. Navon *et al.* studied this process in an ultracold gas of Rb atoms near its transition to a condensed state (see the Perspective by Ferrari). The authors found that the size of the domains froze in time in the vicinity of the

transition and that it depended on the cooling speed, as predicted by theory. — JS
Science, this issue p. 167; see also p. 127

ULTRAFAST DYNAMICS

Traveling a long way past the junction

Diodes are central components of modern electronic circuits. They essentially consist of two semiconductors sandwiched together, with one deficient in electrons (p), the other enriched (n). Najafi *et al.* used ultrafast electron microscopy to study the dynamics in a silicon diode on a time scale of trillionths of a second. They discovered that when light excites the diode's charge carriers, those carriers migrate much farther past the p-n junction than standard models would imply. The authors explain the results using a ballistic transport model. — JSY

Science, this issue p. 164

GUT MICROBIOTA

Gut microbes resist inflammation

It is vital to human well-being that our gut microbiota can be distinguished from harmful, but often very similar, organisms. Cullen *et al.* begin to analyze how one dominant symbiont, *Bacteroidetes thetaiotaomicron*, does this. Our guts release potent antimicrobial peptides when we become infected with pathogenic bacteria such as salmonella, but these symbionts make an outer lipopolysaccharide coat that differs from those of pathogens by only one phosphate molecule. Enzymatic removal of this group is enough to confer resistance to the host's immune response and allow the symbionts to escape damage. — CA

Science, this issue p. 170

COMPUTER SCIENCE

I'll see your program and raise you mine

One of the fundamental differences between playing chess and two-handed poker is that

the chessboard and the pieces on it are visible throughout the entire game, but an opponent's cards in poker are private. This informational deficit increases the complexity and the uncertainty in calculating the best course of action—to raise, to fold, or to call. Bowling *et al.* now report that they have developed a computer program that can do just that for the heads-up variant of poker known as Limit Texas Hold 'em (see the Perspective by Sandholm). — GJC

Science, this issue p. 145; see also p. 122

DNA REPAIR

A factor for repairing broken DNA

Unprogrammed DNA double-strand breaks are extremely dangerous for genomic stability. Nonhomologous end-joining (NHEJ) repair systems are present in all domains of life and help deal with these potentially lethal lesions. Ochi *et al.* have discovered a new factor involved in NHEJ by searching for proteins with structural similarities to known NHEJ proteins. Specifically, PAXX, a paralog of XRCC1 and XLF, interacts with a key repair pathway protein, Ku, and helps promote ligation of the broken DNA. — GR

Science, this issue p. 185

VASCULAR BIOLOGY

Peroxidized lipids dilate blood vessels

Cerebral arteries must maintain constant blood flow to the brain even though blood pressure fluctuates constantly. Sullivan *et al.* characterized a signaling pathway that is specific to the endothelial cells that line cerebral arteries. Reactive oxygen species (ROS) cause lipid peroxidation. In endothelial cells in cerebral arteries, locally produced ROS oxidized lipids, which triggered calcium influx through the ion channel TRPA1. In turn, this calcium influx activated a potassium-permeable channel, resulting in the dilation of cerebral arteries. — WW

Sci. Signal. **8**, ra3 (2014).

IN OTHER JOURNALS

Edited by **Kristen Mueller**
 and **Jesse Smith**



GLACIOLOGY

Losing traction at higher speeds

How, exactly, will glaciers and ice sheets respond to climate warming? We know that they will melt faster as temperatures rise, but the way they slide over the ground below also should be affected, and that could have a significant impact on how fast they fall apart at their margins. Zoet and Anderson conduct a laboratory study to investigate how drag between ice and the surface that supports it changes

with increased sliding speed. They find that drag decreases with increased sliding speed if there exist the right kinds of gaps between the ice and the surface below, which means that weather or climate variability has the potential to cause even more rapid glacier motion, and thus faster sea-level rise. — HJS

J. Glaciology 10.3189/2015JoG14J174 (2014).

CASPASES

For caspases, an escape from death

Caspase proteins are well known for their role in degrading proteins and causing programmed cell death, but researchers now show that they may have nondeadly jobs, too. While looking for proteins that partner with microRNAs (small non-coding RNAs that silence gene expression) to regulate how the nematode *Caenorhabditis elegans* develops, Weaver *et al.* found the caspase CED-3. Further experimentation revealed that CED-3 cleaved proteins that play important



An Alaskan glacier sliding to its destruction

PHOTOS: (TOP TO BOTTOM) © HENNY VAN EGDOM/ BUITEN BEELD/MINDEN PICTURES/CORBIS; MOELYN PHOTOS/GETTY IMAGES



Female great tits have superior memories when it comes to food.

ANIMAL COGNITION

Greater challenge, smarter birds

Males of many species, including humans, perform better than females at spatial navigation tasks. Great tits, a common European songbird, rely on spatial navigation for feeding—they pilfer stores of food cached by other bird species. Brodin and Urhan studied whether male and female great tits differed in their ability to find food after watching it get cached. Surprisingly, they found that females remembered the locations of the hidden food better than males. The authors attribute this to male dominance in foraging interactions, which makes finding food harder for females, but also makes them smarter about doing so. — SNV

Behav. Ecol. Sociobiol. 10.1007/s00265-014-1836-2 (2014).

roles in temporal cell fate patterning, stem cell pluripotency, and microRNA processing.
— BAP

eLife 10.7554/eLife.04265 (2014).

PSYCHOLOGY

Filing words away makes room for more

Google's search engine makes remembering facts less important than it used to be; Internet access in many countries is 24/7, so finding facts like the speed of sound (340 m/s) is quick and easy. To better understand how people remember new information they encounter digitally, Strom and Stone had subjects use computers to study two PDF files containing lists of words. They found that the metaphorical savings of space, gained by saving the first PDF file to the computer, translated into more memory available for encoding a second list of words. Subjects who saved the first file improved the number of words recalled from the second list. — GJC

Psychol. Sci. 10.1177/0956797614559285 (2014).

MENTAL HEALTH

Biology undermines clinician empathy

The translation of biological insight into therapeutic success is the Holy Grail of biomedical researchers. In the field of mental health, a clinician's empathy with patients also is a key to successful outcomes. Lebowitz and Ahn show that a focus on biological roots for mental disorders can threaten this empathy and the therapeutic alliance between clinician and patient. Mental health providers were presented with descriptions of patients experiencing depression, social phobia, schizophrenia, or obsessive compulsive disorder. Clinicians expressed more empathy when those descriptions emphasized potential causes that were psychosocial (e.g., aspects of life history) rather than biological (e.g., genetics or neurobiology). The pattern held whether the clinician had more medical training (psychiatry) or less (psychologist or social worker). — BW

Proc. Natl. Acad. Sci. U.S.A. 10.1073/pnas.1414058111 (2014).

PALEOBIOLOGY

Microbes driving the time machine

Preservation of the tissues of Earth's earliest animals—those that were present before and during the Cambrian explosion—required a lot of luck. According to new isotope data from *Conotubus hemiannulatus* fossils from Shaanxi Province, China, that luck was a function mostly of microbial activity. Schiffbauer *et al.* show that decaying carbon-rich animals are preserved typically either by being replaced three-dimensionally by pyrite crystals or compressed as carbonaceous films. Sedimentation rate ultimately controlled whether and for how long animal tissues were exposed to zones of bacterial sulfate reduction or methanogenesis within the sediment and thus their preservational style. — NW

Nat. Commun. 10.1038/ncomms6754 (2014).

HIV CONTROL

For HIV drugs, location trumps all

When resources are limiting, HIV-control programs need to be geographically selective. Gerberry *et al.* reached this conclusion after performing a comparative study of strategies for deploying prophylactic antiretroviral drugs in sub-Saharan Africa. The researchers used geospatial modeling to compare programs that would provide equal access to

drugs with programs that would maximize the overall societal benefit, two guiding principles created by the World Health Organization for allocating scarce resources. The authors' analysis suggests that the utilitarian principle, which maximizes overall societal benefits by locally distributing drugs to high-incidence areas, trumps access to all. — CA

Nat. Commun. 10.1038/ncomms6454 (2014).

MOLECULAR MEDICINE

Bat-filled tree source of Ebola epidemic?

Ground zero for the Ebola epidemic in West Africa may have been a hollow tree where children played and bats roosted. A year ago, a toddler in the Guinean village of Meliandou died of a mysterious disease; his family became infected shortly after. Bats are leading suspects for how the toddler caught the disease; in March 2014, scientists went to Guinea to look for signs of an Ebola outbreak in wildlife. But Saéz *et al.* report finding no such evidence and no direct evidence of Ebola infections in 169 bats they did find a clue: A tree stump near the toddler's house that burned on 24 March 2014, causing a "rain of bats," villagers said. Ash around the tree contained DNA fragments matching the Angolan free-tailed bat, known to survive infections with Ebola. — GV

EMBO Mol. Med. 10.15252/emmm.201404792 (2014).



An HIV-infected woman in the Central African Republic

ALSO IN SCIENCE JOURNALS

Edited by Melissa McCartney and Margaret Moerchen

RNA SPLICING

Predicting defects in RNA splicing

Most eukaryotic messenger RNAs (mRNAs) are spliced to remove introns. Splicing generates uninterrupted open reading frames that can be translated into proteins. Splicing is often highly regulated, generating alternative spliced forms that code for variant proteins in different tissues. RNA-binding proteins that bind specific sequences in the mRNA regulate splicing. Xiong *et al.* develop a computational model that predicts splicing regulation for any mRNA sequence (see the Perspective by Guigó and Valcárcel). They use this to analyze more than half a million mRNA splicing sequence variants in the human genome. They are able to identify thousands of known disease-causing mutations, as well as many new disease candidates, including 17 new autism-linked genes. — GR
Science, this issue p. 144; see also p. 124

BATTERIES

Watching the silver lining inside

Some types of batteries contain both a transition metal reducible metal, such as the cathode material $\text{Ag}_2\text{VP}_2\text{O}_8$. During operation, both Ag and V ions are reduced, and the Ag atoms can form wires to enhance the internal conductivity. Kirshenbaum *et al.* probe the discharge of a battery at different rates and track the formation of Ag atoms using *in situ* energy-dispersive x-ray diffraction (see the Perspective by Dudney and Li). They show how the discharge rate affects whether the Ag or

V is preferentially reduced and also the distribution of the Ag atoms, and then correlate this to the loss of battery capacity at higher discharge rates. — MSL
Science, this issue p. 149; see also p. 131

MATERIALS SCIENCE

Popping materials and devices from 2D into 3D

Curved, thin, flexible complex three-dimensional (3D) structures can be very hard to manufacture at small length scales. Xu *et al.* develop an ingenious design strategy for the microfabrication of complex geometric 3D mesostructures that derive from the out-of-plane buckling of an originally planar structural layout (see the Perspective by Ye and Tsukruk). Finite element analysis of the mechanics makes it possible to design the two 2D patterns, which is then attached to a previously strained substrate at a number of points. Relaxing of the substrate causes the patterned material to bend and buckle, leading to its 3D shape. — MSL

Science, this issue p. 154; see also p. 130

BIOMATERIALS

Mechanically soft neural implants

When implanting a material into the body, not only does it need the right functional properties, but it also needs to have mechanical properties that match the native tissue or organ. If the material is too soft, it will be mechanically degraded, and if it is too hard it may get covered with scar tissue or it may damage the surrounding tissues. Starting with a transparent silicone

substrate, Minev *et al.* patterned microfluidic channels to allow for drug delivery, and soft platinum/silicone electrodes and stretchable gold interconnects for transmitting electrical excitations and transferring electrophysiological signals. In tests of spinal cord implants, the soft neural implants showed biointegration and functionality within the central nervous system. — MSL

Science, this issue p. 159

METABOLISM

Getting specific about amino acid sensing

The protein kinase complex mTORC1 regulates growth and metabolism, and its activity is controlled in response to the abundance of cellular amino acids. Jewell *et al.* report that control of mTORC1 in response to glutamine does not require the Rag guanosine triphosphatase (GTPase) implicated in the sensing of other amino acids such as leucine (see the Perspective by Abraham). For sensing of glutamine, another GTPase, Arf1, was required. Distinct mechanisms thus appear to couple various amino acids to signaling by the mTORC1 complex. — LBR

Science, this issue p. 194; see also p. 128

STRUCTURAL BIOLOGY

Dueling dimers serve dual purposes

Both bacteria and mitochondria produce NADPH for amino acid biosynthesis and to remove reactive oxygen species. The enzyme that makes NADPH must translocate a proton across the membrane and transfer a hydride from NADH to

NADP⁺—processes that happen some 40 Å apart. To understand this complex geometry, Leung *et al.* solved the structures of the entire transhydrogenase enzyme and the membrane domain from the bacterium *Thermus thermophilus* (see the Perspective by Kregel and Törnroth-Horsefield). The entire enzyme exists as a dimer, with the two membrane domains in alternate orientations. One of the membrane domains interacts with the membrane component for proton translocation, whereas the other domain exchanges hydride with NAD(H) in another large soluble domain. — NW

Science, this issue p. 178; see also p. 125

METABOLISM

Sensing amino acids at the lysosome

The mTORC1 protein kinase is a complex of proteins that functions to regulate growth and metabolism. Activity of mTORC1 is sensitive to the abundance of amino acids, but how the sensing of amino acids is coupled to the control of mTORC1 has been unclear. Wang *et al.* searched for predicted membrane proteins that interacted with regulators of mTORC1. They identified a protein currently known only as SLC38A9. Interaction of SLC38A9 with mTORC1 regulators was sensitive to the presence of amino acids. SLC38A9 has sequence similarity to amino acid transporters. Effects of modulation of SLC38A9 in cultured human cells indicate that it may be the sensor that connects the abundance of arginine and leucine to mTORC1 activity. — LBR

Science, this issue p. 188

RESEARCH ARTICLE SUMMARY

RNA SPLICING

The human splicing code reveals new insights into the genetic determinants of disease

Hui Y. Xiong,* Babak Alipanahi,* Leo J. Lee,* Hannes Bretschneider, Daniele Merico, Ryan K. C. Yuen, Yimin Hua, Serge Gueroussov, Hamed S. Najafabadi, Timothy R. Hughes, Quaid Morris, Yoseph Barash, Adrian R. Krainer, Nebojsa Jojic, Stephen W. Scherer, Benjamin J. Blencowe, Brendan J. Frey†

INTRODUCTION: Advancing whole-genome precision medicine requires understanding how gene expression is altered by genetic variants, especially those that are far outside of protein-coding regions. We developed a computational technique that scores how strongly genetic variants affect RNA splicing, a critical step in gene expression whose disruption contributes to many diseases, including cancers and neurological disorders. A genome-wide analysis reveals tens of thousands of variants that alter splicing and are enriched with a wide

range of known diseases. Our results provide insight into the genetic basis of spinal muscular atrophy, hereditary nonpolyposis colorectal cancer, and autism spectrum disorder.

RATIONALE: We used “deep learning” computer algorithms to derive a computational model that takes as input DNA sequences and applies general rules to predict splicing in human tissues. Given a test variant, which may be up to 300 nucleotides into an intron, our model can be used to compute a score for how much

the variant alters splicing. The model is not biased by existing disease annotations or population data and was derived in such a way that it can be used to study diverse diseases and disorders and to determine the consequences of common, rare, and even spontaneous variants.

RESULTS: Our technique is able to accurately classify disease-causing variants and provides insights into the role of aberrant splicing in disease. We scored more than 650,000 DNA variants and found that disease-causing variants have higher scores than common variants and even those associated with disease in genome-wide association studies (GWAS). Our model predicts substantial and unexpected aberrant splicing due to variants within introns and exons, including those far from the splice site. For example, among intronic variants that are

ON OUR WEB SITE

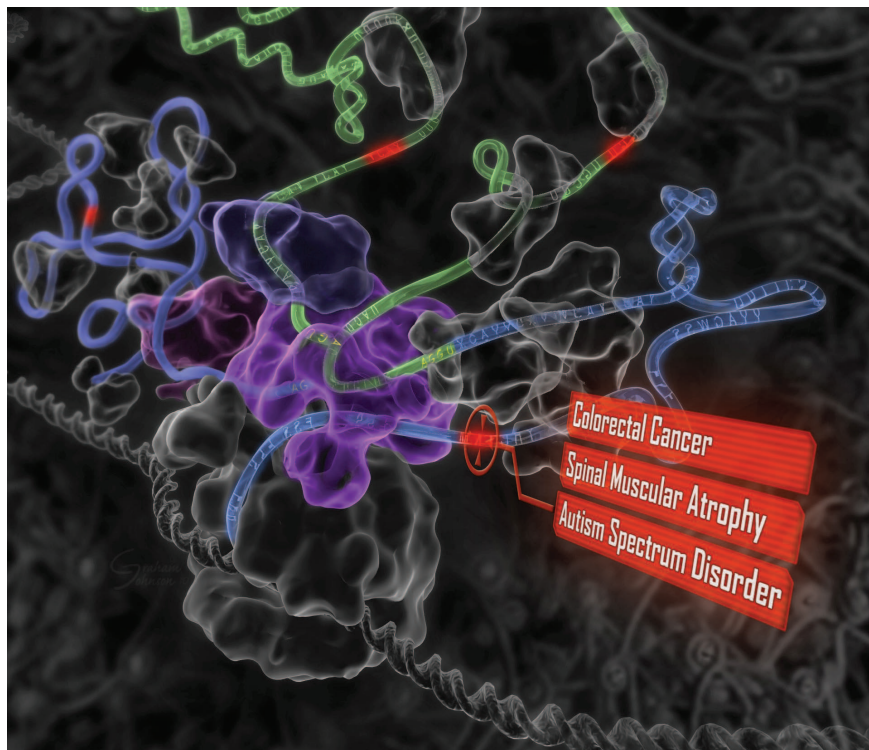
Read the full article at <http://dx.doi.org/10.1126/science.1254806>

more than 30 nucleotides away from any splice site, known disease variants alter splicing nine times as often as common variants; among missense exonic disease variants, those that least affect protein function are more than five times as likely as other variants to alter splicing.

Autism has been associated with disrupted splicing in brain regions, so we used our method to score variants detected using whole-genome sequencing data from individuals with and without autism. Genes with high-scoring variants include many that have previously been linked with autism, as well as new genes with known neurodevelopmental phenotypes. Most of the high-scoring variants are intronic and cannot be detected by exome analysis techniques.

When we scored clinical variants in spinal muscular atrophy and colorectal cancer genes, up to 94% of variants found to alter splicing using minigene reporters were correctly classified.

CONCLUSION: In the context of precision medicine, causal support for variants independent of existing whole-genome variant studies is greatly needed. Our computational model was trained to predict splicing from DNA sequence alone, without using disease annotations or population data. Consequently, its predictions are independent of and complementary to population data, GWAS, expression-based quantitative trait loci (QTL), and functional annotations of the genome. As such, our technique greatly expands the opportunities for understanding the genetic determinants of disease. ■



“Deep learning” reveals the genetic origins of disease. A computational system mimics the biology of RNA splicing by correlating DNA elements with splicing levels in healthy human tissues. The system can scan DNA and identify damaging genetic variants, including those deep within introns. This procedure has led to insights into the genetics of autism, cancers, and spinal muscular atrophy.

The list of author affiliations is available in the full article online.

*These authors contributed equally to this work.

†Corresponding author. E-mail: frey@psi.toronto.edu

Cite this article as H. Y. Xiong et al., *Science* 347, 1254806 (2015). DOI: 10.1126/science.1254806

RESEARCH ARTICLE

RNA SPLICING

The human splicing code reveals new insights into the genetic determinants of disease

Hui Y. Xiong,^{1,2,3*} Babak Alipanahi,^{1,2,3*} Leo J. Lee,^{1,2,3*} Hannes Bretschneider,^{1,3,4} Daniele Merico,^{5,6,7} Ryan K. C. Yuen,^{5,6,7} Yimin Hua,⁸ Serge Gueroussov,^{2,7} Hamed S. Najafabadi,^{1,2,3} Timothy R. Hughes,^{2,3,7} Quaid Morris,^{1,2,3,7} Yoseph Barash,^{1,2,9} Adrian R. Krainer,⁸ Nebojsa Jojic,¹⁰ Stephen W. Scherer,^{3,5,6,7} Benjamin J. Blencowe,^{2,5,7} Brendan J. Frey^{1,2,3,4,5,7,10,†}

To facilitate precision medicine and whole-genome annotation, we developed a machine-learning technique that scores how strongly genetic variants affect RNA splicing, whose alteration contributes to many diseases. Analysis of more than 650,000 intronic and exonic variants revealed widespread patterns of mutation-driven aberrant splicing. Intronic disease mutations that are more than 30 nucleotides from any splice site alter splicing nine times as often as common variants, and missense exonic disease mutations that have the least impact on protein function are five times as likely as others to alter splicing. We detected tens of thousands of disease-causing mutations, including those involved in cancers and spinal muscular atrophy. Examination of intronic and exonic variants found using whole-genome sequencing of individuals with autism revealed misspliced genes with neurodevelopmental phenotypes. Our approach provides evidence for causal variants and should enable new discoveries in precision medicine.

Regulatory cis elements constitute a substantial portion of the human genome (1, 2) and form the “regulatory code” that directs gene expression, depending on cellular conditions. The development of computational “regulatory models” that can read the code for any gene and predict relative concentrations of transcripts (3–5) raises the possibility that these models can be used to identify variants that lead to misregulated gene expression and human disease (6). Unlike many existing approaches (7–9), regulatory models do not suffer from the ascertainment biases inherent in databases of disease annotations. Here, we describe a system that uses a regulatory model

of splicing to find and score disease mutations (Fig. 1A).

A computational model of splicing

Misregulation of splicing contributes substantially to human disease (10), so we developed a computational model of splicing regulation that can be applied to any sequence containing a triplet of exons (Fig. 1B). The method extracts DNA sequence features (or cis elements) and, for a given cell type, uses them to predict the percentage of transcripts with the central exon spliced in (Ψ), along with a Bayesian confidence estimate. To train the model, we mined 10,689 exons that displayed evidence of alternative splicing and extracted 1393 sequence features from each exon and its neighboring introns and exons. RNA sequencing (RNA-seq) data from the Illumina Human Body Map 2.0 project (NCBI GSE30611) were used to estimate Ψ for each exon in each of 16 human tissues, and the model was trained to predict Ψ given the tissue type and the sequence features. Unlike existing methods (3, 11, 12), our computational model was derived using human data, incorporates over 300 new sequence features, and outputs real-valued absolute Ψ values for individual tissues, rather than categorical Ψ values for tissue differences (13).

We observed good agreement ($R^2 = 0.65$) between code-predicted Ψ and RNA-seq-assessed Ψ for exons that were held out during training (Fig. 1C). On the task of classifying high ($\Psi \geq 67\%$)

versus low ($\Psi \leq 33\%$) inclusion, the area under the receiver-operator characteristic curve (AUC) is 95.5%. For quality control, we only examined exon-tissue combinations ($n = 56,784$) for which the standard deviation of the RNA-seq-assessed Ψ was less than 10%, and cross-validation was used to ensure that test cases were not used during training (13) (table S3). The prediction accuracy was even higher ($R^2 = 0.94$, AUC = 99.1%) for the 50% of predictions with highest confidence ($n = 28,392$). The model is robust and accurate for categories of data that were not included during training, including genes with low expression, genes from excluded chromosomes, tissue differences in splicing levels, tissues from independent sources, and splicing levels quantified by reverse transcription polymerase chain reaction (RT-PCR) (13).

We next investigated whether our computational model accounts for the effects of known RNA-binding proteins (RBPs), which are key splicing regulators. We compared how well the calculated RBP binding affinity from Ray *et al.* (14) correlated with the observed variation in splicing and found 2080 strong correlations ($P < 0.01$, multiple hypothesis-corrected permutation test). Then we correlated the RBP binding affinities with the residual splicing activity not captured by the code, which was obtained by subtracting the code predictions from the observed values. The number of strong correlations dropped to 60, which suggests that our computational model mostly encompasses the collective effects of known RBPs (Fig. 2) (13).

Our model also accounts for the effects of disruptions in trans-acting factors. We examined knockdown data for Muscleblind-like (MBNL) RBPs in HeLa cells (15). There were 664 exons that exhibited a significant change in RNA-seq-assessed Ψ upon MBNL knockdown, as well as 26,457 exons whose levels did not change significantly upon knockdown. When we scored exons according to how much the model predicted that Ψ would change when the MBNL features were removed in silico, we found that MBNL-regulated exons frequently had higher scores [$P = 6.2 \times 10^{-57}$, Kolmogorov-Smirnov (KS) test, 31.4%]. The computational model predicted the effects of MBNL knockdown more accurately than direct examination of MBNL binding sites [10.9% improvement in the AUC; $P = 1.4 \times 10^{-14}$, bootstrap test (13)].

In contrast to correlation-based linear methods, where sequence features act independently, our computational model incorporates crucial context-dependent effects. When we derived tissue-specific linear models by searching over the most predictive set of sequence features, they always accounted for significantly less data variance ($R^2 < 0.49$) than our context-dependent model ($R^2 = 0.65$). We found that in our model, the same feature can influence Ψ differently in different cis contexts established by other sequence features and in different trans contexts specified by cell type (13) (figs. S14 and S15). For instance, 40 of the 100 most strongly predictive sequence features frequently switched

¹Department of Electrical and Computer Engineering, University of Toronto, Toronto, Ontario M5S 3G4, Canada.

²Donnelly Centre for Cellular and Biomolecular Research, University of Toronto, Toronto, Ontario M5S 3E1, Canada.

³Program on Genetic Networks and Program on Neural Computation & Adaptive Perception, Canadian Institute for Advanced Research, Toronto, Ontario M5G 1Z8, Canada.

⁴Department of Computer Science, University of Toronto, Toronto, Ontario M5S 3G4, Canada. ⁵McLaughlin Centre, University of Toronto, Toronto, Ontario M5G 0A4, Canada.

⁶Centre for Applied Genomics, Hospital for Sick Children, Toronto, Ontario M5G 1X8, Canada. ⁷Department of Molecular Genetics, University of Toronto, Toronto, Ontario M5S 1A8, Canada. ⁸Cold Spring Harbor Laboratory, Cold Spring Harbor, NY 11724, USA. ⁹School of Medicine, University of Pennsylvania, Philadelphia, PA 19104, USA.

¹⁰eScience Group, Microsoft Research, Redmond, WA 98052, USA.

*These authors contributed equally to this work. †Corresponding author. E-mail: frey@psi.toronto.edu

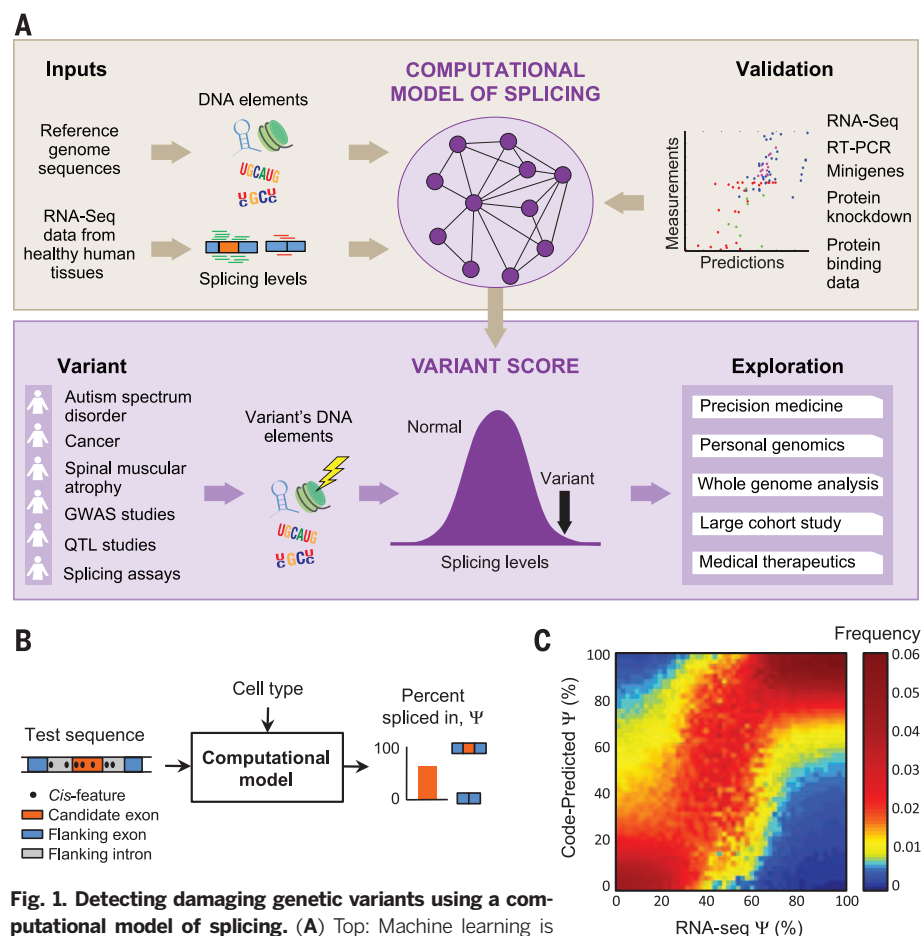


Fig. 1. Detecting damaging genetic variants using a computational model of splicing. (A) Top: Machine learning is used to infer a computational model of splicing, by correlating DNA elements with splicing levels in healthy human tissues. Bottom: Genetic variants arising from a wide array of diseases and technologies can be detected and filtered using the computational model, enabling explorations into the genetics of disease. (B) For a given cell type, the computational model extracts the regulatory code from a test DNA sequence and predicts the percentage of transcripts with the exon spliced in, Ψ . (C) Predictions are made for 10,689 test exons profiled in 16 tissues; exons and tissues are binned according to their RNA-seq-assessed values of Ψ , and for each bin (column) the distribution of code-predicted Ψ is plotted ($n = 56,104$).

the direction of their effect in at least one tissue, depending on cis context.

We wondered whether our computational model could accurately predict differences in splicing levels between individuals using only their genotype. We analyzed genotype and RNA-seq data for lymphoblastoid cell lines from four individuals (16) and used our model to predict Ψ in white blood cells, for pairs of individuals that have differing SNPs (13). When we examined 99 exons that exhibited a significant difference in RNA-seq-assessed Ψ between pairs of individuals and whose predicted difference in Ψ was above a noise threshold, we found that our technique correctly predicted the direction of change in 73% of cases ($P = 3.5 \times 10^{-6}$, binomial test).

Genome-wide analysis of splicing misregulation and disease

To assess the implications of genetic variation for splicing regulation, we mapped 658,420 single-

nucleotide variations (SNVs) to exonic and intronic sequences containing the regulatory code for ~120,000 exons in ~16,000 genes (13). Of these SNVs, 543,525 are single-nucleotide polymorphisms (SNPs), which are common (minor allele frequency or MAF > 1%) (17), whereas 114,895 have been linked to diseases and are mostly rare (MAF < 1%) (18). To score the effect of every SNV on splicing regulation, we applied the regulatory model to the sequence with and without the SNV and computed the difference in predicted splicing level, $\Delta\Psi$, for each tissue (Fig. 3A). We studied the effects of SNVs using the largest value of $\Delta\Psi$ across tissues, as well as a “regulatory score” that aggregates the magnitude of $\Delta\Psi$ across tissues (13).

The code provides an unprecedented view of the impact of SNVs on splicing regulation (Fig. 3B). It reveals 20,813 unique SNVs that disrupt splicing ($|\Delta\Psi| \geq 5\%$; table S4), frequently in a way that depends on cis context (13) (fig. S21). Diverse methods of validation support the func-

tional impact of these disruptions. Intronic SNVs that are close to splice sites frequently cause misregulation, but 465 intronic SNVs that are more than 30 nucleotides (nt) from any splice site also induce substantive changes. Within exons, we found that significant deviations are induced by 9525 nonsense SNVs and 1273 missense SNVs but also by 579 synonymous SNVs—a result supported by recent data showing that synonymous mutations frequently contribute to human cancer (19).

To explore the causal implications of high-scoring SNVs in the context of disease, we examined whether disease SNVs are predicted to disrupt splicing ($|\Delta\Psi| \geq 5\%$) more frequently than common SNPs, of which a large portion are thought to be under neutral selection (20). We plotted the locations and $\Delta\Psi$ for 81,608 disease SNVs located up to 100 nt into exons or up to 300 nt into their adjacent introns (Fig. 3C).

Our technique reveals widespread processes whereby disease SNVs cause misregulation of splicing. Databases of disease annotations were not used to train our model, so it is not susceptible to overfitting already discovered disease SNVs or inherent ascertainment biases (7–9).

We found that intronic disease SNVs that are more than 30 nt from any splice site are 9.0 times as likely to disrupt splicing regulation relative to common SNPs in the same region ($P = 5.1 \times 10^{-68}$, two-sample t test, $n = 1639$ and $n = 24,535$). Within exons, synonymous disease SNVs are on average 9.3 times as likely as synonymous SNPs to disrupt splicing regulation ($P = 8.0 \times 10^{-116}$, two-sample t test, $n = 2652$ and $n = 4510$).

Missense SNVs have previously been examined mainly in the context of how they alter protein function (7). Our method enables the exploration of their effects on splicing regulation. We found that missense disease SNVs are not more likely to disrupt splicing than missense SNPs ($P = 0.22$, two-sample t test, $n = 58,918$ and $n = 2981$), which contradicts previously published evidence that they do ($P \approx 0.05$) (9). However, when we examined 789 and 1757 missense disease SNVs that minimally and maximally alter protein function as indicated by Condel (21) analysis, we found that SNVs that minimally alter protein function are on average 5.6 times as likely to disrupt splicing regulation ($P = 4.5 \times 10^{-14}$, two-sample t test), elucidating a “disease by misregulation” mechanism (13).

We found that within introns, the regulatory scores of 457 SNPs that were implicated in genome-wide association studies (GWAS) and that map to regulatory regions (22) are quite similar to non-GWAS SNPs ($P = 0.27$, KS test, $n = 262,804$), whereas the scores of disease SNVs are significantly higher ($P < 1 \times 10^{-320}$, KS test, 71.2%, $n = 280,638$). Fewer than 5% of GWAS SNPs are estimated to cause misregulation in a fashion similar to disease SNVs (13), indicating that our method can detect disease SNVs that are not detectable by GWAS (Fig. 4A). In further support of the functional specificity of our approach, we found that the regulatory scores of disease SNVs with

strong experimental evidence are substantially higher than those with weak or indirect evidence (Fig. 4B).

Next, we used the computational model to analyze three human diseases with different characteristics: spinal muscular atrophy (autosomal-

recessive single gene), nonpolyposis colorectal cancer (oligogenic), and autism spectrum disorder (multigenic).

Spinal muscular atrophy (SMA)

To explore misregulation of *SMN1/2*, which is associated with SMA, a leading cause of infant mortality (23), we used the computational model to simulate the effects of more than 700 known and novel mutations around exon 7 in *SMN1/2*. We first examined the regulatory consequences of four nucleotides that differ between *SMN1* and *SMN2*, labeled C6T, G-44A, A100G, and A215G in Fig. 5A, where “-44” indicates 44 nt upstream of the 3' splice site. These substitutions are known to lead to decreased inclusion of exon 7 in *SMN2* and loss of function.

Our method predicts that exon 7 skipping is predominantly caused by C6T and to a much lesser degree by G-44A, whereas A100G and A215G are predicted not to have a significant impact on splicing. The prediction for C6T is consistent with previously published mutagenesis data (23). Mutagenesis data indicate that A100G enhances skipping by 36% to 63% (24) in the *SMN2* context. Using a Z-score threshold of 1, our computational model also predicts a small but significant skipping effect of A100G

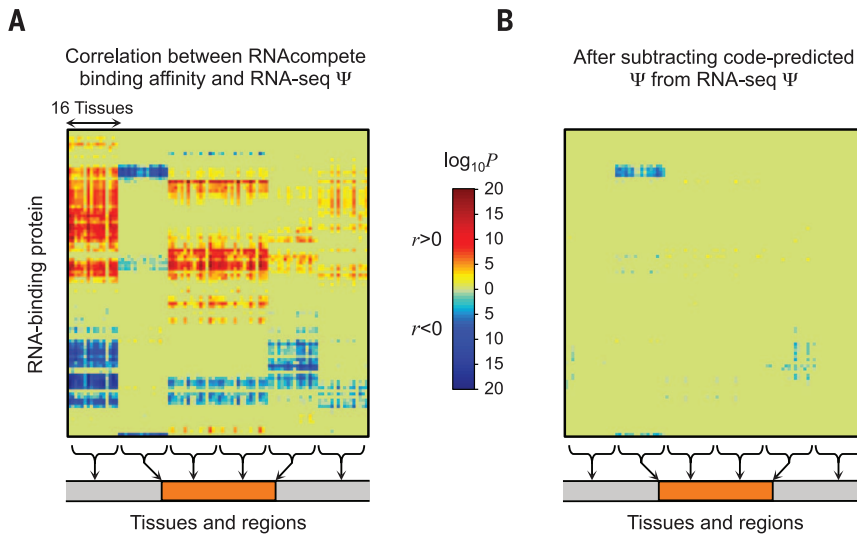


Fig. 2. Accounting for RNA-binding proteins (RBPs). (A) Correlations between RNA-seq Ψ and the affinities of RBPs assayed in 98 in vitro experiments (14). (B) When code-predicted Ψ values are subtracted from RNA-seq-assessed values of Ψ , their correlations with the binding affinities mostly vanish.

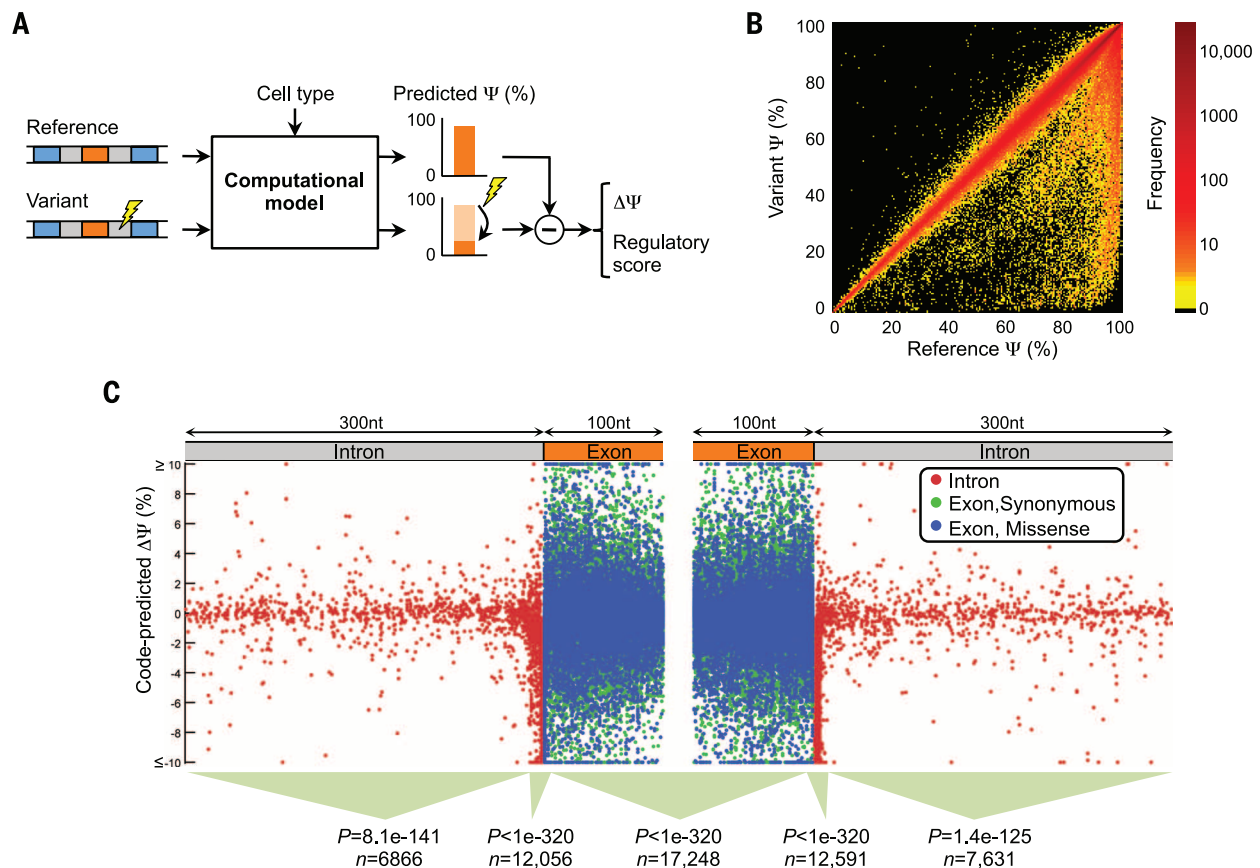


Fig. 3. Genome-wide analysis of genetic variations. (A) To assess the effect of a single-nucleotide variation (SNV), the computational model is applied to the reference sequence and the variant. Then, the maximum difference $\Delta\Psi$ across tissues is computed, along with a “regulatory score” that also accounts for prediction confidence (13). (B) The effect on Ψ of 658,420 intronic and exonic SNVs. (C) Locations and predicted $\Delta\Psi$ of 81,608 disease-annotated intronic SNVs and synonymous or missense exonic SNVs. In different sequence regions, the scores of disease SNVs tend to be larger than those of SNPs (Ansari-Bradley tests for equal dispersion; n includes both types).

in the *SMN2* context. We used minigene reporters to test our predictions and found that in all cases they are supported by the experimental data, including the negligible effect of A100G mutation in the *SMN1* context (Fig. 5B, red). Further, our prediction for G-44A is consistent with antisense oligonucleotide experiments indicating that it overlaps with a splicing suppressor (25).

To explore mutations that may result in gain of *SMN2* function, we simulated the regulatory effects of all 420 possible point mutations in 140 nt of intronic sequence upstream of exon 7 (Fig. 5B). Minigene reporter data for the top three predictions confirm that none of them exhibit decreased inclusion and two of them cause increased inclusion (Fig. 5, B and C, green). Together, the predictions for *SMN1* and *SMN2*

mutations (Fig. 5C) have a Spearman correlation of 0.82 with the experimental data ($P = 0.017$, $n = 7$, one-sided permutation test).

We generated a literature-curated compendium of mutagenesis data for 85 variations located in three exonic regulatory regions previously tested using in vivo selection, plus an intronic region. When our model is used to predict $\Delta\Psi$ for these cases (Fig. 5D), the direction of regulation is correct in 85% of cases and the Spearman correlation is 0.74 ($P = 5.7 \times 10^{-16}$, one-sided permutation test). We additionally used our method to simulate $\Delta\Psi$ for 101 mutants selected in vivo to increase Ψ , with point mutations in the first 6 nt in exon 7 and also in the entire exon (23). Increases in Ψ are correctly predicted in 98.7% of the 78 high-confidence cases (table S6).

Nonpolyposis colorectal cancer

Lynch syndrome, or hereditary nonpolyposis colorectal cancer, accounts for ~3% of colorectal cancer cases (26), and nearly 90% of reported variations occur in the DNA mismatch repair genes *MLH1* and *MSH2* (27). Numerous studies have shown that misregulation of splicing accounts for a major portion of cases (28) but also that existing computational predictions for variations that do not directly disrupt splice sites

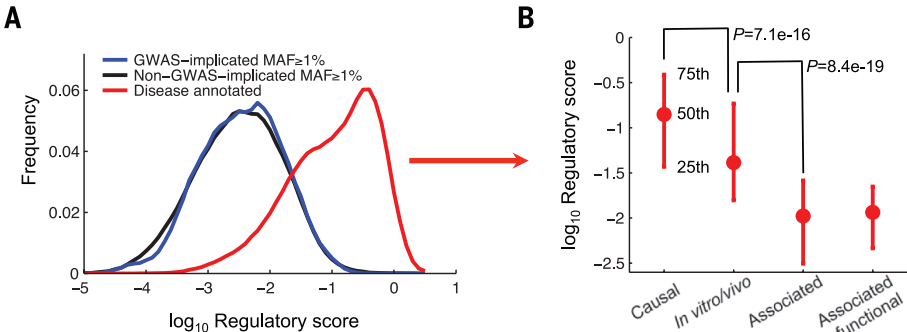


Fig. 4. Regulatory scores of GWAS SNPs. (A) Distributions of regulatory scores for GWAS-implicated SNPs ($n = 457$), non-GWAS-implicated SNPs ($n = 262,347$), and disease SNVs ($n = 18,291$) in introns. (B) Regulatory scores of disease-annotated intronic SNVs that are causal ($n = 17,631$), supported by in vitro and in vivo data ($n = 224$), only associated ($n = 324$), or associated but have additional functional evidence ($n = 112$). P values (t test) are indicated.

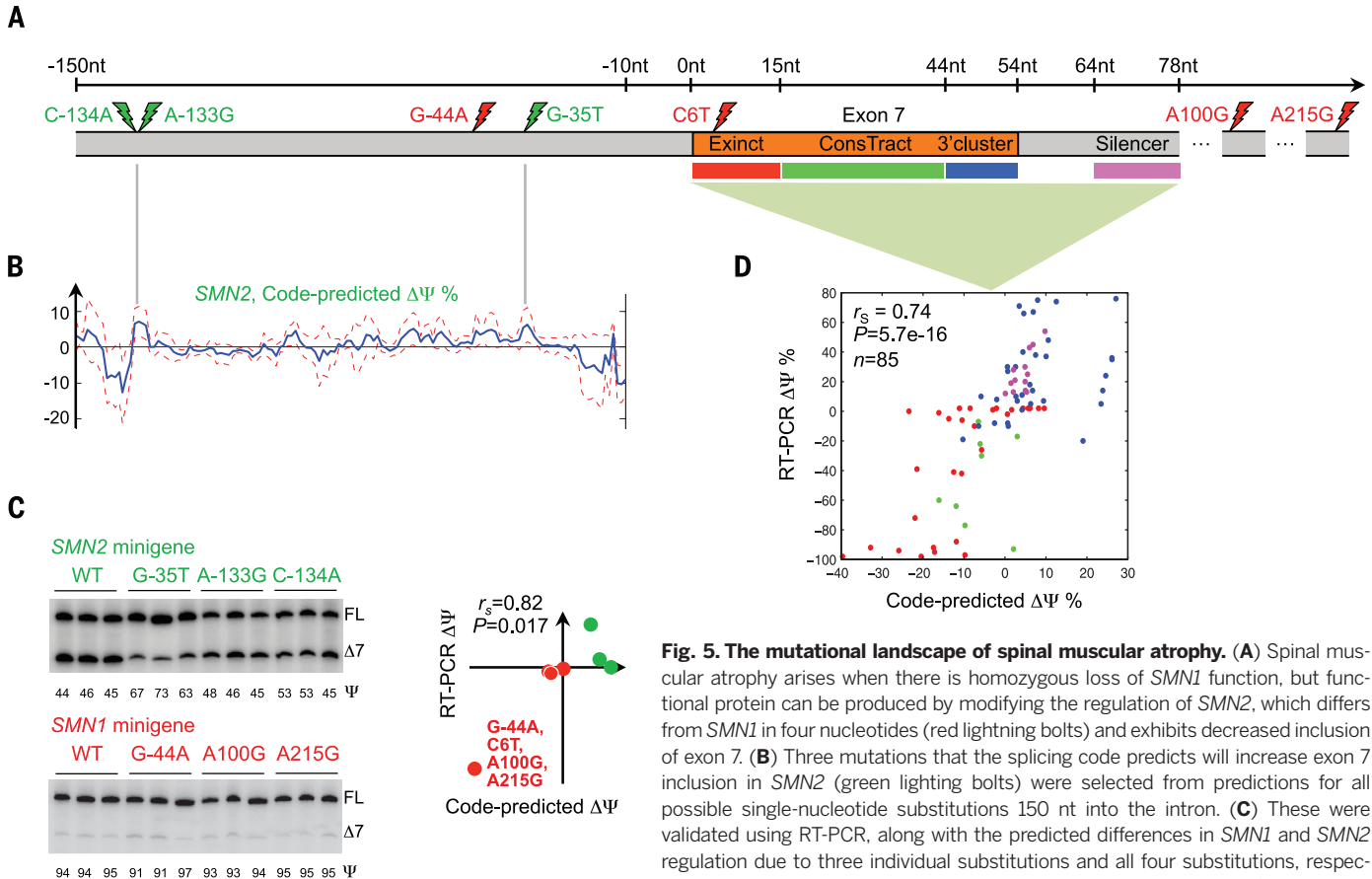


Fig. 5. The mutational landscape of spinal muscular atrophy. (A) Spinal muscular atrophy arises when there is homozygous loss of *SMN1* function, but functional protein can be produced by modifying the regulation of *SMN2*, which differs from *SMN1* in four nucleotides (red lightning bolts) and exhibits decreased inclusion of exon 7. (B) Three mutations that the splicing code predicts will increase exon 7 inclusion in *SMN2* (green lightning bolts) were selected from predictions for all possible single-nucleotide substitutions 150 nt into the intron. (C) These were validated using RT-PCR, along with the predicted differences in *SMN1* and *SMN2* regulation due to three individual substitutions and all four substitutions, respectively. Predictions and RT-PCR data have a Spearman correlation of 0.82 ($P = 0.017$, one-sided permutation test). (D) Predicted $\Delta\Psi$ values for 85 individual mutations located in four regions are plotted against RT-PCR-assessed values; the Spearman correlation is 0.74 ($P = 5.7 \times 10^{-16}$, one-sided permutation test).

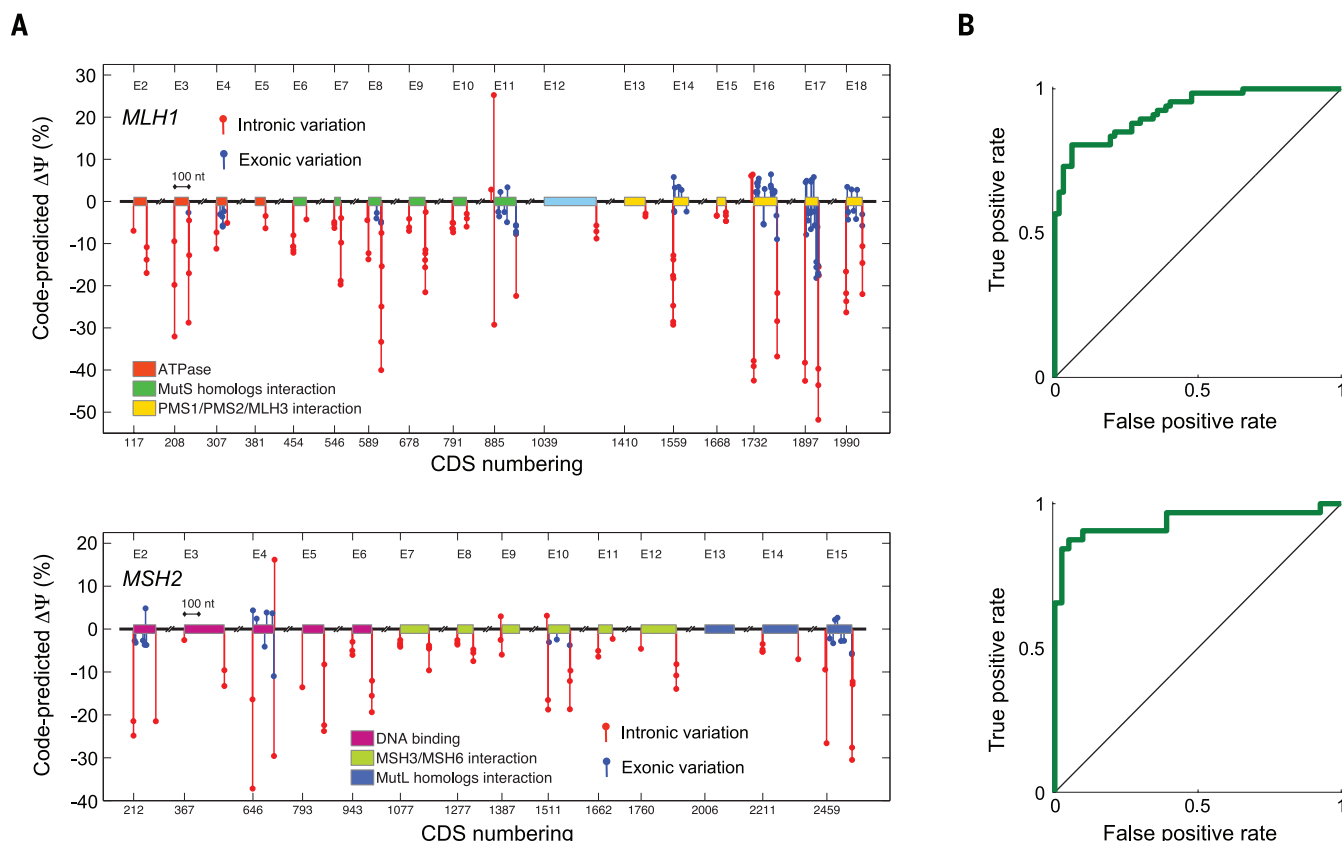


Fig. 6. The mutational landscape of nonpolyposis colorectal cancer. (A) Predicted $\Delta\Psi$ for mutations in *MLH1* and *MSH2* arising in patients with nonpolyposis colorectal cancer, or Lynch syndrome. Coding sequence (CDS) numbering is based on GenBank NM_000249.3 and NM_000251.2 and starts at A of the ATG translation initiation codon. (B) Validation using 134 *MLH1* variations tested by RT-PCR (AUC = 92.4%, $P = 2.8 \times 10^{-24}$, one-sided permutation test) and 73 *MSH2* variations (AUC = 93.8%, $P = 8.7 \times 10^{-15}$, one-sided permutation test).

are not correlated with experimental data (28, 29). It has been suggested that this is because existing tools do not take interactions between regulatory features into account (29).

We evaluated 977 SNVs, 156 of which are non-sense, in *MLH1* and *MSH2* (27) using our computational model and found that high levels of misregulation are predicted (Fig. 6A and tables S7 and S8) (13): 32.3% of SNVs exhibited a $\Delta\Psi$ that was larger than that of 95% of common SNVs ($P = 4.2 \times 10^{-135}$, one-sided binomial test). To avoid bias, we excluded *MLH1*, *MSH2*, and their variants during model training. Additionally, the majority of predictions are concordant with published RT-PCR data (tables S9 and S10). When predicted $\Delta\Psi$ was used to classify increased skipping versus no change for SNVs where RT-PCR data were available, AUCs of 92.4% and 93.8% (Fig. 6B) were achieved for 134 *MLH1* and 73 *MSH2* variants [$P = 2.8 \times 10^{-24}$ and $P = 8.7 \times 10^{-15}$, one-sided permutation tests (13)].

To further test the specificity of our method, we mapped 80 common SNPs to *MLH1* and *MSH2* and compared their regulatory scores to those of the SNVs found in patients. Common SNPs had significantly lower scores ($P = 8.1 \times 10^{-11}$, KS test, 40.0%, $n = 1058$), indicating that our method successfully detects causal variants (13).

Our method sheds light on unresolved hypotheses for the mechanisms of specific muta-

tions. Three missense substitutions in the second nucleotide of codon 659 in exon 17 of *MLH1* are observed in Lynch syndrome patients: c.1976G>T, c.1976G>C, and c.1976G>A. Evidence indicates that c.1976G>A likely does not change protein function, which suggests that the mechanism is splicing misregulation (30–32). Indeed, RT-PCR data indicate that c.1976G>T and c.1976G>C induce increased exon skipping (30). However, previous computational analyses either fail to predict misregulation (31) or, because the mutations increase the strength of an exonic splicing enhancer, erroneously predict increased exon inclusion (13, 33). We applied our computational model and found that it confidently and correctly predicts increased skipping in all three cases (table S10) and also correctly predicts that c.1976G>C has a stronger effect than c.1976G>T. We can thus hypothesize that c.1976G>A induces aberrant splicing and renders the translated protein dysfunctional.

Autism spectrum disorder (ASD)

ASD is a neurodevelopmental condition characterized by language deficiency, restricted and repetitive interests, and challenges in social skills. It is highly heritable, but its substantial clinical and genetic heterogeneity has complicated the identification of all etiologic genetic variants (34). Through the study of rare genetic

variants, ~100 genes have now been implicated in ASD (35), and these are estimated to account for ~20% of the etiologic cause in different cohorts examined (36, 37). More recent studies using whole-genome sequencing revealed higher yields of contributing mutations, but these studies have focused only on exonic regions (38). Common genetic variants may also have an effect in ASD, but few studies replicate the same loci (39). Splicing misregulation as a cause of ASD is evidenced by examples of genes involved in ASD, such as neurexins and neuroligins, that are extensively alternatively spliced (40), as well as by recent transcriptomic analyses showing consistent deviations in alternative splicing patterns in the cortical regions of ASD cases (41).

To identify genes with SNVs that potentially cause splicing misregulation in ASD cases, we used our regulatory model to analyze the genomes of five idiopathic ASD cases, which do not have ASD-associated cytogenetic markers such as chromosome 15q duplication (13). We sequenced these genomes using brain samples from the Autism Tissue Program (42) and selected the genomes of 12 controls consisting of three subgroups of four controls each. As a control, we clustered the ASD and control genomes using genome-wide genetic similarity and verified that they cluster by ethnic group but not by disease condition or other covariates; this

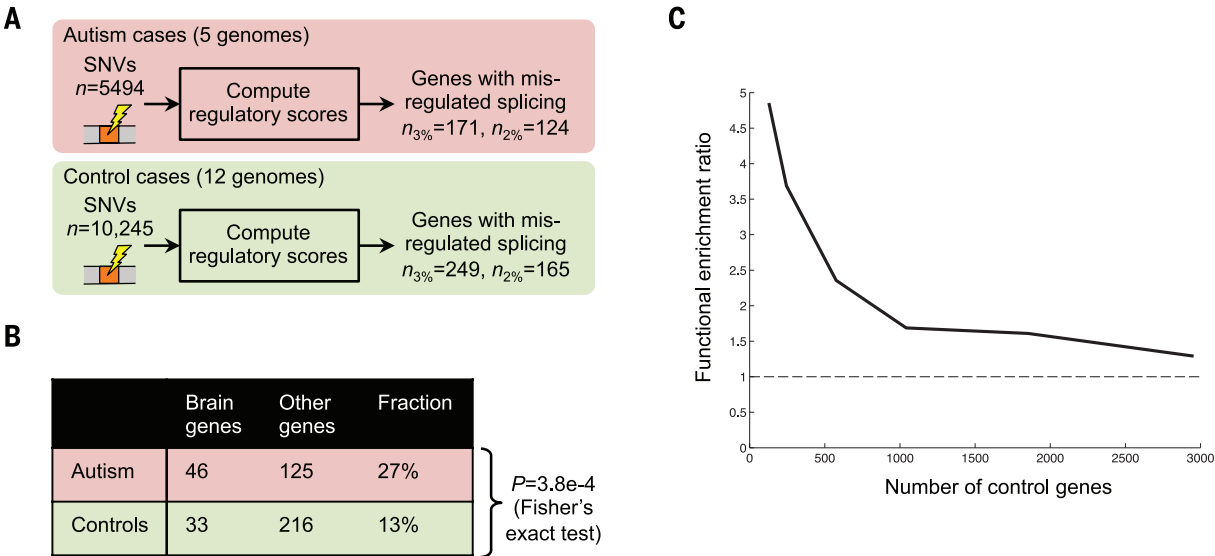


Fig. 7. Splicing misregulation in individuals with autism. (A) Genes containing at least one SNV that the computational model predicts will cause decreased exon inclusion were identified in five autism spectrum disorder (ASD) cases and 12 controls by thresholding $\Delta\Psi$ using either the 2nd or 3rd percentile of $\Delta\Psi$ for SNPs. (B) Genes that our method predicts are misregulated in ASD cases more frequently have high expression in brain tissues than in control cases. (C) The effect of varying the threshold on $\Delta\Psi$, and thus the number of case and control genes, on the odds ratio for the enrichment of central nervous system development genes (GO:0007417); in all cases, $P < 0.05$.

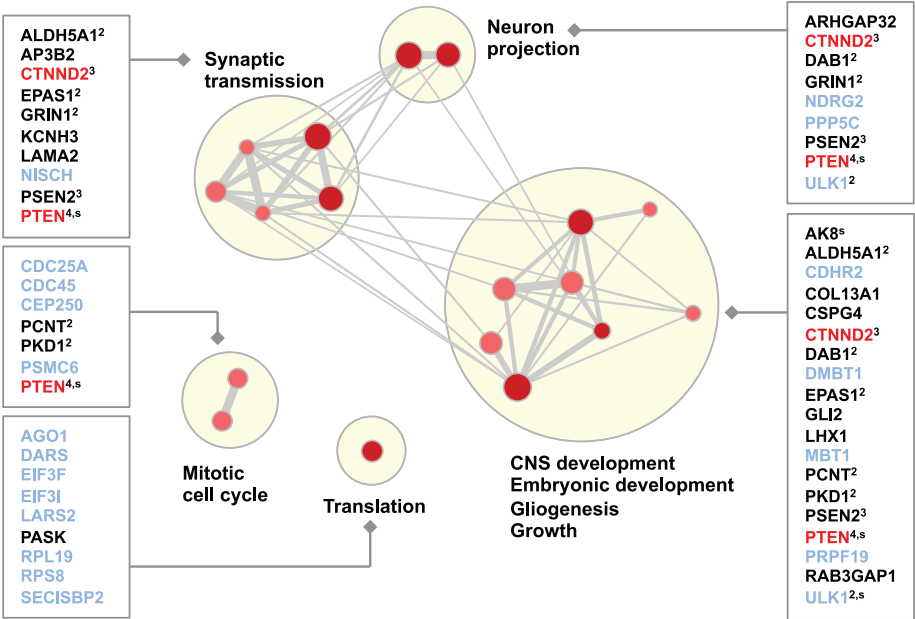


Fig. 8. Misregulated genes and functional categories enriched in individuals with autism. Gene Ontology and pathway categories that are enriched ($P \leq 0.01$, Fisher's exact test) in misregulated genes from ASD cases relative to controls were identified ($n = 18$), along with the corresponding set of genes from ASD cases. Each gene set is shown as a red or pink dot, depending on whether the 2nd- or 3rd-percentile threshold was used for detection (Fig. 7A), and size is proportional to the number of genes in the set. Edge thickness indicates the fraction of genes shared between two sets. Groups of functionally related gene sets are highlighted by blond discs. The names of novel genes that are not already implicated in ASD and have neural-related phenotypes are shown in black, the names of genes already implicated in ASD are in red, and other gene names are in pale blue. If a gene is in multiple categories, the number of categories is shown in superscript; genes in which a stop codon is introduced by the SNV are labeled "s."

result indicates that the ASD and control SNVs are not grossly biased by nondisease effects (13) (fig. S27).

The genomes of cases and controls were scanned for SNVs (13) and, to focus our analysis on rare variants, we retained only high-quality

homozygous and heterozygous reference SNVs (in which one allele matches the reference allele) that did not correspond to common SNPs. This resulted in a median of ~42,000 SNVs per subject.

We examined genes with high expression in brain tissues, which are more frequently implicated in ASD, and did not find an enrichment of SNVs in ASD cases versus controls [$P = 0.24$, Fisher's exact test (13)]. Aiming to separate causal SNVs from noncausal ones, we identified SNVs that our technique predicts will cause splicing misregulation (Fig. 7A). All variants were mapped onto the splicing code within canonical Ensembl transcripts, resulting in 15,739 SNVs, whose code-predicted $\Delta\Psi$ s were then computed (table S13). We identified genes with misregulated splicing in cases and also in controls by applying a threshold to $\Delta\Psi$ equal to the 2nd and also the 3rd percentile of $\Delta\Psi$ for common SNPs (Fig. 7B) (13), and genes misregulated in both cases and controls were removed from further analysis.

Among genes that our technique predicts are misregulated in ASD cases ($n = 171$), 27% have high expression in brain, whereas for controls ($n = 249$), only 13% have high expression in brain ($P = 3.8 \times 10^{-4}$, Fisher's exact test). When we examined genes with low or no expression in brain tissues, we did not observe significant differences (13). Further, when we made the threshold used to identify misregulated genes more stringent, we found that enrichment of ASD-related functions was amplified (Fig. 7C). These results open the door to discovering new genetic determinants of ASD and also suggest that more generally, our splicing model can be used to sift through variants to support precision medicine and whole-genome variant studies.

We tested Gene Ontology annotation and pathway-based gene sets for enrichment in misregulated genes; to account for biases such as gene length, we tested the gene enrichment in ASD genomes relative to control genomes. Interestingly, we found categories related to synaptic transmission and to neuron projection and growth (Fig. 8). Gene permutation analysis shows that enrichment in neurodevelopmental gene sets is significant (empirical false discovery rate < 4%). In addition, repeating the analysis for a subset of control genomes versus another subset of control genomes did not produce any significant results, and top-ranking gene sets were not neurodevelopmental.

We found 39 genes with predicted splicing alterations that are associated with at least one enriched function, and we additionally prioritized 19 of these genes as more compelling ASD disease candidates because they are known to have neurological, neurobehavioral, or neurodevelopmental phenotypes in human [Human Phenotype Ontology (HPO) and Online Mendelian Inheritance in Man (OMIM)] or mouse [Mouse Genomics Informatics/Mammalian Phenotype Ontology (MGI/MPO)] (table S16). The analysis reveals interesting candidates, and only *CTNND2* and *PTEN* have been previously implicated or suggested to play a role in ASD (35, 43). Our study suggests new candidate ASD genes, including *ALDH5A1*, *GLI2*, *GRIN1*, *KCNH3*, *LAMA2*, and *NISCH*, in addition to other possibilities. Our results are robust to choices made in the analysis (13) and can be combined with other approaches [e.g., (44)] to develop diagnostic techniques.

Discussion

Our results from profiling the genome-wide effects of more than 650,000 SNVs shed light on how genetic variation affects splicing. Further, our in-depth results from the analysis of thousands of variations in diverse disorders, including spinal muscular atrophy, nonpolyposis colorectal cancer, and autism, exemplify the wide range of applicability of our technique and provide insights into the genetic determinants of these diseases.

In the context of precision medicine, the importance of providing causal evidence for putative variants with the goal of avoiding the effects of confounding factors, such as population stratification, has recently been underscored (45, 46). The ability of our computational technique [SPANR (splicing-based analysis of variants); see (13) and <http://tools.genes.toronto.edu>] to provide regulatory evidence for a variant's disruptiveness is supported by accurate predictions for test sequences that were not used during training, discrimination of disease variants even though the model was not trained using disease labels, and strong correlation between code-predicted changes in splicing induced by mutations and experimental data using minigene reporters.

Our approach contrasts with techniques that use functional annotations of the genome (2, 8, 47), tools that are trained using existing disease

annotations and thus suffer from overfitting to known mutations or severe selection bias (7–9, 48, 49); GWAS (50, 51); and expression-based quantitative trait loci (QTL) (16, 52). To compare our method with using functional genome annotations, we removed missense exonic SNVs that may affect phenotype without changing splicing regulation, yielding 26,403 SNVs that map to canonical Ensembl transcripts. At a false positive rate of 0.1%, we found that scoring SNVs by their overlap with functional annotations detects 1.4% of disease variants, whereas our method is 25 times as sensitive and detects 35.9% of disease variants (13).

Relative to state-of-the-art methods that examine perturbations of motifs and genome annotations but do not account for changes in gene regulation (48, 49), our method is nearly 10 times as sensitive in each of several sequence regions (fig. S18). Our technique does not directly detect variants associated with a phenotype of interest. However, when it is combined with phenotype-matched genotype data such as those generated by whole-genome sequencing, it can detect variants relevant to phenotype, as demonstrated by our autism analysis.

In contrast to GWAS (50), splicing QTL analysis (52), and other methods that use allele frequencies within populations to score variants (47), our technique does not directly depend on allele frequencies. As demonstrated above, our method can reliably detect rare and even spontaneous disease variants. To provide evidence that our method is not dependent on allele frequency, we separately analyzed rare variants ($0.1\% < \text{MAF} < 1\%$), moderately common variants ($1\% < \text{MAF} < 5\%$), and disease variants [annotated in the Human Gene Mutation Database (HGMD), mostly rare]. We found that the disease variants have regulatory scores significantly different from those of the rare and common variants, but the distribution of regulatory scores is indistinguishable for rare and common variants (13). Furthermore, when we examined 15,386 disease variants and 1519 common SNPs within intronic regions with moderate to high conservation across vertebrates (PhastCons score > 0.5), we found that our method more accurately detects disease variants ($P < 1 \times 10^{-320}$, KS test, 60.1%) than scoring them using conservation ($P = 2.2 \times 10^{-166}$, KS test, 38.2%).

Our approach can be combined with population-based methods so as to amplify their specificity and identify causal variants in the context of specific diseases, either by providing more refined scores or by scoring variants in the same linkage disequilibrium block as a GWAS- or QTL-identified noncausal SNP. When we evaluated 453 splicing QTLs that were identified using blood samples and the genotypes of 922 individuals (52), we found that a subset of splicing QTLs had high regulatory scores, as computed using our method, relative to those of common SNPs in general ($P = 4.2 \times 10^{-10}$, KS test, 15.4%).

Potential sources of prediction error include unaccounted-for RNA features, inaccuracies in

computed features, imperfect modeling of splicing levels, and limitations due to a focus on cassette splicing. Even so, the method described here performs well, as assessed both by validation of splicing prediction using several diverse sources of data and by its ability to detect disease mutations.

We anticipate that it will be important to seek regulatory models that encompass other major steps in gene regulation, including chromatin dynamics, transcription, polyadenylation, mRNA turnover, protein synthesis, and protein stabilization. These processes influence transcript levels in a highly integrated manner within the cell, so modeling them jointly should lead to more accurate predictions. Moreover, evidence suggests that DNA elements previously thought to be pertinent to only one regulatory process may in fact span several steps in the regulatory chain. Examples include nucleosome positioning, epigenetic modifications, and chromatin interactions (53).

Materials and methods

Details of all data sets, learning algorithms, statistical analyses, experimental validation, and Web tool implementation are provided in the supplementary materials. In brief, the human splicing code was assembled using 1393 carefully designed sequence features extracted from each of the 10,689 alternatively spliced exons and their corresponding Ψ values profiled in 16 normal tissues from human BodyMap 2.0 (NCBI GSE30611) RNA-seq data. The features of an exon were extracted from its proximal genomic sequences, including exon and intron lengths, splice site signals, counts of splicing factor motifs, trinucleotide frequencies, retrovirus repeats, nucleosome positioning, RNA secondary structures, etc. The computational model was learned using a Bayesian deep learning algorithm, with extreme care exercised to prevent overfitting. Because the model was built using the reference genome only, its performance was first validated using held-out data, including additional RNA-seq (54), RT-PCR, RBP binding (14), and MBNL knockdown (15) data sets. The model was further evaluated using genome-wide SNVs, including common SNPs in dbSNP135 (17), point mutations in HGMD (18), and rare variants from ANNOVAR (55). Finally, the splicing model was applied in three disease studies: SMA, hereditary nonpolyposis colorectal cancer, and ASD. A large amount of literature-curated data from splicing assays was used to validate our predictions for SMA and nonpolyposis colorectal cancer mutations, with additional mutagenesis experiments carried out for SMA. When applying our computational model to ASD, we performed whole-genome sequencing on five ASD and four control subjects (deposited at the European Genome-Phenome Archive, www.ebi.ac.uk/ega, with accession number EGAS00001000928). Our SPANR Web tool (<http://tools.genes.toronto.edu>) is programmed in Python under the Flask Web framework (<http://flask.pocoo.org>) and makes use of MongoDB (www.mongodb.org) and the Celery distributed task queue (<http://celery.readthedocs.org>).

REFERENCES AND NOTES

- K. Lindblad-Toh *et al.*, A high-resolution map of human evolutionary constraint using 29 mammals. *Nature* **478**, 476–482 (2011). doi: [10.1038/nature10530](https://doi.org/10.1038/nature10530); pmid: [21993624](https://pubmed.ncbi.nlm.nih.gov/21993624/)
- ENCODE Project Consortium, An integrated encyclopedia of DNA elements in the human genome. *Nature* **489**, 57–74 (2012). doi: [10.1038/nature11247](https://doi.org/10.1038/nature11247); pmid: [22955616](https://pubmed.ncbi.nlm.nih.gov/22955616/)
- Y. Barash *et al.*, Deciphering the splicing code. *Nature* **465**, 53–59 (2010). doi: [10.1038/nature09000](https://doi.org/10.1038/nature09000); pmid: [20445623](https://pubmed.ncbi.nlm.nih.gov/20445623/)
- C. Zhang *et al.*, Integrative modeling defines the Nova splicing-regulatory network and its combinatorial controls. *Science* **329**, 439–443 (2010). doi: [10.1126/science.1191150](https://doi.org/10.1126/science.1191150); pmid: [20558669](https://pubmed.ncbi.nlm.nih.gov/20558669/)
- N. L. Barbosa-Morais *et al.*, The evolutionary landscape of alternative splicing in vertebrate species. *Science* **338**, 1587–1593 (2012). doi: [10.1126/science.1230612](https://doi.org/10.1126/science.1230612); pmid: [23258890](https://pubmed.ncbi.nlm.nih.gov/23258890/)
- E. Segal, J. Widom, From DNA sequence to transcriptional behaviour: A quantitative approach. *Nat. Rev. Genet.* **10**, 443–456 (2009). doi: [10.1038/nrg2591](https://doi.org/10.1038/nrg2591); pmid: [19506578](https://pubmed.ncbi.nlm.nih.gov/19506578/)
- F. Gnad, A. Baucom, K. Mukhyala, G. Manning, Z. Zhang, Assessment of computational methods for predicting the effects of missense mutations in human cancers. *BMC Genomics* **14** (suppl. 3), S7 (2013). pmid: [23819521](https://pubmed.ncbi.nlm.nih.gov/23819521/)
- M. Kircher *et al.*, A general framework for estimating the relative pathogenicity of human genetic variants. *Nat. Genet.* **46**, 310–315 (2014). doi: [10.1038/ng.2892](https://doi.org/10.1038/ng.2892); pmid: [24487276](https://pubmed.ncbi.nlm.nih.gov/24487276/)
- M. Mort *et al.*, MutPred Splice: Machine learning-based prediction of exonic variants that disrupt splicing. *Genome Biol.* **15**, R19 (2014). doi: [10.1186/gb-2014-15-1-r19](https://doi.org/10.1186/gb-2014-15-1-r19); pmid: [24451234](https://pubmed.ncbi.nlm.nih.gov/24451234/)
- T. Sterne-Weiler, J. R. Sanford, Exon identity crisis: Disease-causing mutations that disrupt the splicing code. *Genome Biol.* **15**, 201 (2014). doi: [10.1186/gb4150](https://doi.org/10.1186/gb4150); pmid: [24456648](https://pubmed.ncbi.nlm.nih.gov/24456648/)
- H. Y. Xiong, Y. Barash, B. J. Frey, Bayesian prediction of tissue-regulated splicing using RNA sequence and cellular context. *Bioinformatics* **27**, 2554–2562 (2011). pmid: [21803804](https://pubmed.ncbi.nlm.nih.gov/21803804/)
- Y. Barash *et al.*, AVISPA: A web tool for the prediction and analysis of alternative splicing. *Genome Biol.* **14**, R114 (2013). doi: [10.1186/gb-2013-14-10-r114](https://doi.org/10.1186/gb-2013-14-10-r114); pmid: [24156756](https://pubmed.ncbi.nlm.nih.gov/24156756/)
- See supplementary materials on Science Online.
- D. Ray *et al.*, A compendium of RNA-binding motifs for decoding gene regulation. *Nature* **499**, 172–177 (2013). doi: [10.1038/nature12311](https://doi.org/10.1038/nature12311); pmid: [23846655](https://pubmed.ncbi.nlm.nih.gov/23846655/)
- H. Han *et al.*, MBNL proteins repress ES-cell-specific alternative splicing and reprogramming. *Nature* **498**, 241–245 (2013). doi: [10.1038/nature12270](https://doi.org/10.1038/nature12270); pmid: [23739326](https://pubmed.ncbi.nlm.nih.gov/23739326/)
- T. Lappalainen *et al.*, Transcriptome and genome sequencing uncovers functional variation in humans. *Nature* **501**, 506–511 (2013). doi: [10.1038/nature12531](https://doi.org/10.1038/nature12531); pmid: [24037378](https://pubmed.ncbi.nlm.nih.gov/24037378/)
- S. T. Sherry *et al.*, dbSNP: The NCBI database of genetic variation. *Nucleic Acids Res.* **29**, 308–311 (2001). doi: [10.1093/nar/29.1.308](https://doi.org/10.1093/nar/29.1.308); pmid: [11125122](https://pubmed.ncbi.nlm.nih.gov/11125122/)
- P. D. Stenson *et al.*, The Human Gene Mutation Database: 2008 update. *Genome Med.* **1**, 13 (2009). doi: [10.1186/gm13](https://doi.org/10.1186/gm13); pmid: [19348700](https://pubmed.ncbi.nlm.nih.gov/19348700/)
- F. Supek, B. Miñana, J. Válcárcel, T. Gabaldón, B. Lehner, Synonymous mutations frequently act as driver mutations in human cancers. *Cell* **156**, 1324–1335 (2014). doi: [10.1016/j.cell.2014.01.051](https://doi.org/10.1016/j.cell.2014.01.051); pmid: [24630730](https://pubmed.ncbi.nlm.nih.gov/24630730/)
- M. Kimura, *The Neutral Theory of Molecular Evolution* (Cambridge Univ. Press, Cambridge, 1983).
- A. González-Pérez, N. López-Bigas, Improving the assessment of the outcome of nonsynonymous SNVs with a consensus deleteriousness score, Condel. *Am. J. Hum. Genet.* **88**, 440–449 (2011). doi: [10.1016/j.ajhg.2011.03.004](https://doi.org/10.1016/j.ajhg.2011.03.004); pmid: [21457909](https://pubmed.ncbi.nlm.nih.gov/21457909/)
- L. A. Hindorf *et al.*, Potential etiologic and functional implications of genome-wide association loci for human diseases and traits. *Proc. Natl. Acad. Sci. U.S.A.* **106**, 9362–9367 (2009). doi: [10.1073/pnas.0903103106](https://doi.org/10.1073/pnas.0903103106); pmid: [19474294](https://pubmed.ncbi.nlm.nih.gov/19474294/)
- R. N. Singh, Evolving concepts on human SMN pre-mRNA splicing. *RNA Biol.* **4**, 7–10 (2007). doi: [10.4161/rna.4.1.4535](https://doi.org/10.4161/rna.4.1.4535); pmid: [17592254](https://pubmed.ncbi.nlm.nih.gov/17592254/)
- T. Kashima, N. Rao, J. L. Manley, An intronic element contributes to splicing repression in spinal muscular atrophy. *Proc. Natl. Acad. Sci. U.S.A.* **104**, 3426–3431 (2007). doi: [10.1073/pnas.0700343104](https://doi.org/10.1073/pnas.0700343104); pmid: [17307868](https://pubmed.ncbi.nlm.nih.gov/17307868/)
- Y. Hua, T. A. Vickers, H. L. Okunola, C. F. Bennett, A. R. Krainer, Antisense masking of an hnRNP A1/A2 intronic splicing silencer corrects SMN2 splicing in transgenic mice. *Am. J. Hum. Genet.* **82**, 834–848 (2008). doi: [10.1016/j.ajhg.2008.01.014](https://doi.org/10.1016/j.ajhg.2008.01.014); pmid: [18371932](https://pubmed.ncbi.nlm.nih.gov/18371932/)
- R. A. Barnettson *et al.*, Classification of ambiguous mutations in DNA mismatch repair genes identified in a population-based study of colorectal cancer. *Hum. Mutat.* **29**, 367–374 (2008). doi: [10.1002/humu.20635](https://doi.org/10.1002/humu.20635); pmid: [18033691](https://pubmed.ncbi.nlm.nih.gov/18033691/)
- P. Peltomäki, H. Vasen, Mutations associated with HNPCC predisposition — Update of ICG-HNPCC/INSIGHT mutation database. *Dis. Markers* **20**, 269–276 (2004). doi: [10.1155/2004/305058](https://doi.org/10.1155/2004/305058); pmid: [15528792](https://pubmed.ncbi.nlm.nih.gov/15528792/)
- S. Arnold *et al.*, Classifying MLH1 and MSH2 variants using bioinformatic prediction, splicing assays, segregation, and tumor characteristics. *Hum. Mutat.* **30**, 757–770 (2009). doi: [10.1002/humu.20936](https://doi.org/10.1002/humu.20936); pmid: [19267393](https://pubmed.ncbi.nlm.nih.gov/19267393/)
- B. Betz *et al.*, Comparative in silico analyses and experimental validation of novel splice site and missense mutations in the genes MLH1 and MSH2. *J. Cancer Res. Clin. Oncol.* **136**, 123–134 (2010). doi: [10.1007/s00432-009-0643-z](https://doi.org/10.1007/s00432-009-0643-z); pmid: [19669161](https://pubmed.ncbi.nlm.nih.gov/19669161/)
- M. Nystrom-Lahti *et al.*, Missense and nonsense mutations in codon 659 of MLH1 cause aberrant splicing of messenger RNA in HNPCC kindreds. *Genes Chromosomes Cancer* **26**, 372–375 (1999). doi: [10.1002/\(SICI\)1098-2264\(199912\)26:4<372::AID-GCC12>3.0.CO;2-V](https://doi.org/10.1002/(SICI)1098-2264(199912)26:4<372::AID-GCC12>3.0.CO;2-V); pmid: [10534773](https://pubmed.ncbi.nlm.nih.gov/10534773/)
- P. Lastella, N. C. Surdo, N. Resta, G. Guanti, A. Stella, In silico and in vivo splicing analysis of MLH1 and MSH2 missense mutations shows exon- and tissue-specific effects. *BMC Genomics* **7**, 243 (2006). doi: [10.1186/1471-2164-7-243](https://doi.org/10.1186/1471-2164-7-243); pmid: [16995940](https://pubmed.ncbi.nlm.nih.gov/16995940/)
- J. Kosinski, I. Hinrichsen, J. M. Bujnicki, P. Friedhoff, G. Plotz, Identification of Lynch syndrome mutations in the MLH1-PMS2 interface that disturb dimerization and mismatch repair. *Hum. Mutat.* **31**, 975–982 (2010). doi: [10.1002/humu.21301](https://doi.org/10.1002/humu.21301); pmid: [20533529](https://pubmed.ncbi.nlm.nih.gov/20533529/)
- P. J. Smith *et al.*, An increased specificity score matrix for the prediction of SF2/ASF-specific exonic splicing enhancers. *Hum. Mol. Genet.* **15**, 2490–2508 (2006). doi: [10.1093/hmg/ddl171](https://doi.org/10.1093/hmg/ddl171); pmid: [16825284](https://pubmed.ncbi.nlm.nih.gov/16825284/)
- J. D. Buxbaum *et al.*, The Autism Sequencing Consortium: Large-scale, high-throughput sequencing in autism spectrum disorders. *Neuron* **76**, 1052–1056 (2012). doi: [10.1016/j.neuron.2012.12.008](https://doi.org/10.1016/j.neuron.2012.12.008); pmid: [23259942](https://pubmed.ncbi.nlm.nih.gov/23259942/)
- C. Betancur, Etiological heterogeneity in autism spectrum disorders: More than 100 genetic and genomic disorders and still counting. *Brain Res.* **1380**, 42–77 (2011). doi: [10.1016/j.brainres.2010.11.078](https://doi.org/10.1016/j.brainres.2010.11.078); pmid: [21129364](https://pubmed.ncbi.nlm.nih.gov/21129364/)
- B. Devlin, S. W. Scherer, Genetic architecture in autism spectrum disorder. *Curr. Opin. Genet. Dev.* **22**, 229–237 (2012). doi: [10.1016/j.cde.2012.03.002](https://doi.org/10.1016/j.cde.2012.03.002); pmid: [22463983](https://pubmed.ncbi.nlm.nih.gov/22463983/)
- I. Iossifov *et al.*, De novo gene disruptions in children on the autistic spectrum. *Neuron* **74**, 285–299 (2012). doi: [10.1016/j.neuron.2012.04.009](https://doi.org/10.1016/j.neuron.2012.04.009); pmid: [22542183](https://pubmed.ncbi.nlm.nih.gov/22542183/)
- Y. H. Jiang *et al.*, Detection of clinically relevant genetic variants in autism spectrum disorder by whole-genome sequencing. *Am. J. Hum. Genet.* **93**, 249–263 (2013). doi: [10.1016/j.ajhg.2013.06.012](https://doi.org/10.1016/j.ajhg.2013.06.012); pmid: [23849776](https://pubmed.ncbi.nlm.nih.gov/23849776/)
- R. Anney *et al.*, A genome-wide scan for common alleles affecting risk for autism. *Hum. Mol. Genet.* **19**, 4072–4082 (2010). doi: [10.1093/hmg/ddq307](https://doi.org/10.1093/hmg/ddq307); pmid: [20663923](https://pubmed.ncbi.nlm.nih.gov/20663923/)
- T. C. Südhof, Neuroligins and neuexins link synaptic function to cognitive disease. *Nature* **455**, 903–911 (2008). doi: [10.1038/nature07456](https://doi.org/10.1038/nature07456); pmid: [18923512](https://pubmed.ncbi.nlm.nih.gov/18923512/)
- I. Voineagu *et al.*, Transcriptomic analysis of autistic brain reveals convergent molecular pathology. *Nature* **474**, 380–384 (2011). doi: [10.1038/nature10110](https://doi.org/10.1038/nature10110); pmid: [21614001](https://pubmed.ncbi.nlm.nih.gov/21614001/)
- R. F. Wintle *et al.*, A genotype resource for postmortem brain samples from the Autism Tissue Program. *Autism Res.* **4**, 89–97 (2011). doi: [10.1002/aur.173](https://doi.org/10.1002/aur.173); pmid: [21254448](https://pubmed.ncbi.nlm.nih.gov/21254448/)
- D. Pinto *et al.*, Functional impact of global rare copy number variation in autism spectrum disorders. *Nature* **466**, 368–372 (2010). doi: [10.1038/nature09146](https://doi.org/10.1038/nature09146); pmid: [20531469](https://pubmed.ncbi.nlm.nih.gov/20531469/)
- M. Uddin *et al.*, Brain-expressed exons under purifying selection are enriched for de novo mutations in autism spectrum disorder. *Nat. Genet.* **46**, 742–747 (2014). doi: [10.1038/ng.2980](https://doi.org/10.1038/ng.2980); pmid: [24859339](https://pubmed.ncbi.nlm.nih.gov/24859339/)
- E. Skafidas *et al.*, Predicting the diagnosis of autism spectrum disorder using gene pathway analysis. *Mol. Psychiatry* **19**, 504–510 (2014). doi: [10.1038/mp.2012.126](https://doi.org/10.1038/mp.2012.126); pmid: [22965006](https://pubmed.ncbi.nlm.nih.gov/22965006/)
- E. B. Robinson *et al.*, Response to 'Predicting the diagnosis of autism spectrum disorder using gene pathway analysis'. *Mol. Psychiatry* **19**, 860–861 (2014). doi: [10.1038/mp.2013.125](https://doi.org/10.1038/mp.2013.125); pmid: [24145379](https://pubmed.ncbi.nlm.nih.gov/24145379/)
- E. Khurana *et al.*, Integrative annotation of variants from 1092 humans: Application to cancer genomics. *Science* **342**, 1235587 (2013). doi: [10.1126/science.1235587](https://doi.org/10.1126/science.1235587); pmid: [24092746](https://pubmed.ncbi.nlm.nih.gov/24092746/)
- K. H. Lim, L. Ferraris, M. E. Filloux, B. J. Raphael, W. G. Fairbrother, Using positional distribution to identify splicing elements and predict pre-mRNA processing defects in human genes. *Proc. Natl. Acad. Sci. U.S.A.* **108**, 11093–11098 (2011). doi: [10.1073/pnas.1101135108](https://doi.org/10.1073/pnas.1101135108); pmid: [21685335](https://pubmed.ncbi.nlm.nih.gov/21685335/)
- A. Woolfe, J. C. Mullikin, L. Elnitski, Genomic features defining exonic variants that modulate splicing. *Genome Biol.* **11**, R20 (2010). doi: [10.1186/gb-2010-11-2-r20](https://doi.org/10.1186/gb-2010-11-2-r20); pmid: [20158892](https://pubmed.ncbi.nlm.nih.gov/20158892/)
- B. E. Stranger *et al.*, Relative impact of nucleotide and copy number variation on gene expression phenotypes. *Science* **315**, 848–853 (2007). doi: [10.1126/science.1136678](https://doi.org/10.1126/science.1136678); pmid: [17289997](https://pubmed.ncbi.nlm.nih.gov/17289997/)
- J. A. Tennessen *et al.*, Evolution and functional impact of rare coding variation from deep sequencing of human exomes. *Science* **337**, 64–69 (2012). doi: [10.1126/science.1219240](https://doi.org/10.1126/science.1219240); pmid: [22604720](https://pubmed.ncbi.nlm.nih.gov/22604720/)
- A. Battle *et al.*, Characterizing the genetic basis of transcriptome diversity through RNA-sequencing of 922 individuals. *Genome Res.* **24**, 14–24 (2014). doi: [10.1101/gr.155192.113](https://doi.org/10.1101/gr.155192.113); pmid: [24092820](https://pubmed.ncbi.nlm.nih.gov/24092820/)
- U. Braunschweig, S. Gueroussou, A. M. Plocik, B. R. Graveley, B. J. Blencowe, Dynamic integration of splicing within gene regulatory pathways. *Cell* **152**, 1252–1269 (2013). doi: [10.1016/j.cell.2013.02.034](https://doi.org/10.1016/j.cell.2013.02.034); pmid: [23498935](https://pubmed.ncbi.nlm.nih.gov/23498935/)
- D. Brawand *et al.*, The evolution of gene expression levels in mammalian organs. *Nature* **478**, 343–348 (2011). doi: [10.1038/nature10532](https://doi.org/10.1038/nature10532); pmid: [22012392](https://pubmed.ncbi.nlm.nih.gov/22012392/)
- K. Wang, M. Li, H. Hakonarson, ANNOVAR: Functional annotation of genetic variants from high-throughput sequencing data. *Nucleic Acids Res.* **38**, e164 (2010). doi: [10.1093/nar/gkq603](https://doi.org/10.1093/nar/gkq603); pmid: [20601685](https://pubmed.ncbi.nlm.nih.gov/20601685/)

ACKNOWLEDGMENTS

B.J.F. designed the study and wrote the manuscript, with input from B.B.J., S.W.S., B.A., N.J., Y.B., Q.M., and Q.-co-authors. H.Y.X. trained the models. H.Y.X., B.J.F., N.J., and L.J.L. developed the bootstrap method for quantifying Ψ . L.J.L. mined exons, mapped reads and designed additional features, extending the original feature set developed by Y.B., B.J.F., and B.B.J. H.Y.X., B.J.F., H.S.N., Q.M., and T.R.H. analyzed RNAcompete data. B.J.F., H.Y.X., L.J.L., and B.A. performed the genome-wide SNV analysis. L.J.L., Y.H., B.J.F., and A.R.K. tested predictions for SMN1/2. B.A. and B.J.F. tested predictions for MLH1/MSH2. B.A., D.M., R.K.C.Y., B.J.F., and S.W.S. analyzed ASD genomes. S.G. conducted wild-type RT-PCR assays. H.B. developed the Web tool and feature visualization, with input from B.J.F., H.Y.X., B.A., and L.J.L. We thank the Center of Applied Genomics at the Toronto Hospital for Sick Children for providing HGMD annotations, G. Schroth at Illumina for providing the BodyMap RNA-seq data, and M. Brudno, O. Buske, A. Delong, C. Smith, T. Sterne-Weiler, J. Wilson, and J. Valcárcel for comments on the manuscript and the Web tool. Supported by Canadian Institutes for Advanced Research (CIHR), the Natural Sciences and Engineering Research Council of Canada (NSERC), John C. Polanyi, the University of Toronto McLaughlin Centre, and the Ontario Genomics Institute (OGI) (B.J.F.); CIHR and McLaughlin (B.B.J.); McLaughlin, Genome Canada, OGI, and Autism Speaks (S.W.S.); NIH grant R37-GM42699a (A.R.K.); CIHR (Q.M.); an Autism Research Training Fellowship (B.A.); a CIHR Banting Fellowship (H.S.N.); and an NSERC Alexander Graham Bell Scholarship (S.G.). S.W.S. holds the GlaxoSmithKline-CIHR Chair in Genome Sciences. B.B.J. holds the Banbury Chair of Medical Research at the University of Toronto. B.J.F., S.W.S., and T.R.H. are Fellows of the Canadian Institute for Advanced Research. B.J.F. holds the Canada Research Chair in Biological Computation.

SUPPLEMENTARY MATERIALS

www.sciencemag.org/content/347/6218/1254806/suppl/DC1
Materials and Methods
Figs. S1 to S32
Tables S1 to S18
References (56–81)

13 April 2014; accepted 19 November 2014
Published online 18 December 2014;
[10.1126/science.1254806](https://doi.org/10.1126/science.1254806)

RESEARCH ARTICLE

COMPUTER SCIENCE

Heads-up limit hold'em poker is solved

Michael Bowling,^{1*} Neil Burch,¹ Michael Johanson,¹ Oskari Tammelin²

Poker is a family of games that exhibit imperfect information, where players do not have full knowledge of past events. Whereas many perfect-information games have been solved (e.g., Connect Four and checkers), no nontrivial imperfect-information game played competitively by humans has previously been solved. Here, we announce that heads-up limit Texas hold'em is now essentially weakly solved. Furthermore, this computation formally proves the common wisdom that the dealer in the game holds a substantial advantage. This result was enabled by a new algorithm, CFR⁺, which is capable of solving extensive-form games orders of magnitude larger than previously possible.

Games have been intertwined with the earliest developments in computation, game theory, and artificial intelligence (AI). At the very conception of computing, Babbage had detailed plans for an “automaton” capable of playing tic-tac-toe and dreamed of his Analytical Engine playing chess (1). Both Turing (2) and Shannon (3)—on paper and in hardware, respectively—developed programs to play chess as a means of validating early ideas in computation and AI. For more than a half century, games have continued to act as testbeds for new ideas, and the resulting successes have marked important milestones in the progress of AI. Examples include the checkers-playing computer program Chinook becoming the first to win a world championship title against humans (4), Deep Blue defeating Kasparov in chess (5), and Watson defeating Jennings and Rutter on *Jeopardy!* (6). However, defeating top human players is not the same as “solving” a game—that is, computing a game-theoretically optimal solution that is incapable of losing against any opponent in a fair game. Notable milestones in the advancement of AI have also involved solving games, for example, Connect Four (7) and checkers (8).

Every nontrivial game (9) played competitively by humans that has been solved to date is a perfect-information game. In perfect-information games, all players are informed of everything that has occurred in the game before making a decision. Chess, checkers, and backgammon are examples of perfect-information games. In imperfect-information games, players do not always have full knowledge of past events (e.g., cards dealt to other players in bridge and poker, or a seller's knowledge of the value of an item in an auction). These games are more challenging, with theory, computational algorithms, and instances of solved games lagging behind results in the perfect-information setting (10). And although

perfect information may be a common property of parlor games, it is far less common in real-world decision-making settings. In a conversation recounted by Bronowski, von Neumann, the founder of modern game theory, made the same observation: “Real life is not like that. Real life consists of bluffing, of little tactics of deception, of asking yourself what is the other man going to think I mean to do. And that is what games are about in my theory” (11).

Von Neumann's statement hints at the quintessential game of imperfect information: the game of poker. Poker involves each player being dealt private cards, with players taking structured turns making bets on having the strongest hand (possibly bluffing), calling opponents' bets, or folding to give up the hand. Poker played an important role in early developments in the field of game theory. Borel's (12) and von Neumann's

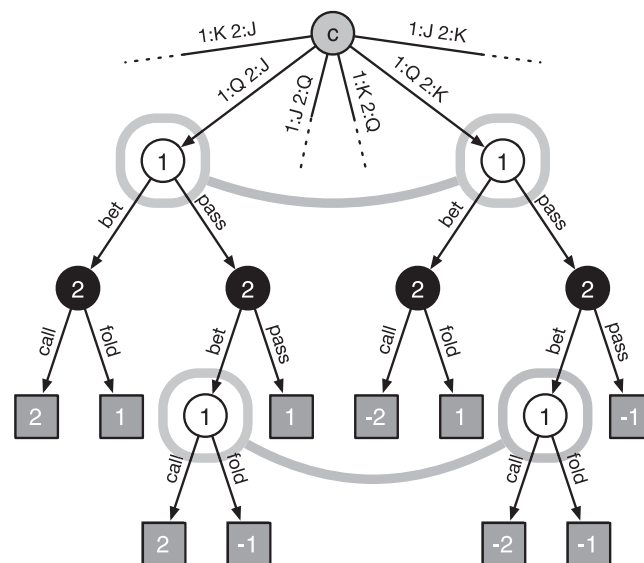
(13, 14) foundational works were motivated by developing a mathematical rationale for bluffing in poker, and small synthetic poker games (15) were commonplace in many early papers (12, 14, 16, 17). Poker is also arguably the most popular card game in the world, with more than 150 million players worldwide (18).

The most popular variant of poker today is Texas hold'em. When it is played with just two players (heads-up) and with fixed bet sizes and a fixed number of raises (limit), it is called heads-up limit hold'em or HULHE (19). HULHE was popularized by a series of high-stakes games chronicled in the book *The Professor, the Banker, and the Suicide King* (20). It is also the smallest variant of poker played competitively by humans. HULHE has 3.16×10^{17} possible states the game can reach, making it larger than Connect Four and smaller than checkers. However, because HULHE is an imperfect-information game, many of these states cannot be distinguished by the acting player, as they involve information about unseen past events (i.e., private cards dealt to the opponent). As a result, the game has 3.19×10^{14} decision points where a player is required to make a decision.

Although smaller than checkers, the imperfect-information nature of HULHE makes it a far more challenging game for computers to play or solve. It was 17 years after Chinook won its first game against world champion Tinsley in checkers that the computer program Polaris won the first meaningful match against professional poker players (21). Whereas Schaeffer *et al.* solved checkers in 2007 (8), heads-up limit Texas hold'em poker had remained unsolved. This slow progress is not for lack of effort. Poker has been a challenge problem for artificial intelligence, operations research, and psychology, with work going back more than 40 years (22); 17 years ago,

Fig. 1. Portion of the extensive-form game representation of three-card Kuhn poker (16).

Player 1 is dealt a queen (Q), and the opponent is given either the jack (J) or king (K). Game states are circles labeled by the player acting at each state (“c” refers to chance, which randomly chooses the initial deal). The arrows show the events the acting player can choose from, labeled with their in-game meaning. The leaves are square vertices labeled with the associated utility for player 1 (player 2's utility is the negation of player 1's). The states connected by thick gray lines are part of the same information set; that is, player 1 cannot distinguish between the states in each pair because they each represent a different unobserved card being dealt to the opponent. Player 2's states are also in information sets, containing other states not pictured in this diagram.



¹Department of Computing Science, University of Alberta, Edmonton, Alberta T6G 2E8, Canada. ²Unaffiliated; <http://jeskola.net>.

*Corresponding author. E-mail: bowlings@cs.ualberta.ca

Koller and Pfeffer (23) declared, “We are nowhere close to being able to solve huge games such as full-scale poker, and it is unlikely that we will ever be able to do so.” The focus on HULHE as one example of “full-scale poker” began in earnest more than 10 years ago (24) and became the focus of dozens of research groups and hobbyists after 2006, when it became the inaugural event in the Annual Computer Poker Competition (25), held in conjunction with the main conference of the Association for the Advancement of Artificial Intelligence (AAAI). This paper is the culmination of this sustained research effort toward solving a “full-scale” poker game (19).

Allis (26) gave three different definitions for solving a game. A game is said to be ultraweakly solved if, for the initial position(s), the game-theoretic value has been determined; weakly solved if, for the initial position(s), a strategy has been determined to obtain at least the game-theoretic value, for both players, under reasonable resources; and strongly solved if, for all legal positions, a strategy has been determined to obtain the game-theoretic value of the position, for both players, under reasonable resources. In an imperfect-information game, where the game-theoretic value of a position beyond the initial position is not unique, Allis’s notion of “strongly solved” is not well defined. Furthermore, imperfect-information games, because of stochasticity in the players’ strategies or the game itself, typically have game-theoretic values that are real-valued rather than discretely valued (such as “win,” “loss,” and “draw” in chess and checkers) and are only achieved in expectation over many playings of the game. As a result, game-theoretic values are often approximated, and so an additional consideration in solving a game is the degree of approximation in a solution. A natural level of approximation under which a game is essentially weakly solved is if a human lifetime of play is not sufficient to establish with statistical significance that the strategy is not an exact solution.

In this paper, we announce that heads-up limit Texas hold’em poker is essentially weakly solved. Furthermore, we bound the game-theoretic value of the game, proving that the game is a winning game for the dealer.

Solving imperfect-information games

The classical representation for an imperfect-information setting is the extensive-form game. Here, the word “game” refers to a formal model of interaction between self-interested agents and applies to both recreational games and serious endeavors such as auctions, negotiation, and security. See Fig. 1 for a graphical depiction of a portion of a simple poker game in extensive form. The core of an extensive-form game is a game tree specifying branches of possible events, namely player actions or chance outcomes. The branches of the tree split at game states, and each is associated with one of the players (or chance) who is responsible for determining the result of that event. The leaves of the tree signify the end of the game and have an associated utility for each player. The states associated with

a player are partitioned into information sets, which are sets of states among which the acting player cannot distinguish (e.g., corresponding to states where the opponent was dealt different private cards). The branches from states within an information set are the player’s available actions. A strategy for a player specifies for each information set a probability distribution over the available actions. If the game has exactly two players and the utilities at every leaf sum to zero, the game is called zero-sum.

The classical solution concept for games is a Nash equilibrium, a strategy for each player such that no player can increase his or her expected utility by unilaterally choosing a different strategy. All finite extensive-form games have at least one Nash equilibrium. In zero-sum games, all equilibria have the same expected utilities for the players, and this value is called the game-theoretic value of the game. An ϵ -Nash equilibrium is a strategy for each player where no player can increase his or her utility by more than ϵ by choosing a different strategy. By Allis’ categories, a zero-sum game is ultraweakly solved if its game-theoretic value is computed, and weakly solved if a Nash equilibrium strategy is computed. We call a game essentially weakly solved if an ϵ -Nash equilibrium is computed for a sufficiently small ϵ to be statistically indistinguishable from zero in a human lifetime of played games. For perfect-information games, solving typically involves a (partial) traversal of the game tree. However, the same techniques cannot apply to imperfect-information settings. We briefly review the advances in solving imperfect-information games, benchmarking the algorithms by their progress in solving increasingly larger synthetic poker games, as summarized in Fig. 2.

Normal-form linear programming

The earliest method for solving an extensive-form game involved converting it into a normal-form game, represented as a matrix of values for every pair of possible deterministic strategies in the original extensive-form game, and then

solving it with a linear program (LP). Unfortunately, the number of possible deterministic strategies is exponential in the number of information sets of the game. So, although LPs can handle normal-form games with many thousands of strategies, even just a few dozen decision points makes this method impractical. Kuhn poker, a poker game with three cards, one betting round, and a one-bet maximum having a total of 12 information sets (see Fig. 1), can be solved with this approach. But even Leduc hold’em (27), with six cards, two betting rounds, and a two-bet maximum having a total of 288 information sets, is intractable, having more than 10^{86} possible deterministic strategies.

Sequence-form linear programming

Romanovskii (28) and later Koller *et al.* (29, 30) established the modern era of solving imperfect-information games, introducing the sequence-form representation of a strategy. With this simple change of variables, they showed that the extensive-form game could be solved directly as an LP, without the need for an exponential conversion to normal form. Sequence-form linear programming (SFLP) was the first algorithm to solve imperfect-information extensive-form games with computation time that grows as a polynomial of the size of the game representation. In 2003, Billings *et al.* (24) applied this technique to poker, solving a set of simplifications of HULHE to build the first competitive poker-playing program. In 2005, Gilpin and Sandholm (31) used the approach along with an automated technique for finding game symmetries to solve Rhode Island hold’em (32), a synthetic poker game with 3.94×10^6 information sets after symmetries are removed.

Counterfactual regret minimization

In 2006, the Annual Computer Poker Competition was started (25). The competition drove advancements in solving larger and larger games, with multiple techniques and refinements being proposed in the years that followed (33, 34). One

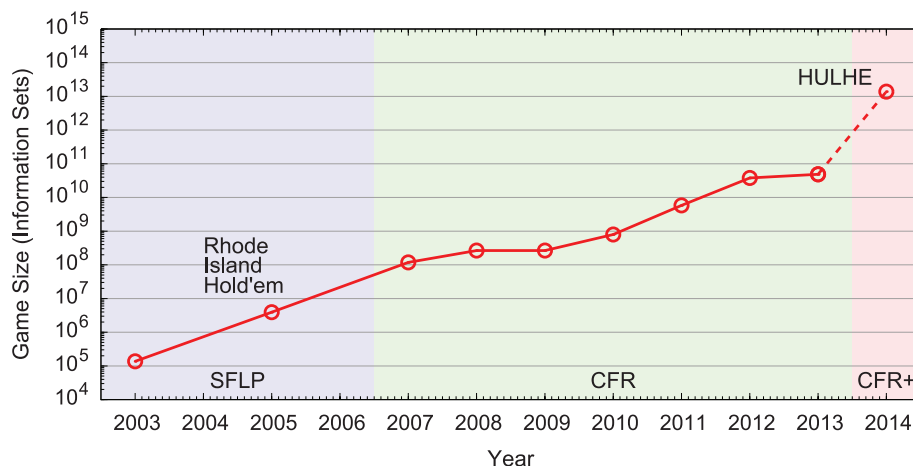


Fig. 2. Increasing sizes of imperfect-information games solved over time measured in unique information sets (i.e., after symmetries are removed). The shaded regions refer to the technique used to achieve the result; the dashed line shows the result established in this paper.

of the techniques to emerge, and currently the most widely adopted in the competition, is counterfactual regret minimization (CFR) (35). CFR is an iterative method for approximating a Nash equilibrium of an extensive-form game through the process of repeated self-play between two regret-minimizing algorithms (19, 36). Regret is the loss in utility an algorithm suffers for not having selected the single best deterministic strategy, which can only be known in hindsight. A regret-minimizing algorithm is one that guarantees that its regret grows sublinearly over time, and so eventually achieves the same utility as the best deterministic strategy. The key insight of CFR is that instead of storing and minimizing regret for the exponential number of deterministic strategies, CFR stores and minimizes a modified regret for each information set and subsequent action, which can be used to form an upper bound on the regret for any deterministic strategy. An approximate Nash equilibrium is retrieved by averaging each player's strategies over all of the iterations, and the approximation improves as the number of iterations increases. The memory needed for the algorithm is linear in the number of information sets, rather than quadratic, which is the case for efficient LP methods (37). Because solving large games is usually bounded by available memory, CFR has resulted in an increase in the size of solved games similar to that of Koller *et al.*'s advance. Since its introduction in 2007, CFR has been used to solve increasingly complex simplifications of HULHE, reaching as many as 3.8×10^{10} information sets in 2012 (38).

Solving heads-up limit hold'em

The full game of HULHE has 3.19×10^{14} information sets. Even after removing game symmetries, it has 1.38×10^{13} information sets (i.e., three orders of magnitude larger than previously solved games). There are two challenges for established CFR variants to handle games at this scale: memory and computation. During computation, CFR must store the resulting solution and the accu-

mulated regret values for each information set. Even with single-precision (4-byte) floating-point numbers, this requires 262 TB of storage. Furthermore, past experience has shown that increasing the number of information sets by three orders of magnitude requires at least three orders of magnitude more computation. To tackle these two challenges, we use two ideas recently proposed by a coauthor of this paper (39).

To address the memory challenge, we store the average strategy and accumulated regrets using compression. We use fixed-point arithmetic by first multiplying all values by a scaling factor and truncating them to integers. The resulting integers are then ordered to maximize compression efficiency, with compression ratios around 13-to-1 on the regrets and 28-to-1 on the strategy. Overall, we require less than 11 TB of storage to store the regrets and 6 TB to store the average strategy during the computation, which is distributed across a cluster of computation nodes. This amount is infeasible to store in main memory, and so we store the values on each node's local disk. Each node is responsible for a set of subgames; that is, portions of the game tree are partitioned on the basis of publicly observed actions and cards such that each information set is associated with one subgame. The regrets and strategy for a subgame are loaded from disk, updated, and saved back to disk, using a streaming compression technique that decompresses and recompresses portions of the subgame as needed. By making the subgames large enough, the update time dominates the total time to process a subgame. With disk pre-caching, the inefficiency incurred by disk storage is approximately 5% of the total time.

To address the computation challenge, we use a variant of CFR called CFR⁺ (19, 39). CFR implementations typically sample only portions of the game tree to update on each iteration. They also use regret matching at each information set, which maintains regrets for each action and chooses among actions with positive regret with probability proportional to that regret. By con-

trast, CFR⁺ does exhaustive iterations over the entire game tree and uses a variant of regret matching (regret matching⁺) where regrets are constrained to be non-negative. Actions that have appeared poor (with less than zero regret for not having been played) will be chosen again immediately after proving useful (rather than waiting many iterations for the regret to become positive). Finally, unlike with CFR, we have empirically observed that the exploitability of the players' current strategies during the computation regularly approaches zero. Therefore, we can skip the step of computing and storing the average strategy, instead using the players' current strategies as the CFR⁺ solution. We have empirically observed CFR⁺ to require considerably less computation, even when computing the average strategy, than state-of-the-art sampling CFR (40), while also being highly suitable for massive parallelization.

Like CFR, CFR⁺ is an iterative algorithm that computes successive approximations to a Nash equilibrium solution. The quality of the approximation can be measured by its exploitability: the amount less than the game value that the strategy achieves against the worst-case opponent strategy in expectation (19). Computing the exploitability of a strategy involves computing this worst-case value, which traditionally requires a traversal of the entire game tree. This was long thought to be intractable for games the size of HULHE. Recently, it was shown that this calculation could be accelerated by exploiting the imperfect-information structure of the game and regularities in the utilities (41). This is the technique we use to confirm the approximation quality of our resulting strategy. The technique and implementation has been verified on small games and against independent calculations of the exploitability of simple strategies in HULHE.

A strategy can be exploitable in expectation and yet, because of chance elements in the game and randomization in the strategy, its worst-case opponent still is not guaranteed to be winning after any finite number of hands. We define a game to be essentially solved if a lifetime of play is unable to statistically differentiate it from being solved at 95% confidence. Imagine someone playing 200 games of poker an hour for 12 hours a day without missing a day for 70 years. Furthermore, imagine that player using the worst-case, maximally exploitive, opponent strategy and never making a mistake. The player's total winnings, as a sum of many millions of independent outcomes, would be normally distributed. Hence, the observed winnings in this lifetime of poker would be 1.64 standard deviations or more below its expected value (i.e., the strategy's exploitability) at least 1 time out of 20. Using the standard deviation of a single game of HULHE, which has been reported to be around 5 bb/g (big-blinds per game, where the big-blind is the unit of stakes in HULHE) (42), we arrive at a threshold of $(1.64 \times 5)/\sqrt{200 \times 12 \times 365 \times 70} \approx 0.00105$. Therefore, an approximate solution with an exploitability less than 1 mbb/g (milli-big-blinds per game) cannot be distinguished with high

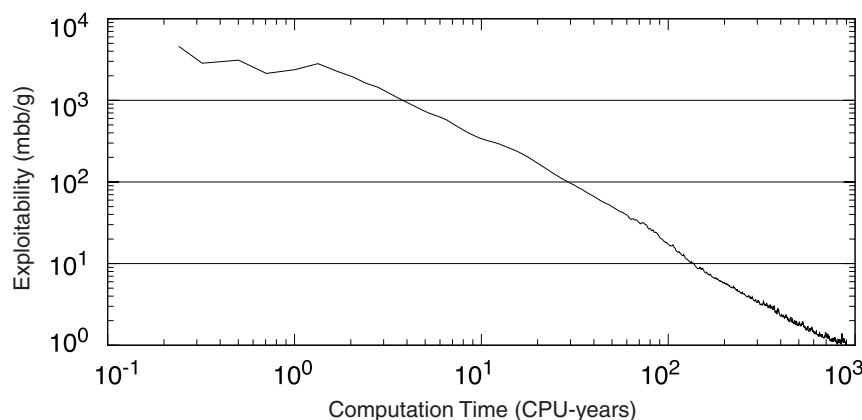


Fig. 3. Exploitability of the approximate solution with increasing computation. The exploitability, measured in milli-big-blinds per game (mbb/g), is that of the current strategy measured after each iteration of CFR⁺. After 1579 iterations or 900 core-years of computation, it reaches an exploitability of 0.986 mbb/g.

confidence from an exact solution, and indeed has a 1-in-20 chance of winning against its worst-case adversary even after a human lifetime of games. Hence, 1 mbb/g is the threshold for declaring HULHE essentially solved.

The solution

Our CFR⁺ implementation was executed on a cluster of 200 computation nodes each with 24 2.1-GHz AMD cores, 32 GB of RAM, and a 1-TB local disk. We divided the game into 110,565 subgames (partitioned according to preflop betting, flop cards, and flop betting). The subgames were split among 199 worker nodes, with one parent node responsible for the initial portion of the game tree. The worker nodes performed their updates in parallel, passing values back to the parent node for it to perform its update, taking 61 min on average to complete one iteration. The computation was then run for 1579 iterations, taking 68.5 days, and using a total of 900 core-years of computation (43) and 10.9 TB of disk space, including file system overhead from the large number of files.

Figure 3 shows the exploitability of the computed strategy with increasing computation. The strategy reaches an exploitability of 0.986 mbb/g, making HULHE essentially weakly solved. Using the separate exploitability values for each position (as the dealer and nondealer), we get exact bounds on the game-theoretic value of the game: between 87.7 and 89.7 mbb/g for the dealer, proving the common wisdom that the dealer holds a substantial advantage in HULHE.

The final strategy, as a close approximation to a Nash equilibrium, can also answer some fundamental and long-debated questions about game-theoretically optimal play in HULHE. Figure 4 gives a glimpse of the final strategy in two early decisions of the game. Human players have disagreed about whether it may be desirable to “limp” (i.e., call as the very first action rather

than raise) with certain hands. Conventional wisdom is that limping forgoes the opportunity to provoke an immediate fold by the opponent, and so raising is preferred. Our solution emphatically agrees (see the absence of blue in Fig. 4A). The strategy limps just 0.06% of the time and with no hand more than 0.5%. In other situations, the strategy gives insights beyond conventional wisdom, indicating areas where humans might improve. The strategy almost never “caps” (i.e., makes the final allowed raise) in the first round as the dealer, whereas some strong human players cap the betting with a wide range of hands. Even when holding the strongest hand—a pair of aces—the strategy caps the betting less than 0.01% of the time, and the hand most likely to cap is a pair of twos, with probability 0.06%. Perhaps more important, the strategy chooses to play (i.e., not fold) a broader range of hands as the nondealer than most human players (see the relatively small amount of red in Fig. 4B). It is also much more likely to re-raise when holding a low-rank pair (such as threes or fours) (44).

Although these observations are for only one example of game-theoretically optimal play (different Nash equilibria may play differently), they confirm as well as contradict current human beliefs about equilibria play and illustrate that humans can learn considerably from such large-scale game-theoretic reasoning.

Conclusion

What is the ultimate importance of solving poker? The breakthroughs behind our result are general algorithmic advances that make game-theoretic reasoning in large-scale models of any sort more tractable. And, although seemingly playful, game theory has always been envisioned to have serious implications [e.g., its early impact on Cold War politics (45)]. More recently, there has been a surge in game-theoretic applications involving security, including systems being deployed

for airport checkpoints, air marshal scheduling, and coast guard patrolling (46). CFR algorithms based on those described above have been used for robust decision-making in settings where there is no apparent adversary, with potential application to medical decision support (47). With real-life decision-making settings almost always involving uncertainty and missing information, algorithmic advances such as those needed to solve poker are the key to future applications. However, we also echo a response attributed to Turing in defense of his own work in games: “It would be disingenuous of us to disguise the fact that the principal motive which prompted the work was the sheer fun of the thing” (48).

REFERENCES AND NOTES

1. C. Babbage, *Passages from the Life of a Philosopher* (Longman, Green, Longman, Roberts, and Green, London, 1864), chap. 34.
2. A. Turing, in *Faster Than Thought*, B. V. Bowden, Ed. (Pitman, London, 1976), chap. 25.
3. C. E. Shannon, *Philos. Mag. Series 7* **41**, 256–275 (1950).
4. J. Schaeffer, R. Lake, P. Lu, M. Bryant, *AI Mag.* **17**, 21 (1996).
5. M. Campbell, A. J. Hoane Jr., F. Hsu, *Artif. Intell.* **134**, 57–83 (2002).
6. D. Ferrucci, *IBM J. Res. Dev.* **56**, 1 (2012).
7. V. Allis, thesis, Vrije Universiteit Brussel (1988).
8. J. Schaeffer et al., *Science* **317**, 1518–1522 (2007).
9. We use the word “trivial” to describe a game that can be solved without the use of a machine. The one near-exception to this claim is oshi-zumo, but it is not played competitively by humans and is a simultaneous-move game that otherwise has perfect information (49). Furthermore, almost all nontrivial games played by humans that have been solved to date also have no chance elements. The one notable exception is hypergammon, a three-checker variant of backgammon invented by Sconyers in 1993, which he then strongly solved (i.e., the game-theoretic value is known for all board positions). It has seen play in human competitions (see www.bkgrn.com/variants/HyperBackgammon.html).
10. For example, Zermelo proved the solvability of finite, two-player, zero-sum, perfect-information games in 1913 (50), whereas von Neumann’s more general minimax theorem appeared in 1928 (13). Minimax and alpha-beta pruning, the fundamental computational algorithms for perfect-information games, were developed in the 1950s; the first polynomial-time technique for imperfect-information games was introduced in the 1960s but was not well known until the 1990s (29).
11. J. Bronowski, *The Ascent of Man* [documentary] (1973), episode 13.
12. É. Borel, J. Ville, *Applications de la théorie des probabilités aux jeux de hasard* (Gauthier-Villars, Paris, 1938).
13. J. von Neumann, *Math. Ann.* **100**, 295–320 (1928).
14. J. von Neumann, O. Morgenstern, *Theory of Games and Economic Behavior* (Princeton Univ. Press, Princeton, NJ, ed. 2, 1947).
15. We use the word synthetic to describe a game that was invented for the purpose of being studied or solved rather than played by humans. A synthetic game may be trivial, such as Kuhn poker (16), or nontrivial, such as Rhode Island hold’em (32).
16. H. Kuhn, in *Contributions to the Theory of Games*, H. Kuhn, A. Tucker, Eds. (Princeton Univ. Press, Princeton, NJ, 1950), pp. 97–103.
17. J. F. Nash, L. S. Shapley, in *Contributions to the Theory of Games*, H. Kuhn, A. Tucker, Eds. (Princeton Univ. Press, Princeton, NJ, 1950), pp. 105–116.
18. “Poker: A big deal,” *Economist* (22 December 2007), p. 31.
19. See supplementary materials on Science Online.
20. M. Craig, *The Professor, the Banker, and the Suicide King: Inside the Richest Poker Game of All Time* (Grand Central, New York, 2006).
21. J. Rehmeyer, N. Fox, R. Rico, *Wired* **16**, 186–191 (2008).
22. D. Billings, A. Davidson, J. Schaeffer, D. Szafron, *Artif. Intell.* **134**, 201–240 (2002).
23. D. Koller, A. Pfeffer, *Artif. Intell.* **94**, 167–215 (1997).

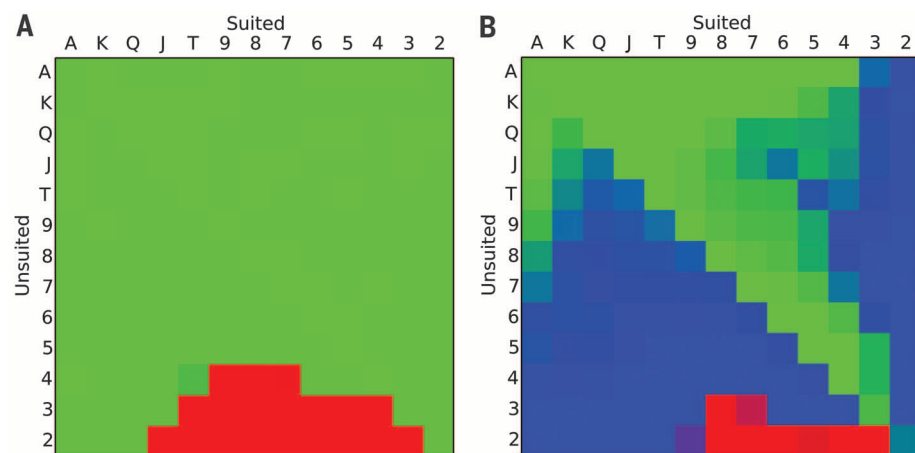


Fig. 4. Action probabilities in the solution strategy for two early decisions. (A) The action probabilities for the dealer’s first action of the game. **(B)** The action probabilities for the nondealer’s first action in the event that the dealer raises. Each cell represents one of the possible 169 hands (i.e., two private cards), with the upper right diagonal consisting of cards with the same suit and the lower left diagonal consisting of cards of different suits. The color of the cell represents the action taken: red for fold, blue for call, and green for raise, with mixtures of colors representing a stochastic decision.

24. D. Billings *et al.*, in *Proceedings of the Eighteenth International Joint Conference on Artificial Intelligence* (2003), pp. 661–668.
25. M. Zinkevich, M. Littman, The AAAI Computer Poker Competition. *J. Int. Comput. Games Assoc.* **29**, 166 (2006).
26. V. L. Allis, thesis, University of Limburg (1994).
27. F. Southey *et al.*, in *Proceedings of the 21st Conference on Uncertainty in Artificial Intelligence* (2005), pp. 550–558.
28. I. V. Romanovskii, *Sov. Math.* **3**, 678–681 (1962).
29. D. Koller, N. Megiddo, *Games Econ. Behav.* **4**, 528–552 (1992).
30. D. Koller, N. Megiddo, B. von Stengel, *Games Econ. Behav.* **14**, 247–249 (1996).
31. A. Gilpin, T. Sandholm, *J. ACM* **54**, 25 (2007).
32. J. Shi, M. L. Littman, in *Revised Papers from the Second International Conference on Computers and Games* (2000), pp. 333–345.
33. T. Sandholm, *AI Mag.* **31**, 13–32 (2010).
34. J. Rubin, I. Watson, *Artif. Intell.* **175**, 958–987 (2011).
35. Another notable algorithm to emerge from the Annual Computer Poker Competition is an application of Nesterov's excessive gap technique (51) to solving extensive-form games (52). The technique has some desirable properties, including better asymptotic time complexity than what is known for CFR. However, it has not seen widespread use among competition participants because of its lack of flexibility in incorporating sampling schemes and its inability to be used with powerful (but unsound) abstractions that make use of imperfect recall. Recently, Waugh and Bagnell (53) have shown that CFR and the excessive gap technique are more alike than different, which suggests that the individual advantages of each approach may be attainable in the other.
36. M. Zinkevich, M. Johanson, M. Bowling, C. Piccione, in *Advances in Neural Information Processing Systems 20* (2008), pp. 905–912.
37. N. Karmarkar, in *Proceedings of the 16th Annual ACM Symposium on Theory of Computing* (1984), pp. 302–311.
38. E. Jackson, in *Proceedings of the 2012 Computer Poker Symposium* (2012); www.ualberta.ca/~archibal/papers/jackson.pdf. Jackson reports a higher number of information sets, which counts terminal information sets rather than only those where a player is to act.
39. O. Tammelin, <http://arxiv.org/abs/1407.5042> (2014).
40. M. Johanson, N. Bard, M. Lanctot, R. Gibson, M. Bowling, in *Proceedings of the 11th International Conference on Autonomous Agents and Multi-Agent Systems* (2012), pp. 837–846.
41. M. Johanson, K. Waugh, M. Bowling, M. Zinkevich, in *Proceedings of the 22nd International Joint Conference on Artificial Intelligence* (2011), pp. 258–265.
42. M. Bowling, M. Johanson, N. Burch, D. Szafron, in *Proceedings of the 25th International Conference on Machine Learning* (2008), pp. 72–79.
43. The total time and number of core-years is larger than was strictly necessary, as it includes computation of an average strategy that was later measured to be more exploitable than the current strategy and so was discarded. The total space noted, on the other hand, is without storing the average strategy.
44. These insights were the result of discussions with Bryce Paradis, previously a professional poker player who specialized in HULHE.
45. O. Morgenstern, *New York Times Magazine* (5 February 1961), pp. 21–22.
46. M. Tambe, *Security and Game Theory: Algorithms, Deployed Systems, Lessons Learned* (Cambridge Univ. Press, Cambridge, 2011).
47. K. Chen, M. Bowling, in *Advances in Neural Information Processing Systems 25* (2012), pp. 2078–2086.
48. P. Mirowski, in *Toward a History of Game Theory*, E. R. Weintraub, Ed. (Duke Univ. Press, Durham, NC, 1992), pp. 113–147. Mirowski cites Turing as author of the paragraph containing this remark. The paragraph appeared in (2), in a chapter with Turing listed as one of three contributors. Which parts of the chapter are the work of which contributor, particularly the introductory material containing this quote, is not made explicit.
49. M. Buro, *Adv. Comput. Games* **135**, 361–366 (2004).
50. E. Zermelo, in *Proceedings of the Fifth International Congress of Mathematics* (Cambridge Univ. Press, Cambridge, 1913), pp. 501–504.
51. Y. Nesterov, *SIAM J. Optim.* **16**, 235–249 (2005).
52. A. Gilpin, S. Hoda, J. Peña, T. Sandholm, in *Proceedings of the Third International Workshop on Internet and Network Economics* (2007), pp. 57–69.
53. K. Waugh, J. A. Bagnell, in *AAAI Workshop on Computer Poker and Imperfect Information*; www.cs.cmu.edu/~jwaugh/publications/unify15.pdf.

ACKNOWLEDGMENTS

The author order is alphabetical reflecting equal contribution by the authors. The idea of CFR⁺ and compressing the regrets and strategy originated with O.T. (39). This research was supported by Natural Sciences and Engineering Research Council of Canada and Alberta Innovates Technology Futures through the Alberta Innovates Centre for Machine Learning and was made possible by the computing resources of Compute Canada and Calcul Québec. We thank all of the current and past members of the University of Alberta Computer Poker Research Group, where the idea to solve heads-up limit Texas hold'em was first discussed; J. Schaeffer, R. Holte, D. Szafron, and A. Brown for comments on

early drafts of this article; and B. Paradis for insights into the conventional wisdom of top human poker players.

SUPPLEMENTARY MATERIALS

www.sciencemag.org/content/347/6218/145/suppl/DC1
Source code used to compute the solution strategy
Supplementary Text
Fig. S1
References (54–62)

30 July 2014; accepted 1 December 2014
10.1126/science.1259433

REPORTS

BATTERIES

In situ visualization of Li/Ag₂VP₂O₈ batteries revealing rate-dependent discharge mechanism

Kevin Kirshenbaum,¹ David C. Bock,² Chia-Ying Lee,³ Zhong Zhong,¹ Kenneth J. Takeuchi,^{2,4*} Amy C. Marschilok,^{2,4*} Esther S. Takeuchi^{1,2,4*}

The functional capacity of a battery is observed to decrease, often quite dramatically, as discharge rate demands increase. These capacity losses have been attributed to limited ion access and low electrical conductivity, resulting in incomplete electrode use. A strategy to improve electronic conductivity is the design of bimetallic materials that generate a silver matrix in situ during cathode reduction. Ex situ x-ray absorption spectroscopy coupled with in situ energy-dispersive x-ray diffraction measurements on intact lithium/silver vanadium diphosphate (Li/Ag₂VP₂O₈) electrochemical cells demonstrate that the metal center preferentially reduced and its location in the bimetallic cathode are rate-dependent, affecting cell impedance. This work illustrates that spatial imaging as a function of discharge rate can provide needed insights toward improving realizable capacity of bimetallic cathode systems.

Following the introduction of lithium iron phosphate (1), polyanion framework materials have emerged as a cathode class of interest due to increased thermal stability and higher operating voltage relative to oxides. Materials with multiple metal centers—such as LiCo_{1/3}Mn_{1/3}Ni_{1/3}O₂ (2), LiMn_{0.15}Fe_{0.85}PO₄ (3), and LiNi_{0.5}Mn_{1.5}O₄ (4), as well as numerous bimetallic sulfates (5, 6)—are being explored for use in high-voltage electrodes; however, high electronic resistance and low volumetric capacity are two inherent limitations that have been observed in these materials. Various strategies have been implemented to facilitate ion access through the use of nanosized materials and for mitigation of resistance on a practical level, including intimate mixing or coating with conductive carbon (7). Sub-

stantial gains in power output were achieved, albeit at the expense of gravimetric and volumetric energy density.

An alternate conceptual approach is the rational design of multifunctional bimetallic polyanion framework materials in which a redox active center offering the opportunity for multiple electron reductions per formula unit (i.e., vanadium) is used in conjunction with a redox active center that reduces to form a conductive metal (i.e., silver) (8). Design of active cathode materials that form conductive networks in situ can reduce or potentially eliminate the need for conductive additives that do not add to the capacity of the cell and require additional processing, thereby providing a greater overall energy density. One such polyanionic material, silver vanadium diphosphate (Ag₂VP₂O₈), displays a reduction displacement mechanism (9) in which both vanadium and silver are reduced during the discharge process. The overall reduction processes can be expressed as Ag₂V⁴⁺P₂O₈ + (x+y)Li⁰ → Li_{x+y}Ag_{2-y}V^{(4-x)+}P₂O₈ + yAg⁰.

Here we seek to determine the effect that discharge rate has on the discharge mechanism, including homogeneity and spatial distribution of discharged material in the cathode. Determination of the discharge conditions yielding an optimal

¹Brookhaven National Laboratory, 2 Center Street, Upton, NY 11973-5000, USA. ²Department of Chemistry, Stony Brook University, Stony Brook, NY 11794-3400, USA. ³Department of Chemical and Biological Engineering, University at Buffalo, Buffalo, NY 14260-4200, USA. ⁴Department of Materials Science and Engineering, Stony Brook University, Stony Brook, NY 11794-2275, USA.

*Corresponding author. E-mail: kenneth.takeuchi1@stonybrook.edu (K.J.T.); amy.marschilok@stonybrook.edu (A.C.M.); esther.takeuchi@stonybrook.edu (E.S.T.)

24. D. Billings *et al.*, in *Proceedings of the Eighteenth International Joint Conference on Artificial Intelligence* (2003), pp. 661–668.
25. M. Zinkevich, M. Littman, The AAAI Computer Poker Competition. *J. Int. Comput. Games Assoc.* **29**, 166 (2006).
26. V. L. Allis, thesis, University of Limburg (1994).
27. F. Southey *et al.*, in *Proceedings of the 21st Conference on Uncertainty in Artificial Intelligence* (2005), pp. 550–558.
28. I. V. Romanovskii, *Sov. Math.* **3**, 678–681 (1962).
29. D. Koller, N. Megiddo, *Games Econ. Behav.* **4**, 528–552 (1992).
30. D. Koller, N. Megiddo, B. von Stengel, *Games Econ. Behav.* **14**, 247–249 (1996).
31. A. Gilpin, T. Sandholm, *J. ACM* **54**, 25 (2007).
32. J. Shi, M. L. Littman, in *Revised Papers from the Second International Conference on Computers and Games* (2000), pp. 333–345.
33. T. Sandholm, *AI Mag.* **31**, 13–32 (2010).
34. J. Rubin, I. Watson, *Artif. Intell.* **175**, 958–987 (2011).
35. Another notable algorithm to emerge from the Annual Computer Poker Competition is an application of Nesterov's excessive gap technique (51) to solving extensive-form games (52). The technique has some desirable properties, including better asymptotic time complexity than what is known for CFR. However, it has not seen widespread use among competition participants because of its lack of flexibility in incorporating sampling schemes and its inability to be used with powerful (but unsound) abstractions that make use of imperfect recall. Recently, Waugh and Bagnell (53) have shown that CFR and the excessive gap technique are more alike than different, which suggests that the individual advantages of each approach may be attainable in the other.
36. M. Zinkevich, M. Johanson, M. Bowling, C. Piccione, in *Advances in Neural Information Processing Systems 20* (2008), pp. 905–912.
37. N. Karmarkar, in *Proceedings of the 16th Annual ACM Symposium on Theory of Computing* (1984), pp. 302–311.
38. E. Jackson, in *Proceedings of the 2012 Computer Poker Symposium* (2012); www.ualberta.ca/~archibal/papers/jackson.pdf. Jackson reports a higher number of information sets, which counts terminal information sets rather than only those where a player is to act.
39. O. Tammelin, <http://arxiv.org/abs/1407.5042> (2014).
40. M. Johanson, N. Bard, M. Lanctot, R. Gibson, M. Bowling, in *Proceedings of the 11th International Conference on Autonomous Agents and Multi-Agent Systems* (2012), pp. 837–846.
41. M. Johanson, K. Waugh, M. Bowling, M. Zinkevich, in *Proceedings of the 22nd International Joint Conference on Artificial Intelligence* (2011), pp. 258–265.
42. M. Bowling, M. Johanson, N. Burch, D. Szafron, in *Proceedings of the 25th International Conference on Machine Learning* (2008), pp. 72–79.
43. The total time and number of core-years is larger than was strictly necessary, as it includes computation of an average strategy that was later measured to be more exploitable than the current strategy and so was discarded. The total space noted, on the other hand, is without storing the average strategy.
44. These insights were the result of discussions with Bryce Paradis, previously a professional poker player who specialized in HULHE.
45. O. Morgenstern, *New York Times Magazine* (5 February 1961), pp. 21–22.
46. M. Tambe, *Security and Game Theory: Algorithms, Deployed Systems, Lessons Learned* (Cambridge Univ. Press, Cambridge, 2011).
47. K. Chen, M. Bowling, in *Advances in Neural Information Processing Systems 25* (2012), pp. 2078–2086.
48. P. Mirowski, in *Toward a History of Game Theory*, E. R. Weintraub, Ed. (Duke Univ. Press, Durham, NC, 1992), pp. 113–147. Mirowski cites Turing as author of the paragraph containing this remark. The paragraph appeared in (2), in a chapter with Turing listed as one of three contributors. Which parts of the chapter are the work of which contributor, particularly the introductory material containing this quote, is not made explicit.
49. M. Buro, *Adv. Comput. Games* **135**, 361–366 (2004).
50. E. Zermelo, in *Proceedings of the Fifth International Congress of Mathematics* (Cambridge Univ. Press, Cambridge, 1913), pp. 501–504.
51. Y. Nesterov, *SIAM J. Optim.* **16**, 235–249 (2005).
52. A. Gilpin, S. Hoda, J. Peña, T. Sandholm, in *Proceedings of the Third International Workshop on Internet and Network Economics* (2007), pp. 57–69.
53. K. Waugh, J. A. Bagnell, in *AAAI Workshop on Computer Poker and Imperfect Information*; www.cs.cmu.edu/~jwaugh/publications/unify15.pdf.

ACKNOWLEDGMENTS

The author order is alphabetical reflecting equal contribution by the authors. The idea of CFR⁺ and compressing the regrets and strategy originated with O.T. (39). This research was supported by Natural Sciences and Engineering Research Council of Canada and Alberta Innovates Technology Futures through the Alberta Innovates Centre for Machine Learning and was made possible by the computing resources of Compute Canada and Calcul Québec. We thank all of the current and past members of the University of Alberta Computer Poker Research Group, where the idea to solve heads-up limit Texas hold'em was first discussed; J. Schaeffer, R. Holte, D. Szafron, and A. Brown for comments on

early drafts of this article; and B. Paradis for insights into the conventional wisdom of top human poker players.

SUPPLEMENTARY MATERIALS

www.sciencemag.org/content/347/6218/145/suppl/DC1
Source code used to compute the solution strategy
Supplementary Text
Fig. S1
References (54–62)

30 July 2014; accepted 1 December 2014
10.1126/science.1259433

REPORTS

BATTERIES

In situ visualization of Li/Ag₂VP₂O₈ batteries revealing rate-dependent discharge mechanism

Kevin Kirshenbaum,¹ David C. Bock,² Chia-Ying Lee,³ Zhong Zhong,¹ Kenneth J. Takeuchi,^{2,4*} Amy C. Marschilok,^{2,4*} Esther S. Takeuchi^{1,2,4*}

The functional capacity of a battery is observed to decrease, often quite dramatically, as discharge rate demands increase. These capacity losses have been attributed to limited ion access and low electrical conductivity, resulting in incomplete electrode use. A strategy to improve electronic conductivity is the design of bimetallic materials that generate a silver matrix in situ during cathode reduction. Ex situ x-ray absorption spectroscopy coupled with in situ energy-dispersive x-ray diffraction measurements on intact lithium/silver vanadium diphosphate (Li/Ag₂VP₂O₈) electrochemical cells demonstrate that the metal center preferentially reduced and its location in the bimetallic cathode are rate-dependent, affecting cell impedance. This work illustrates that spatial imaging as a function of discharge rate can provide needed insights toward improving realizable capacity of bimetallic cathode systems.

Following the introduction of lithium iron phosphate (1), polyanion framework materials have emerged as a cathode class of interest due to increased thermal stability and higher operating voltage relative to oxides. Materials with multiple metal centers—such as LiCo_{1/3}Mn_{1/3}Ni_{1/3}O₂ (2), LiMn_{0.15}Fe_{0.85}PO₄ (3), and LiNi_{0.5}Mn_{1.5}O₄ (4), as well as numerous bimetallic sulfates (5, 6)—are being explored for use in high-voltage electrodes; however, high electronic resistance and low volumetric capacity are two inherent limitations that have been observed in these materials. Various strategies have been implemented to facilitate ion access through the use of nanosized materials and for mitigation of resistance on a practical level, including intimate mixing or coating with conductive carbon (7). Sub-

stantial gains in power output were achieved, albeit at the expense of gravimetric and volumetric energy density.

An alternate conceptual approach is the rational design of multifunctional bimetallic polyanion framework materials in which a redox active center offering the opportunity for multiple electron reductions per formula unit (i.e., vanadium) is used in conjunction with a redox active center that reduces to form a conductive metal (i.e., silver) (8). Design of active cathode materials that form conductive networks in situ can reduce or potentially eliminate the need for conductive additives that do not add to the capacity of the cell and require additional processing, thereby providing a greater overall energy density. One such polyanionic material, silver vanadium diphosphate (Ag₂VP₂O₈), displays a reduction displacement mechanism (9) in which both vanadium and silver are reduced during the discharge process. The overall reduction processes can be expressed as Ag₂V⁴⁺P₂O₈ + (x+y)Li⁰ → Li_{x+y}Ag_{2-y}V^{(4-x)+}P₂O₈ + yAg⁰.

Here we seek to determine the effect that discharge rate has on the discharge mechanism, including homogeneity and spatial distribution of discharged material in the cathode. Determination of the discharge conditions yielding an optimal

¹Brookhaven National Laboratory, 2 Center Street, Upton, NY 11973-5000, USA. ²Department of Chemistry, Stony Brook University, Stony Brook, NY 11794-3400, USA. ³Department of Chemical and Biological Engineering, University at Buffalo, Buffalo, NY 14260-4200, USA. ⁴Department of Materials Science and Engineering, Stony Brook University, Stony Brook, NY 11794-2275, USA.

*Corresponding author. E-mail: kenneth.takeuchi1@stonybrook.edu (K.J.T.); amy.marschilok@stonybrook.edu (A.C.M.); esther.takeuchi@stonybrook.edu (E.S.T.)

conductive matrix (i.e., uniformly distributed throughout the cathode) is expected to improve the realizable capacity by using the entire cathode. The first task in this regard is identification of an appropriate marker to track the discharge process. The Ag^0 metal product formed upon discharge is a strong x-ray scatterer, and as such its presence can be detected in small amounts (10, 11). In previous studies, it was shown that pure $\text{Ag}_2\text{VP}_2\text{O}_8$ cathodes free from binders and conductive additives can be discharged, facilitating direct interrogation of the progress of the active material reduction process via tracking of silver metal as a reduction product by using thick cathode pellets (0.5 mm) to enable spatial visualization of the discharge progress within an active electrode (12). This study explores the effect of discharge rate and combines spatially resolved in situ energy-dispersive x-ray diffraction (EDXRD) data with ex situ x-ray absorption spectroscopy (XAS) measurements to elucidate the conditions under which a more optimal conductive network can be formed. We will show that these techniques offer an ap-

proach for the exploration of active materials by providing information about the redox mechanism as well as the location of the reactivity within the electrode. These techniques could be applied to other bimetallic electrode materials for which the rate of discharge may influence the reduction mechanism and affect its performance.

$\text{Li}/\text{Ag}_2\text{VP}_2\text{O}_8$ cells were discharged at C/168, C/608, and C/1440 rates (fig. S1). The fastest discharge rate (C/168, 7-day) was used to provide a condition with notable evidence of polarization, whereas the slower rates (C/608, 25-day; C/1440, 60-day) were used to provide conditions with reduced polarization. It is noted that higher battery volumetric energy density can be achieved through the use of thicker cathodes and minimizing inert components. Thus, appropriate discharge rates were selected for this high-capacity cell design containing pure $\text{Ag}_2\text{VP}_2\text{O}_8$ cathodes free from binders and conductive additives. The ac impedance results further highlight the effect of discharge rate (table S1), with details concerning the equivalent circuit fits provided in the supplement-

tary materials and methods. The ac impedance data was fit to the equivalent circuit pictured in fig. S2. Upon partial discharge [0.5 electron equivalents (elec. equiv.)], the value of the charge transfer resistance (R_{ct}) decreases by more than three orders of magnitude, from ~1 megohm in the nondischarged cell to <10 kilohm for the cells discharged at C/168 and C/1440. However, when comparing the fast-discharged (C/168) and slow-discharged (C/1440) cells, R_{ct} is three times higher in the cell discharged at the faster rate at the same discharge level, indicating considerably higher impedance resulting from the faster discharge rate.

Energy-dispersive x-ray diffraction can be used to achieve spatial resolution of the electrochemical reduction process within the electrode inside an intact electrochemical cell. White-beam radiation coupled with a synchrotron “wiggler” insertion device emits high-energy radiation, which can penetrate bulk engineering materials such as steel, enabling in situ measurement of conventionally designed prototype and production-level batteries (13) to obtain a tomographic profile as a

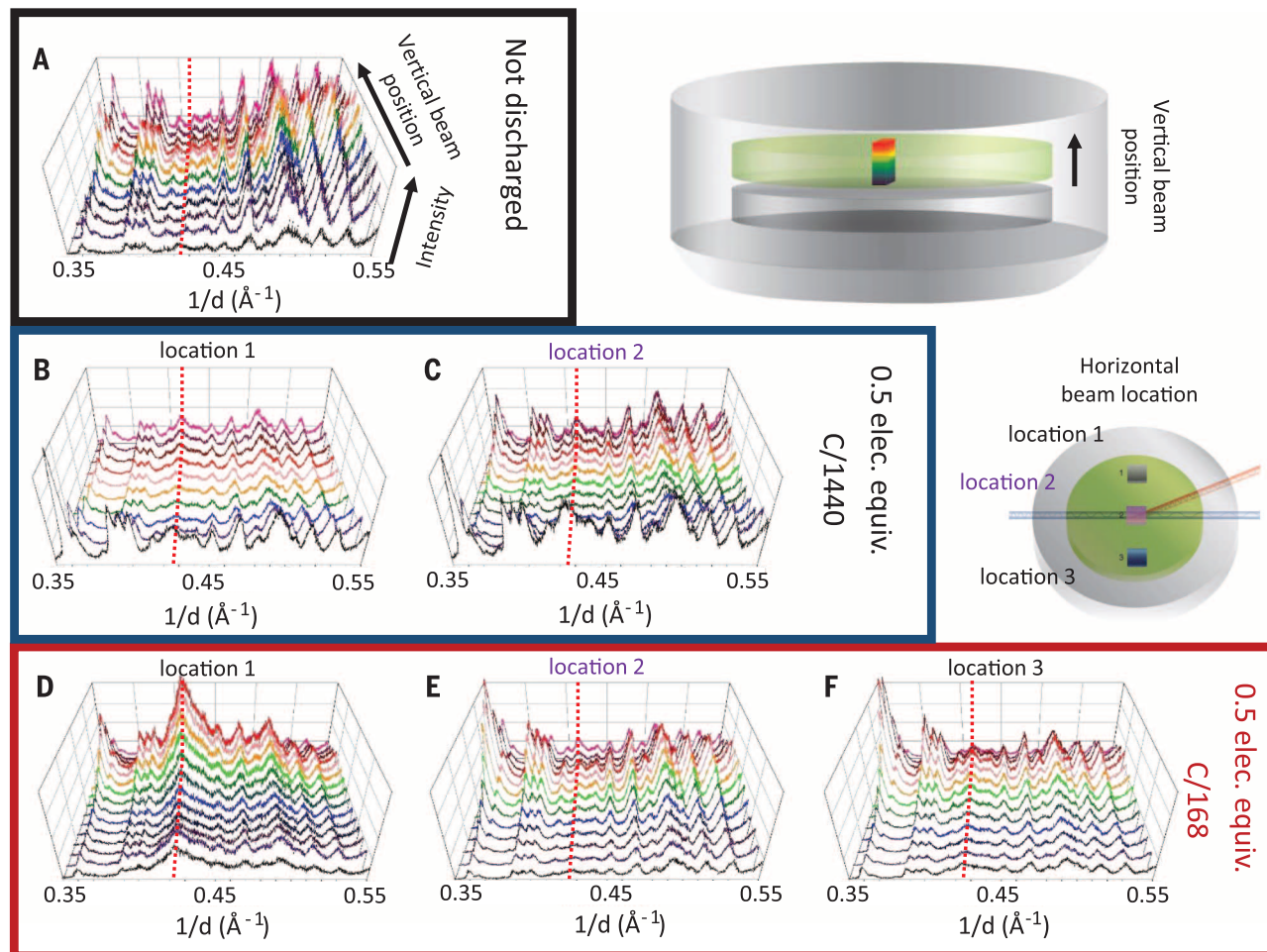


Fig. 1. Experimental setup and EDXRD spectra resulting from in situ measurements. EDXRD spectra obtained within three coin cells: (A) the nondischarged cell, (B and C) two different locations within a cell discharged to 0.5 elec. equiv. at C/1440, and (D to F) three different locations within a cell discharged to 0.5 elec. equiv. at C/168. Spectra were obtained every 20 μm through the cathode; for clarity, only half of the scans are presented in the figure. Spectra toward the top of the figure (red hues) were obtained within the side of the cathode closer to the stainless steel coil cell top, and spectra toward the bottom of the figure (black hues) were obtained closer to the Li anode.

function of both depth of discharge and spatial location within the electrode (13, 14). In situ EDXRD was measured at several x -direction locations spaced 3 mm apart in several stainless steel coin cells with $\text{Ag}_2\text{VP}_2\text{O}_8$ cathodes discharged to 0.5 elec. equiv. (Fig. 1). At each location, spectra were collected in 20- μm increments through the thickness of the electrode. For comparison, an as-prepared (not discharged) cell was also analyzed by EDXRD.

The nondischarged cell shows a uniform diffraction pattern throughout the cathode thickness (Fig. 1A), with differences apparent only in the first (black) scan [Ag(111) peak apparent at

$1/d = 0.4239 \text{ \AA}^{-1}$ (where d is the interplane spacing in the crystal lattice)], indicating formation of some Ag^0 near the cathode surface at the side opposing the anode (12). The source of this diffraction peak was further investigated. Previous studies of bimetallic silver vanadium oxide materials have shown that the silver ion can dissolve into the electrolyte due to ion exchange and dissolution (15). Once the silver ion is in solution, it migrates to the anode surface and is reduced at the anode, forming a silver metal layer. Thus, it is likely that the silver metal that appears near the cathode surface is actually located at the anode surface

and appears near the cathode surface due to a small amount of cell tilt during the EDXRD experiment. Ex situ analysis of the cathode of a nondischarged cell showed small numbers of dark spots on the surface where the inhomogeneous distribution of reduction products at the cathode surface is identified with optical images of cathode pellets (fig. S3). The presence of silver metal could not be identified by ex situ x-ray diffraction (XRD), providing further support that the silver metal observed near the cathode-anode interface by EDXRD may be due to silver metal deposited on the anode.

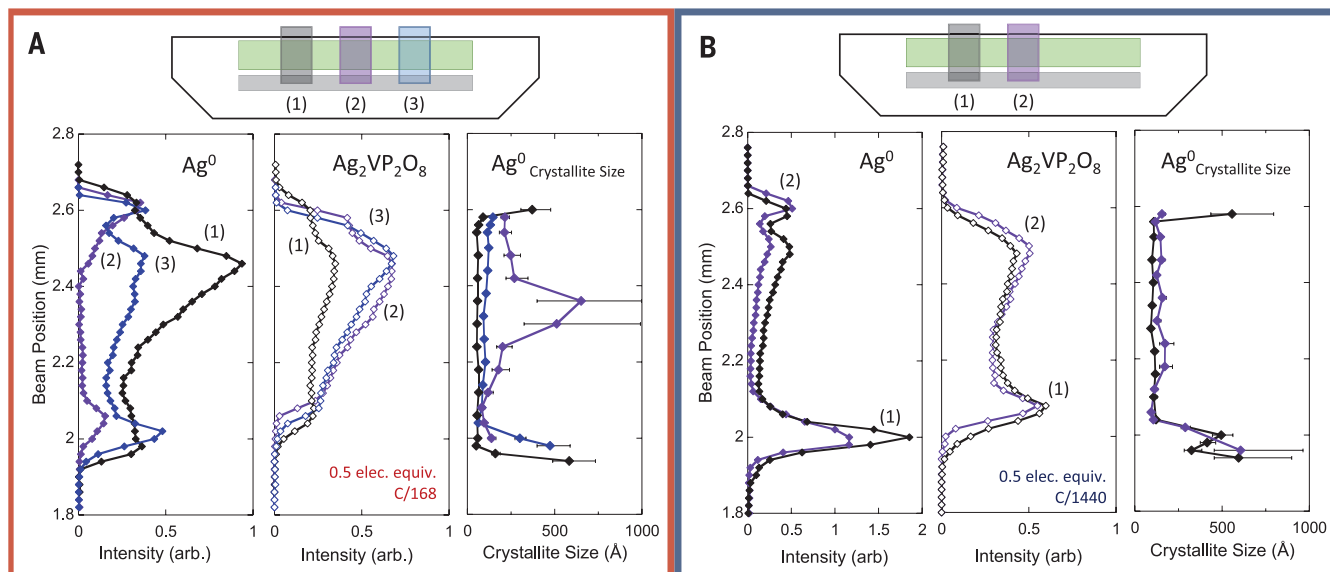


Fig. 2. Intensities of Ag and $\text{Ag}_2\text{VP}_2\text{O}_8$ and crystallite size of Ag as a function of beam position along the z direction. (A) Cathode discharged to 0.5 elec. equiv. at the faster rate (C/168). Three x -direction locations were measured (see schematic inset). (B) Cathode discharged to 0.5 elec. equiv. at the slower rate (C/1440). Two locations along the x direction were measured in this cell (see schematic inset). Error bars represent the uncertainty in the fit (see supplementary materials).

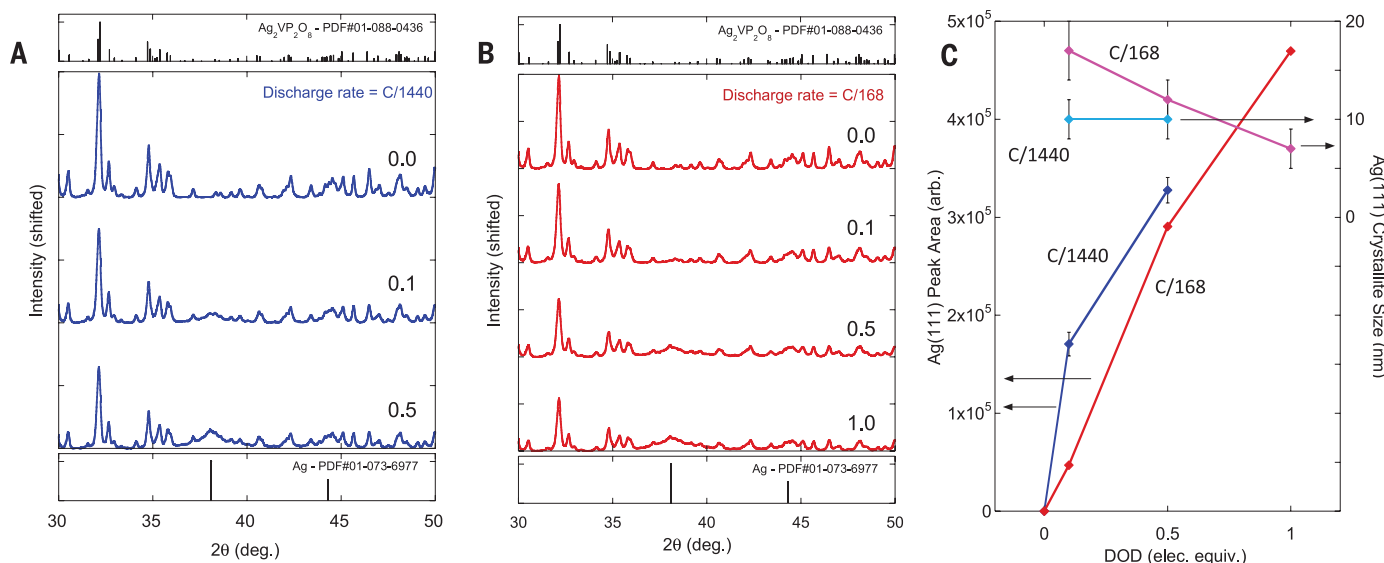


Fig. 3. Ex situ XRD patterns of $\text{Ag}_2\text{VP}_2\text{O}_8$ cathodes. (A) Spectra were obtained from cells discharged at the slower rate (C/1440) to 0.1 and 0.5 elec. equiv.. (B) Spectra were obtained from cells discharged at the faster rate (C/168). (C) Area of the Ag(111) peak and crystallite size, as determined by the peak width. Error bars represent the uncertainty in the fit (see supplementary materials).

The spectra for the two positions in the slower-discharged cell (Fig. 1, B and C) are similar. The Ag(III) peak intensity at $1/d = 0.4239 \text{ \AA}$ relative to the intensity of the $\text{Ag}_2\text{VP}_2\text{O}_8$ peaks is also similar between the two positions. In contrast, at the faster discharge rate (C/168), the intensity of the Ag(III) peak varies greatly between the three positions. At position 1 (Fig. 1D), the intensity of the Ag peak is larger than that observed at positions 2 (Fig. 1E) and 3 (Fig. 1F). To further clarify this point, the intensities of several characteristic peaks as a function of beam position along the z direction for the slow- and fast-discharged cells were determined (Fig. 2). Details are provided in the supplementary materials and methods section.

The three x -direction locations in the cell discharged at the faster rate show a large spatial distribution of silver (Fig. 2A): At location 1, the intensity of the Ag(III) peak is higher than that of the $\text{Ag}_2\text{VP}_2\text{O}_8$ peak. At location 3, the intensities are comparable, whereas at location 2, the Ag(III) peak is absent through most of the bulk of the cathode. The intensity of the $\text{Ag}_2\text{VP}_2\text{O}_8$ peaks is also lower at location 1 than at locations 2 and 3, indicative of a heterogeneous (nonuniform) discharge process under the higher (C/168) discharge rate. In contrast, the results from the cell discharged at the slower rate (Fig. 2B) show a much more uniform discharge across the cathode, with similar spatial distributions of Ag^0 corresponding to comparable local depths of discharge. This uniformity allows for a more complete discharge of the active material by providing electron access to more of the active material simultaneously, thereby increasing the functional capacity of the cell.

The thickness of the cathode is uneven in the cell discharged at the faster rate. From the onset and offset of the Ag^0 and $\text{Ag}_2\text{VP}_2\text{O}_8$ intensities, the cathode is $\sim 60 \mu\text{m}$ ($\sim 10\%$) thicker at location 1 than it is at location 2, where location 1 shows the lowest intensity of Ag^0 through the thickness of the cathode (Fig. 2A). Complete discharge from $\text{Ag}_2\text{VP}_2\text{O}_8$ to $\text{Li}_2\text{VP}_2\text{O}_8$ (corresponding to total replacement of Ag by Li) would result in $>8\%$ decrease in the interlayer spacing, where micro-scale particle fracture may result from the crystallographic stress (9). Thus, we conclude that the uneven swelling of the cathode is related to the local depth of discharge (DOD), potentially due to fracturing of the particles of $\text{Ag}_2\text{VP}_2\text{O}_8$ as they discharge. In the cell discharged at the slower rate, there is no difference in thickness between the two positions, suggesting uniform interlayer spacing through the active material (Fig. 2B).

In every discharged cathode, the Ag(III) peak is much broader than the nearby $\text{Ag}_2\text{VP}_2\text{O}_8$ peaks, indicative of small Ag particles on the order of several nanometers (Fig. 1). The size of the Ag^0 crystallites within the cathodes was determined from the broadening of the Ag(III) peak by applying a derivation of the Scherrer equation in reciprocal space (see supplementary materials and methods for details). This derivation was included as the Scherrer equation is typically used

for diffraction data collected at a fixed wavelength, unlike the data reported here. In the cell discharged at the slower rate, we determined that the crystallite size was ~ 10 to 14 nm at both horizontal locations and did not vary appreciably through the thickness of the cathode (Fig. 2B). In the cell discharged at the faster rate, however, the crystallite size varied greatly between the three locations: At location 1, the crystallites were $\sim 5 \text{ nm}$, whereas at location 2, there were crystallites larger than 500 nm (Fig. 2A).

To complement these data, ex situ x-ray powder diffraction spectra were acquired (Fig. 3). During this process, the complete cathodes from an as-prepared cell and cells tested to various depths of discharge under slower (C/1440) and faster (C/168) discharge rates were removed and ground before measurement (see supplementary materials and methods section for details).

The cathode that had not been discharged was found to be pure $\text{Ag}_2\text{VP}_2\text{O}_8$, with no Ag^0 detected. As the cells are discharged, the intensity of the

$\text{Ag}_2\text{VP}_2\text{O}_8$ peaks decreases, indicating that the active material becomes amorphous on discharge, as determined by XRD (Fig. 3, A and B). Similar results have been found in the related compounds $\text{Ag}_2\text{VO}_2\text{PO}_4$ (16), $\text{AgV}_3\text{O}_{5.5}$ (17), and $\text{Ag}_4\text{V}_2\text{O}_6\text{F}_2$ (18). Under both discharge rates, an increase in the Ag(III) peak area was observed, consistent with the formation of additional silver on discharge (Fig. 3C). In the discharged materials, the Ag^0 crystallite size ranged from 5 to 20 nm , consistent with the 7 - to 8-nm crystallite size of Ag nanoparticles found in pure, graphite-free cathodes composed of the related material $\text{Ag}_2\text{VO}_2\text{PO}_4$ (8). Under the slower discharge rate (C/1440), the silver crystallite size remained constant in the cells discharged to 0.1 and 0.5 elec. equiv., whereas under the faster discharge rate, a measurable decrease in average Ag crystallite size was observed in the cells discharged to 0.1 , 0.5 , and 1.0 elec. equiv. Under the faster rate, we propose that additional heterogeneous nucleation sites are generated as a result of particle fracture upon

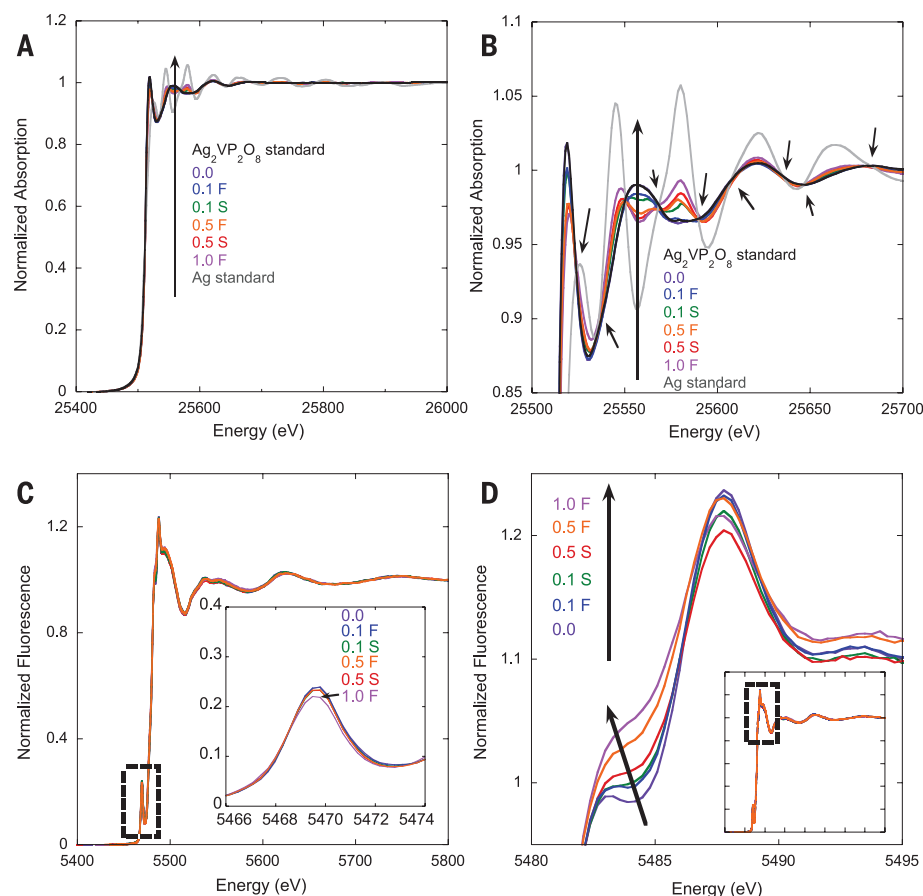


Fig. 4. X-ray absorption (XAS) and fluorescence (XRF) measurements of partially discharged $\text{Ag}_2\text{VP}_2\text{O}_8$. Data in this figure are from cells discharged to 0.1 and 0.5 elec. equiv. at C/1440 (slow rate, S) and 0.1 , 0.5 , and 1.0 elec. equiv. at C/168 (fast rate, F), as well as $\text{Ag}_2\text{VP}_2\text{O}_8$ and Ag standards. (A) Normalized absorption at the Ag K-edge. (B) Ag K-edge near-edge region. Arrows point to isosbestic points supporting the existence of a two-phase system ($\text{Ag}^+ \rightarrow \text{Ag}^0$). (C) Normalized fluorescence of V K-edge. (Inset) Pre-edge peak showing no change in peak height or position until DOD reached 1.0 elec. equiv. (D) Post-edge white line for normalized fluorescence data highlighting the dependence of the shoulder feature on DOD and discharge rate. (Inset) Normalized fluorescence of the V K-edge. The dashed box shows the region that is emphasized in the figure.

local discharge of $\text{Ag}_2\text{VP}_2\text{O}_8$ to $\text{Li}_2\text{VP}_2\text{O}_8$. These nucleation sites promote formation of additional small silver crystallites, leading to a smaller average crystallite size for the overall population as a function of discharge. In contrast, under the slower rate, the material discharges more uniformly, with lower local stresses. Thus, a consistent Ag^0 crystallite size is observed throughout.

The ex situ XRD results also suggested a difference in discharge mechanism of the bimetallic material due to a slight increase in the amount of Ag^0 present at the slower discharge rate than at the faster discharge rate at the same depth of discharge (Fig. 3C). To confirm these results the relative amount of Ag^0 and Ag^+ and the ratio of $\text{V}^{3+}/\text{V}^{4+}$ were measured in discharged cathodes from cells discharged at three rates (C/168, C/608, and C/1440) and were compared with as-formed $\text{Ag}_2\text{VP}_2\text{O}_8$ powder that was never placed in a cell and Ag^0 powder as references, using the oxidation state-sensitive measurements of XAS at the Ag K-edge and x-ray fluorescence spectroscopy (XRF) at the V K-edge (Fig. 4).

As $\text{Ag}_2\text{VP}_2\text{O}_8$ is discharged and Ag^+ is reduced to Ag^0 , more than eight discrete isosbestic points can be observed in these spectra (Fig. 4, A and B). These points are an indicator that the silver in these pellets exists as a linear combination of two states: octahedrally coordinated Ag^+ found in $\text{Ag}_2\text{VP}_2\text{O}_8$ and metallic (BCC) Ag^0 found in silver metal (19, 20). As asymmetry increased as a function of oxidation state in vanadium oxides, the intensity of the pre-edge peak for the V K-edge (Fig. 4C) can be used to determine oxidation state changes (21, 22). Because the V-O bond lengths in $\text{Ag}_2\text{VP}_2\text{O}_8$ are more anisotropic than those in either V_2O_3 or VO_2 , the pre-edge peak intensity is greater, and these materials cannot be used as standards. Therefore, we compare only this peak intensity among $\text{Ag}_2\text{VP}_2\text{O}_8$ samples discharged at different rates to look for small changes to the oxidation state. We observe no measurable change in the pre-edge peak intensity until a DOD of 1.0 elec. equiv., providing further evidence that at low DOD, Ag^+ reduces preferentially over V^{4+} .

Another feature showing subtle changes with discharge is the post-edge shoulder highlighted in Fig. 4D. The post-edge peak (white line) has been assigned as the $1s \rightarrow 4p$ transition and the shoulder as the $1s \rightarrow 4p$ shakedown transition (21, 22). In our data, we see the height of this shoulder increasing as a function of DOD. Although this is not an indicator of oxidation state, shakedown transitions are associated with metal-to-ligand charge transfer; thus, these changes to the shoulder may be related to slight distortions in the density of states near the vanadium atoms. Previous studies have shown similar changes to the white line/shoulder feature: One study of the lithiation of $\text{Li}_x\text{V}_6\text{O}_{13}$ showed a similar feature and assigned it to a possible ligand field splitting effect (23). The height of the shoulder is greater in cells discharged at the faster rate, indicating a greater effect on the local vanadium environment.

Linear combination fitting (LCF) was applied to the Ag and V K-edge data to gain additional information regarding changes in oxidation state as a function of discharge (Fig. 5). Because the silver transitions directly between two states, the ratio of Ag^+ to Ag^0 present in each sample could be determined using nondischarged $\text{Ag}_2\text{VP}_2\text{O}_8$ and an Ag foil as the end members in a linear combination fit (Fig. 5A). To estimate the ratio of V^{3+} to V^{4+} , we used as-prepared $\text{Ag}_2\text{VP}_2\text{O}_8$ as the V^{4+} standard and $\text{Ag}_2\text{VP}_2\text{O}_8$ discharged fully to 3 elec. equiv. at C/608 as the V^{3+} standard when performing LCF on the V K-edge (Fig. 5B).

Linear combination fitting indicates that Ag^+ begins to reduce even at the lowest DOD measured in this study and increases monotonically as DOD increases (Fig. 5A). For cells discharged at the slower rate, the linear combination fits show a greater amount of Ag^0 at the same DOD compared with the cells discharged at the faster rate, consistent with the observation of greater Ag^0 intensity by EDXRD in the slow-discharged cell, particularly at the anode interface (Fig. 3). As DOD increases, this difference becomes more apparent; at 1 electron equivalent, there is twice as much Ag^0 in the cells discharged at the slower

rate. The Ag^0 content of the cells discharged at the two slower rates (C/608 and C/1440) is consistent, as expected based on the overlapping discharge curves (fig. S1). For the cells discharged at C/608, the Ag^0 content remains consistent between 2 and 3 elec. equiv., indicating that most of the silver has reduced by 2 elec. equiv. of discharge.

As with Ag reduction, the amount of V^{3+} present in the samples is comparable for the two slower rates (C/608, C/1440) and is, as expected, lower than the amount of V^{3+} in the cells discharged at the faster rate (C/168) (Fig. 5B). There is a sharp upturn in the amount of V^{3+} above 2 elec. equiv., consistent with our previous conclusion that by 2 electrons equivalents, most of the Ag^+ has reduced and the remaining electrons must come from V^{4+} . Tabular LCF results are provided in the supplementary materials (table S2).

Thus, two different reduction processes for the multifunctional bimetallic $\text{Ag}_2\text{VP}_2\text{O}_8$ cathode material become apparent: Ag^+ ions exit the structure and are reduced to Ag^0 , and V^{4+} is reduced to V^{3+} . Although at all discharge rates both reduction processes occur, the ratio of the reduction of silver to that of vanadium changes with discharge rate where the reduction of Ag^+ is favored by slower discharge rates. The spatial distribution of Ag^0 is more uniform in the cell discharged at the slower rate, indicating a comparatively even discharge throughout the cathode with consistent Ag^0 crystallite size. In the cell discharged at the faster rate, nonuniform reduction is observed with regions of higher and lower local Ag^0 content, leading to more and less favorable electron conduction pathways through the thickness of the cathode. Upon further discharge, reduction will continue to occur preferentially at these favorable locations with enhanced electron access, with incomplete use under high rate discharge as a consequence.

By combining in situ EDXRD with ex situ XRD and XAS measurements, we are able to visualize the formation of the conductive silver matrix within the $\text{Ag}_2\text{VP}_2\text{O}_8$ electrode and elucidate a rate-dependent discharge mechanism. The results of this study show that by using lower current densities early in the discharge of a multifunctional bimetallic cathode-containing cell, it is possible to preferentially form metallic silver that is more evenly distributed, resulting in the opportunity for more complete cathode use and higher functional capacity. Thus, this approach can be extended to other bimetallic and polyanionic electrode materials to probe their discharge mechanisms and spatially resolve changes as a function of usage profile, providing the insight needed to optimize these materials for their use in the next generation of batteries.

REFERENCES AND NOTES

1. A. K. Padhi, K. S. Nanjundaswamy, J. B. Goodenough, *J. Electrochem. Soc.* **144**, 1188–1194 (1997).
2. X. Liu et al., *Nat. Commun.* **4**, 2568 (2013).
3. X. Zhou, Y. F. Deng, L. N. Wan, X. S. Qin, G. H. Chen, *J. Power Sources* **265**, 223–230 (2014).
4. J. Zhou et al., *Phys. Chem. Chem. Phys.* **16**, 13838–13842 (2014).
5. M. Reynaud et al., *ECS Trans.* **50**, 11–19 (2013).
6. G. Rousseau, J. M. Tarascon, *Chem. Mater.* **26**, 394–406 (2014).

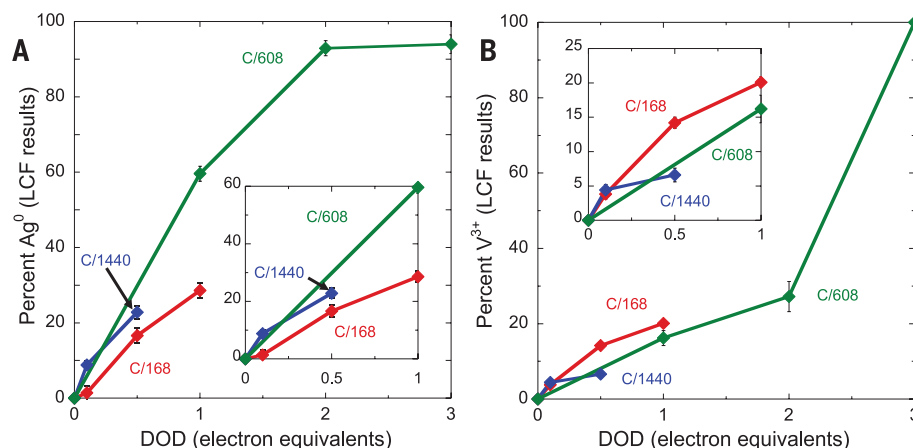


Fig. 5. Linear combination fits of data from Fig. 4. (A) Ag K-edge. (B) V K-edge. Error bars represent the uncertainty in the fit (see supplementary materials). (Insets) Enhancement of the linear combination fit results up to 1 elec. equiv.

7. H. Huang, S. C. Yin, L. F. Nazar, *Electrochem. Solid-State Lett.* **4**, A170–A172 (2001).
8. E. S. Takeuchi et al., *Chem. Mater.* **21**, 4934–4939 (2009).
9. E. S. Takeuchi et al., *J. Solid State Chem.* **200**, 232–240 (2013).
10. E. S. Takeuchi et al., *Energy Environ. Sci.* **6**, 1465–1470 (2013).
11. F. Sauvage, V. Bodenez, J. M. Tarascon, K. R. Poeppelmeier, *Inorg. Chem.* **49**, 6461–6467 (2010).
12. K. C. Kirshenbaum et al., *Phys. Chem. Chem. Phys.* **16**, 9138–9147 (2014).
13. J. Rijnssenbeek et al., *J. Power Sources* **196**, 2332–2339 (2011).
14. M. Ebner, F. Marone, M. Stambanoni, V. Wood, *Science* **342**, 716–720 (2013).
15. D. C. Bock, K. J. Takeuchi, A. C. Marschilok, E. S. Takeuchi, *Dalton Trans.* **42**, 13981–13989 (2013).
16. A. C. Marschilok et al., *J. Power Sources* **195**, 6839–6846 (2010).
17. R. A. Leising, W. C. Thiebolt, E. S. Takeuchi, *Inorg. Chem.* **33**, 5733–5740 (1994).
18. F. Sauvage et al., *Inorg. Chem.* **47**, 8464–8472 (2008).
19. S. Calvin, in *XAFS for Everyone* (CRC Press, Boca Raton, FL, 2013), p. xxvi.
20. C. J. Patridge et al., *J. Phys. Chem. C* **115**, 14437–14447 (2011).
21. P. Chaurand et al., *J. Phys. Chem. B* **111**, 5101–5110 (2007).
22. J. Wong, F. W. Lytle, R. P. Messmer, D. H. Maylotte, *Phys. Rev. B* **30**, 5596–5610 (1984).
23. P. E. Stallworth, S. Kostov, M. L. denBoer, S. G. Greenbaum, C. Lampe-Onnerud, *J. Appl. Phys.* **83**, 1247–1255 (1998).

ACKNOWLEDGMENTS

E.S.T., K.J.T., A.C.M., C.-Y.L., and D.C.B. acknowledge funding from the U.S. Department of Energy (DOE), Office of Basic Energy Sciences, under grant DE-SC0008512. Use of the National

Synchrotron Light Source beamline X17B1 was supported by DOE contract DE-AC02-98CH10886. K.K. acknowledges postdoctoral support from Brookhaven National Laboratory and the Gertrude and Maurice Goldhaber Distinguished Fellowship Program. We thank M. C. Croft for helpful discussions and Y. Belyavina for assistance with the conceptual schematics shown in Fig. 1.

SUPPLEMENTARY MATERIALS

www.sciencemag.org/content/347/6218/149/suppl/DC1

Materials and Methods

Supplementary Text

Figs. S1 to S3

Tables S1 and S2

References (24–30)

11 June 2014; accepted 27 November 2014

10.1126/science.1257289

MATERIALS SCIENCE

Assembly of micro/nanomaterials into complex, three-dimensional architectures by compressive buckling

Sheng Xu,^{1*} Zheng Yan,^{1*} Kyung-In Jang,¹ Wen Huang,² Haoran Fu,^{3,4} Jeonghyun Kim,^{1,5} Zijun Wei,¹ Matthew Flavin,¹ Joselle McCracken,⁶ Renhan Wang,¹ Adina Badea,⁶ Yuhao Liu,¹ Dongqing Xiao,⁶ Guoyan Zhou,^{3,7} Jungwoo Lee,^{1,5} Ha Uk Chung,¹ Huanyu Cheng,^{1,3} Wen Ren,⁶ Anthony Banks,¹ Xiuling Li,² Ungyu Paik,⁵ Ralph G. Nuzzo,^{1,6} Yonggang Huang,^{3,†} Yihui Zhang,^{3,8,†} John A. Rogers^{1,2,6,9,†}

Complex three-dimensional (3D) structures in biology (e.g., cytoskeletal webs, neural circuits, and vasculature networks) form naturally to provide essential functions in even the most basic forms of life. Compelling opportunities exist for analogous 3D architectures in human-made devices, but design options are constrained by existing capabilities in materials growth and assembly. We report routes to previously inaccessible classes of 3D constructs in advanced materials, including device-grade silicon. The schemes involve geometric transformation of 2D micro/nanostructures into extended 3D layouts by compressive buckling. Demonstrations include experimental and theoretical studies of more than 40 representative geometries, from single and multiple helices, toroids, and conical spirals to structures that resemble spherical baskets, cuboid cages, starbursts, flowers, scaffolds, fences, and frameworks, each with single- and/or multiple-level configurations.

Controlled formation of 3D functional mesostructures is a topic of broad and increasing interest, particularly in the past decade (1–9). Uses of such structures have been envisioned in nearly every type of micro/nanosystem technology, including biomedical devices (10–12), microelectromechanical components (13, 14), photonics and optoelectronics (15–17), metamaterials (16, 18–21), electronics (22, 23), and energy storage (24, 25). Although volumetric optical exposures (4, 6, 19), fluidic self-assembly (3, 26, 27), residual stress-induced bending (1, 13, 21, 28–31), and templated growth (7, 8, 32) can be used to realize certain classes of structures in certain types of materials, techniques that rely on rastering of fluid nozzles or focused beams of light provide the greatest versatility in design (5, 6). The applicability of these latter methods, however, only extends directly to materials that can be formulated as inks or patterned by exposure to light or other energy sources, and indirectly to those that can be depo-

sited onto or into sacrificial 3D structures formed with these materials (5, 6, 18, 19). Integration of more than one type of any material into a single structure can be challenging. Furthermore, the serial nature of these processes sets practical constraints on operating speeds and overall addressable areas. These and other limitations stand in stark contrast with the exceptional fabrication capabilities that exist for the types of planar micro/nanodevices that are ubiquitous in state-of-the-art semiconductor technologies. Routes to 3D mesostructures that exploit this existing base of competencies can provide options in high-performance function that would otherwise be unobtainable.

Methods based on residual stress-induced bending are naturally compatible with modern planar technologies, and they offer yields and throughputs necessary for practical applications. Such schemes provide access to only certain classes of geometries, through either rotations of rigid plates to yield tilted panels,

rectangular cuboids, pyramids, or other hollow polyhedra, or rolling motions of flexible films to form tubes, scrolls, or related shapes with cylindrical symmetry [for reviews, see (1, 9, 13)]. Here, we present a different set of concepts in which strain relaxation in an elastomeric substrate simultaneously imparts forces at a collection of lithographically controlled locations on the surfaces of planar precursor structures. The resulting processes of controlled, compressive buckling induce rapid, large-area geometric extension into the third dimension, capable of transforming the most advanced functional materials and planar microsystems into mechanically tunable 3D forms with broad geometric diversity.

As a simple illustrative example, we present results of finite-element analyses (FEAs) (33) of the steps for assembly of a pair of 3D conical helices made of monocrystalline silicon in Fig. 1A. The process begins with planar micro/nanofabrication of 2D filamentary serpentine silicon ribbons (2 μm thick, 60 μm wide), with spatial gradients in their arc radii. Lithographically defined exposure of these structures to ozone formed using ultraviolet light creates precisely controlled patterns of surface hydroxyl terminations at strategic locations (red dots in Fig. 1A) along their lengths. A soft silicone

¹Department of Materials Science and Engineering and Frederick Seitz Materials Research Laboratory, University of Illinois at Urbana-Champaign, Urbana, IL 61801, USA.

²Department of Electrical and Computer Engineering, University of Illinois at Urbana-Champaign, Urbana, IL 61801, USA.

³Department of Civil and Environmental Engineering and Department of Mechanical Engineering, Center for Engineering and Health, and Skin Disease Research Center, Northwestern University, Evanston, IL 60208, USA.

⁴Department of Civil Engineering and Architecture, Zhejiang University, Hangzhou 310058, P.R. China. ⁵Department of Materials Science and Engineering, Department of Energy Engineering, Hanyang University, Seoul 133-791, Republic of Korea. ⁶Department of Chemistry, University of Illinois at Urbana-Champaign, Urbana, IL 61801, USA. ⁷Key Laboratory of Pressure Systems and Safety (MOE), School of Mechanical and Power Engineering, East China University of Science and Technology, Shanghai 200237, P.R. China.

⁸Center for Mechanics and Materials, Tsinghua University, Beijing 100084, P.R. China. ⁹Beckman Institute for Advanced Science and Technology, University of Illinois at Urbana-Champaign, Urbana, IL 61801, USA.

*These authors contributed equally to this work. †Corresponding author. E-mail: jrogers@illinois.edu (J.A.R.); y-huang@northwestern.edu (Y.H.); yihui.zhang2011@gmail.com (Y.Z.)

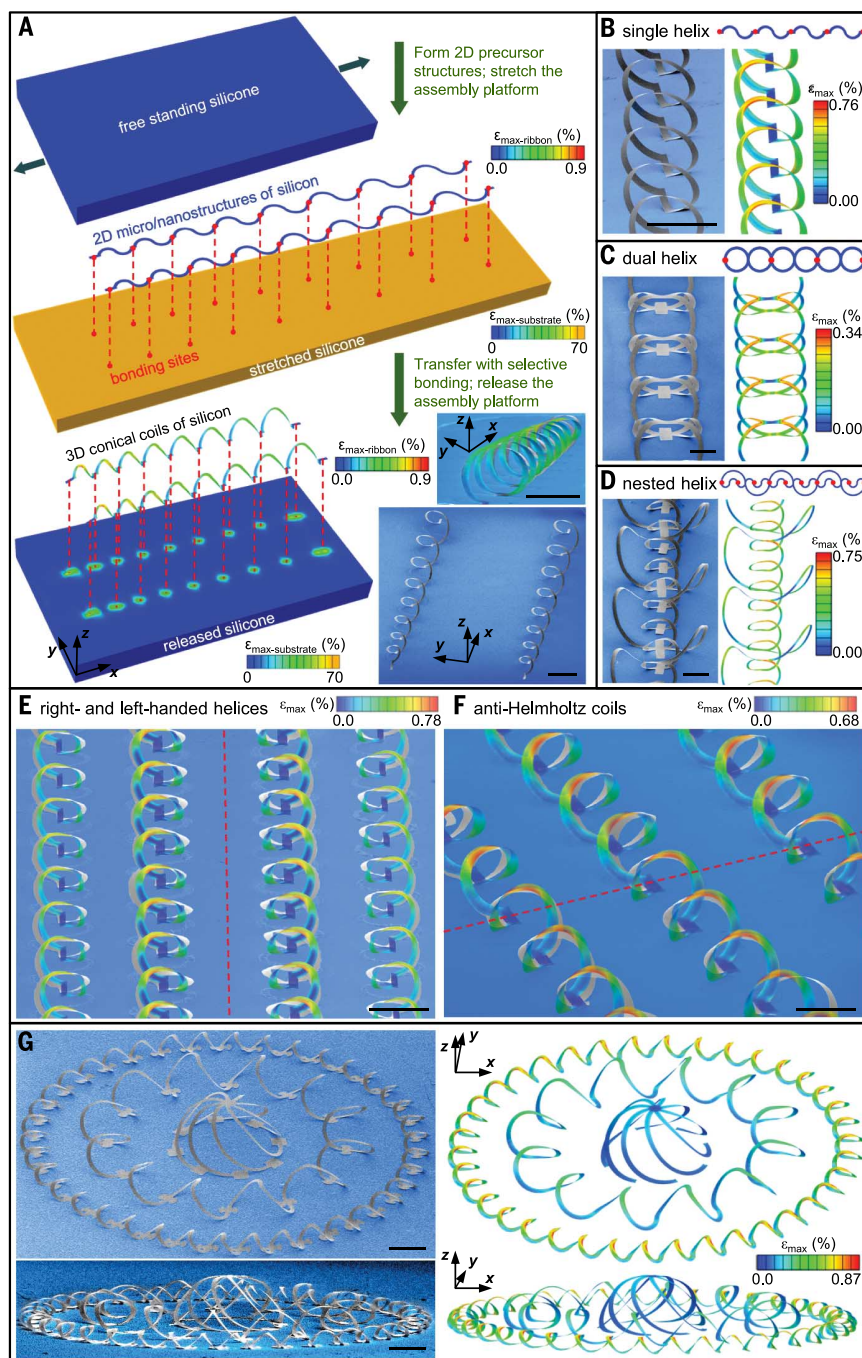


Fig. 1. Process for deterministic assembly of 3D mesostructures of monocrystalline silicon from 2D precursors. (A) Finite-element analysis (FEA) results that correspond to the formation of 3D conical helices from 2D filamentary serpentine ribbons of silicon bonded at selected points (red dots) to a stretched slab of silicone elastomer. Compressive forces induced by relaxing the strain in the elastomer lead to coordinated out-of-plane buckling, twisting, and translational motions in the silicon, yielding 3D mesostructures. The scanning electron microscope (SEM) images at the lower right show an experimental result. (B) Schematic diagram of a 2D silicon precursor and its bonding sites (top), an SEM image of a single-helical coil formed from this precursor (left), and corresponding FEA prediction (right). (C and D) Similar results for a dual-helix coil (C) and a nested, coaxial pair of connected helical coils (D). (E) SEM image with overlaid FEA prediction of helical coils with right- and left-handed chirality, on the left and right sides of the dashed red line, respectively. (F) SEM image with overlaid FEA prediction of structures whose chirality changes abruptly at the locations defined by the dashed red line. (G) SEM images and FEA predictions of a complex 3D mesostructure formed from a 2D precursor that consists of closed-loop circular filamentary serpentes and radially oriented ribbons, selectively bonded to a biaxially stretched elastomer substrate. In all cases, the color in the FEA results corresponds to the maximum principal strains. Scale bars, 400 μm .

elastomer substrate (Dragon Skin; Smooth-On, Easton, PA) that is uniaxially stretched to a large level of prestrain ($\epsilon_{\text{pre}} = \Delta L/L$, where ΔL is the increase in length and is comparable to or larger than L ; $\epsilon_{\text{pre}} \approx 70\%$ for the case shown here) and is then exposed to ozone to generate a uniform coverage of surface hydroxyl groups serves as a platform that guides the mechanical assembly process. Transfer printing of the 2D serpentes onto this surface leads to strong, spatially selective bonding [work of adhesion $>8 \text{ J/m}^2$ (33)] via covalent linkages that form upon contact as a result of condensation reactions at the regions of the silicon that present hydroxyl groups (34, 35). Comparatively weak van der Waals forces dominate interfacial interactions at all other locations [work of adhesion $\sim 0.2 \text{ J/m}^2$ (36)].

Allowing the substrate to return to its original shape induces large compressive forces on the serpentine precursors. Forces above a certain threshold initiate a controlled buckling process that lifts the weakly bonded regions of the serpentes out of contact with the substrate surface and, at the same time, induces spatially dependent deformations (in terms of twisting and bending) and in- and out-of-plane translations. The 3D structures involve a balance between the forces of adhesion to the substrate and the strain energies of the bent, twisted ribbons. The latter (W_{strain}) depends on the elastic modulus (E) and the thickness (t) and lateral dimension (w) of the ribbons via a simple scaling law, $W_{\text{strain}} \propto Ewt^3$. The 3D structures formed by these correlated motions represent self-supporting frameworks that remain tethered to the assembly platform at the covalent bonding sites. This process leaves residual strains in the substrate that are negligible everywhere except for the immediate vicinity of these sites, as well as strains in the silicon that are well below fracture thresholds (Fig. 1A). This mechanically guided, deterministic process of geometric transformation from 2D to 3D is governed by (i) the 2D layout of the precursor materials, their dimensions and mechanical properties; (ii) the pattern of sites for selective bonding; and (iii) the nature and magnitude of the prestrain in the assembly platform. The resulting 3D structures differ qualitatively from surface buckling or wrinkling patterns that can occur in thin films [e.g., (37–39)]. Quantitative analysis captures all of these aspects, as illustrated by the excellent agreement between experiment and computation in Fig. 1A and fig. S1. The coils shown here have eight turns, with a pitch (i.e., dimension along x axis) that varies gradually from $\sim 454 \mu\text{m}$ to $\sim 817 \mu\text{m}$, a width (i.e., dimension along y axis) from $\sim 252 \mu\text{m}$ to $\sim 474 \mu\text{m}$, and a height (i.e., dimension along z axis) from $\sim 240 \mu\text{m}$ to $\sim 459 \mu\text{m}$. The relative differences between the experimentally observed structural geometries and those from FEA predictions are $<8.5\%$. See (33) and figs. S2 and S3 for detailed materials and fabrication procedures.

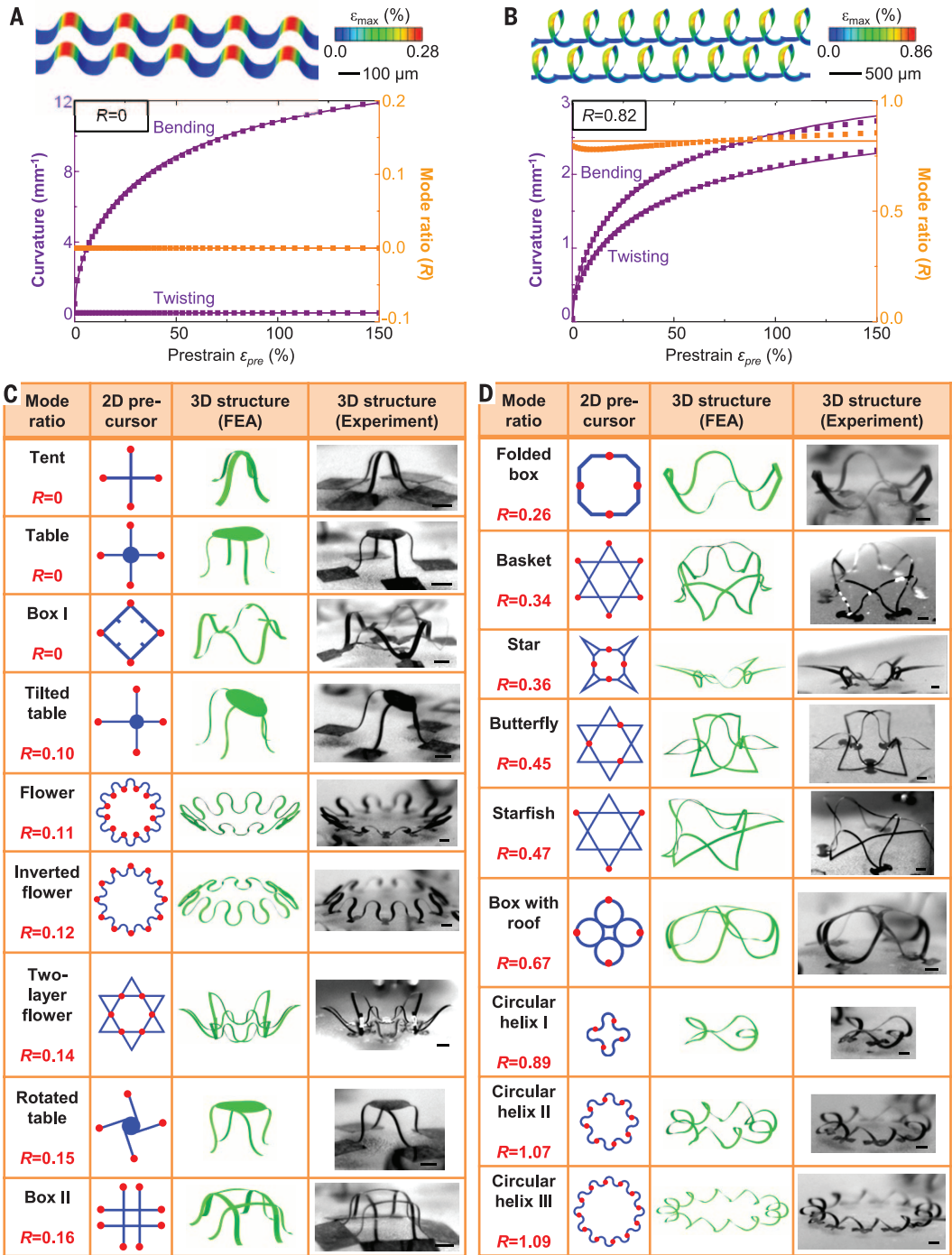
With this scheme, diverse feature sizes and wide-ranging geometries can be realized in many different classes of materials. A simple case related to that in Fig. 1A results from a precursor that

consists of a 2D serpentine ribbon in a spatially invariant periodic geometry (2 μm thick, 50 μm wide; schematic top-view illustration in the upper panel of Fig. 1B). Here, selective bonding to an assembly platform that is strained uniaxially to $\epsilon_{\text{pre}} = 90\%$ yields a uniform, single-helical coil (Fig. 1B). The experimental results are in quantitative agreement with FEA (Fig. 1B and fig. S4) and with analytical parametric equations developed by exploring key characteristics of the deformations (33) (fig. S5). Such models establish the relationship between geometric configurations and ϵ_{pre} , indi-

cating that the heights of the helices increase with ϵ_{pre} while the widths remain largely unchanged, as might be expected. Modifying the structure of the 2D precursor within this theme while changing the distribution of the bonding sites enables access to dual helices (Fig. 1C), nested coaxial structures (Fig. 1D), helices with opposite chirality (Fig. 1E), and even structures whose chirality changes abruptly at selected locations (Fig. 1F). In all of the examples in Fig. 1, the maximum principal strains in the silicon (from $\sim 0.34\%$ to 0.90%) occur at locations of large changes in

curvature. Computational models provide quantitative guidance in the selection of designs that avoid strains at levels that could result in fracture of the constituent materials, localized deformation, or self-contact. For simple cases, some of these guidelines can be captured in analytical forms (33) (fig. S6). In single helices, the maximum strains increase linearly with both the thicknesses and widths of the 2D precursors, with greater sensitivity to the thickness. The assembled structures are not restricted to geometries with axial symmetry. Joining

Fig. 2. Experimental and computational studies of various 3D mesostructures and classification according to their modes of deformation. (A) Average curvature components and mode ratio of a 3D mesostructure (3D wavy ribbon) that involves only bending, as a function of prestrain in the stretched assembly platform. (B) Similar results for a 3D mesostructure (3D single-helical coil) that involves both bending and twisting. Dots represent FEA results; solid lines represent the scaling law $\kappa_{\text{bend}}, \kappa_{\text{twist}} \propto \sqrt{\epsilon_{\text{compr}}}$. The colors in the 3D FEA correspond to the maximum principal strains. (C and D) 2D precursors, mode ratios, optical micrographs, and FEA predictions for 18 3D mesostructures that exhibit bending-dominated modes (C) and bending-twisting mixed modes (D). Scale bars, 200 μm .



closed-form circular 2D serpentine with equally biaxially stretched assembly platforms (fig. S7) yields toroidal coils in isolation, in extended arrays, or in nested configurations. Figure 1G shows an elaborate 3D silicon mesostructure that consists of a concentric pair of toroids, with a separate hemispherical “cage” construct at the center; the corresponding 2D precursor is shown in fig. S8. The remarkably good agreement be-

tween experimental results and FEA predictions for this highly complex architecture provides further evidence of the fidelity of the assembly process and the accuracy of the models. The result is a deterministic route to 3D mesostructures with validated design tools that can assist in the selection of 2D precursor geometries, bonding sites, and stretching configurations for wide-ranging classes of topologies and architectures.

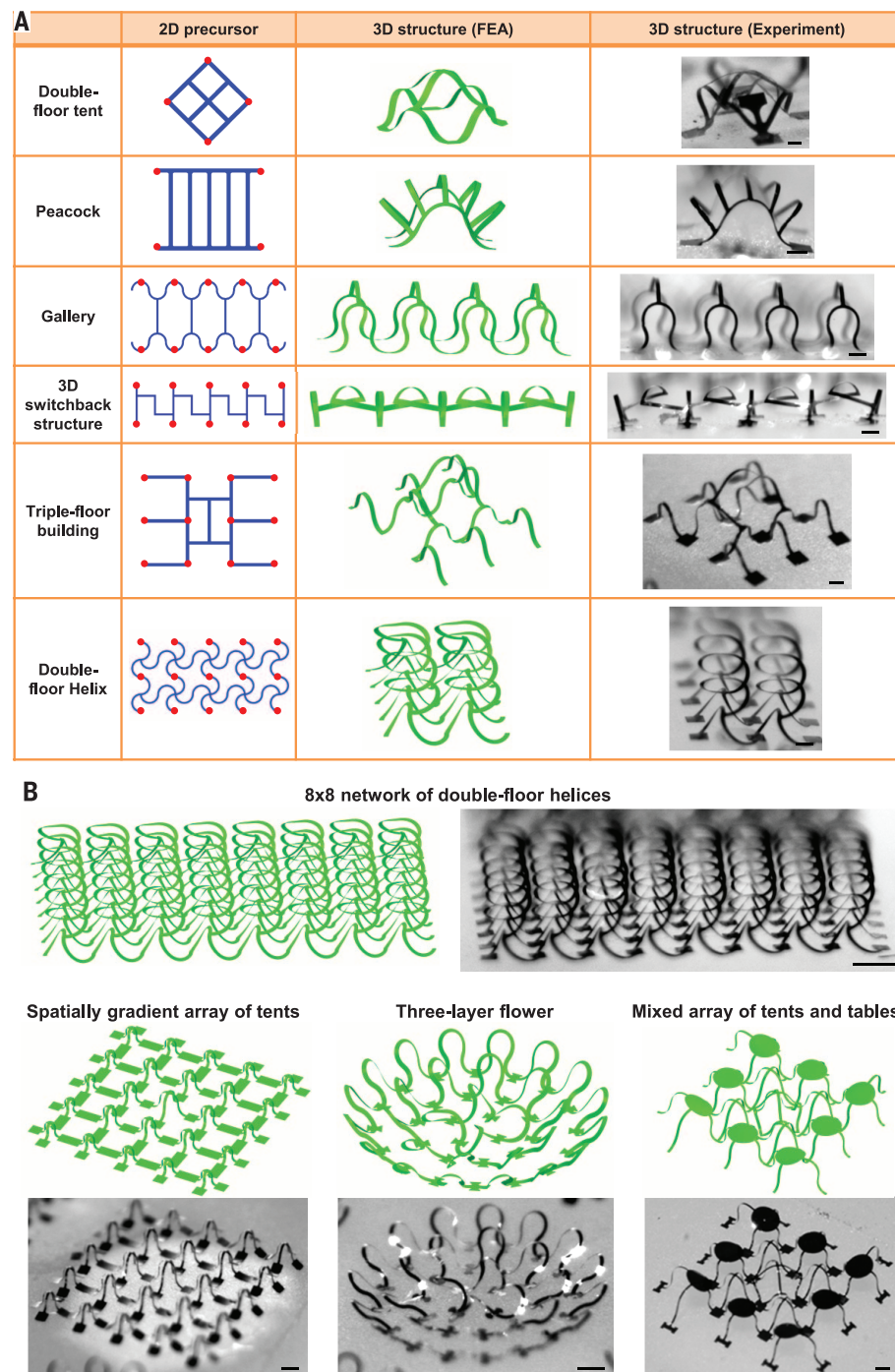


Fig. 3. 3D mesostructures with multilevel configurations and/or extended network architectures. (A) 2D precursors, FEA predictions, and optical micrographs for six 3D mesostructures that have double- or triple-level configurations. (B) Distributed 3D mesoscale networks comprising interconnected collections of the 3D structures in Figs. 2 and 3A. Scale bars, 200 μm (A), 400 μm (B).

Dozens of basic 3D shapes, each identified with a descriptive name, are summarized in Fig. 2. A quantitative classification scheme follows from consideration of the buckling characteristics. In general, motions of ribbon-type precursors (i.e., thickness t much smaller than width w) are dominated by out-of-plane bending and twisting deformations coupled with large-scale translational motion (fig. S9). By comparison, in-plane bending is energetically unfavorable because the corresponding stiffness ($\propto w^3 t$) is much larger than that for out-of-plane bending or twisting ($\propto wt^3$). The magnitudes of bending and twisting deformations can be quantified by evaluating curvatures that are defined using a local coordinate system (fig. S9). The bending and torsional degrees of freedom of these developable ribbons are constrained by the isometric nature of the deformations (i.e., length invariant, as measured along the central axes of the ribbons) associated with formation of the 3D structures.

Buckling always involves considerable bending, whereas the amount of twisting depends strongly on the 2D structural details. One means of classification relies on a quantity, R , defined by the ratio of the average twisting curvature (κ_{twist}) to the average bending curvature (κ_{bend}), which can be determined by FEA (33). A given 3D mesostructure belongs to the bending-dominated mode when R , referred to as the mode ratio, is smaller than a critical value (e.g., 0.2 for the present purposes); otherwise, it belongs to the bending-twisting mixed mode. Representative examples presented in Fig. 2, A and B, fall into these two different regimes: a 3D wavy ribbon ($R = 0$) and a 3D helical coil ($R = 0.82$). The magnitudes of both κ_{twist} and κ_{bend} increase with compressive strain (ϵ_{compr}) applied to the 2D precursor, where $\epsilon_{\text{compr}} = \epsilon_{\text{pre}} / (1 + \epsilon_{\text{pre}})$. Quantitative analyses show that both curvature components scale with the square root of ϵ_{compr} , thereby suggesting that R is independent of the compression level. This finding applies to all of the 3D mesostructures examined here, obtained with a diverse set of topologies and formed on assembly platforms with uniaxial as well as biaxial strains (Fig. 2, A and B, and figs. S10 and S11).

The layout of the 2D precursor and the configuration of the bonding sites both play crucial roles in determining the final 3D geometry (Fig. 2, C and D). With the same 2D precursor (e.g., the circular serpentine pattern or Kagome lattice), different distributions of bonding sites yield different 3D configurations, with widely varying values of R . By comparison to these two factors, the cross-sectional dimensions (i.e., w and t) of the precursor have minor effect. For 3D mesostructures that exhibit a bending-dominated mode (e.g., the flower and two-layer flower of Fig. 2C), R is insensitive to changes in the width or thickness (fig. S12). For bending-twisting mixed modes (e.g., straight helix in Fig. 1B and circular helix III in Fig. 2D), the width and thickness can lead to changes in R , but with magnitudes insufficient to induce a transition into the bending-dominated mode.

Multiple, hierarchical scales of buckling are also possible with the appropriate choice of design.

Examples of 3D mesostructures that have multi-level constructions in the out-of-plane direction are presented in Fig. 3A. Such layouts can be achieved by adding filamentary ribbons to 2D precursors that yield single-level 3D shapes like those of Fig. 2. In the most extreme examples, these additional ribbons connect the precursor structures together at regions where the assembly process would otherwise yield the maximum out-of-plane displacements. Upon release of strain in the assembly platform, these ribbons—such as those that form the cross in the double-floor tent structure, the array of vertical ribbons in the peacock and gallery structures, or the horizontally aligned serpentine ribbons in the double-floor helix structure—undergo an additional level of buckling to form an elevated “second floor” suspended above the reach of buckling that represents the “first floor.” This process substantially extends the maximum elevation above the substrate, thereby enhancing the 3D nature of the system. The triple-floor building structure provides a specific example. Here, the maximum out-of-plane displacement is ~ 1 mm for assembly using a biaxial prestrain of $\sim 100\%$. This distance is up to ~ 2 times the maximum in-plane extent along the narrow dimension of the central part of the supporting structure.

The 3D mesostructures shown in Figs. 2 and 3A can be viewed as building blocks to yield large-scale, interconnected 3D mesoscale networks. The examples in Fig. 3B follow from repeating, mixing, joining, and/or nesting of these building blocks. The top frame shows an 8×8 array of the double-floor helix structure that consists of eight evenly spaced helices on the first floor and another eight helices, with the axial direction rotated by 90° , on the second floor (fig. S13). The lower left panel of Fig. 3B illustrates a 5×5 array of the 3D tent structure with a spatial gradient in the height, such that the largest tent appears at the center and smaller ones reside at the outermost peripheral regions. To its right is a dual, nested 3D flower structure with a fourfold symmetric toroid at the center. The rightmost example corresponds to a mixed array consisting of four regular table structures, four tilted tables, four tents, and one double-floor tent at the center. Some other 3D mesostructures (e.g., raised ring, scaffold, toroid inside a flower, nested box, etc.) appear in fig. S14. These networks exhibit geometries that agree quantitatively with FEA predictions. An important point is that all 3D mesostructures—even those with the highest complexity and largest extent in the out-of-plane direction—are deterministic and form consistently into unique geometries because the strain energies of the first-order buckling modes (i.e., energetically the most probable configuration) are lower than those of all other modes by approximately a factor of 2 or more (fig. S15).

Summarized in Fig. 4A and fig. S16 are results that illustrate the applicability of this assembly approach to additional classes of materials, including metals (e.g., Ni), dielectrics (e.g., polyimide and epoxy), and patterned combinations

of these, in polycrystalline and amorphous forms. Submicrometer features are also possible, as demonstrated in a “starfish” framework that incorporates silicon ribbons with widths of 800 nm and thicknesses of 100 nm (Fig. 4B). Two more examples of submicrometer features are provided in fig. S17. Here, the large differences in contact areas between the filaments and the bonding sites provide the necessary contrast in adhesion. The same strategy also enables the assembly of micrometer-sized 3D silicon features with ribbon widths of $3 \mu\text{m}$ and thicknesses of 300 nm (fig. S18). In these and all

other cases, mechanical strain applied to the assembly platforms can affect reversible, controlled changes in the geometries of the supported structures, thereby providing tunable 3D configurations. The results in Fig. 4C show top and angled views of the influence of uniaxial tensile deformation (50%) on a structure with a variant of the starfish layout, in which all six tip corners serve as sites for bonding. Overlaid FEA results exhibit quantitative agreement with the observed geometries. Results in fig. S19 demonstrate that the 3D mesostructures are bendable and can be placed on curved surfaces.

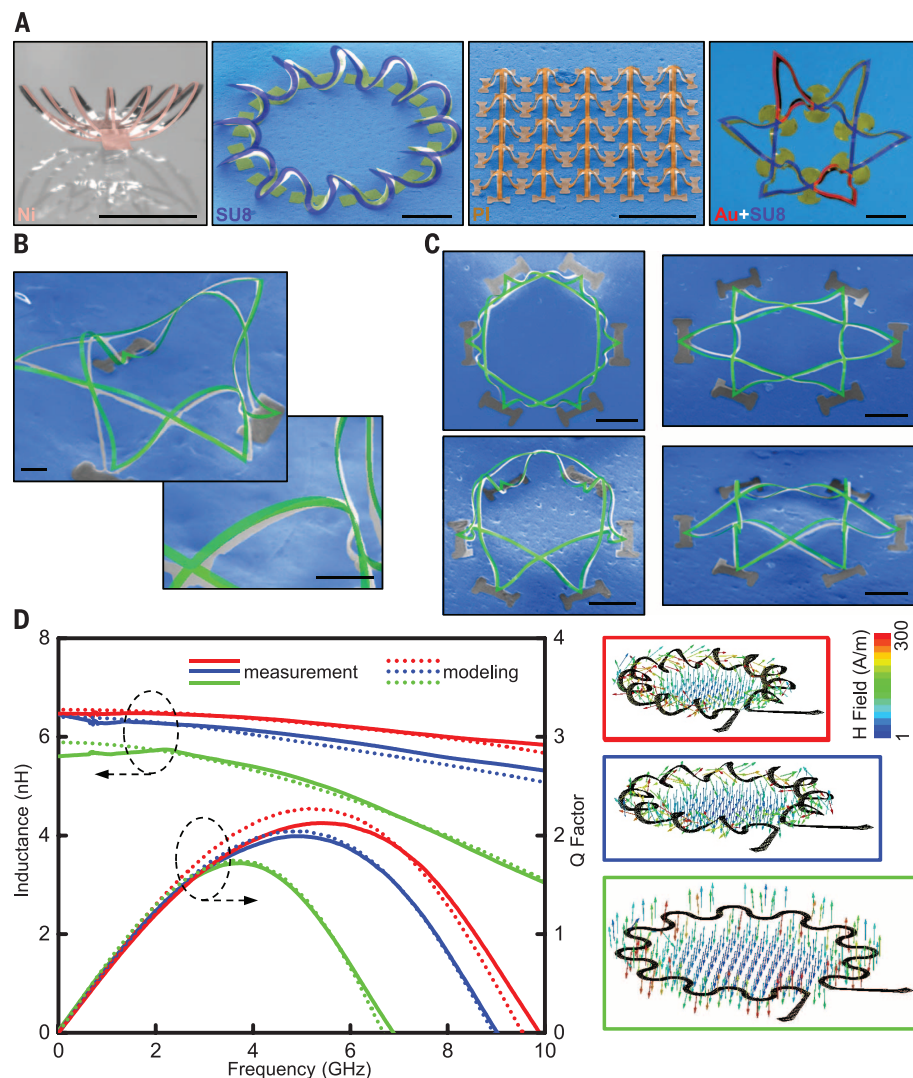


Fig. 4. 3D structures with various material compositions and feature sizes, and results for electrical behaviors in a tunable 3D toroidal inductor. (A) Experimental images and overlaid FEA predictions of 3D mesostructures made of metal (Ni), polymer [photodefinable epoxy (SU8) and polyimide (PI)], and heterogeneous combinations of materials (Au and SU8). Scale bars, 500 μm . (B) 3D mesostructures of silicon with lateral dimensions and thicknesses in the submicrometer regime, with overlaid FEA predictions. Scale bars, 5 μm . (C) 3D mesostructure of silicon in its as-fabricated state (left column) and in a configuration that results from uniaxially stretching the substrate (right column), all with overlaid FEA predictions. Scale bars, 50 μm . (D) Measured and computed frequency dependence of the inductance and the Q factor of a single 3D toroidal inductor mechanically configured into two different shapes by partial (21%, in an absolute sense, of an original prestrain of 54%; blue) and then complete release of prestrain (red), along with the corresponding 2D precursor (green) as reference. The panels on the right show simulated magnetic field distributions of these structures for feed-in power of 1 W. The arrows indicate direction and their colors indicate magnitude.

The ability to naturally integrate state-of-the-art electronic materials and devices represents an essential, defining characteristic of these approaches. A mechanically tunable inductor based on a 3D toroidal structure with feed and ground lines, all constructed with polyimide encapsulation (1.2 μm) and Ni conducting layers (400 nm), provides an example. Here, the geometry is similar to the “circular helix III” in Fig. 2D, with the addition of contact pads located at the periphery for electrical probing. The graph of Fig. 4D shows measurements and modeling results for the frequency dependence of the inductance and the quality (Q) factor for a 2D closed-loop serpentine precursor and a single 3D toroid structure in two different mechanically adjusted configurations. In both cases, the 3D cage structure enhances the mutual inductance between adjacent twisted turns. The maximum Q factors and resonant frequencies increase systematically from 1.7 to 2.2 GHz and from 6.8 to 9.5 GHz, respectively, as the structure transforms from 2D to two distinct 3D shapes associated with partial release (about half of the total initial prestrain of 54%) and then complete release of the prestrain. These trends arise from a systematic reduction in substrate parasitic capacitance with increasing three-dimensional character (40). The measured results correspond well to modeling that involves computation of the electromagnetic properties associated with the predicted 3D structure geometries from FEA, as shown in the right panels of Fig. 4D [see (33) and figs. S20 to S23].

The ideas presented here combine precise, lithographic control of the thicknesses, widths, and layouts of 2D structures with patterned sites of adhesion to the surfaces of high-elongation elastomer substrates to enable rapid assembly of broad classes of 3D mesostructures of relevance to diverse microsystem technologies. The process, which can be implemented with any substrate that is capable of controlled, large-scale dimensional change, expands and complements the capabilities of other approaches in 3D materials assembly. Compatibility with the most advanced materials (e.g., monocrystalline inorganics), fabrication methods (e.g., photolithography), and processing techniques (e.g., etching, deposition) that are available in the semiconductor and photonics industries suggest many possibilities for achieving sophisticated classes of 3D electronic, optoelectronic, and electromagnetic devices.

REFERENCES AND NOTES

- V. B. Shenoy, D. H. Gracias, *MRS Bull.* **37**, 847–854 (2012).
- F. Li, D. P. Josephson, A. Stein, *Angew. Chem. Int. Ed.* **50**, 360–388 (2011).
- N. B. Crane, O. Onen, J. Carballo, Q. Ni, R. Guldiken, *Microfluid. Nanofluid.* **14**, 383–419 (2013).
- J. H. Jang et al., *Adv. Funct. Mater.* **17**, 3027–3041 (2007).
- J. Fischer, M. Wegener, *Laser Photonics Rev.* **7**, 22–44 (2013).
- K. A. Arpin et al., *Adv. Mater.* **22**, 1084–1101 (2010).
- W. L. Noorduin, A. Grinthal, L. Mahadevan, J. Aizenberg, *Science* **340**, 832–837 (2013).
- P. X. Gao et al., *Science* **309**, 1700–1704 (2005).
- M. Huang, F. Cavallo, F. Liu, M. G. Lagally, *Nanoscale* **3**, 96–120 (2011).
- B. Tian et al., *Nat. Mater.* **11**, 986–994 (2012).
- T. G. Leong et al., *Proc. Natl. Acad. Sci. U.S.A.* **106**, 703–708 (2009).
- M. Yu et al., *ACS Nano* **5**, 2447–2457 (2011).
- D. Bishop, F. Pardo, C. Bolle, R. Giles, V. Aksyuk, *J. Low Temp. Phys.* **169**, 386–399 (2012).
- R. J. Wood, *Am. Sci.* **102**, 124–131 (2014).
- R. Songmuang, A. Rastelli, S. Mendach, O. G. Schmidt, *Appl. Phys. Lett.* **90**, 091905 (2007).
- J. H. Lee et al., *Adv. Mater.* **26**, 532–569 (2014).
- M. Schumann, T. Buckmann, N. Gruhler, M. Wegener, W. Pernice, *Light Sci. Appl.* **3**, e175 (2014).
- X. Zheng et al., *Science* **344**, 1373–1377 (2014).
- T. A. Schaedler et al., *Science* **334**, 962–965 (2011).
- C. M. Soukoulis, M. Wegener, *Nat. Photonics* **5**, 523–530 (2011).
- J. H. Cho et al., *Small* **7**, 1943–1948 (2011).
- B. Y. Ahn et al., *Science* **323**, 1590–1593 (2009).
- W. Huang et al., *Nano Lett.* **12**, 6283–6288 (2012).
- H. Zhang, X. Yu, P. V. Braun, *Nat. Nanotechnol.* **6**, 277–281 (2011).
- K. Sun et al., *Adv. Mater.* **25**, 4539–4543 (2013).
- W. Zheng, H. O. Jacobs, *Adv. Funct. Mater.* **15**, 732–738 (2005).
- X. Guo et al., *Proc. Natl. Acad. Sci. U.S.A.* **106**, 20149–20154 (2009).
- V. Y. Prinz et al., *Physica E* **6**, 828–831 (2000).
- O. G. Schmidt, K. Eberl, *Nature* **410**, 168–168 (2001).
- L. Zhang et al., *Microelectron. Eng.* **83**, 1237–1240 (2006).
- G. Hwang et al., *Nano Lett.* **9**, 554–561 (2009).
- W. Gao et al., *Nano Lett.* **14**, 305–310 (2014).
- See supplementary materials on Science Online.
- D. C. Duffy, J. C. McDonald, O. J. A. Schueller, G. M. Whitesides, *Anal. Chem.* **70**, 4974–4984 (1998).
- Y. Sun, W. M. Choi, H. Jiang, Y. Y. Huang, J. A. Rogers, *Nat. Nanotechnol.* **1**, 201–207 (2006).
- D. H. Kim et al., *Science* **333**, 838–843 (2011).
- S. Yang, K. Khare, P. C. Lin, *Adv. Funct. Mater.* **20**, 2550–2564 (2010).
- S. Singamaneni, V. V. Tsukruk, *Soft Matter* **6**, 5681–5692 (2010).
- D. H. Kim, N. S. Lu, Y. G. Huang, J. A. Rogers, *MRS Bull.* **37**, 226–235 (2012).
- C. P. Yue, S. S. Wong, *IEEE Trans. Electron. Dev.* **47**, 560–568 (2000).

ACKNOWLEDGMENTS

Supported by the U.S. Department of Energy, Office of Science, Basic Energy Sciences, under award DE-FG02-07ER46741. We thank S. B. Gong for providing the RF testing equipment in this study, and K. W. Nan, H. Z. Si, J. Mabon, J. H. Lee, Y. M. Song, and S. Xiang for technical support and stimulating discussions. Full data are in the supplementary materials.

SUPPLEMENTARY MATERIALS

www.sciencemag.org/content/347/6218/154/suppl/DC1
Materials and Methods
Supplementary Text
Figs. S1 to S23

7 September 2014; accepted 17 November 2014
10.1126/science.1260960

BIOMATERIALS

Electronic dura mater for long-term multimodal neural interfaces

Ivan R. Mineev,^{1*} Pavel Musienko,^{2,3*} Arthur Hirsch,¹ Quentin Barraud,² Nikolaus Wenger,² Eduardo Martin Moraud,⁴ Jérôme Gandar,² Marco Capogrosso,⁴ Tomislav Milekovic,² Léonie Asboth,² Rafael Fajardo Torres,² Nicolas Vachicouras,^{1,2} Qihan Liu,⁵ Natalia Pavlova,^{2,3} Simone Duis,² Alexandre Larmagnac,⁶ Janos Vörös,⁶ Silvestro Micera,^{4,7} Zhigang Suo,⁵ Grégoire Courtine,^{2,†} Stéphanie P. Lacour^{1,†}

The mechanical mismatch between soft neural tissues and stiff neural implants hinders the long-term performance of implantable neuroprostheses. Here, we designed and fabricated soft neural implants with the shape and elasticity of dura mater, the protective membrane of the brain and spinal cord. The electronic dura mater, which we call e-dura, embeds interconnects, electrodes, and chemotrodes that sustain millions of mechanical stretch cycles, electrical stimulation pulses, and chemical injections. These integrated modalities enable multiple neuroprosthetic applications. The soft implants extracted cortical states in freely behaving animals for brain-machine interface and delivered electrochemical spinal neuromodulation that restored locomotion after paralyzing spinal cord injury.

Implantable neuroprostheses are engineered systems designed to study and treat the injured nervous system. Cochlear implants restore hearing in deaf children, deep brain stimulation alleviates Parkinsonian symptoms, and spinal cord neuromodulation attenuates chronic neuropathic pain (1). New methods for recording and modulation of neural activity using electrical, chemical, and/or optical modalities open promising therapeutic perspectives for neuroprosthetic treatments. These advances have triggered the development of myriad neural technologies to design multimodal neural implants (2–5). However, the conversion of these sophisticated technologies into implants mediating long-lasting therapeutic benefits has yet to be achieved. A recurring challenge restricting long-term biointegration is the substantial biomechanical mismatch between implants and neural tissues (6–8).

Neural tissues are viscoelastic (9, 10) with elastic and shear moduli in the 100- to 1500-kPa range. They are mechanically heterogeneous (11, 12) and endure constant body dynamics (13, 14). In contrast, most electrode implants—even thin, plastic interfaces—present high elastic moduli in the gigapascal range, thus are rigid compared to neural tissues (3, 15). Consequently, their surgical insertion triggers both acute and long-term tissue responses (6–8, 14). Here, we tested the hypothesis that neural implants with mechanical properties matching the statics and dynamics of host tissues will display long-term biointegration and functionality within the brain and spinal cord.

We designed and engineered soft neural interfaces that mimic the shape and mechanical behavior of the dura mater (Fig. 1, A and B, and fig. S1). The implant, which we called electronic dura mater or e-dura, integrates a transparent silicone

substrate (120 μm in thickness), stretchable gold interconnects (35 nm in thickness), soft electrodes coated with a platinum-silicone composite (300 μm in diameter), and a compliant fluidic microchannel (100 μm by 50 μm in cross section) (Fig. 1, C and D, and figs. S2 to S4). The interconnects and electrodes transmit electrical excitation and transfer electrophysiological signals. The microfluidic channel, termed chemotrode (16), delivers drugs locally (Fig. 1C and fig. S4). The substrate, encapsulation, and microchannel silicone layers are prepared with soft lithography and assembled by covalent bonding following oxygen plasma activation (Fig. 1D and fig. S2). Interconnects are thermally evaporated through a stencil mask, whereas electrodes are coated with the soft composite by screen-printing (fig. S2). Microcracks in the gold interconnects (17) and soft platinum-silicone composite electrodes confer exceptional stretchability to the entire implant (Fig. 1D and movie S1).

Most implants used experimentally or clinically to assess and treat neurological disorders are placed above the dura mater (15, 18–20). The compliance of the soft implant enables surgical insertion below the dura mater through a small opening (Fig. 1, A and C, and fig. S5). This location provides an intimate interface between electrodes and targeted neural tissues (Fig. 1E) and allows direct delivery of drugs into the intrathecal space. To illustrate these properties, we fabricated implants tailored to the spinal cord, one of the most demanding environments of the central nervous system. We developed a vertebral orthosis to secure the connector (Fig. 1F) and dedicated surgical procedures for subdural implantation (fig. S5). The soft implant smoothly integrated the subdural space along the entire extent of lumbosacral segments (2.5 cm in length and 0.3 cm in width), conforming to the delicate spinal neural tissue (Fig. 1, E and F).

We next tested the long-term biointegration of soft implants compared to stiff, plastic implants (6 weeks of implantation). A stiff implant was fabricated by means of a 25- μm -thick polyimide film, which corresponds to standard practices for flexible neural implants (27) and is robust enough to withstand the surgical procedure. Both types of implants were inserted into the subdural space of lumbosacral segments in healthy rats. A sham-operated group of animals received the headstage,

connector, and vertebral orthosis but without spinal implant.

To assess motor performance, we obtained high-resolution kinematic recordings of whole-body movement during basic walking and skilled locomotion across a horizontal ladder. In the chronic stages, the behavior of rats with soft implants was indistinguishable from that of sham-operated animals (Fig. 2A, fig. S6, and movie S2). By contrast, rats with stiff implants displayed significant motor deficits that emerged around 1 to 2 weeks after implantation and deteriorated over time. They failed to accurately position their

paws onto the rungs of the ladder (Fig. 2A). Even during basic walking, rats with stiff implants showed pronounced gait impairments, including altered foot control, reduced leg movement, and postural imbalance (fig. S6).

The spinal cords were explanted after 6 weeks of implantation. Both soft and stiff implants occupied the targeted location within the subdural space. Minimal connective tissue was observed around the implants. To evaluate potential macroscopic damage to the spinal cord that may explain motor deficits, we reconstructed the explanted lumbosacral segments in three dimensions. A

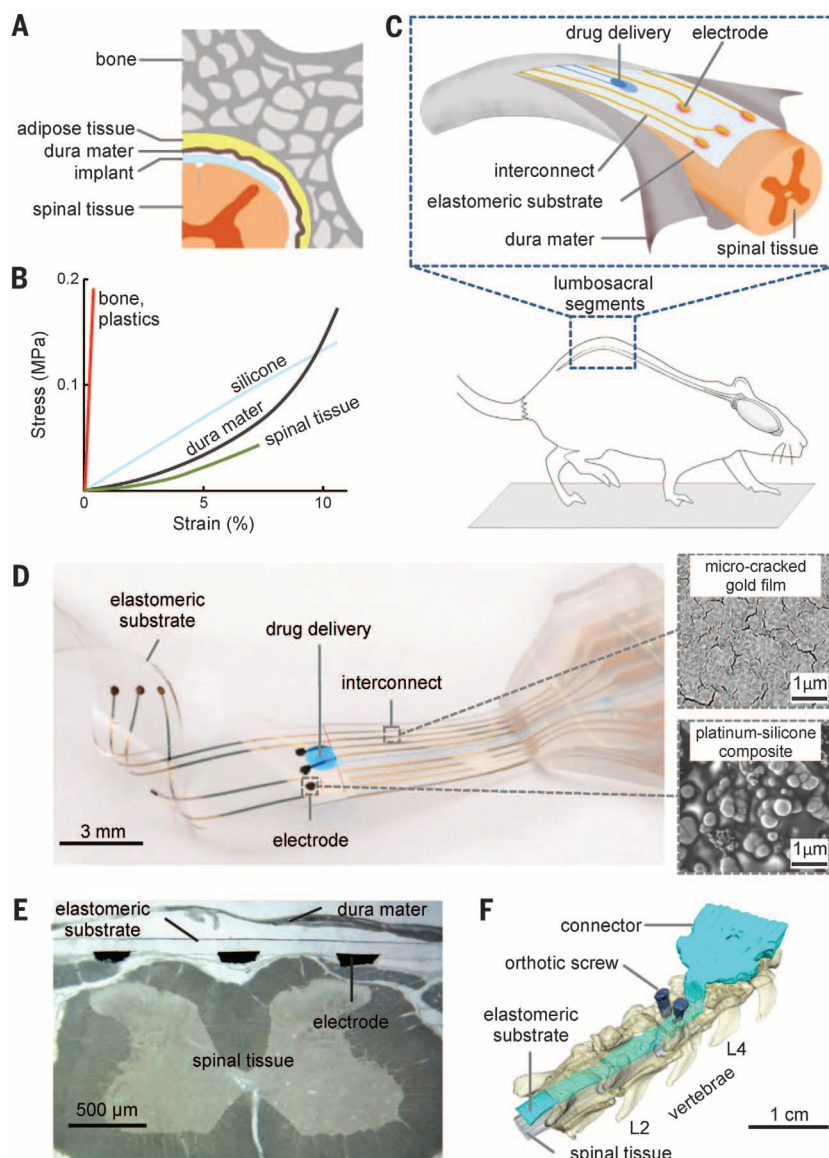


Fig. 1. Electronic dura mater, “e-dura,” tailored for the spinal cord. (A) Schematic cross section of the vertebral column with the soft implant inserted in the spinal subdural space. (B) Strain-stress curves of spinal tissues, dura mater, and implant materials. Plastics (polyimide), silicone, and dura mater responses are experimental data. Spinal tissue response is adapted from the literature (see supplementary materials). (C) Illustration of the e-dura implant inserted in the spinal subdural space of rats. (D) Optical image of an implant, and scanning electron micrographs of the gold film and the platinum-silicone composite. (E) Cross-section of an e-dura inserted for 6 weeks in the spinal subdural space. (F) Reconstructed 3D micro-computed tomography scans of the e-dura inserted in the spinal subdural space covering L2 to S1 spinal segments in rats. The scan was obtained in vivo at week 5 after implantation.

¹Bertarelli Foundation Chair in Neuroprosthetic Technology, Laboratory for Soft Bioelectronic Interfaces, Centre for Neuroprosthetics, Institute of Microengineering and Institute of Bioengineering, Ecole Polytechnique Fédérale de Lausanne (EPFL), Switzerland. ²International Paraplegic Foundation Chair in Spinal Cord Repair, Centre for Neuroprosthetics and Brain Mind Institute, EPFL, Switzerland. ³Pavlov Institute of Physiology, St. Petersburg, Russia. ⁴Translational Neural Engineering Laboratory, Centre for Neuroprosthetics and Institute of Bioengineering, EPFL, Lausanne, Switzerland. ⁵School of Engineering and Applied Sciences, Kavli Institute for Bionano Science and Technology, Harvard University, Cambridge, MA, USA. ⁶Laboratory for Biosensors and Bioelectronics, Institute for Biomedical Engineering, University and ETH Zurich, Switzerland. ⁷The BioRobotics Institute, Scuola Superiore Sant’Anna, Pisa 56025, Italy. *These authors contributed equally to this work. †These authors contributed equally to this work. ‡Corresponding author. E-mail: gregoire.courtine@epfl.ch (G.C.); stephanie.lacour@epfl.ch (S.P.L.)

cross-sectional circularity index was calculated to quantify changes in shape. All the rats with stiff implants displayed significant deformation of spinal segments under the implant ($P < 0.05$, Fig. 2B), ranging from moderate to extreme compression (fig. S7 and movie S2).

Neuroinflammatory responses at chronic stages were visualized with antibodies against activated astrocytes and microglia (Fig. 2C), two standard cellular markers for foreign-body reaction (7). As anticipated from macroscopic damage, both cell types massively accumulated in the vicinity of stiff implants ($P < 0.05$; Fig. 2C and fig. S8). In marked contrast, no significant difference was found between rats with soft implants and sham-operated animals (Fig. 2C and fig. S8). These results demonstrate the long-term biocompatibility of the soft implants.

We manufactured a model of spinal cord using a hydrogel core to simulate spinal tissues and a

silicone tube to simulate the dura mater (fig. S9A). A soft or stiff implant was inserted into the model (Fig. 2D). The stiff implant induced a pronounced flattening of the simulated spinal cord, whereas the soft implant did not alter the circularity of the model (Fig. 2D and fig. S10). To provide the model with realistic metrics, we quantified the natural flexure of the spine in freely moving rats (fig. S9B). When the model was bent, the stiff implant formed wrinkles that induced local compressions along the hydrogel core. In contrast, the soft implant did not affect the smoothness of simulated spinal tissues (fig. S11). When the model was stretched, the stiff implant slid relative to the hydrogel core, whereas the soft implant elongated together with the entire spinal cord (Fig. 2D and fig. S11). Reducing the thickness of the plastic implant to 2.5 μm improved bending stiffness and conformability. However, the ultrathin, plastic implant still failed to

deform during motion of the soft tissue (fig. S10 and supplementary text).

Patterning extremely thin films into web-like systems offers alternative mechanical designs for elastic surfaces (22–24). For example, fractal-like meshes develop into out-of-plane structures during mechanical loading, which facilitates reversible and local compliance. Medical devices prepared with such three-dimensional (3D) topologies can conform the curvilinear surface of the heart (25) and skin (23). However, this type of interface requires complex, multistep processing and transient packaging. In comparison, fabrication steps of e-dura are remarkably simple. Moreover, the shape and unusual resilience of the soft implant greatly facilitate surgical procedures.

The composite electrodes of the soft implant displayed low impedance ($Z = 5.2 \pm 0.8$ kilohm at 1 kHz, $n = 28$ electrodes) and maintained the electrochemical characteristics of platinum (Fig. 3,

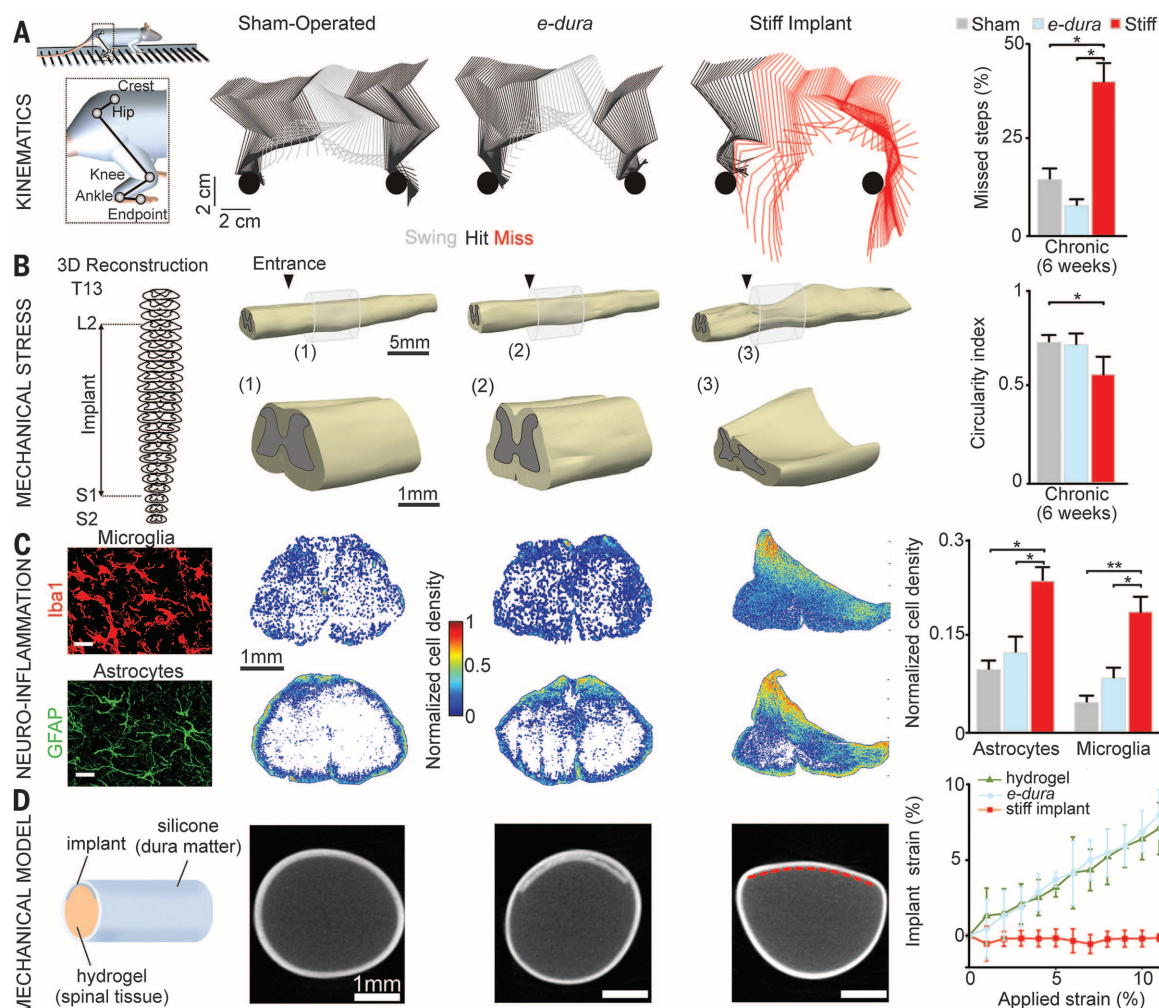


Fig. 2. Biointegration. (A) Hindlimb kinematics during ladder walking 6 weeks after implantation. Bar plots reporting mean percentage of missed steps averaged per animal onto the rungs of the ladder ($n = 8$ trials per rat, $n = 4$ rats per group). (B) 3D spinal cord reconstructions, including enhanced views, 6 weeks after implantation. The arrowheads indicate the entrance of the implant into the subdural space. Bar plots reporting mean values of spinal cord circularity index ($4\pi \times \text{area}/\text{perimeter}^2$). (C) Photographs showing microglia (Iba1) and astrocytes (GFAP, glial fibrillary acidic protein) staining

reflecting neuroinflammation. Scale bars: 30 μm . Heat maps and bar plots showing normalized astrocyte and microglia density. (D) Spinal cord model scanned using micro-computed tomography without and with a soft or stiff implant. e-dura implant is 120 μm thick. The red line materializes the stiff implant (25 μm thick), not visualized because of scanner resolution. Plot reporting local longitudinal strain as a function of global applied strain. Statistical test: Kruskal-Wallis one-way analysis of variance (* $P < 0.05$; ** $P < 0.01$. Error bars: SEM).

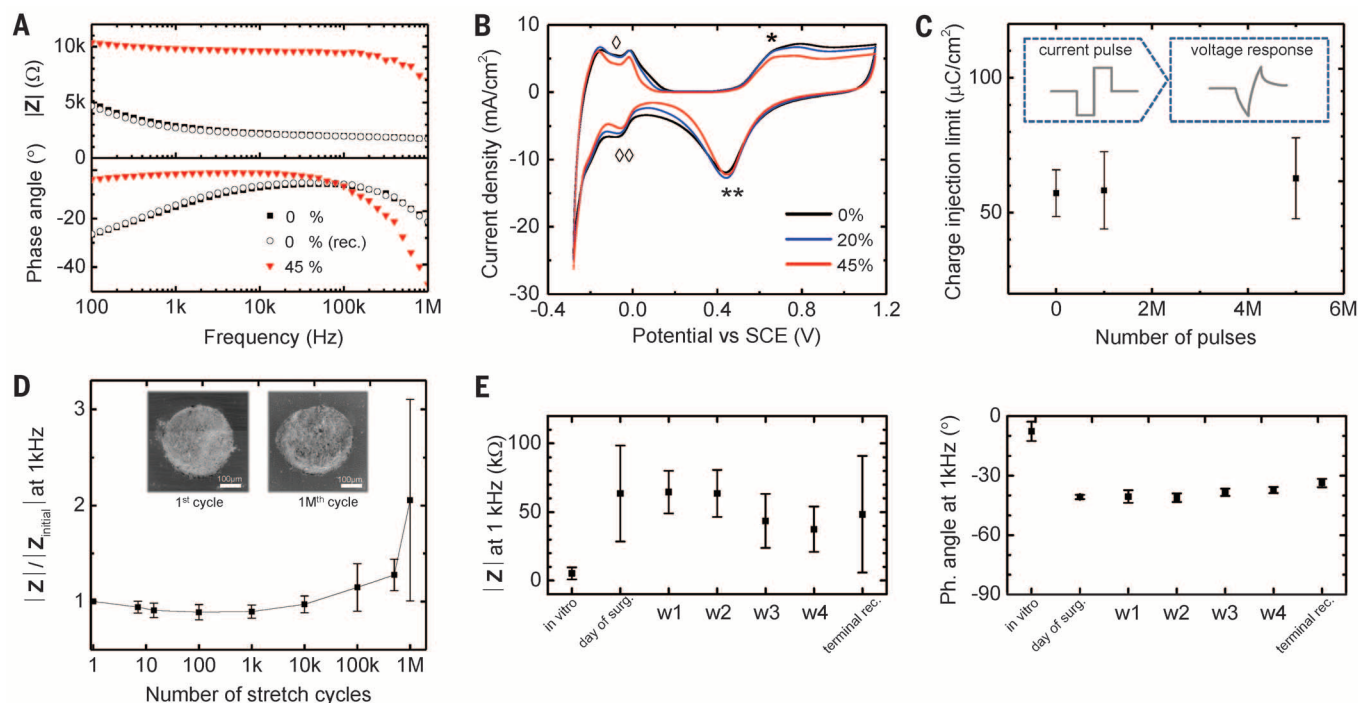


Fig. 3. Properties of e-dura electrodes. (A) Magnitude and phase of electrode impedance recorded in saline solution (pH 7.4). Spectra were collected before (■), at maximum elongation (▼), and after (○) a uniaxial stretch cycle to 45% strain. (B) Cyclic voltammograms recorded in diluted sulfuric acid (pH 0.9) during a uniaxial stretch cycle to 45% strain. Cyclic voltammetry (50 mV/s) reveals high current densities through the electrode even at large strain. Peaks correspond to oxide formation (*), oxide reduction (**), H⁺ adsorption (◇), and

H⁺ desorption (◇) on Pt metal surfaces. (C) Charge injection limit of electrodes ($n = 4$, mean \pm SD) and evolution after repeated pulsing. (D) Relative impedance modulus of electrodes ($n = 7$, mean \pm SD) at 1 kHz and at rest and after uniaxial fatigue cycling to 20% strain. Inset: scanning electron micrographs of an electrode after the first and one millionth stretch cycles. (E) Modulus and phase at 1 kHz ($n = 28$ total electrodes, mean \pm SD, across four rats) recorded in vitro, then in vivo immediately after implantation and weekly until terminal procedure.

A and B). Cyclic voltammograms of the composite electrodes remained unchanged when the implant was stretched up to a strain of 45%. The high effective surface area of the platinum-silicone composite produced a large cathodal charge storage capacity of 46.9 ± 3.3 mC/cm². This value is two orders of magnitude higher than that of smooth platinum (26) and is smaller but comparable to that of highly doped organic electrode coatings (27). The composite electrode supported a charge injection limit of 57 ± 9 μC/cm², which is comparable to the injection limit of platinum (26) (Fig. 3C and fig. S12). These characteristics remained stable even after 5 million electrical pulses, which corresponds to more than 30 hours of continuous stimulation with clinically relevant parameters (40 Hz, charge-balanced, biphasic, 100-μA current pulse, 0.2-ms pulse width).

To demonstrate the robustness of the soft implant against deformation experienced by natural dura mater during daily living activities, we stretched the device to 20% strain over 1 million cycles. The implant, the chemotrode, and the seven embedded electrodes withstood the cyclic deformation, displaying minimal variation in impedance over time (Fig. 3D, figs. S13 and S14, and movie S1). Assuming radical postural changes approximately every 5 min, these results indicate that the soft implant would survive mechanically for nearly a decade in a patient.

Electrode impedance and chemotrode functionality were evaluated over 5 weeks in four rats

($n = 28$ electrodes and 4 chemotrodes in total). Impedance at 1 kHz remained constant throughout the 5 weeks of implantation (Fig. 3E), demonstrating stability of stretchable electrodes in vivo. Daily injections of drugs and hydrodynamic evaluations of microfluidic channels after explantation (fig. S4) confirmed that the chemotrodes remain operational for extended durations in vivo.

These combined results demonstrate electrochemical stability, mechanical robustness, and long-term functionality of the soft electrodes and chemotrodes, fulfilling the challenging requirements for long-term implantation.

We exploited the soft neurotechnology to tailor electronic dura mater for the brain and spinal cord. An e-dura, consisting of a 3×3 electrode array, was placed over the motor cortex of mice expressing the light-sensitive channel channelrhodopsin-2 in the majority of neurons (Fig. 4A). The silicone substrate is optically transparent, enabling concurrent optical stimulation and neural recording. The cortical surface was illuminated with a laser focused on distinct locations to activate neurons locally. The spatial resolution of electrocorticograms recorded from the e-dura allowed extraction of neuronal activation maps that were specific for each site of stimulation (Fig. 4A).

An e-dura was then inserted between the dura mater and motor cortex tissues (fig. S5) to record electrocorticograms in conjunction with whole-body kinematic, and leg muscle activity in freely moving rats (Fig. 4B). Power spectral density analy-

sis applied on electrocorticograms (28) identified standing and locomotor states over several weeks of recordings (Fig. 4B and fig. S15). To verify whether neural recordings could also be obtained from an e-dura chronically implanted over spinal tissues, we measured electrospinalgrams in response to electrical stimulation of the motor cortex or the sciatic nerve. Descending motor command was reliably recorded (fig. S16), and peripheral sensory feedback was detected with notable spatial and temporal selectivity after 6 weeks of implantation (Fig. 4C and fig. S16).

We finally exploited the e-dura to restore locomotion after spinal cord injury (4, 19). Adult rats received a clinically relevant contusion at the thoracic level, which spared less than 10% of spinal tissues at the lesion epicenter and led to permanent paralysis of both legs (Fig. 4D). An e-dura covering lumbosacral segments (Fig. 1) was used to engage spinal locomotor circuits located below injury. A serotonergic replacement therapy (5HT_{1A/7} and 5HT₂ agonists) (29) was injected through the chemotrode, and continuous electrical stimulation was delivered on the lateral aspect of L2 and S1 segments (40 Hz, 0.2 ms, 50 to 150 μA) (30). The concurrent and colocalized electrical and chemical stimulations enabled the paralyzed rats to walk (Fig. 4E). Intrathecal delivery allowed a reduction of injected drug volume to one-quarter the volume of intraperitoneal injection required to obtain the same facilitation of stepping (fig. S17). Subdural drug delivery through the chemotrode eliminated side effects of serotonergic

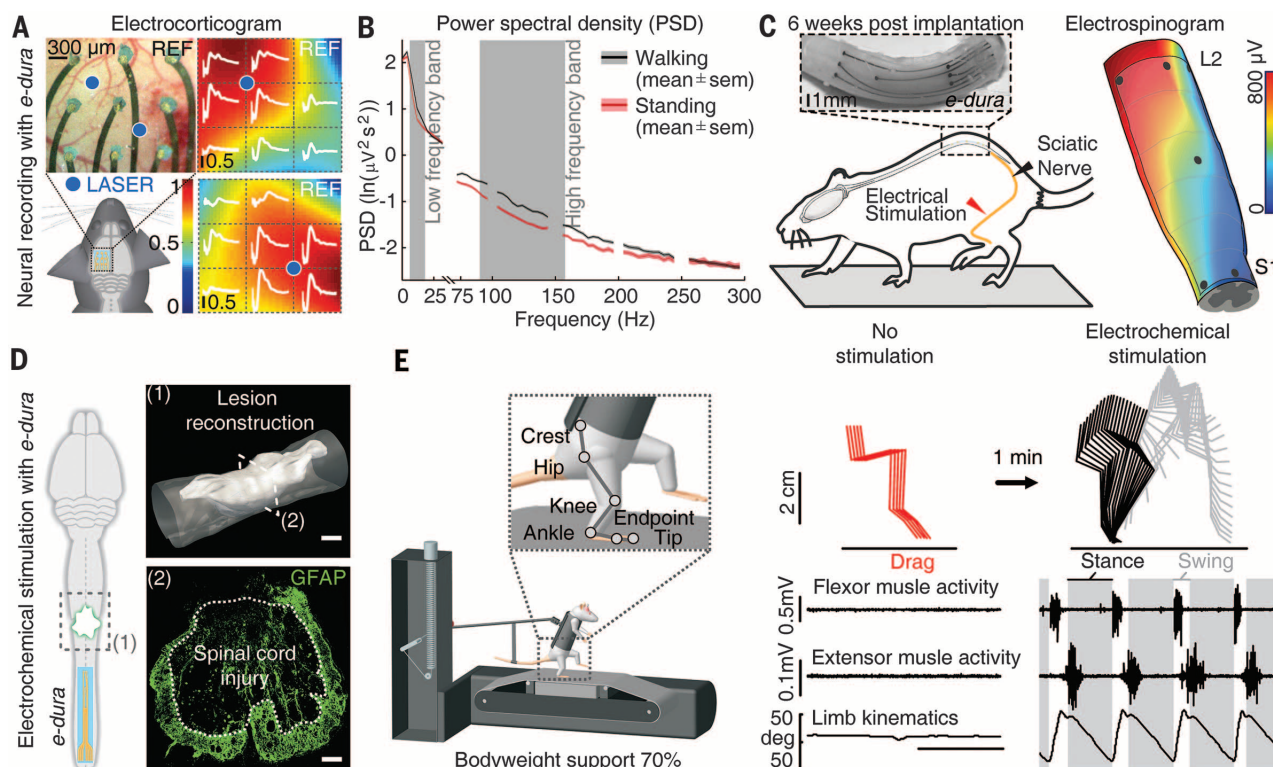


Fig. 4. Recordings and stimulation with e-dura. (A) e-dura implant positioned over the cortical surface of a Thy1-ChR2-YFP (yellow fluorescent protein) mouse. Blue spot indicates laser location. Cortical activation maps were reconstructed from normalized electrocorticograms, shown in white (150-μs duration). (B) Power spectral density computed from motor cortex electrocorticograms recorded 3 weeks after e-dura implantation in rats. Increased neural activity in low- and high-frequency bands differentiate cortical states during walking from those during standing. (C) Spinal

cord activation map was reconstructed from electrospinograms recorded 6 weeks after e-dura implantation in response to left sciatic nerve stimulation. (D) Rats were implanted with a spinal e-dura covering lumbosacral segments and received a severe spinal cord injury. (E) Recording without and with electrochemical stimulation during bipedal locomotion under robotic support after 3 weeks of rehabilitation. Stick diagram decompositions of hindlimb movements are shown together with leg muscle activity and hindlimb oscillations.

agents on autonomic systems (fig. S17). The distributed electrodes delivered stimulation restricted to specific segments, which allowed facilitation of left versus right leg movements (fig. S18 and movie S3). The e-dura mediated reliable therapeutic effects during the 6-week rehabilitation period.

We have introduced soft neural implants that show long-term biointegration and functionality within the central nervous system. Computerized and mechanical simulations demonstrated that the biomechanical coupling between implants and neural tissues is critical to obtain this symbiosis. Neural implants prepared with elastic materials met the demanding static and dynamic mechanical properties of spinal and brain tissues. Even in the subdural space, the soft implant triggered limited foreign-body reaction. This location enables local drug application, reducing side effects; high-resolution neuronal recordings; and concurrent delivery of electrical and chemical neuromodulation, alleviating neurological deficits for extended periods of time. The integration of tissue-matched implants with higher electrode density, implantable pumps for drug delivery, and embedded electronics to read and write into the nervous system in real time will require additional technological developments.

REFERENCES AND NOTES

- D. Borton, S. Micera, J. R. Millán, G. Courtine, *Sci. Transl. Med.* **5**, 210rv2 (2013).
- D.-H. Kim et al., *Nat. Mater.* **9**, 511–517 (2010).
- P. Fattahi, G. Yang, G. Kim, M. R. Abidian, *Adv. Mater.* **26**, 1846–1885 (2014).
- R. van den Brand et al., *Science* **336**, 1182–1185 (2012).
- D. W. Park et al., *Nat. Commun.* **5**, 5258 (2014).
- J. C. Barrese et al., *J. Neural Eng.* **10**, 066014 (2013).
- P. Moshayedi et al., *Biomaterials* **35**, 3919–3925 (2014).
- K. A. Potter et al., *Acta Biomater.* **10**, 2209–2222 (2014).
- Y.-B. Lu et al., *Proc. Natl. Acad. Sci. U.S.A.* **103**, 17759–1776 (2006).
- B. S. Elkin, A. I. Ilankovan, B. Morrison 3rd, *J. Neurotrauma* **28**, 2235–2244 (2011).
- A. F. Christ et al., *J. Biomech.* **43**, 2986–2992 (2010).
- B. S. Elkin, E. U. Azeloglu, K. D. Costa, B. Morrison 3rd, *J. Neurotrauma* **24**, 812–822 (2007).
- D. R. Enzmann, N. J. Pelc, *Radiology* **185**, 653–660 (1992).
- D. E. Harrison, R. Cailliet, D. D. Harrison, S. J. Troyanovich, S. O. Harrison, *J. Manipulative Physiol. Ther.* **22**, 227–234 (1999).
- P. Konrad, T. Shanks, *Neurobiol. Dis.* **38**, 369–375 (2010).
- P. Musienko, R. van den Brand, O. Maerzendorfer, A. Larmagnac, G. Courtine, *IEEE Trans. Biomed. Eng.* **56**, 2707–2711 (2009).
- S. P. Lacour, D. Chan, S. Wagner, T. Li, Z. Suo, *Appl. Phys. Lett.* **88**, 204103 (2006).
- A. Mailis-Gagnon, A. D. Furlan, J. A. Sandoval, R. Taylor, *Cochrane Database Syst. Rev.* (3): CD003783 (2004).
- C. A. Angeli, V. R. Edgerton, Y. P. Gerasimenko, S. J. Harkema, *Brain* **137**, 1394–1409 (2014).
- P. Gad et al., *J. Neuroeng. Rehabil.* **10**, 2 (2013).
- NeuroNexus, Surface Probes. <http://neuronexus.com/products/neural-probes/surface-probes>, (2014).
- C. F. Guo, T. Sun, Q. Liu, Z. Suo, Z. Ren, *Nat. Commun.* **5**, 3121 (2014).
- J. A. Fan et al., *Nat. Commun.* **5**, 3266 (2014).
- J. Vanfleteren et al., *Procedia Technol.* **15**, 208–215 (2014).
- D.-H. Kim et al., *Proc. Natl. Acad. Sci. U.S.A.* **109**, 19910–19915 (2012).
- S. F. Cogan, *Annu. Rev. Biomed. Eng.* **10**, 275–309 (2008).
- U. A. Aregueta-Robles, A. J. Woolley, L. A. Poole-Warren, N. H. Lovell, R. A. Green, *Front. Neuroeng.* **7**, 15 (2014).
- T. Pistohl, A. Schulze-Bonhage, A. Aertsen, C. Mehring, T. Ball, *Neuroimage* **59**, 248–260 (2012).
- P. Musienko et al., *J. Neurosci.* **31**, 9264–9278 (2011).
- G. Courtine et al., *Nat. Neurosci.* **12**, 1333–1342 (2009).

ACKNOWLEDGMENTS

We thank D. Pioletti for providing access to the micro-computed tomography (CT) scanner. Financial support was provided by the Fondation Bertarelli, the International Paraplegic Foundation, Starting Grants from the European Research Council (ERC 259419 *ESKIN* and ERC 261247 *Walk-Again*), Nano-tera.ch (20NA_145923 *SpineRepair*), the Swiss National Science Foundation through the National Centre of Competence in Research (NCCR) in Robotics, European Commission's Seven Framework Program (CP-IP 258654 *NeuWalk*), and the National Science Foundation Materials Research Science and Engineering Center (DMR-0820484). A patent application (PCT/EP2014/059779) describing aspects of the implant fabrication was filed on 13 May 2014.

SUPPLEMENTARY MATERIALS

www.sciencemag.org/content/347/6218/159/suppl/DC1
Materials and Methods
Supplementary Text
Table S1
Figs. S1 to S18
Movies S1 to S3
References (31, 32)

22 August 2014; accepted 27 November 2014
10.1126/science.1260318

ULTRAFAST DYNAMICS

Four-dimensional imaging of carrier interface dynamics in p-n junctions

Ebrahim Najafi,¹ Timothy D. Scarborough,¹ Jau Tang,^{1,2} Ahmed Zewail^{1*}

The dynamics of charge transfer at interfaces are fundamental to the understanding of many processes, including light conversion to chemical energy. Here, we report imaging of charge carrier excitation, transport, and recombination in a silicon p-n junction, where the interface is well defined on the nanoscale. The recorded images elucidate the spatiotemporal behavior of carrier density after optical excitation. We show that carrier separation in the p-n junction extends far beyond the depletion layer, contrary to the expected results from the widely accepted drift-diffusion model, and that localization of carrier density across the junction takes place for up to tens of nanoseconds, depending on the laser fluence. The observations reveal a ballistic-type motion, and we provide a model that accounts for the spatiotemporal density localization across the junction.

Multiple spectroscopic techniques have enhanced the understanding of charge carrier dynamics in semiconductors (1–3). However, as the size approaches the critical limit of the nanoscale (4), it becomes necessary to investigate the behavior of carriers at a high spatiotemporal resolution to elucidate the extent of spatial and density localizations at these scales. In semiconductors, carrier excitation, transport, and recombination occur on time scales that span a wide range, from a few femtoseconds to hundreds of microseconds (5), and these processes are dramatically altered in nanostructures due to their low dimensionality and the large surface-to-volume ratio (6, 7). Although a large body of literature exists on carrier dynamics in bulk semiconductors, studies of surfaces and interfaces demand the resolution of the dynamics in both space and time with high enough sensitivity. Recently developed scanning electron-probe microscopies, which combine the spatial resolution of electron microscopy and the temporal resolution of laser spectroscopy, make such studies possible (8).

Here, we report direct imaging of carrier interfacial dynamics in the silicon p-n junction by scanning ultrafast electron microscopy (SUEM). We image the spatiotemporal evolution of carrier density after excitation and follow the behavior of transport and recombination of carriers. It is shown, with the spatial resolution of the electron probe, that optically induced long-range carrier transport can span tens of micrometers. Snapshots of the carrier density on the picosecond time scale indicate the localization of excess carriers and the associated electric field across the junction. The displaced carriers remain localized in both space and time (up to tens of nanoseconds) until they cross the junction and

recombine. With high excitation fluence, carrier localization distorts the effective junction potential and acts as a locally time-dependent field, providing an energetically favorable pathway to recombination. These observations were accounted for by developing a model that describes both the ballistic-type carrier transport and the decay of energy to the lattice.

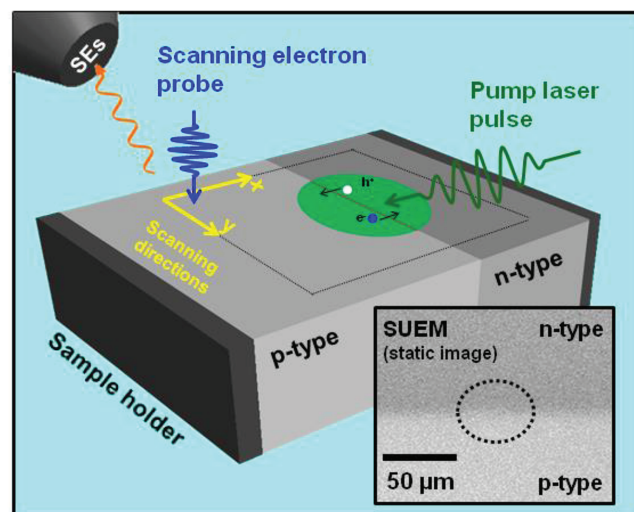
The p-n junction diodes were purchased as wafers from EL-CAT Inc. and used without further modifications. The wafers consisted of phosphorus-doped n-type silicon ($1.4 \times 10^{14} \text{ cm}^{-3}$) epitaxially grown on boron-doped p-type silicon ($9.4 \times 10^{18} \text{ cm}^{-3}$) with (111) crystal orientation; this results in an intrinsic potential ($V_{\text{intrinsic}}$) of 0.79 V (fig. S1). No external field was applied to the junction. The samples were cleaved and immediately transferred into the SUEM chamber, where the pressure was maintained at 1.2×10^{-6} torr. Surfaces with the root mean square (RMS) roughness of less than 100 nm [orders of magnitude smaller than the estimated diffusion length in silicon (9)]

were selected for this experiment to minimize interruptions of carrier diffusion. As shown below, the ballistic coherence length of carriers is tens of micrometers, a much larger value than the roughness scale, and thus it is relatively irrelevant on the picosecond time scale. Images of a typical surface studied statically—i.e., without time resolution—are provided in Fig. 1 and fig. S2.

In SUEM, femtosecond infrared pulses (1030 nm, 300 fs) are split to generate green (515 nm) and ultraviolet (UV) (257 nm) pulses. The green is used to pump the specimen samples, whereas the UV is directed toward the microscope's photocathode to generate short pulses of electrons from the field emission tip; details of the design and operation were given previously (10). The time delay between the optical pump and electron probe pulses was controlled, covering the range from -680 ps to $+3.32$ ns with the snapshot resolution of ~ 2 ps. The pulsed electrons, accelerated to 30.0 kV by electrostatic lenses, produce secondary electrons (SEs) from the top 1 to 5 nm (11) of the sample's surface, which are then collected by the SE detector. To generate an image, the electron probe was scanned across the area of interest, which included the image region for carrier transport, typically using a resolution of 200 nm, which is sufficient for a surface scan over tens of micrometers. It has been shown that this spatial resolution can be made better than 10 nm (10). The experimental setup is schematically depicted in Fig. 1.

Under our experimental conditions, the transient surface charge density in the local vacuum is estimated to be less than $\sim 10^7 \text{ cm}^{-2}$ due to the fluences used (maximum 1.28 mJ/cm^2), indicating that surface field transients do not strongly interfere with the electron probe (12). Within a given material, the number of emitted SEs depends on the topography and composition (13), but, in all SUEM experiments presented here, we obtain the change in carrier density by subtracting the image recorded at negative time

Fig. 1. Schematic of SUEM and imaging of the junction. The 515-nm optical pump initiates carrier excitation to the conduction band. Transport of charges to the junction then takes place in the diode while the scanning electron probe measures the induced changes at different time delays. The inset is an SUEM image of the diode recorded at -680 ps; the well-known but unintuitive contrast between n-type and p-type silicon in the diode is due to the energetics of the local bending of the vacuum level (15–18) and simply reflects the (\pm) surface charge involvement in enhancing or suppressing SEs in the p (n) regions.



¹Physical Biology Center for Ultrafast Science and Technology, Arthur Amos Noyes Laboratory of Chemical Physics, California Institute of Technology, Pasadena, CA 91125, USA. ²Institute of Photonics, National Chiao Tung University, 300 Hsinchu, Taiwan.

*Corresponding author. E-mail: zewail@caltech.edu

(reference image recorded at -680 ps) from the image obtained at a given positive time, i.e., $I(r^{x,y}, t_+) - I(r^{x,y}, t_-)$, where $r^{x,y}$ is the spatial pixels scanned and t_+ and t_- are the frame times after time zero (t_+) and before time zero (t_-). This results in the so-called “contrast image” in which the bright and dark contrasts correspond, respectively, to increases in local electron and hole densities (fig. S3), and the difference image becomes insensitive to collection and other possible fluctuations. Such images provide the snapshots that are used to construct movies S1 to S3.

After optical excitation in the specimen, electrons are promoted to the conduction band, and in this case the junction separates electron-hole (e-h) pairs, with e and h drifting in opposite directions, a process usually described by the drift-diffusion model (14); this locally increases the density of majority carriers in both n-type and p-type. In the absence of additional fields, the charge separation occurs solely in the vicinity of the junction, where excited carriers are influenced by the static junction potential. The inset in Fig. 1 shows the raw SUEM image of the diode recorded at a negative time delay

(-680 ps), long before the arrival of the initiating pump pulse. The observed difference in brightness between p-type and n-type regions in the image agrees with previous observations (15, 16) and is attributed to the difference in effective electron affinities between the two regions (17, 18). The pump pulse was guided to symmetrically illuminate n-type and p-type, as highlighted by the dotted ellipse in Fig. 1. A deviation of up to several micrometers in beam placement may occur, although it can be accounted for, as discussed below.

To understand the influence of the junction on the dynamics, we first examined n-type and p-type silicon individually without the junction and with doping levels and crystal orientations similar to their counterparts in the diode. Figure 2, A and B, shows contrast images recorded for n-type and p-type silicon, respectively, at various time delays. The images clearly display a bright contrast in both samples after the optical excitation; the contrast is rather weak in n-type, with a spatial spread comparable to the laser profile on the surface, but is considerably stronger in p-type, with a larger spatial extent. This is attributed to

the larger absorption cross section in heavily doped p-type silicon (19). In both samples, the bright contrast gradually decays at long times. Such behavior in lightly doped n-type and heavily doped p-type is independent of laser fluence. If the presence of the junction potential does not alter the dynamics, we would expect to observe the same behaviors in the n-type and p-type regions of the diode as those shown in Fig. 2, A and B.

The temporal behavior of the junction is summarized in Fig. 2C for 1.28 mJ/cm² fluence; full sets of contrast images can be viewed in movies S1 to S3. The dynamics can qualitatively be described as follows. Immediately after the excitation (the frame at $+6.7$ ps), both layers are bright, mirroring their individual behaviors in the absence of the junction. After 36.7 ps, charges are transported toward the junction, resulting in excess electron and hole density in n-type and p-type, respectively; the depletion layer at the junction remains dark due to surface patch fields that hinder SE detection (17, 18). After transport across the junction ($+80$ ps), the density of excess carriers reaches its maximum. The spatial extent of charge separation is estimated to span tens of micrometers within the first ~ 80 ps. The observed “bending” at the junction is due to the asymmetry in the pump beam placement, as discussed in the supplementary materials. Such drastic difference in contrast behavior, with and without the junction, provides the underpinning for obtaining the density evolution.

At longer times, the diode relaxes toward equilibrium as carriers move back across the junction to recombine. Analysis of images for all regions (fig. S11) indicates that the relaxation toward equilibrium occurs more quickly at higher fluences. In fact, at 0.16 mJ/cm² fluence, the decays essentially plateau within the experimental time scale of 3.32 ns. The transients suggest that the recombination dynamics are influenced by the number of displaced carriers; specifically, as the system is removed further from equilibrium at larger fluences, recombination is increasingly facilitated. Moreover, the high spatial resolution of SUEM provides a range of apparent dynamics throughout the illuminated region due to the spatial profile of the laser pulse; carriers near the center of the laser profile, where the local fluence is highest, recombine more quickly than regions farther away.

The rapid transport of carriers over tens of micrometers in only ~ 80 ps is not expected from the conventional drift-diffusion model. According to such a model, carrier drift occurs only within the depletion layer, where the intrinsic electric field is nonzero. The longitudinal diffusion coefficient of electrons in silicon as a function of electric field strength (at 300 K) has been measured (9) and ranges from 10 to 30 cm²/s. It follows that such values for a 50 - μ m distance will yield dynamics on the microsecond time scale, contrary to our observation. Furthermore, the involvement of lattice phonons at a velocity of 10^3 m/s cannot account for the observed picosecond time scale behavior. For these reasons, we have developed the following model, illustrated

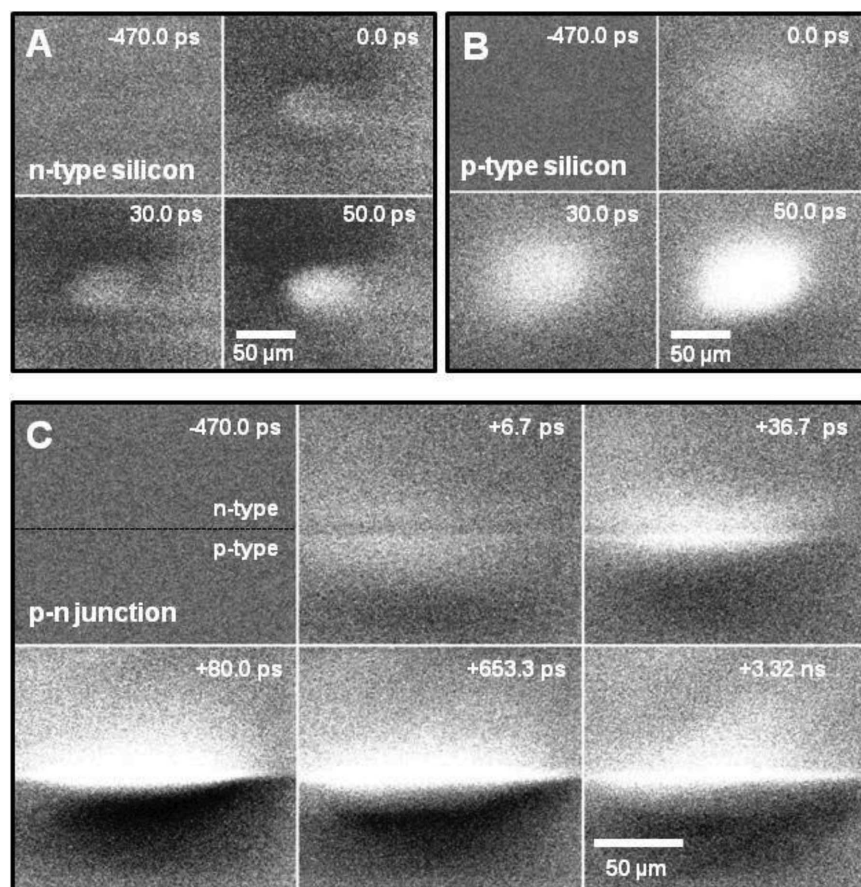


Fig. 2. Dynamics with and without the junction. Silicon (A) n-type and (B) p-type samples without a junction were studied as individual wafers. Both n-type (1.4×10^{14} cm⁻³ P-doped) and p-type (9.4×10^{18} cm⁻³ B-doped) show a bright signal (increased electron density) under laser illumination, in contrast to the behavior when the junction is present. (C) A series of contrast images in which the bright and dark contrasts correspond to the local electron and hole densities, respectively, relative to the signal at negative time. These frames were chosen to display the unperturbed signal (-470 ps), excitation (6.7 ps), carrier separation after transport (36.7 , 80 ps), and relaxation toward equilibrium (653.3 ps, 3.32 ns).

in Fig. 3, A and D, which accounts for the observed results.

The excitation of the junction with 2.41 eV photons results in carriers with excess energy equivalent to a temperature of $\sim 10^4$ K. In the model, the important point is that these carriers move ballistically at a relatively high speed, on the order of 10^6 m/s, and on the picosecond time scale the lattice phonons cannot fully quench such motion. In the supplementary materials, we consider the influence of the lattice, which drains the energy (and reduces the speed) as a function of time. It is shown that, even for electron-lattice interaction times on the order of 10 ps, the observed carrier behavior is robust. The initial ex-

cited carrier population follows the laser profile. With the junction placed at $x = 0$ in the surface (x - y) plane, the initial e-h pair density is determined for p-type ($\rho_{e,h}^p$) and n-type ($\rho_{e,h}^n$) and takes on a Gaussian profile (see the supplementary materials). The velocities of motion in the x - y plane can similarly be expressed for a given temperature and for the subpicosecond equilibrated carriers.

As shown in the supplementary materials, the initial density profile at $t = 0$ moves $(x - vt)$ with velocity v . By integrating over all velocities of the product of density and the Maxwell-Boltzmann velocity distribution, and considering the carrier density asymmetry at the interface, we can ex-

press the spatiotemporal evolution of the density in the x - y plane. For p-type, we have

$$\rho_e^p(x, y; t) = \frac{N_p}{2\pi(\sigma^2 + v_e^2 t^2)} \exp\left(-\frac{x^2 + y^2}{2(\sigma^2 + v_e^2 t^2)}\right) \times \left[1 - \operatorname{erf}\left(\frac{\sigma}{v_e t \sqrt{2(\sigma^2 + v_e^2 t^2)}} x\right)\right] \quad (1)$$

$$\rho_h^p(x, y; t) = \frac{N_p}{\pi(\sigma^2 + v_h^2 t^2)} \exp\left(-\frac{x^2 + y^2}{2(\sigma^2 + v_h^2 t^2)}\right) \times \eta(-x) \quad (2)$$

where N_p is the total number of photoexcited e-h pairs; σ is the RMS half-width of the laser focus;

Fig. 3. Theoretical modeling of carrier separation and transport. Shown are the behaviors of isotropically expanding electrons (red) and holes (blue) after the excitation in (A) p-type and (D) n-type; the arrows represent the initial (x) velocity directions. In both layers, the minority carriers are able to cross the junction, whereas the majority carriers are reflected by the junction. This results in net charge separation represented in the figure by the shaded regions. Calculated also are the (B) electron and (C) hole densities originated in p-type and the (E) electron and (F) hole densities originated in n-type. All density calculations reflect the behavior after +20 ps of propagation time. These calculations show the extent of carrier expansion in space and at different times. The scale of the normalized density shown (0 to 2×10^{-4}) when multiplied by N_p , which is 10^9 e-h pairs, gives the actual density.

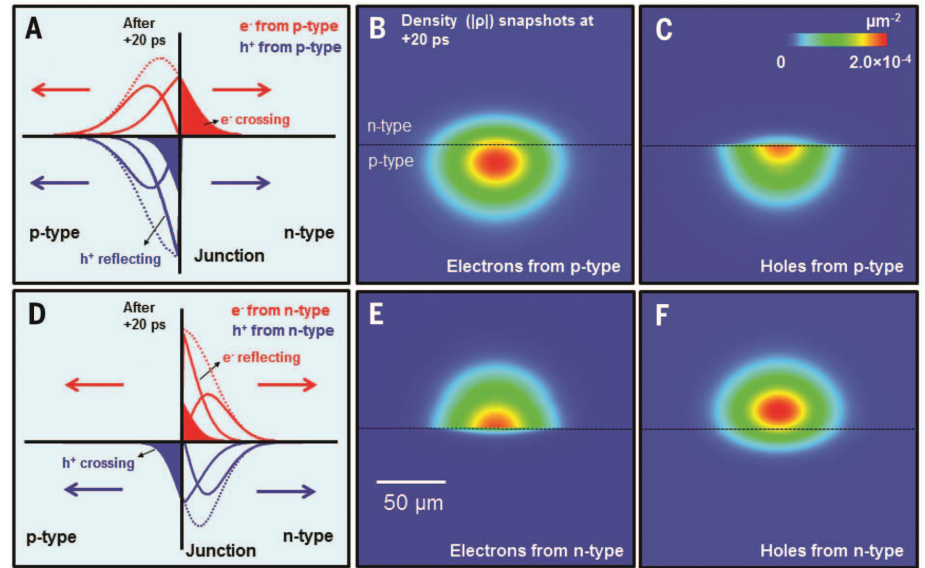
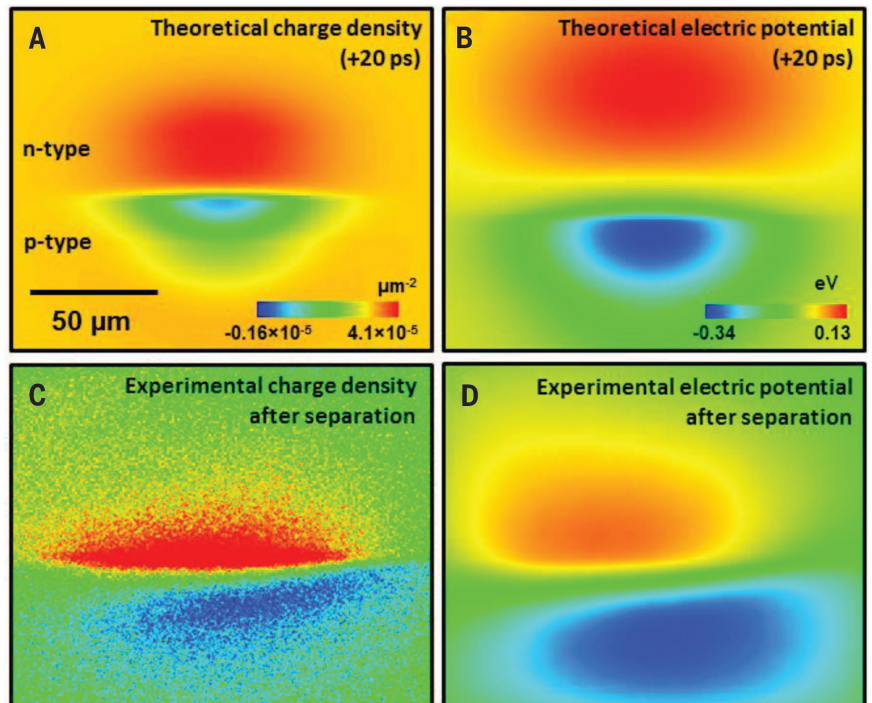


Fig. 4. Comparison between experiment and theory.

Shown are comparisons between experimental charge density and electric potential and those predicted by the theoretical model following transport. (A) The net theoretical charge density at +20 ps (the asymmetry of excitation is included). The presence of long-range transport, up to tens of micrometers, is evident. The scale of the normalized density shown (-0.16×10^{-5} to 4.1×10^{-5}) when multiplied by N_p , which is 10^9 e-h pairs, gives the actual density. (B) The landscape calculated directly from the Coulomb interactions between separated carriers. The dynamic potential (due to net charge localization) reaches more than 300 meV, which is of the same order of magnitude as the junction potential (0.79 eV). This influences charge localization and carrier recombination. (C) Experimental contrast image of the junction that mirrors charge densities in n-type and p-type after charge separation. (D) The dynamic potential map calculated directly from the experimental data after charge separation by considering each pixel of the net electrons and holes corresponding to bright and dark contrast and calculating the Coulomb potential. The apparent tilt in the figure is due to the inclined angle of the incident laser beam, which is about 15° with respect to the junction.



v_e and v_h are the average thermal velocities of electrons and holes, respectively; and $\eta(-x)$ is the Heaviside step function. Similar analysis for n-type is presented in the supplementary materials.

Figure 3 displays the density distributions in space as a snapshot at $t = +20$ ps; adding up the distributions for carriers originating in p-type (Fig. 3, B and C) and n-type (Fig. 3, E and F) affords the net carrier density. The net electron (red) and hole (blue) densities at $t = +20$ ps (from Eqs. 1 and 2) in Fig. 3, A and D, are shown as dotted curves. Taking p-type as an example, electrons with initial velocity toward the junction are transported to n-type, whereas holes moving toward the junction face an impassable barrier. This gating behavior is illustrated in Fig. 3A (charges initially from p-type) and Fig. 3D (charges initially from n-type). The net charge separation leads to localization of electrons on one side and holes on the other, shown as shaded regions. This creates a long-range electric field, the potential of which is given in Fig. 4.

The sum of these four images, weighted to reflect the increased absorption in p-type, is presented in Fig. 4A. The figure depicts the long-range separation of carriers in agreement with the experimental observations. Separation due to the gating effect creates a net carrier distribution localized across the junction. The resultant Coulomb interactions distort the electric potential landscape as illustrated in Fig. 4B. For comparison, we present an experimental contrast image (Fig. 4C), which mirrors the net carrier distribution, and a potential map (Fig. 4D) calculated directly from the experimental data. Comparison between simulation and experiment shows agreement on the spatial extent of the distortions; this agreement validates the ballistic expansion of carriers as the underlying mechanism. The resulting electric potential, which opposes the intrinsic built-in junction potential, acts as spatiotemporally isolated “forward bias.” At high fluences, this distortion induces a larger restoring force, which explains the fluence-dependent recombination rates observed in fig. S11.

Four-dimensional space-time imaging of carrier dynamics at interfaces, using SUEM, has the potential of unraveling in other complex structures the mechanism of charge transport, with ultrafast time resolution and nanometer-scale scanning capability. The unexpected ballistic carrier velocity (toward the junction) and the gated localization of charges (at the junction) are not predicted by the widely accepted drift-diffusion model, and these features may be characteristics of other materials when examined with the spatiotemporal resolutions of SUEM. At interfaces, the created transient density and electric field are dependent on the optical excitation, and it should be possible to control the properties of nano-to-micrometer-scale heterojunctions using the temporal, spatial, and pulse-shape characteristics of applied light fields.

REFERENCES AND NOTES

- K.-T. Tsen, Ed., *Ultrafast Dynamical Processes in Semiconductors* (Springer-Verlag, New York, 2004).
- J. Shah, *Ultrafast Spectroscopy of Semiconductors and Semiconductor Nanostructures* (Springer-Verlag, New York, 1999).
- D. H. Auston, *Top. Appl. Phys.* **60**, 183–233 (1993).
- P. Rodgers, Ed., *Nanoscience and Technology: A Collection of Reviews from Nature Journals* (World Scientific, London, 2010).
- M. Saraniti, U. Ravaioli, *Nonequilibrium Carrier Dynamics in Semiconductors: Proceedings of the 14th International Conference, July 25–29, 2005, Chicago, USA* (Springer Proceedings in Physics, Berlin, 2006).
- P. Hommelhoff, M. F. Kling, M. I. Stockman, *Ann. Phys.* **525**, A13–A14 (2013).
- R. P. Prasankumar, P. C. Upadhy, A. J. Taylor, *Phys. Status Solidi B*, **246**, 1973–1995 (2009).
- A. H. Zewail, *Science* **328**, 187–193 (2010).
- R. Brunetti et al., *J. Appl. Phys.* **52**, 6713–6722 (1981).
- O. F. Mohammed, D. S. Yang, S. K. Pal, A. H. Zewail, *J. Am. Chem. Soc.* **133**, 7708–7711 (2011).
- Y. Lin, D. C. Joy, *Surf. Interface Anal.* **37**, 895–900 (2005).
- S. Schäfer, W. X. Liang, A. H. Zewail, *Chem. Phys. Lett.* **493**, 11–18 (2010).
- J. Goldstein et al., *Scanning Electron Microscopy and X-ray Microanalysis* (Springer, New York, 2007).
- B. Sapoval, C. Hermann, *Physics of Semiconductors* (Springer-Verlag, New York, 1995).
- K. W. A. Chee, C. Rodenburg, C. J. Humphreys, *J. Phys. Conf. Ser.* **126**, 012033 (2008).
- K. W. A. Chee, C. Rodenburg, C. J. Humphreys, *Microscopy of Semiconducting Materials 2007*, A. G. Cullis, P. A. Midgley, Eds. (Springer-Verlag, Berlin, 2008).
- S. L. Elliott, R. F. Broom, C. J. Humphreys, *J. Appl. Phys.* **91**, 9116–9122 (2002).
- C. P. Sealy, M. R. Castell, P. R. Wilshaw, *J. Electron Microsc.* **49**, 311–321 (2000).
- G. E. Jellison Jr., F. A. Modine, C. W. White, R. F. Wood, R. T. Young, *Phys. Rev. Lett.* **46**, 1414–1417 (1981).

ACKNOWLEDGMENTS

This work was supported by NSF grant DMR-0964886 and Air Force Office of Scientific Research grant FA9550-11-1-0055 in the Physical Biology Center for Ultrafast Science and Technology at California Institute of Technology, which is supported by the Gordon and Betty Moore Foundation.

SUPPLEMENTARY MATERIALS

www.sciencemag.org/content/347/6218/164/suppl/DC1
Materials and Methods
Supplementary Text
Figs. S1 to S11
Movies S1 to S3
References (20–24)

8 October 2014; accepted 2 December 2014
10.1126/science.aaa0217

QUANTUM GASES

Critical dynamics of spontaneous symmetry breaking in a homogeneous Bose gas

Nir Navon,^{*,†} Alexander L. Gaunt,[†] Robert P. Smith, Zoran Hadzibabic

Kibble-Zurek theory models the dynamics of spontaneous symmetry breaking, which plays an important role in a wide variety of physical contexts, ranging from cosmology to superconductors. We explored these dynamics in a homogeneous system by thermally quenching an atomic gas with short-range interactions through the Bose-Einstein phase transition. Using homodyne matter-wave interferometry to measure first-order correlation functions, we verified the central quantitative prediction of the Kibble-Zurek theory, namely the homogeneous-system power-law scaling of the coherence length with the quench rate. Moreover, we directly confirmed its underlying hypothesis, the freezing of the correlation length near the transition. Our measurements agree with a beyond-mean-field theory and support the expectation that the dynamical critical exponent for this universality class is $z = 3/2$.

Continuous symmetry-breaking phase transitions are ubiquitous, from the cooling of the early universe to the λ transition of superfluid helium. Near a second-order transition, critical long-range fluctuations have a diverging correlation length ξ , and details of the short-range physics are largely unimportant. Consequently, all systems can be classified into a small number of universality classes, according to their generic features such as symmetries, dimensionality, and range of interactions (*1*). Close to the critical point, many physical quantities exhibit power-law behaviors governed by critical exponents characteristic of a universality class. Specifically, for a classical phase transition,

$\xi \sim |(T - T_c)/T_c|^{-\nu}$, where T_c is the critical temperature and ν is the (static) correlation-length critical exponent. Importantly, the corresponding relaxation time τ , needed to establish a diverging ξ , also diverges: $\tau \sim \xi^z$, where z is the dynamical critical exponent (*2*). An elegant framework for understanding the implications of this critical slowing down for the dynamics of symmetry breaking is provided by the Kibble-Zurek (KZ) theory (*3, 4*).

Qualitatively, as T is reduced toward T_c at a finite rate, beyond some point in time the correlation length can no longer adiabatically follow its diverging equilibrium value. Consequently, at time $t = t_c$, the transition occurs without ξ ever having reached the size of the whole system. This results in the formation of finite-sized domains that display independent choices of the symmetry-breaking order parameter (Fig. 1A). [At the domain

Cavendish Laboratory, University of Cambridge, J. J. Thomson Avenue, Cambridge CB3 0HE, UK.

*Corresponding author. E-mail: nn270@cam.ac.uk †These authors contributed equally to this work.

boundaries, rare long-lived topological defects can also form (5), their nature and density depending on the specific physical system.] Such domain formation was discussed in a cosmological context and linked to relativistic causality (3), whereas the connection to laboratory systems, critical slowing down, and universality classes was made in (4).

The main quantitative prediction of the KZ theory is that, under some generic assumptions (5), the average domain size d follows a universal scaling law. The crucial KZ hypothesis is that in the nonadiabatic regime close to t_c , the correlations remain essentially frozen. Then, for a smooth temperature quench, the theory predicts

$$d = \lambda_0 \left(\frac{\tau_Q}{\tau_0} \right)^b \quad (1)$$

with the KZ exponent

$$b = \frac{v}{1 + vz} \quad (2)$$

where τ_Q is the quench time defined so that close to the transition $T/T_c = 1 + (t_c - t)/\tau_Q$, and λ_0 and τ_0 are a system-specific microscopic length scale and time scale, respectively.

Signatures of KZ physics have been observed in a wide range of systems, including liquid crystals (6), liquid helium (7, 8), superconductors (9–11), atomic Bose-Einstein condensates (BECs) (12–18), multiferroics (19), and trapped ions (20–22). However, despite this intense activity, a direct quantitative comparison with Eqs. 1 and 2 has remained elusive; some common complications include system inhomogeneity, modified statistics of low-probability defects, and uncertainties over the nature of the transition being crossed [for a recent review, see (5)]. In this work, we studied the dynamics of spontaneous symmetry breaking in a homogeneous atomic Bose gas, which is in the same universality class as the three-dimensional (3D) superfluid ^4He . For this class, mean-field (MF) theory predicts $v = 1/2$ and $z = 2$, giving $b = 1/4$, whereas a beyond-MF dynamical critical theory, the so-called F model (2), gives $v \approx 2/3$ and $z = 3/2$, so $b \approx 1/3$. We prepared a homogeneous Bose gas by loading 3×10^5 ^{87}Rb atoms into a cylindrical optical-box trap (23) of length $L \approx 26 \mu\text{m}$ along the horizontal x axis and radius $R \approx 17 \mu\text{m}$. Initially, $T \approx 170$ nK, corresponding to $T/T_c \approx 2$. We then evaporatively cooled the gas by lowering the trap depth, crossed $T_c \approx 70$ nK with 2×10^5 atoms, and had 10^5 atoms at $T \lesssim 10$ nK ($T/T_c \lesssim 0.2$). In our system, λ_0 is expected to be set by the thermal wavelength at the critical point, $\lambda_{cl} \approx 0.7 \mu\text{m}$, and τ_0 by the elastic scattering time τ_{el} (13, 24); for our parameters, a classical estimate gives $\tau_{el} \approx 30$ ms.

Qualitatively, random phase inhomogeneities in rapidly quenched clouds are revealed in time-of-flight (TOF) expansion as density inhomogeneities (14, 25), such as shown in Fig. 1B (here the gas was cooled to $T \ll T_c$ in 1 s). In our finite-sized box, we can also produce essentially pure and fully coherent (single-domain) BECs, by cooling the gas slowly (over $\gtrsim 5$ s). In TOF, such a BEC develops the characteristic diamond shape (26) seen in Fig. 1C.

To quantitatively study the coherence of our clouds, we probed the first-order two-point correlation function

$$g_1(\mathbf{r}, \mathbf{r}') \propto \langle \hat{\Psi}^\dagger(\mathbf{r}) \hat{\Psi}(\mathbf{r}') \rangle \quad (3)$$

where $\hat{\Psi}(\mathbf{r})$ is the Bose field. Our method (Fig. 2A) is inspired by (27). We use a short (0.1 ms) Bragg-diffraction light pulse to create a small copy of the cloud (containing $\approx 5\%$ of the atoms) moving along the x axis with recoil velocity $v_r \approx 3$ mm/s (26). A second identical pulse is applied a time Δt later, when the two copies are shifted by $x = v_r \Delta t$ and for $x < L$ still partially overlap. This results in interference of the two displaced copies of the cloud in the overlap region of length $L - x$. After the second Bragg pulse, the fraction of diffracted atoms (for $x < L$) is (28)

$$\frac{N_r}{N} = \frac{1}{2} \left[1 + \left(1 - \frac{x}{L} \right) g_1(x) \right] \sin^2 \theta \quad (4)$$

where $g_1(x) \equiv \text{Re}[g_1(\mathbf{r}, \mathbf{r} + x\hat{x})]$ is the correlation function corresponding to periodic boundary conditions and normalized so that $g_1(0) = 1$, and θ is the area of each Bragg pulse (in our case $\theta \approx \pi/7$). Allowing the recoiling atoms to fully separate from the main cloud (in 140 ms of TOF) and counting N_r and N , we directly measured $G_1(x) \equiv (1 - x/L)g_1(x)$, with a spatial resolution of $\approx 0.7 \mu\text{m}$. Our resolution was limited by the duration of the Bragg pulses and the (inverse) recoil momentum; we experimentally assessed it by measuring G_1 in a thermal cloud with a thermal wavelength $< 0.5 \mu\text{m}$.

In Fig. 2B we show examples of $G_1(x)$ functions measured in equilibrium (blue) and after a quench (red). In an essentially pure equilibrium BEC (prepared slowly, as for Fig. 1C), $g_1(x) = 1$

and $G_1(x)$ is simply given by the triangular function $1 - x/L$ (dark blue solid line). In equilibrium at $T/T_c \approx 0.7$, we see a fast initial decay of G_1 , reflecting the significant thermal fraction. However, importantly, the coherence still spans the whole system, with the slope of the long-ranged part of G_1 giving the condensed fraction (light blue line is a guide to the eye). By comparison, the G_1 functions for quenched clouds clearly have no equilibrium interpretation. Here $T/T_c \approx 0.2$, corresponding to a phase space density > 25 , and yet coherence extends over only a small fraction of L . These data are fitted well by $g_1 \propto \exp(-x/\ell)$ (red lines), which provides a simple and robust way to extract the coherence length. This exponential form is further supported by a 1D calculation shown in the inset of Fig. 2B. Here we generated a wave function with a fixed number of domains \mathcal{D} , randomly positioning the domain walls and assigning each domain a random phase. Averaging over many realizations, we obtained $g_1(x)$ that is fitted very well by an exponential with $\ell = L/\mathcal{D} = d$. (In our 3D experiments, the total number of domains was $\sim \mathcal{D}^3$ and $g_1(x)$ was effectively averaged over $\sim \mathcal{D}^2$ 1D distributions.)

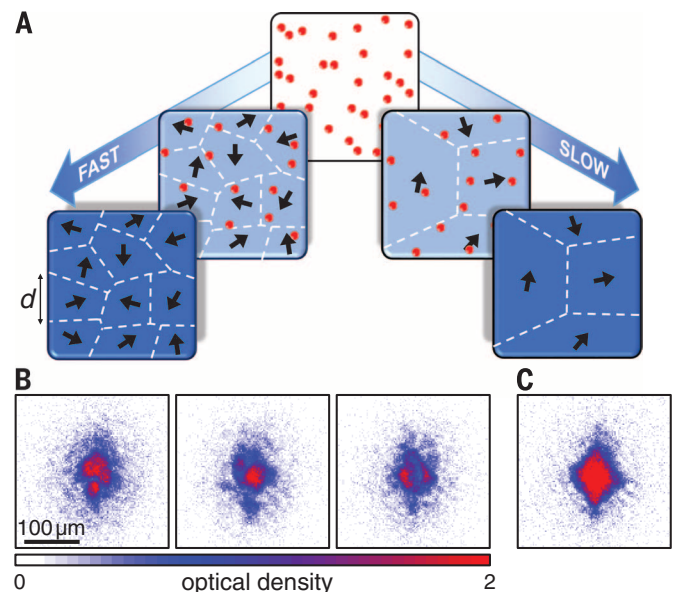
We now turn to a quantitative study of ℓ for different quench protocols (Fig. 3). For the KZ scaling law of Eqs. 1 and 2 to hold, a crucial assumption is that the correlation length is essentially frozen in time near t_c . Specifically, for $vz = 1$, which in our case holds for both MF theory and the F model, the freeze-out time of ℓ for $t > t_c$ is expected to be (4)

$$\hat{t} = f \sqrt{\tau_Q \tau_0}, \quad (5)$$

where f is a dimensionless number of order unity. Although intuitively appealing, this assumption is in principle only approximative, and the dynamics

Fig. 1. Domain formation during spontaneous symmetry breaking in a homogeneous Bose gas.

(A) Red points depict thermal atoms and blue areas coherent domains, in which the $U(1)$ gauge symmetry is spontaneously broken. The arrows indicate the independently chosen condensate phase at different points in space, and dashed lines delineate domains over which the phase is approximately constant. The average size d of the domains formed at the critical point depends on the cooling rate. Further cooling can increase the population of each



domain before the domain boundaries evolve. (B) Phase inhomogeneities in a deeply degenerate gas are revealed in TOF expansion as density inhomogeneities. Shown are three realizations of cooling the gas in 1 s from $T \approx 170$ nK, through $T_c \approx 70$ nK, to ≤ 10 nK. Each realization of the experiment results in a different pattern, and averaging over many images results in a smooth, featureless distribution. (C) Preparing a $T \lesssim 10$ nK gas more slowly (over 5 s) results in an essentially pure BEC with a spatially uniform phase.

of the system coarsening (i.e., merging of the domains) at times $t > t_c$ is still a subject of theoretical work (29). Practically, a crucial question is when one should measure ℓ in order to verify the universal KZ scaling. We resolved these issues by using two different quench protocols outlined in Fig. 3A, which allow us both to observe the KZ scaling and to directly verify the freeze-out hypothesis, without an a priori knowledge of the exact values of f and τ_0 .

In the first quench protocol (QP1), we followed cooling trajectories such as shown in Fig. 3A and varied only the total cooling time t_Q . We restricted t_Q to values between 0.2 and 3.5 s, for which we observed that the cooling curves were self-similar (as seen in Fig. 3A). We always crossed $T_c = 70(10)$ nK at $t_c = 0.72(5)t_Q$ (vertical dashed line) and always had the same atom number (within $\pm 20\%$) at the end of cooling. The self-similarity of the measured cooling trajectories and the essentially constant evaporation efficiency indicate that for this range of t_Q values, the system is always sufficiently thermalized, the

temperature (as determined from the thermal wings in TOF) is well defined during the quench (30), and to a good approximation τ_Q is simply proportional to t_Q . (For $t_Q < 0.2$ s, the evaporation is less efficient and the cooling trajectories are no longer self-similar.)

In Fig. 3B we plot ℓ versus t_Q , measured using QP1 (blue points). For $t_Q \leq 1$ s, we observed a slow power-law growth of ℓ , in good agreement with the expected KZ scaling (blue shaded area). However, for longer t_Q , this scaling breaks down and ℓ grows faster, quickly approaching the system size. Importantly, this breakdown can also be fully understood within the KZ framework. We note that the time between crossing T_c and the end of cooling is $t_Q - t_c \approx 0.28 t_Q \propto t_Q$, whereas the KZ freeze-out time is $\hat{t} \propto \sqrt{\tau_Q} \propto \sqrt{t_Q}$, so for slow enough quenches, $t_Q - t_c$ inevitably exceeds \hat{t} . Hence, although it may be impossible to adiabatically cross T_c , in practice the system can unfreeze and heal significantly before it is observed (31). From the point where the KZ scaling breaks down in Fig. 3B, $t_Q^{\text{br}} \approx 1$ s, we posit that

for $t_Q = t_Q^{\text{br}}$, we have $\hat{t} \approx 0.28 t_Q^{\text{br}}$ and hence, from Eq. 5, more generally $\hat{t} \approx 0.28 \sqrt{t_Q t_Q^{\text{br}}}$.

To verify this picture, we employed a second quench protocol (QP2), which involved two cooling steps, as shown by the orange points in the bottom panel of Fig. 3A. We initially followed the QP1 trajectory for a given t_Q , but then at a variable “kink” time $t_k \geq t_c$, we accelerated the cooling; the last part of the trajectory always corresponds to the final portion of our fastest, 0.2-s cooling trajectory. This way, even for $t_Q > t_Q^{\text{br}}$ we can complete the cooling and measure g_1 before the system has time to unfreeze.

In Fig. 3C, the orange points show the QP2 measurements of ℓ for $t_Q = 3.2$ s and various values of the kink position t_k/t_Q . These data reveal two notable facts. First, for a broad range of t_k values, ℓ is indeed constant (within errors), and the width of this plateau agrees with our estimate $\hat{t} \approx 0.5$ s for $t_Q = 3.2$ s, indicated by the horizontal arrow. Second, the value of ℓ within the plateau region falls in line with the KZ scaling law in Fig. 3B. We also show analogous QP2

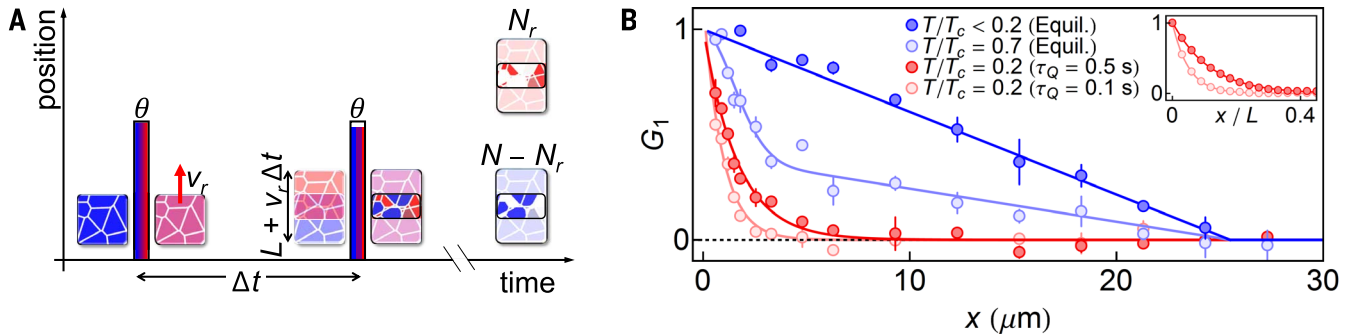


Fig. 2. Two-point correlation functions in equilibrium and quenched gases. (A) Homodyne interferometric scheme. The first Bragg-diffraction pulse (θ) creates a superposition of a stationary cloud and its copy moving with a center-of-mass velocity v_r . After a time Δt , a second pulse is applied. In the region where the two copies of the cloud displaced by $x = v_r \Delta t$ overlap, the final density of the diffracted atoms depends on the relative phase of the

overlapping domains; $g_1(x)$ is deduced from the diffracted fraction N_r/N (see text). (B) Correlation function $G_1(x) = (1 - x/L)g_1(x)$ measured in equilibrium (blue) and after a quench (red) for, respectively, two different T/T_c values and two different quench times. (Inset) 1D calculation of G_1 for a fragmented BEC containing $D = 10$ (red) and 20 (light red) domains of random sizes and phases. The solid lines correspond to $g_1 = \exp(-x\mathcal{D}/L)$.

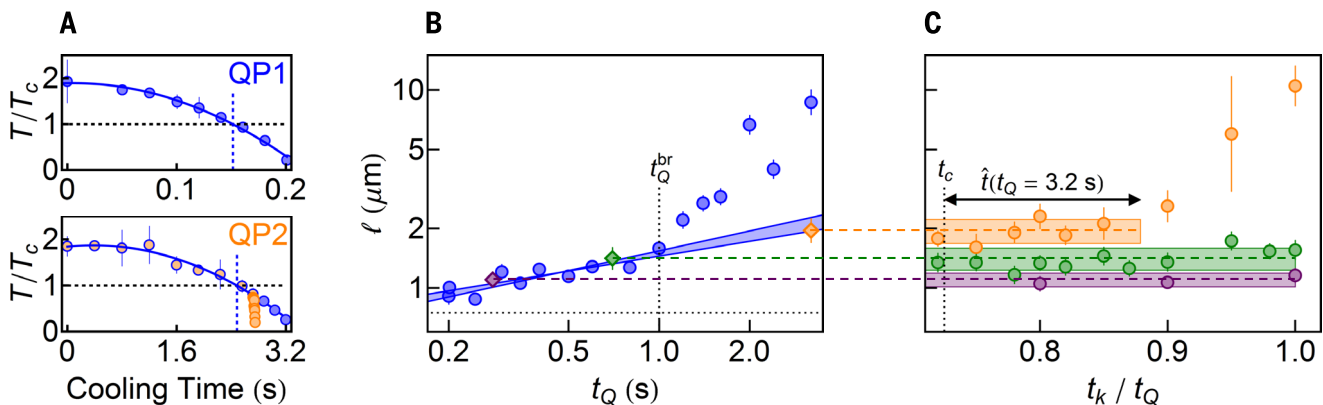


Fig. 3. KZ scaling and freeze-out hypothesis. (A) Quench protocols. The self-similar QP1 trajectories are shown in blue for total cooling time $t_Q = 0.2$ s (upper panel) and 3.2 s (lower panel). We use polynomial fits to the data (solid lines) to deduce t_c and τ_Q . QP2 is shown in the lower panel by the orange points, with the kink at $t_k = 0.85 t_Q$. (B) Coherence length ℓ as a function of t_Q . Blue points correspond to QP1. The shaded blue area shows power-law fits with $1/4 < b < 1/3$ to the data with $t_Q \leq t_Q^{\text{br}}$. The

horizontal dotted line indicates our instrumental resolution. (C) Coherence length ℓ measured following QP2, as a function of t_k/t_Q , for $t_Q = 3.2$ s (orange), 0.7 s (green), and 0.3 s (purple). The shaded areas correspond to the essentially constant ℓ (and its uncertainty) in the freeze-out period $t_k - t_c < \hat{t}$. (For $t_Q < t_Q^{\text{br}}$ the system never unfreezes.) The (average) ℓ values within these plateaus are shown in their respective colors as diamonds in (B).

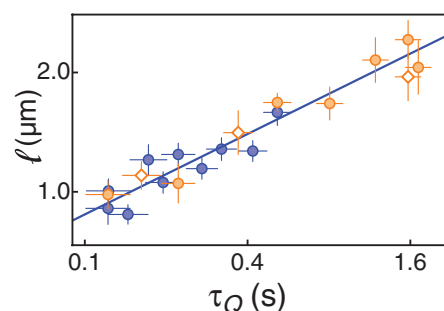


Fig. 4. Critical exponents of the interacting BEC transition. Orange circles and diamonds show ℓ values obtained using QP2, as in Fig. 3C; the diamonds show the same three data points as in Fig. 3B. Blue circles show the same QP1 data, with $t_Q \leq 1$ s as in Fig. 3B. We obtained $b = 0.35(4)$ (solid line), in agreement with the F-model prediction $b \approx 1/3$, corresponding to $\nu \approx 2/3$ and $z = 3/2$, and excluding the mean-field value $b = 1/4$.

measurements for $t_Q = 0.7$ s (green) and 0.3 s (purple); in these cases, $t_Q < t_Q^{\text{br}}$, so \hat{t} is longer than $t_Q - t_c$, the system never unfreezes, and thus the acceleration of the cooling has no effect on ℓ . These results provide direct support for the KZ freeze-out hypothesis.

To accurately determine the KZ exponent b , we made extensive measurements following QP2, extracting ℓ from the plateaued regions of width $\min[\hat{t}, t_Q - t_c]$, as in Fig. 3C. In Fig. 4, we combine these data with the QP1 measurements for $t_Q \leq 1$ s, and plot ℓ versus τ_Q . The plotted values of τ_Q and their uncertainties include the small systematic variation of the derivative of our cooling trajectory between t_c and $t_c - \hat{t}$. We finally obtain $b = 0.35(4)$, which strongly favors the F-model prediction $b \approx 1/3$ over the MF value $b = 1/4$ (32).

Having observed excellent agreement with the KZ theory, we discuss the implications of our measurements for the critical exponents of the interacting BEC phase transition, which is in the same universality class as the λ transition of ^4He . Whereas $\nu \approx 0.67$ has been measured in both liquid helium [see (33)] and atomic gases (34), the dynamical exponent z has presented a challenge to experiments [see (2, 35)]. Using the well-established $\nu = 0.67$ and Eq. 2, we obtain $z = 1.4(4)$. In contrast, MF theory does not provide a self-consistent interpretation of our results, as fixing $\nu = 1/2$ yields an inconsistent $z = 0.9(4)$. Interestingly, if we instead fix $\nu z = 1$, which holds at both the MF and F-model levels, from Eq. 2 we obtain a slightly more precise $z = 1.4(2)$ and also recover $\nu = 0.70(8)$.

It would be interesting to study the effect of tunable interactions in a homogeneous atomic gas on the value of b . According to the Ginzburg criterion, near the critical point, MF breaks down for $\xi \geq \xi_G = \lambda_c^2 / (\sqrt{128}\pi^2 a)$, where a is the s-wave scattering length. It is tempting to combine the (dynamical) KZ and (equilibrium) Ginzburg arguments and speculate that one should observe the MF value of b if on approach to T_c the KZ freeze-out occurs before MF breaks down, and the F value of b if the reverse is true. In our ex-

periments, $\xi_G \approx 0.8$ μm and the freeze-out values of ℓ are systematically higher. However, with use of a Feshbach resonance, the opposite regime should be within reach. Another interesting study could focus on the dynamics of domain coarsening. Finally, our methods could potentially be extended to studies of higher-order correlation functions and the full statistics of the domain sizes.

REFERENCES AND NOTES

1. M. Kardar, *Statistical Physics of Fields* (Cambridge Univ. Press, Cambridge, 2007).
2. P. C. Hohenberg, B. I. Halperin, *Rev. Mod. Phys.* **49**, 435–479 (1977).
3. T. W. B. Kibble, *J. Phys. A* **9**, 1387–1398 (1976).
4. W. H. Zurek, *Nature* **317**, 505–508 (1985).
5. A. del Campo, W. H. Zurek, *Int. J. Mod. Phys. A* **29**, 1430018 (2014).
6. I. Chuang, R. Durrer, N. Turok, B. Yurke, *Science* **251**, 1336–1342 (1991).
7. C. Bauerle, Y. M. Bunkov, S. Fisher, H. Godfrin, G. Pickett, *Nature* **382**, 332–334 (1996).
8. V. Ruutu et al., *Nature* **382**, 334–336 (1996).
9. R. Carmi, E. Polturak, *Phys. Rev. B* **60**, 7595–7600 (1999).
10. R. Carmi, E. Polturak, G. Koren, *Phys. Rev. Lett.* **84**, 4966–4969 (2000).
11. R. Monaco, J. Mygind, R. J. Rivers, *Phys. Rev. Lett.* **89**, 080603 (2002).
12. L. E. Sadler, J. M. Higbie, S. R. Leslie, M. Vengalattore, D. M. Stamper-Kurn, *Nature* **443**, 312–315 (2006).
13. C. N. Weiler et al., *Nature* **455**, 948–951 (2008).
14. D. Chen, M. White, C. Borries, B. DeMarco, *Phys. Rev. Lett.* **106**, 235304 (2011).
15. G. Lamporesi, S. Donadello, S. Serafini, F. Dalfvo, G. Ferrari, *Nat. Phys.* **9**, 656–660 (2013).
16. S. Braun et al., <http://arxiv.org/abs/1403.7199> (2014).
17. L. Corman et al., *Phys. Rev. Lett.* **113**, 135302 (2014).
18. L. Chomaz et al., <http://arxiv.org/abs/1411.3577> (2014).
19. S. C. Chae et al., *Phys. Rev. Lett.* **108**, 167603 (2012).
20. S. Ulm et al., *Nat. Commun.* **4**, 2290 (2013).
21. K. Pyka et al., *Nat. Commun.* **4**, 2291 (2013).

22. S. Ejtemaee, P. Haljan, *Phys. Rev. A* **87**, 051401(R) (2013).
23. A. L. Gaunt, T. F. Schmidutz, I. Gotlibovych, R. P. Smith, Z. Hadzibabic, *Phys. Rev. Lett.* **110**, 200406 (2013).
24. J. R. Anglin, W. H. Zurek, *Phys. Rev. Lett.* **83**, 1707–1710 (1999).
25. S. Dettmer et al., *Phys. Rev. Lett.* **87**, 160406 (2001).
26. I. Gotlibovych et al., *Phys. Rev. A* **89**, 061604(R) (2014).
27. E. W. Hagley et al., *Phys. Rev. Lett.* **83**, 3112–3115 (1999).
28. See the supplementary materials on Science Online.
29. G. Biroli, L. F. Cugliandolo, A. Sicilia, *Phys. Rev. E* **81**, 050101(R) (2010).
30. Near T_c , the mean free path for classical elastic collisions is about four times larger than the size of the box. Hence, although the evaporation takes place at the box walls, we can also safely assume that T is uniform across the sample.
31. The unfreezing and healing of the system reconcile the small $b \approx 0.3$ and the fact that a fully coherent homogeneous BEC (as in Fig. 1C) can be produced in a relatively modest cooling time, $\sim 10^2 \tau_{\text{el}}$. In harmonically trapped Bose gases, $b \geq 1$ is observed (5, 15), which makes the physics significantly different. In that case, cooling with $\tau_Q \sim 10^2 \tau_{\text{el}}$ is sufficiently slow to directly produce essentially fully coherent BECs.
32. Scaling ℓ to λ_c and τ_Q to τ_{el} , for each data series separately, affects b by < 0.01 .
33. A. A. Pogorelov, I. M. Suslov, *JETP Lett.* **86**, 39–45 (2007).
34. T. Donner et al., *Science* **315**, 1556–1558 (2007).
35. R. Folk, G. Moser, *J. Phys. A* **39**, R207–R313 (2006).

ACKNOWLEDGMENTS

We thank M. Robert-de-Saint-Vincent for experimental assistance; R. Fletcher for comments on the manuscript; and N. Cooper, J. Dalibard, G. Ferrari, B. Phillips, and W. Zwerger for insightful discussions. This work was supported by AFOSR, ARO, DARPA OLE, and EPSRC (grant no. EP/K003615/1). N.N. acknowledges support from Trinity College, Cambridge, and R.P.S. from the Royal Society.

SUPPLEMENTARY MATERIALS

www.sciencemag.org/content/347/6218/167/suppl/DC1
Methods
Fig. S1

14 July 2014; accepted 5 December 2014
10.1126/science.1258676

GUT MICROBIOTA

Antimicrobial peptide resistance mediates resilience of prominent gut commensals during inflammation

T. W. Cullen,^{1,2} W. B. Schofield,^{1,2} N. A. Barry,^{1,2} E. E. Putnam,^{1,2} E. A. Rundell,¹ M. S. Trent,³ P. H. Degnan,⁴ C. J. Booth,⁵ H. Yu,⁶ A. L. Goodman^{1,2*}

Resilience to host inflammation and other perturbations is a fundamental property of gut microbial communities, yet the underlying mechanisms are not well understood. We have found that human gut microbes from all dominant phyla are resistant to high levels of inflammation-associated antimicrobial peptides (AMPs) and have identified a mechanism for lipopolysaccharide (LPS) modification in the phylum Bacteroidetes that increases AMP resistance by four orders of magnitude. *Bacteroides thetaiotaomicron* mutants that fail to remove a single phosphate group from their LPS were displaced from the microbiota during inflammation triggered by pathogen infection. These findings establish a mechanism that determines the stability of prominent members of a healthy microbiota during perturbation.

Human gut microbial communities reside in an open ecosystem subject to disruptions ranging from dietary change to toxin exposure and pathogen invasion. Many of these perturbations, and functional disor-

ders such as irritable bowel syndrome, are accompanied by nonspecific immune responses that disrupt community structure and function (1, 2). Host inflammatory mechanisms to remove harmful organisms and restrict bacteria to the lumen

commonly target conserved molecular patterns found on pathogens and commensals alike, yet healthy gut microbial communities can remain stable for years in humans (3).

Because cationic antimicrobial peptides (AMPs) represent one of the most prominent and non-specific components of the host response to pathogens, we determined the minimum inhibitory concentration (MIC) of polymyxin B (PMB) for a common human gut commensal, *Bacteroides thetaiotaomicron*. PMB is a bacterial cationic AMP with a mode of action similar to that of mammalian AMPs (4). Notably, this commensal exhibits 680- to 2400-fold increased resistance to PMB compared with mammalian enteropathogens or *Escherichia coli* (Fig. 1A, fig. S1, and table S1). A survey of 17 prominent human commensals, representing the three major bacterial phyla in the gut (5), revealed that resistance against multiple inflammation-associated human and murine AMPs is a general feature of the human gut microbiota (Fig. 1B, fig. S1, and table S1).

We screened transposon mutant populations of five human gut commensal species for genes required for fitness in the presence of PMB. This approach identified a single gene (encoded by *BT1854* in *B. thetaiotaomicron*) that mediated PMB resistance in all species tested (Fig. 2A and tables S2 to S4). Targeted deletion and complementation of *BT1854* confirmed this phenotype for multiple AMPs (Fig. 2B and table S1).

BT1854 has limited homology to the phospholipid biosynthetic enzyme PgpB, a phosphatidylglycerol phosphatase (6) that is not implicated in AMP resistance. However, an unusual PgpB homolog, LpxF, catalyzes the removal of the negatively charged 4'-phosphate group from the lipopolysaccharide (LPS) lipid A anchor in a small, phylogenetically heterogeneous group of AMP-resistant pathogens (7–9). Notably, *B. thetaiotaomicron* produces an underphosphorylated lipid A structure when compared to most Gram-negative organisms (10) (fig. S2, A and B).

Mass spectrometry (MS) analysis of lipid A extracted from *B. thetaiotaomicron* revealed a predominant peak at a mass-to-charge ratio (m/z) of 843.6, consistent with the published (10) doubly deprotonated $[M-2H]^{2-}$ ion structure of penta-acylated 4'-dephosphorylated lipid A (predicted exact mass: 844.7 m/z) (Fig. 2C). By contrast, MS analysis of lipid A extracted from the *B. thetaiotaomicron* BT1854 deletion mutant revealed a peak consistent with the $(M-2H)^{2-}$ ion of penta-acylated, bis-phosphorylated lipid A (predicted exact mass: 884.6 m/z) (Fig. 2C). An additional minor peak consistent with a tetra-acylated structure is observed for all strains (Fig. 2C and fig. S2, C and D). Complementation restores the wild-type lipid A profile (fig. S2E). Based on these results, we designated this protein as LpxF.

Characterization of wild-type and *lpxF* mutant strains showed that LpxF increased resistance to inflammation-associated AMPs by neutralizing the negative charge of the cell (Fig. 2D), decreasing AMP binding at the bacterial surface (Fig. 2E and fig. S3A), and reducing AMP-dependent membrane disruption (Fig. 2F and fig. S3B).

If resistance to inflammation-associated AMPs determines Bacteroidetes fitness in the gut, then a strain with reduced AMP resistance should be outcompeted by an isogenic wild-type strain in a mammalian host during inflammation. We established a gnotobiotic model of gut inflamma-

tion by colonizing germ-free mice with a mixture of wild-type, *lpxF* deletion mutant, and complemented (*lpxF*, *lpxF*⁺) *B. thetaiotaomicron* strains 7 days before infection with *Citrobacter rodentium*, a murine enteropathogen that mimics human gastrointestinal infection (11), or an avirulent *tir* mutant incapable of inducing colitis (fig. S4, A to C) (12).

We next monitored the relative abundance of each strain over time in these animals. The *B. thetaiotaomicron* *lpxF* deletion mutant was rapidly displaced by wild-type and *lpxF*, *lpxF*⁺ complemented strains in mice infected with *C. rodentium* (Fig. 3A and table S5). Displacement occurred at the onset of inflammation (fig. S5, A and B) and concurrent with increased AMP secretion measured from colonic tissue explants (fig. S5C). By contrast, the *lpxF* deletion mutant was able to persist in mice that had not been infected with *C. rodentium* (Fig. 3B) and in mice infected with the noninflammatory *C. rodentium* *tir* mutant, which colonizes the gut to levels similar to those of the wild-type pathogen (Fig. 3C). The *lpxF* mutant was also outcompeted in gnotobiotic mice exposed to dextran sulfate sodium (DSS), a chemical inducer of intestinal inflammation, at the onset of inflammation (Fig. 3D; fig. S4, A to C; and fig. S5). Exposure in vitro to numerous AMPs, but not *C. rodentium* or DSS, recapitulates the in vivo results (fig. S4, D and E). LpxF thus appears to be a general determinant of resilience during inflammation and not a specific requirement for response to *C. rodentium*.

If resistance to AMPs is also important for resilience in the context of a multiphylum human gut microbiota residing in the mammalian gut environment, then a mutant sensitive to AMPs should exhibit a loss of resilience in this community. We colonized germ-free mice with 14 bacterial species, including wild-type *B. thetaiotaomicron*, that represent the three dominant phyla observed in the human gut (tables S6 to S8) (13). Notably, this community remained largely stable through the

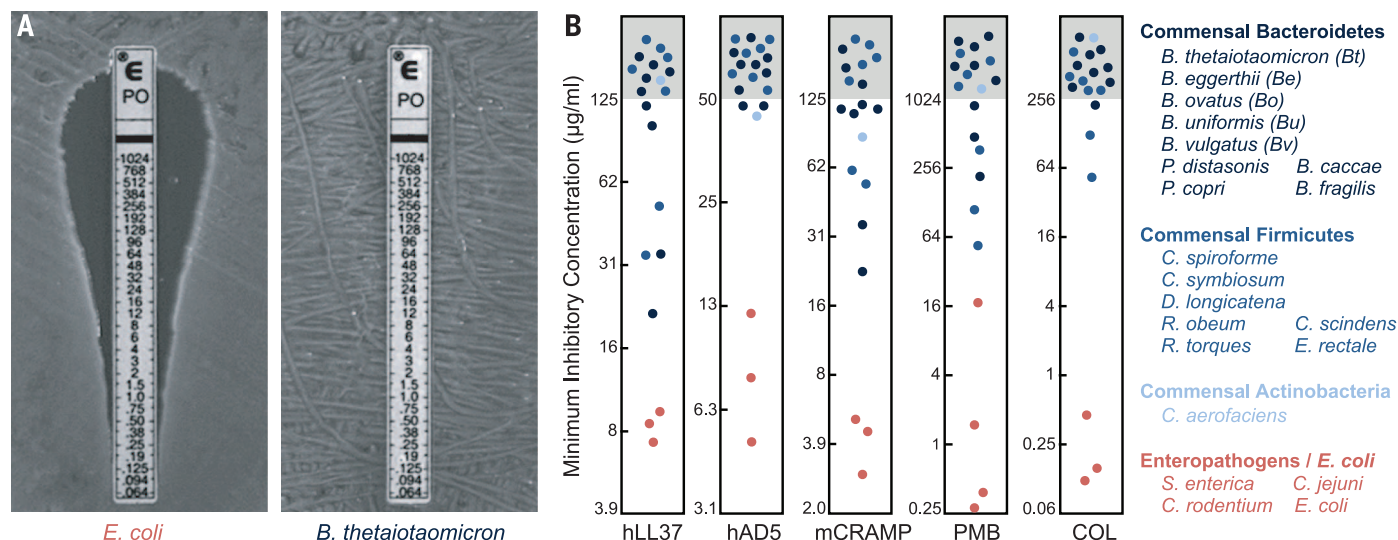


Fig. 1. Human gut commensals are highly resistant to cationic AMPs. (A) MIC of PMB against *E. coli* and *B. thetaiotaomicron*. **(B)** MICs of human and mouse inflammation-induced AMPs and bacterial surrogates against prominent human gut commensal bacteria (blue) and enteropathogens (red). MICs of PMB and colistin were determined with E-test strips; others were determined with the microtiter broth dilution method. See also fig. S1 and table S1.

course of *C. rodentium* infection (Fig. 4A) and associated inflammatory events. To determine whether LpxF is required for this stability during

perturbation, we replaced *B. thetaiotaomicon* with the *lpxF* deletion mutant. Unlike wild-type *B. thetaiotaomicon*, the *lpxF* mutant was rapidly

and specifically displaced from the defined human gut microbiome upon *C. rodentium* infection and consequent host inflammation (Fig. 4B)

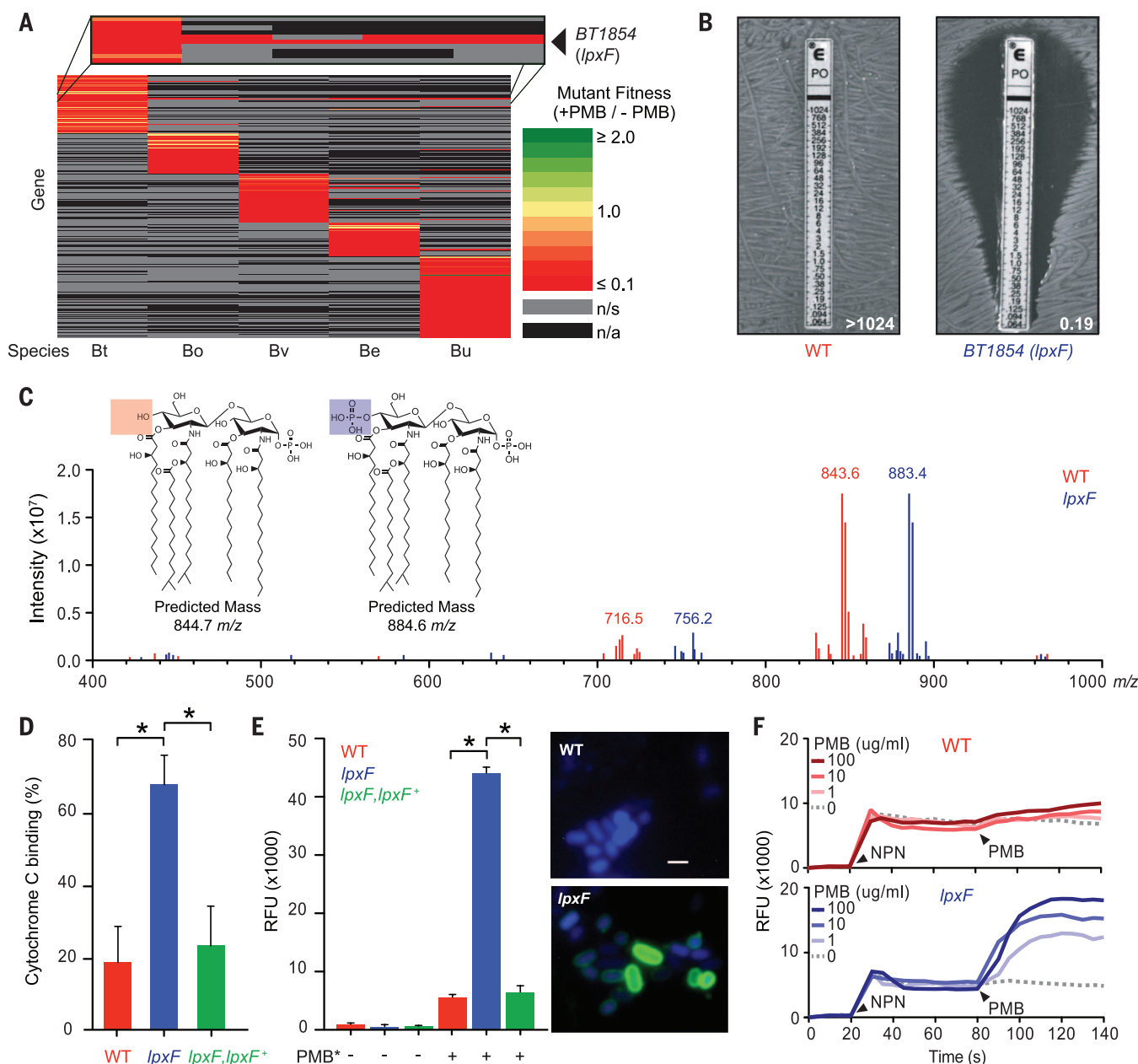


Fig. 2. Lipid A dephosphorylation mediates AMP resistance in prominent human gut bacteria. (A) Heat map of the relative fitness of transposon mutant strains in the presence and absence of PMB. Columns indicate human gut bacterial species tested (abbreviations from Fig. 1B); rows indicate gene orthologs with insertions displaying a significantly altered fitness ($q < 0.05$) in the presence of PMB in at least one species. n/s, not significantly altered; n/a, no ortholog. (B) BT1854 (*lpxF*) is necessary for PMB resistance in *B. thetaiotaomicon*. Representative MIC assessed with the E-test method is shown. (C) LpxF is required for dephosphorylation of lipid A. Fourier transformation cyclotron resonance MS analysis of lipid A isolated from wild-type (red) and *lpxF* deletion mutant (blue) *B. thetaiotaomicon* revealed a shift of the predominant peak by ~ 40 m/z, consistent with the gain of a single phosphate group. Inset shows predicted structures and m/z values of the doubly deprotonated ($[M-2H]^{2-}$) ions for monophosphorylated (red) and bis-phosphorylated (blue)

penta-acylated lipid A. Minor peaks are consistent with tetra-acylated lipid A structures (fig. S2, C and D). (D) Deletion of *lpxF* increases cationic cytochrome c binding to *B. thetaiotaomicon*, indicating altered surface charge. (E) Increased PMB-Oregon Green (PMB*) binding to *lpxF* deletion mutant cells measured by fluorescence quantification (left panel) and microscopy (right panels). Error bars represent SDs and asterisks indicate significance ($P < 0.01$). Representative fluorescence microscopy images of bacterial cells incubated with PMB* (green) are shown as an overlay with 4',6'-diamino-2-phenylindole (DAPI) (blue). Scale bar indicates 2 μ m. (F) LpxF protects the outer membrane from PMB perturbation. 1-N-phenyl naphthylamine (NPN) uptake profiles of select strains were measured followed by challenge with the indicated concentration of PMB. Arrowheads indicate the addition of NPN (20 s) and PMB (80 s). Readings were taken in 5-s intervals. Each experiment was performed in triplicate with representative results shown. See fig. S3 for complementation.

and fig. S6A). By contrast, in the absence of *C. rodentium* infection, both the *B. thetaiotaomicron* wild-type and *lpxF* mutant-containing communities remained stable for the duration of the experiment (fig. S6B).

Germ-free mice have an immature innate immune system (14) that is largely rescued by colonization with mouse, but not human, microbiota (15). We tested whether *B. thetaiotaomicron* requires LpxF in animals with a complete mouse microbiota and a mature innate immune system. Because human gut *Bacteroides* spp. are rapidly outcompeted in specific pathogen-free (SPF) wild-type mice (16), we screened multiple strains of mice and found that *B. thetaiotaomicron*, like *B. fragilis* (16), stably colonized SPF *Rag*^{-/-} animals (Fig. 4C). In these mice, the *B. thetaiotaomicron* *lpxF* deletion mutant colonized to levels equivalent to those of the wild type (Fig. 4C). *B. thetaiotaomicron* resilience during *C. rodentium* infection of these SPF mice remained dependent on LpxF, indicating that the inflammation caused by pathogen infection, rather than other members of the commensal mouse microbiota, mediated the requirement for AMP resistance (Fig. 4D). Many innate immune defects observed in germ-free

mice are also abrogated by segmented filamentous bacteria (SFB), a mouse commensal that interacts directly with the gut epithelium (15). The *lpxF* deletion mutant remained stable over time in gnotobiotic mice monoassociated with SFB, indicating that even a pure population of immunostimulatory commensal members of the host's native microbiota does not induce a requirement for AMP resistance (fig. S6C).

LpxF orthologs are readily identified in all sequenced human-associated Bacteroidetes, and all characterized LPS structures in this phylum reveal an underphosphorylated lipid A structure (fig. S7), suggesting that all human gut Bacteroidetes use this mechanism to resist inflammatory perturbations. We conducted a human study to determine whether our observations from sequenced type strains extend to gut commensals captured directly from humans. To this end, we cultured 733 species-level phylotypes from 12 unrelated, healthy donors (table S9). These cultured strains represent ~98% of the donors' original, uncultured communities at the phylum level, ~95% at the class and order levels, ~80% at the family level, and ~50% at the genus level (fig. S8A). Quantification of PMB resistance across these culture

collections established that the AMP resistance profiles of fecal microbial communities isolated directly from humans mirror the phylum-level patterns observed in sequenced type strains (Fig. 4E and fig. S8B).

Understanding mechanisms of microbiota stability is important for efforts to manipulate these communities for therapeutic purposes. We found that the ability of prominent human gut commensal bacteria to resist killing by AMPs also mediated stability during infection. This resilience hinges on a protein that removes a single phosphate group from the bacterial LPS to determine whether the host maintains or removes commensal bacteria in response to inflammation. In this way, commensal-encoded mechanisms for persistence in the host during inflammation complement host-encoded mechanisms for immune tolerance of the microbiota (17). As observed in certain pathogens, lipid A modification may provide additional benefits to commensal microbes beyond AMP resistance, including reduced activation of the host Toll-like receptor 4-myeloid differentiation factor 2 (TLR4-MD2) complex that recognizes common forms of bacterial LPS (7, 8, 10, 18–23). Our studies indicate

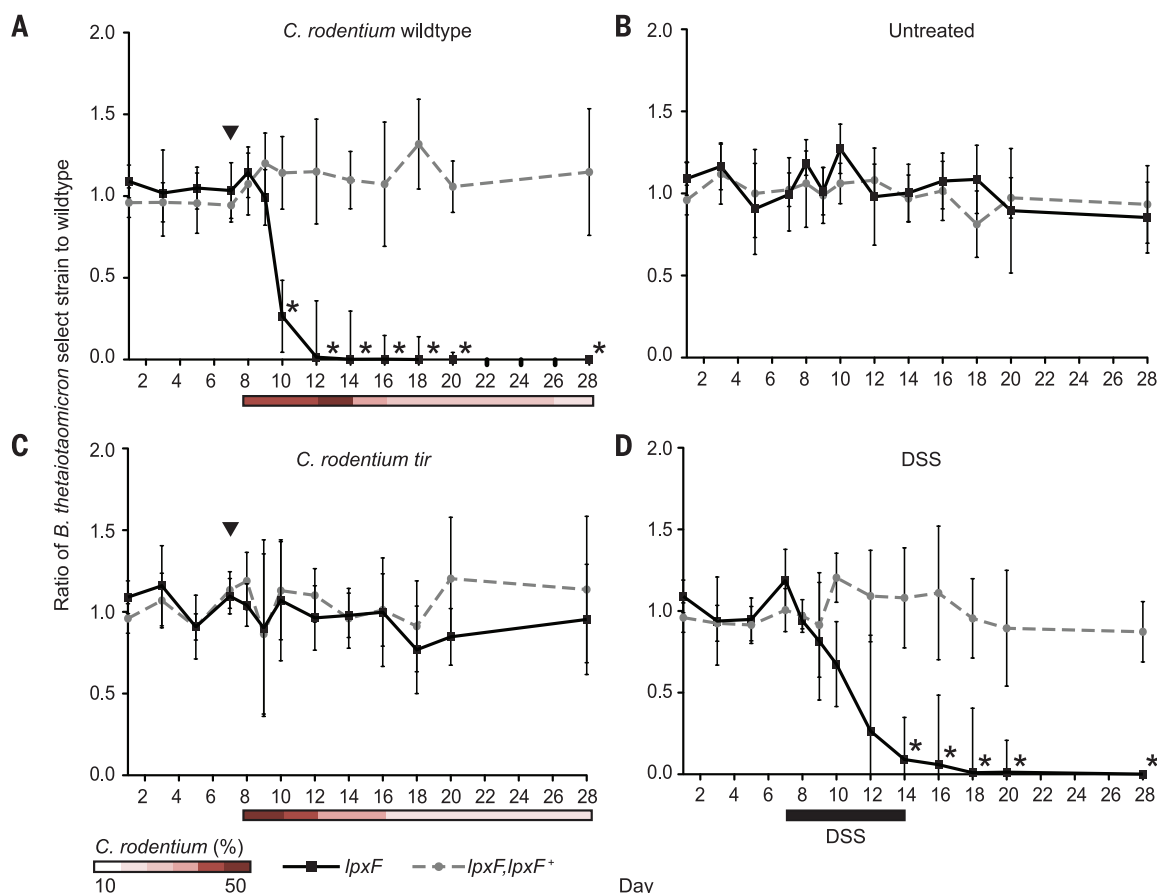


Fig. 3. AMP resistance determines the resilience of a prominent human gut symbiont in gnotobiotic mice with colitis. Germ-free mice ($n = 5$ per group) were colonized with wild-type, the *lpxF* deletion mutant (solid lines), and complemented (*lpxF, lpxF*⁺; dashed lines) *B. thetaiotaomicron* strains 7 days before initiation of inflammation by *C. rodentium* infection (A); no further

treatment (B), infection with a noninflammatory *C. rodentium tir* mutant (C), or exposure to 3% DSS ad libitum for 7 days (black bar) (D). Infection with *C. rodentium* strains is indicated by black arrowheads, and relative *C. rodentium* abundances are reported as percentage of total fecal DNA (shaded bars); error bars represent SD and asterisks indicate significant ($P < 0.01$) differences.

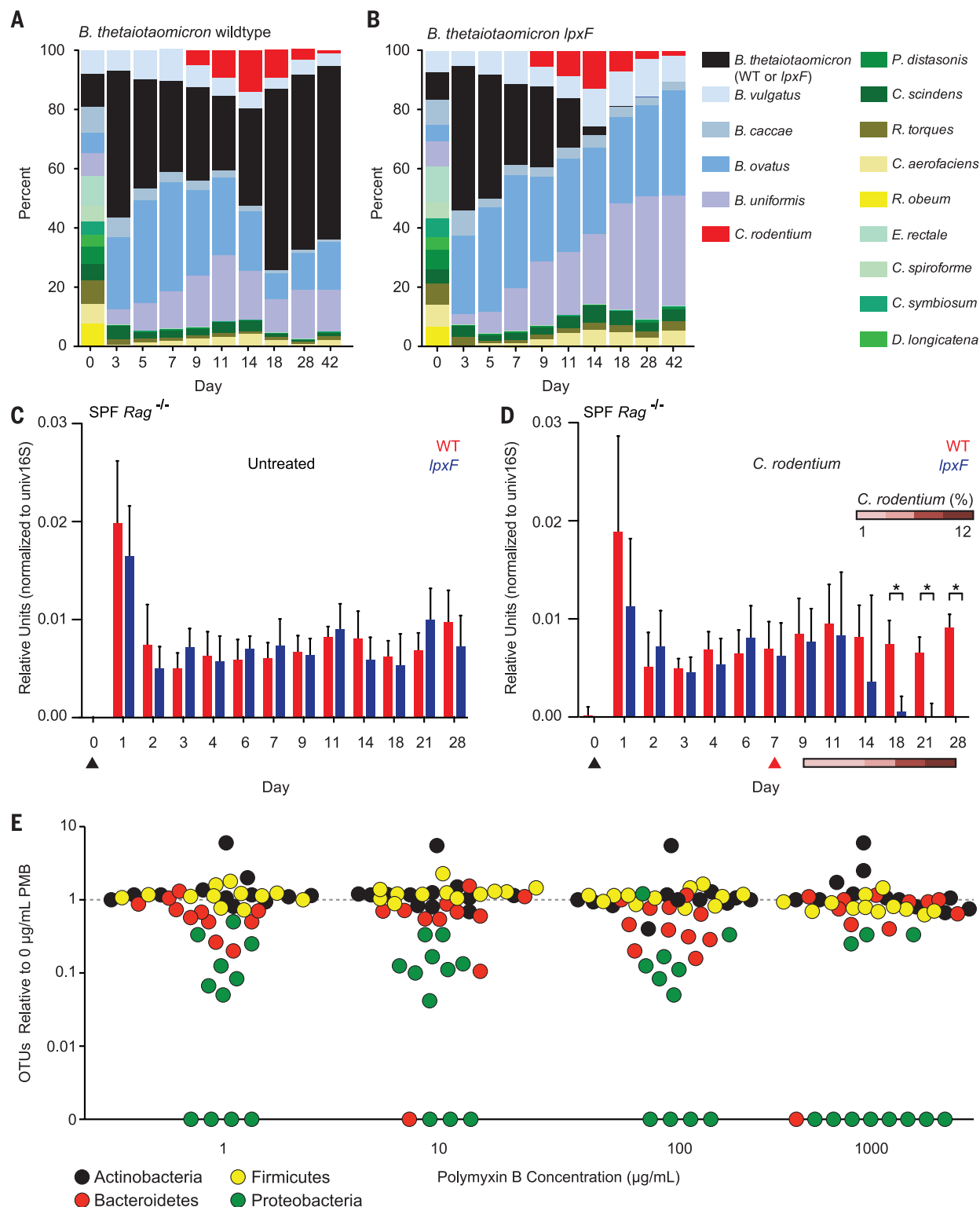


Fig. 4. AMP resistance determines commensal resilience in the context of a human or murine gut microbiota. (A and B) Germ-free mice ($n = 5$ per group) were colonized with 14 prominent human gut microbes, including *B. thetaiotaomicroon* wild-type or *lpxF* deletion mutant, 7 days before infection with *C. rodentium*;

community composition was monitored by species-specific quantitative polymerase chain reaction (QPCR) and reported as median percentage of total. Uninfected controls are shown in fig. S6B. (C and D) Specific pathogen-free *Rag*^{-/-} mice ($n = 5$ per group) were gavaged (black arrowhead) with either *B. thetaiotaomicroon* wild-type or *lpxF* deletion mutant; in (D), mice were infected with *C. rodentium* 7 days later (red

arrowhead). Colonization levels were assessed by QPCR from fecal DNA. *C. rodentium* levels are reported as the percentage of total fecal DNA. Error bars indicate SD and asterisks indicate significance ($P < 0.05$). (E) AMP resistance is a general feature of human gut Bacteroidetes, Firmicutes, and Actinobacteria. Fecal samples from 12 unrelated, healthy human donors were cultured on varying PMB concentrations (x axis), and the number of species-level phylotypes (operational taxonomic units; OTUs) belonging to each phylum observed from each donor (points, colored by phylum) was normalized to the number observed in culture in the absence of PMB. A weighted (abundance) analysis provides similar results (fig. S8B).

that LpxF is dispensable in the absence of inflammation, suggesting that the broad conservation of this enzyme across commensal Bacteroidetes reflects selective pressures imposed by periodic inflammatory events. A delicate balance between microbial resilience and host tolerance thus allows for commensal persistence throughout a diverse range of perturbations while preventing commensal overgrowth or depletion, either of which could have deleterious effects on the host.

REFERENCES AND NOTES

1. J. Langhorst et al., *Am. J. Gastroenterol.* **104**, 404–410 (2009).
2. L. V. Hooper, D. R. Littman, A. J. Macpherson, *Science* **336**, 1268–1273 (2012).
3. J. J. Faith et al., *Science* **341**, 1237439 (2013).
4. M. Vaara, *Microbiol. Rev.* **56**, 395–411 (1992).
5. J. Qin et al., *Nature* **464**, 59–65 (2010).
6. T. Icho, C. R. Raetz, *J. Bacteriol.* **153**, 722–730 (1983).
7. T. W. Cullen et al., *PLOS Pathog.* **7**, e1002454 (2011).
8. S. R. Coats, T. T. To, S. Jain, P. H. Braham, R. P. Darveau, *Int. J. Oral Sci.* **1**, 126–135 (2009).
9. X. Wang, S. C. McGrath, R. J. Cotter, C. R. Raetz, *J. Biol. Chem.* **281**, 9321–9330 (2006).
10. S. R. Coats et al., *Infect. Immun.* **79**, 203–210 (2011).
11. R. Mundy, T. T. MacDonald, G. Dougan, G. Frankel, S. Wiles, *Cell. Microbiol.* **7**, 1697–1706 (2005).
12. E. M. Mallick et al., *Front. Microbiol.* **3**, 11 (2012).
13. A. L. Goodman et al., *Cell Host Microbe* **6**, 279–289 (2009).
14. J. L. Round, S. K. Mazmanian, *Nat. Rev. Immunol.* **9**, 313–323 (2009).
15. H. Chung et al., *Cell* **149**, 1578–1593 (2012).
16. S. M. Lee et al., *Nature* **501**, 426–429 (2013).
17. S. Vaishnava et al., *Science* **334**, 255–258 (2011).
18. E. T. Rietschel et al., *FASEB J.* **8**, 217–225 (1994).
19. T. W. Cullen, M. S. Trent, *Proc. Natl. Acad. Sci. U.S.A.* **107**, 5160–5165 (2010).
20. N. L. Que-Gewirth et al., *J. Biol. Chem.* **279**, 25420–25429 (2004).
21. D. Kanistanon et al., *PLOS Pathog.* **4**, e24 (2008).
22. N. J. Phillips, B. Schilling, M. K. McLendon, M. A. Apicella, B. W. Gibson, *Infect. Immun.* **72**, 5340–5348 (2004).
23. R. S. Munford, *Infect. Immun.* **76**, 454–465 (2008).

ACKNOWLEDGMENTS

We thank E. Groisman, J. Galan, and the Goodman lab for helpful suggestions; C. Jacobs-Wagner for microscopy assistance; J. Leong for *C. rodentium* strains; and I. Ivanov for SFB. This work was supported by NIH grants DK089121, GM103574, GM105456, the Global Probiotics Council, and the Crohn's and Colitis Foundation of America to A.L.G. NIH grants AI064184 and AI76322 to M.S.T.; and Army Research Office grant W911NF-12-1-0390 to M.S.T. All human studies were conducted with approval from the Yale University Human Investigation Committee, and the sequences reported in this paper have been deposited with the European Bioinformatics Institute under accession number PRJEB7697.

SUPPLEMENTARY MATERIALS

www.sciencemag.org/content/347/6218/170/suppl/DC1
Materials and Methods

Figs. S1 to S8

Tables S1 to S9

References (24–53)

29 August 2014; accepted 21 November 2014
10.1126/science.1260580

EPIDEMIOLOGY

Opposite effects of anthelmintic treatment on microbial infection at individual versus population scales

Vanessa O. Ezenwa^{1*} and Anna E. Jolles²

Parasitic worms modulate host immune responses in ways that affect microbial co-infections. For this reason, anthelmintic therapy may be a potent tool for indirectly controlling microbial pathogens. However, the population-level consequences of this type of intervention on co-infecting microbes are unknown. We evaluated the effects of anthelmintic treatment on bovine tuberculosis (BTB) acquisition, mortality after infection, and pathogen fitness in free-ranging African buffalo. We found that treatment had no effect on the probability of BTB infection, but buffalo survival after infection was ninefold higher among treated individuals. These contrasting effects translated into an approximately eightfold increase in the reproductive number of BTB for anthelmintic-treated compared with untreated buffalo. Our results indicate that anthelmintic treatment can enhance the spread of microbial pathogens in some real-world situations.

Helminths are among the most ubiquitous parasites on earth, infecting more than 1 billion people (1) and causing substantial production losses in livestock (2). Because chronic helminth infection can modulate host immune responses, there is considerable interest in the role helminth infection may play in the progression of co-infecting microbial diseases (3, 4). In the laboratory, mouse and nonhuman primate studies show that helminths can skew host immunity in ways that alter the outcomes of viral and bacterial infec-

tions (5–7). Specifically, T helper cell 2 (T_H2) responses triggered by helminths can bias the mammalian immune responses away from antiviral or antibacterial T_H1 responses, increasing host vulnerability to certain intracellular pathogens. Some human studies have also linked helminth coinfection to enhanced morbidity for other infectious diseases, such as tuberculosis and HIV (8–11). Although individual studies suggest that the specific outcomes of helminth coinfection can vary by pathogen system, important trends have emerged linking concurrent helminth infection to changes in host responses to microbial infections (4). This general observation has triggered calls for integrating anthelmintic treatment into control efforts for some microbial diseases of humans as a means of improving disease outcomes (12–14). However, few data exist to show how such individual-level interventions might

affect population-level disease patterns of target microbes.

We used a wild population of African buffalo (*Syncerus caffer*), naturally infected with gastrointestinal helminths (strongyle nematodes of various species) and exposed to bovine tuberculosis (BTB, *Mycobacterium bovis*), to investigate the consequences of anthelmintic treatment on BTB dynamics (15). Patterns of BTB and nematode infection in buffalo indicate strong immune-mediated interactions between the two parasites (16). Moreover, short-term anthelmintic treatment of buffalo has been shown to increase T_H1 immunity, demonstrating that helminth-mediated immune suppression occurs in this species (17). By monitoring a cohort of more than 200 anthelmintic-treated and control animals, we tested for the effects of treatment on immunity, BTB infection probability, and BTB-associated mortality and then explored the implications of treatment for the fitness of *M. bovis*, as measured by this pathogen's reproductive number (15). We found that treatment improved the survival of individual hosts infected with BTB but also enhanced pathogen fitness.

We captured 216 female African buffalo in Kruger National Park, South Africa, approximately every 182 days over a 4-year period. At capture, animals in the experimental group ($n = 108$) received a long-lasting anthelmintic bolus (Panacur; Intervet, UK), whereas controls ($n = 108$) were left untreated. At the beginning of the experiment, all of these animals were BTB-free. Before anthelmintic treatment, the treated and control groups did not differ in their likelihood of being infected with worms (control = 57 of 103; treated = 55 of 107; Pearson's χ^2 test, $\chi^2 = 0.33$, $P = 0.57$) nor in the number of worm eggs they were shedding in feces (Wilcoxon rank sum test, $Z = 1.16$, $P = 0.25$). After treatment, treated individuals were less likely to be infected with worms [generalized linear mixed model (GLMM), $n = 214$ individuals, 1134 observations, β estimate \pm SE (control) = 1.69 ± 0.27 , $P < 0.0001$ (table S1)] and were shedding significantly fewer worm eggs than were

¹Odom School of Ecology and Department of Infectious Diseases, College of Veterinary Medicine, University of Georgia, Athens, GA 30602, USA. ²College of Veterinary Medicine and Department of Integrative Biology, Oregon State University, Corvallis, OR 97331, USA.

*Corresponding author. E-mail: vezenwa@uga.edu

controls [GLMM, $n = 214$ individuals, 1134 observations, β estimate \pm SE (control) = 2.49 ± 0.491 , $P < 0.0001$ (table S2)]. The probability of worm infection and egg count were also correlated with the time since last drug administration (capture interval). Infection was more likely and egg count higher as the capture interval lengthened [GLMM, infection probability, β estimate \pm SE = 0.008 ± 0.002 , $P < 0.0001$ (table S1); egg count, β estimate \pm SE = $0.002 \pm 6.3 \times 10^{-5}$, $P < 0.0001$ (table S2)]. The capture interval effect was most likely the result of reinfection in treated individuals over time. The treatment significantly affected host T_H1 immunity, measured by interferon- γ (IFN- γ) secretion in response to a pokeweed mitogen challenge. IFN- γ plays a central role in the host's defense against tuberculosis (18), and treated animals mounted stronger IFN- γ responses than did controls, suggesting that anthelmintic treatment increased T_H1 immunity (Fig. 1A and table S3).

With the loss of worms and increase of T_H1 immunity, we expected disease parameters to change. Of 201 animals with BTB test histories, 69 acquired BTB infection during the study period (control, 36 of 101; treated, 33 of 100). Accounting for herd, the relative risk of BTB conversion for control animals compared with treated animals was approximately one. Anthelmintic treatment was not a significant predictor of BTB infection risk [hazard ratio (HR) = 0.988, 95% confidence interval (CI) 0.615 to 1.586, $P = 0.959$ (Fig. 2B and table S4)]. However, anthelmintic treatment status was a strong predictor of mortality risk after BTB infection. Of 58 BTB positive animals with known fates, 13 died during the study period (control, 11 of 30; treated, 2 of 28). Mortality risk was approximately ninefold higher among controls than among treated animals after accounting for age [HR = 9.28, 95% CI 1.93 to 44.6, $P = 0.0054$ (Fig. 2C and table S5)]. Thus, although anthelmintic treatment had no observable effect on BTB infection probability, the mortality of BTB-positive individuals was significantly reduced by treatment.

IFN- γ is known to limit tuberculosis severity in cattle, mice, and humans (18, 19); thus, the enhanced survival of anthelmintic-treated BTB-positive buffalo may be a direct consequence of improved T_H1 immunity. The role of IFN- γ in BTB protection in wildlife species is unknown, but our survival result corroborates correlational data from another buffalo population, suggesting that BTB-infected buffalo with worm infections suffer higher mortality than that of individuals infected with either BTB or worms alone (16).

The lack of a treatment effect on BTB incidence could arise for at least two reasons. First, in herd animals such as buffalo, exposure to BTB may be frequent because of high contact rates among individuals. In this situation, a modest reduction in susceptibility by improved T_H1 immunity may not be sufficient to cause a detectable reduction in BTB infection risk. Second, initial protection from tuberculosis infection involves several innate immune defenses, and suc-

cessful elimination of *Mycobacteria* can occur before the onset of T cell-mediated adaptive immunity in humans and laboratory animals (20). Therefore, enhancement of T_H1 cell immunity alone may be insufficient to confer effective protection from BTB infection. In a recent study, human subjects with lower peripheral blood neutrophil counts were found to be at higher risk of *M. tuberculosis* infection, and neutrophil depletion impaired the ability of whole blood to restrict growth of *M. tuberculosis* and *M. bovis* bacille Calmette Guérin (21). However, we found no difference in neutrophil numbers between control and treated buffalo (Fig. 1B and table S3).

Our observation that anthelmintic treatment had asymmetrical effects on BTB infection probability and mortality has implications for BTB dynamics. The population-level consequences can be visualized by considering the impact of treatment on the basic reproductive number (R_0) of BTB. In a fully susceptible buffalo population, the R_0 of BTB can be calculated as the rate at which new infections arise multiplied by the infectious period: $\beta N \times 1/(\mu + \alpha)$, where β is the transmission rate, N is the population size, μ is the background host mortality rate, and α is the disease-induced mortality rate. Because buffalo develop life-long BTB infections (22), we do not consider pathogen clearance in our calculations. Anthelmintic treatment may decrease R_0 by reducing the susceptibility of buffalo to BTB infection or by decreasing pathogen shedding among infected hosts. Alternatively, treatment could increase R_0 by reducing disease-induced host mortality. We estimated R_0 for treated and control subsets of our buffalo population, accounting for the negligible effects of treatment on BTB susceptibility and strong effects on disease-induced mortality that we observed. We found that anthelmintic treatment resulted in an almost eightfold increase in the relative magnitude of R_0 for BTB in the treated subpopulation (7.73, 95% CI

1.71 to 34.9). Translating this into absolute values, we estimated R_0 for control individuals to be 2, as compared with 15 for treated individuals (Fig. 2D). Because the spread of a pathogen through a host population is generally more rapid with increasing R_0 (23), if BTB were introduced into a fully naïve population, such a difference in the value of R_0 would result in a higher probability of an outbreak occurring and higher overall disease prevalence.

Our results reveal a tension between individual- and population-level consequences of anthelmintic therapy for outcomes of intracellular pathogen co-infections. At the individual level, the outcome of such an intervention is positive because it reduces BTB-induced host mortality in our case and, as recently reported in the literature, the progression or severity of other pathogens such as HIV (10, 24) and *Streptococcus pneumoniae* (25). At the population level, however, the consequences of intervention are negative because surviving, BTB-positive, anthelmintic-treated individuals continue to spread the pathogen. This conflict arises because there is no reduction in BTB infection risk in anthelmintic-treated individuals. Even if treatment reduced bacterial shedding, which could help moderate transmission, there would have to be an almost 90% reduction in *M. bovis* shedding among treated animals to overcome the increase in pathogen fitness resulting from the extended lifespan of these hosts (Fig. 2E).

Because our drug treatment did not eliminate worms from the experimental subjects for the entire duration of the study, it is possible that we failed to observe an effect of anthelmintic treatment on BTB infection risk as a result of poor efficacy. Similarly, most large-scale deworming programs in human populations do not achieve consistent and complete parasite clearance (26). Hence, our results may accurately reflect the outcome of treatment programs applied in real populations.

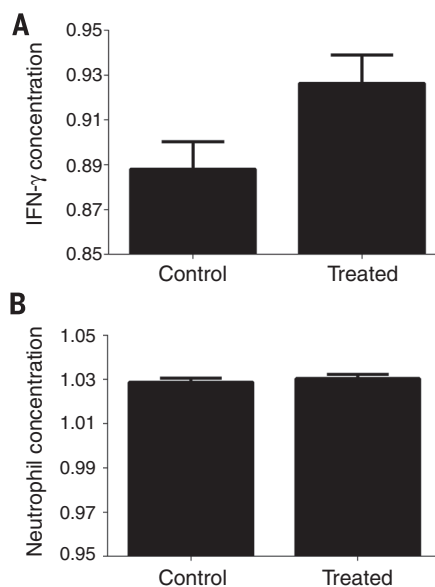


Fig. 1. Effects of anthelmintic treatment on buffalo immunity. (A) Treatment increased IFN- γ responses to pokeweed mitogen stimulation. Accounting for season, herd, age, and capture interval, treated individuals had significantly higher IFN- γ levels than those of controls [linear mixed model (LMM), $n = 212$ individuals, 1020 observations, β estimate \pm SE (control) = -0.0378 ± 0.0162 , $P = 0.02$ (table S3)]. (B) Treatment had no effect on circulating neutrophil concentrations. Accounting for the same covariates as in (A), there was no difference between treated and control individuals in neutrophils [LMM, $n = 211$ individuals, 941 observations, β estimate \pm SE (control) = -0.0011 ± 0.0023 , $P = 0.63$ (table S3)]. Both IFN- γ and neutrophil concentrations were power-transformed for analysis.

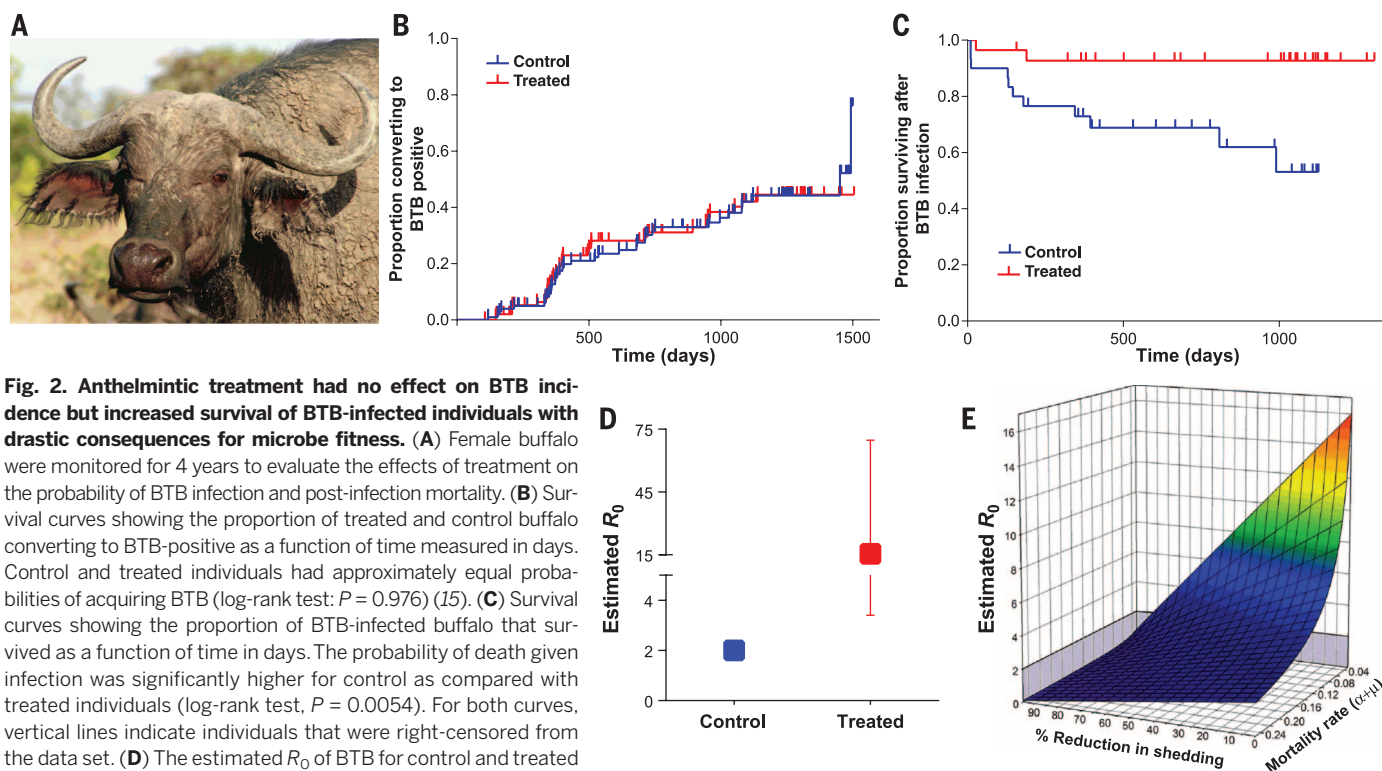


Fig. 2. Anthelmintic treatment had no effect on BTB incidence but increased survival of BTB-infected individuals with drastic consequences for microbe fitness. (A) Female buffalo

were monitored for 4 years to evaluate the effects of treatment on the probability of BTB infection and post-infection mortality. (B) Survival curves showing the proportion of treated and control buffalo converting to BTB-positive as a function of time measured in days. Control and treated individuals had approximately equal probabilities of acquiring BTB (log-rank test: $P = 0.976$) (15). (C) Survival curves showing the proportion of BTB-infected buffalo that survived as a function of time in days. The probability of death given infection was significantly higher for control as compared with treated individuals (log-rank test, $P = 0.0054$). For both curves, vertical lines indicate individuals that were right-censored from the data set. (D) The estimated R_0 of BTB for control and treated subsets of the buffalo population. R_0 is approximately eight times higher for treated individuals (2 versus 15.5), with upper and lower estimates of 3.4 and 69.8, respectively (CIs were not calculated for controls). (E) Estimated R_0 of BTB across the range of mortality rates observed for treated buffalo and control buffalo (~0.03 to 0.24), accounting for possible reductions in bacteria shedding due to treatment (range, 0 to 90%). The area shaded in gray shows the baseline R_0 for control buffalo ($R_0 = 2$). At a mortality rate of ~0.03, as observed for treated buffalo, a reduction in shedding of at least 90% is needed to decrease R_0 to baseline levels.

Large-scale treatment programs that target human helminth infections are expanding around the globe (27). Reduced morbidity in individuals with microbial co-infections is considered a potential added benefit of such treatment programs (27, 28), but based on our findings with BTB, anthelmintic treatment could improve individual morbidity or mortality and simultaneously exacerbate pathogen transmission. This is especially likely for chronic infections such as HIV/AIDS and TB, two human microbial diseases for which anthelmintic treatment strategies are being considered (10, 11). Studies exploring individual- and population-level consequences of different intervention strategies, ranging from mass deworming alone to combined anthelmintic and microbial treatments (13), are urgently needed to establish under what conditions anthelmintic therapy is more likely to alleviate, or exacerbate, the health impacts of microbial co-infections.

REFERENCES AND NOTES

- R. L. Pullan, J. L. Smith, R. Jasrasaria, S. J. Brooker, *Parasites Vectors* **7**, 37 (2014).
- J. Charlier, M. van der Voort, F. Kenyon, P. Suce, J. Vercauteren, *Trends Parasitol.* **30**, 361–367 (2014).
- H. J. McSorley, R. M. Maizels, *Clin. Microbiol. Rev.* **25**, 585–608 (2012).
- P. Salgame, G. S. Yap, W. C. Gause, *Nat. Immunol.* **14**, 1118–1126 (2013).
- T. A. Reese et al., *Science* **345**, 573–577 (2014).
- A. L. Chenine et al., *PLOS Negl. Trop. Dis.* **2**, e265 (2008).
- L. Su et al., *Infect. Immun.* **82**, 3855–3866 (2014).
- A. J. Lankowski et al., *PLOS Negl. Trop. Dis.* **8**, e3036 (2014).
- P. J. George et al., *J. Immunol.* **190**, 5161–5168 (2013).
- J. L. Watson, B. R. Herrin, G. John-Stewart, *Cochrane Database Syst. Rev.* (3): CD006419 (2009).
- W. Rafi, R. Ribeiro-Rodrigues, J. J. Ellner, P. Salgame, *Curr. Opin. HIV AIDS* **7**, 239–244 (2012).
- P. J. Hotez et al., *PLOS Med.* **3**, e102 (2006).
- J. Noblick, R. Skolnik, P. J. Hotez, *PLOS Negl. Trop. Dis.* **5**, e1022 (2011).
- G. Borkow, C. Teicher, Z. Bentwich, *PLOS Negl. Trop. Dis.* **1**, e160 (2007).
- Materials and methods are available as supplementary materials on Science Online.
- A. E. Jolles, V. O. Ezenwa, R. S. Etienne, W. C. Turner, H. Olff, *Ecology* **89**, 2239–2250 (2008).
- V. O. Ezenwa, R. S. Etienne, G. Luikart, A. Beja-Pereira, A. Jolles, *Am. Nat.* **176**, 613–624 (2010).
- J. L. Flynn, J. Chan, *Annu. Rev. Immunol.* **19**, 93–129 (2001).
- M. D. Welsh et al., *Immunology* **114**, 101–111 (2005).
- R. van Crevel, T. H. Ottenhoff, J. W. van der Meer, *Clin. Microbiol. Rev.* **15**, 294–309 (2002).
- A. R. Martineau et al., *J. Clin. Invest.* **117**, 1988–1994 (2007).
- R. G. Bengis, *Tuberculosis*, M. E. Fowler, R. E. Miller, Eds. (W. B. Saunders, Philadelphia, 1999).
- R. M. Anderson, R. M. May, *Infectious Diseases of Humans: Dynamics and Control* (Oxford University Press, Oxford, 1991).
- A. Mulu, M. Maier, U. G. Liebert, *Int. J. Infect. Dis.* **17**, e897–e901 (2013).
- N. Apiwatanakul, P. G. Thomas, R. E. Kuhn, D. R. Herbert, J. A. McCullers, *Med. Microbiol. Immunol. (Berl.)* **203**, 357–364 (2014).
- T. W. Jia, S. Melville, J. Utzinger, C. H. King, X. N. Zhou, *PLOS Negl. Trop. Dis.* **6**, e1621 (2012).
- D. A. Bundy, J. L. Watson, K. L. Watkins, *Trends Parasitol.* **29**, 142–148 (2013).
- P. J. Hotez, *PLOS Negl. Trop. Dis.* **7**, e2570 (2013).

ACKNOWLEDGMENTS

We thank South African National Parks (SANParks) for permission to conduct this study in Kruger and M. Hofmeyr, P. Buss, and the entire SANParks Veterinary Wildlife Services Department for invaluable assistance with animal captures and project logistics. We thank R. Spaan, J. Spaan, K. Thompson, B. Beecher, P. Snyder, and B. Henrichs for work on animal captures and sample processing; A. Park for illuminating discussion about R_0 estimation; and S. Altizer and the Ezenwa and Altizer lab groups for valuable comments on earlier drafts of the manuscript. Animal protocols for this study were approved by the University of Georgia (UGA) and Oregon State University (OSU) Institutional Animal Care and Use Committees (UGA AUP A2010 10-190-Y3-A5; OSU AUP 3822 and 4325). This study was supported by a National Science Foundation Ecology of Infectious Diseases Grant (EF-0723918/DEB-1102493, EF-0723928). The authors report no conflicts of interest related to this research. Data presented in this paper are available from the Dryad Digital Repository (DOI: 10.5061/dryad.q2m38).

SUPPLEMENTARY MATERIALS

www.sciencemag.org/content/347/6218/175/suppl/DC1
Materials and Methods
Tables S1 to S7
References (29–42)

25 September 2014; accepted 5 December 2014
10.1126/science.1261714

STRUCTURAL BIOLOGY

Division of labor in transhydrogenase by alternating proton translocation and hydride transfer

Josephine H. Leung,¹ Lici A. Schurig-Briccio,² Mutsuo Yamaguchi,¹ Arne Moeller,^{3*} Jeffrey A. Speir,³ Robert B. Gennis,² Charles D. Stout^{1†}

NADPH/NADP⁺ (the reduced form of NADP⁺/nicotinamide adenine dinucleotide phosphate) homeostasis is critical for countering oxidative stress in cells. Nicotinamide nucleotide transhydrogenase (TH), a membrane enzyme present in both bacteria and mitochondria, couples the proton motive force to the generation of NADPH. We present the 2.8 Å crystal structure of the transmembrane proton channel domain of TH from *Thermus thermophilus* and the 6.9 Å crystal structure of the entire enzyme (holo-TH). The membrane domain crystallized as a symmetric dimer, with each protomer containing a putative proton channel. The holo-TH is a highly asymmetric dimer with the NADP(H)-binding domain (dIII) in two different orientations. This unusual arrangement suggests a catalytic mechanism in which the two copies of dIII alternatively function in proton translocation and hydride transfer.

Nicotinamide nucleotide transhydrogenase (TH) is an integral membrane protein that can utilize the proton motive force for hydride transfer from NADH (the reduced form of NAD⁺) to NADP⁺ (nicotinamide adenine dinucleotide phosphate), forming NADPH (I): $\text{NADH} + \text{NADP}^+ + \text{H}^+_{\text{out}} \leftrightarrow \text{NAD}^+ + \text{NADPH} + \text{H}^+_{\text{in}}$, where “out” denotes the space outside the prokaryotic plasma membrane and “in” denotes the cytosol (or mitochondrial intermembrane space and matrix in eukaryotes). The resultant NADPH is used for amino acid biosynthesis and by glutathione reductase and glutathione peroxidase to remove reactive oxygen species (2). Mutations in *Nnt* genes, which encode for TH, are correlated with familial glucocorticoid deficiency of the adrenal cortex (3). Mice with mutations in the *Nnt* genes exhibit glucose intolerance and impaired secretion of insulin, as in type 2 diabetes (4, 5).

Functional TH exists as a dimer (6), where each protomer contains three domains: a hydrophilic NAD(H)-binding domain (dI), a transmembrane domain (dII), and a hydrophilic NADP(H)-binding domain (dIII) (Fig. 1A). Despite topological variations of TH subunits across species (fig. S1), dIII is always a C-terminal extension of dII. Hydride transfer between NAD(H) and NADP(H) occurs across the dI-dIII interface; proton translocation is across dII. One proton is translocated across the membrane per hydride transferred between nucleotides (7).

Structures of hydrophilic dI and dIII were previously solved for TH isolated from bovine (8) and human (9) mitochondria as well as from *Rhodospirillum rubrum* (10) and *Escherichia coli* (11). Co-crystallization of dI with dIII results in the asymmetric heterotrimer (dI)₂:dIII (12, 13). We determined the structures of the dimeric (dI)₂ and the heterotrimeric (dI)₂:dIII from *Thermus thermophilus* (*Tt*) TH (fig. S2A and table S1). In each of the heterotrimer structures, the NADP(H)-binding site of dIII is near the NAD(H)-binding site of one copy of dI, poised for direct hydride transfer. If a second copy of dIII were present and obeyed local twofold symmetry, there would be a steric clash between the two copies of dIII (12, 13) (fig. S2B). The structures therefore present a fundamental puzzle: how the second copy of dIII is oriented in the intact enzyme (14, 15) and how hydride

transfer at the dI-dIII interface is coupled to proton translocation across dII, approximately 40 Å away (6, 16). Solving the structures of dII and the intact enzyme from *Tt* TH addresses these questions.

Tt TH is encoded by three genes (α_1 , α_2 , and β): α_1 encodes dI; α_2 encodes the first three transmembrane (TM) helices of dII; and β encodes nine TM helices of dII linked with dIII (Fig. 1B). Based on sequence alignments, two helices (TM1 and TM5) present in TH from some species are missing in *Tt* TH dII (fig. S3). To determine the crystal structure of dII, we made a construct that expresses the α_2 gene and a truncated version of the β gene, in which dIII is replaced by a histidine tag (Fig. 2A). The resulting dII contains 12 TM spans and crystallizes as a symmetric dimer with a twofold axis normal to the membrane plane (Fig. 2B and table S2). The topology is consistent with previous studies of TH from different species, so the fold of dII observed in *Tt* TH is probably universal (17) (fig. S3).

Each dII protomer constitutes a proton pathway where helices TM3-4, TM9-10, and TM13-14 arrange as a hexagram (Fig. 2C). Conserved motifs located at a level corresponding to the middle of the membrane are found within the interior of the hexagram on TM3 (NXXH/S), TM9 (NXXG or HXXV), and TM13 (NXXT/S) (fig. S4). In the *Tt* dII structure, α_2 N39 (TM3), β N89 (TM9), β S132 (TM10), and β N211 (TM13) form a hydrogen bond network (Fig. 2D). Of specific interest is β N89 (TM9); this residue is at the equivalent position as *E. coli* β H91, which has been identified as important for proton translocation by mutagenesis studies (2, 18, 19). Two other residues that have been implicated in proton translocation in *E. coli* TH are β S139 (20) and β N222 (18), which are equivalent to β S132 (TM10) and β N211 (TM13) in *Tt* TH. No ordered water molecules are observed in the structure; hence, this may correspond to an occluded conformation of the proton channel.

On the basis of previous cysteine crosslinking studies, a salt bridge between *E. coli* β D213 and

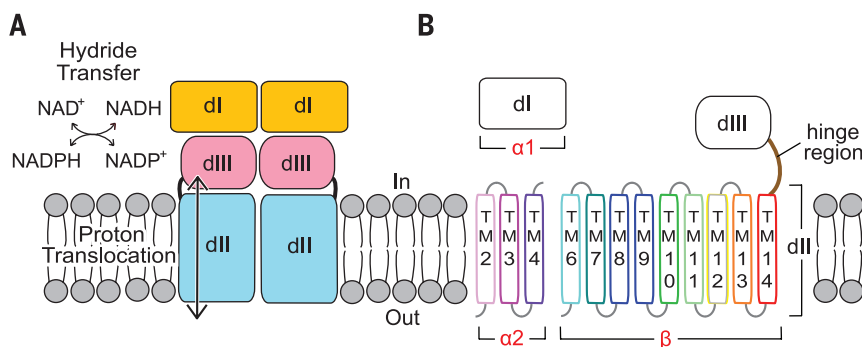


Fig. 1. TH function and structure. (A) Schematic representation of TH function. The NAD(H)-binding domain (dI) and the NADP(H)-binding domain (dIII) catalyze hydride transfer. Proton translocation occurs through the transmembrane domain (dII). “In” represents the prokaryotic cytosol or mitochondrial matrix, and “out” is the space outside the prokaryotic plasma membrane or mitochondrial intermembrane space. (B) A *Tt* TH protomer is encoded by three genes: α_1 encodes dI; α_2 encodes three transmembrane (TM) helices of dII; and the β gene encodes the remaining nine helices of dII, the hinge region, and dIII. TM1 and TM5 of dII are missing in *Tt* TH.

¹Department of Integrative Structural and Computational Biology, The Scripps Research Institute, La Jolla, CA 92037, USA. ²Department of Biochemistry, University of Illinois, Urbana, IL 61801, USA. ³National Resource for Automated Molecular Microscopy, The Scripps Research Institute, La Jolla, CA 92037, USA.

*Present address: Interdisciplinary Nanoscience Center Aarhus University, Gustav Wieds Vej 14, 8000 Aarhus C, Denmark.

†Corresponding author. E-mail: dave@scripps.edu

β R265 has been postulated and implicated as important for both proton translocation in dII and NADP(H) binding in dIII (18, 20, 21). The structure shows that this Asp-Arg salt bridge is formed between the equivalent residues in *Tt* TH, β D202 (TM13), and β R254 (the “hinge region” connecting dII and dIII) and is positioned on the membrane surface adjacent to the entrance of the proton channel (Fig. 2E).

Using the structures of the dI dimer, the dII dimer, and the dIII subunits, we solved the crystal structure of *Tt* holo-TH at 6.9 Å resolution by molecular replacement in Phaser (22) (Fig. 3A and table S3). In the 200-kD holo-TH dimer, two copies of dIII are positioned between the dI and dII dimers in different orientations (fig. S5A). One copy of dIII (dIII-A) has its NADP(H)-binding site “face up” to interact with the NAD(H)-binding site

of dI-A as in the (dI)₂:dIII heterotrimer structures (fig. S2A). The second copy of dIII (dIII-B) occupies the space between dI-B and dII-B, but it is flipped over 180° with its NADP(H)-binding site “face down” toward dII-B. Although the structures of the hinge region between dII and dIII are unknown, both orientations of dIII can be accommodated by the full-length linker in all species (fig. S5B).

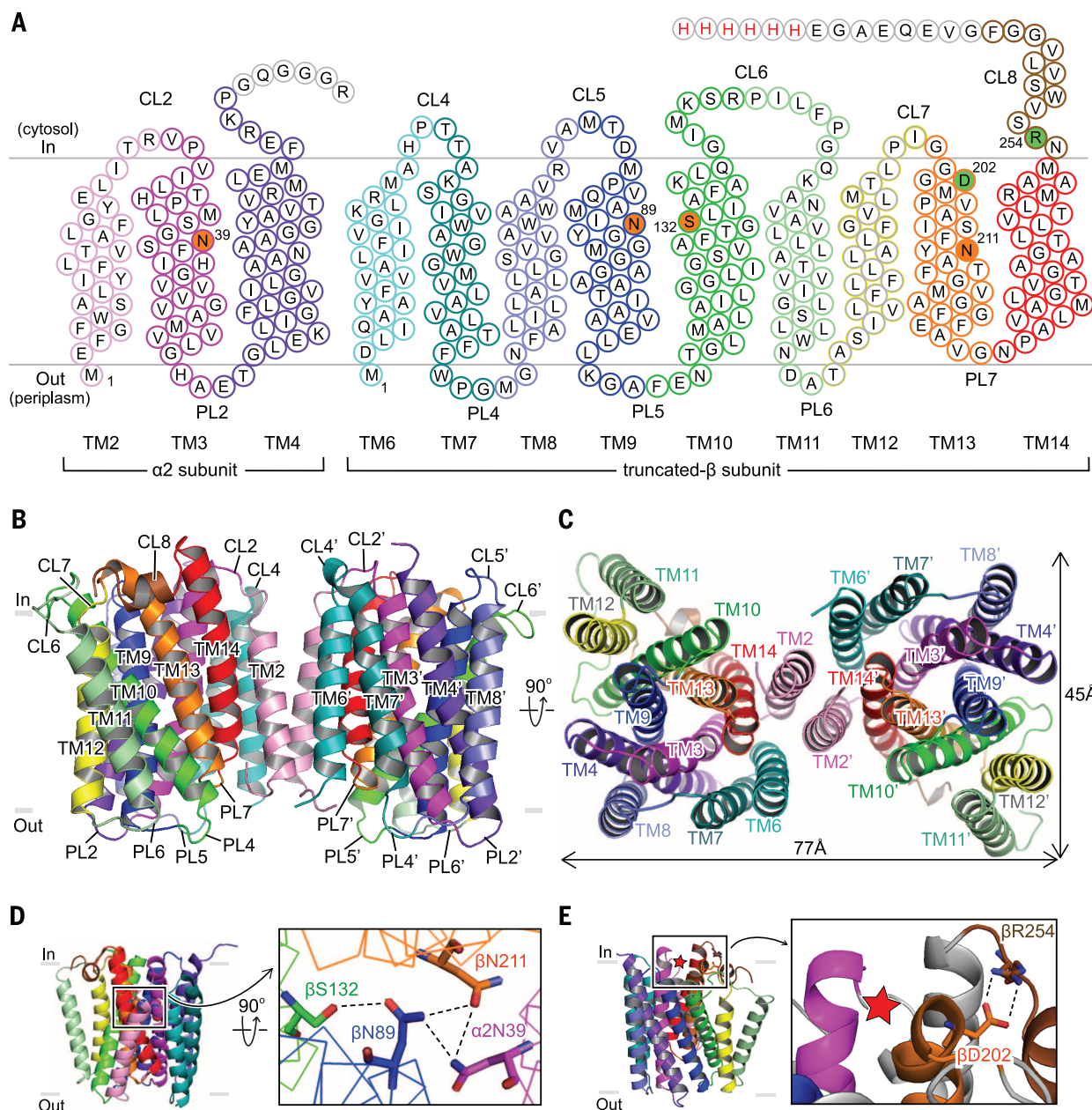


Fig. 2. Structural details of the proton channel. (A) Schematic diagram of the *Tt* dII construct used for crystallization, labeling TM helices, cytoplasmic loops (CL), and periplasmic loops (PL). The *Tt* β gene was truncated at CL8 by a histidine tag (red H). Residues in orange form hydrogen bonds within the proton pathway. Residues in green form a conserved salt bridge. Residues in gray outlines are disordered in the crystal structure. (B and C) Atomic model of the dII dimer viewed from

(B) within the membrane and (C) from the periplasm. TM3, TM9-10, and TM13 form the proton channel. TM2 is at the dimer interface. (D) Residues α N39 (TM3), β N89 (TM9), β S132 (TM10), and β N211 (TM13) form a hydrogen bond network (black dotted lines). (E) The Asp-Arg salt bridge formed by β D202 (TM13) and β R254 (CL8) is located on the membrane surface adjacent to the proton channel opening (red star).

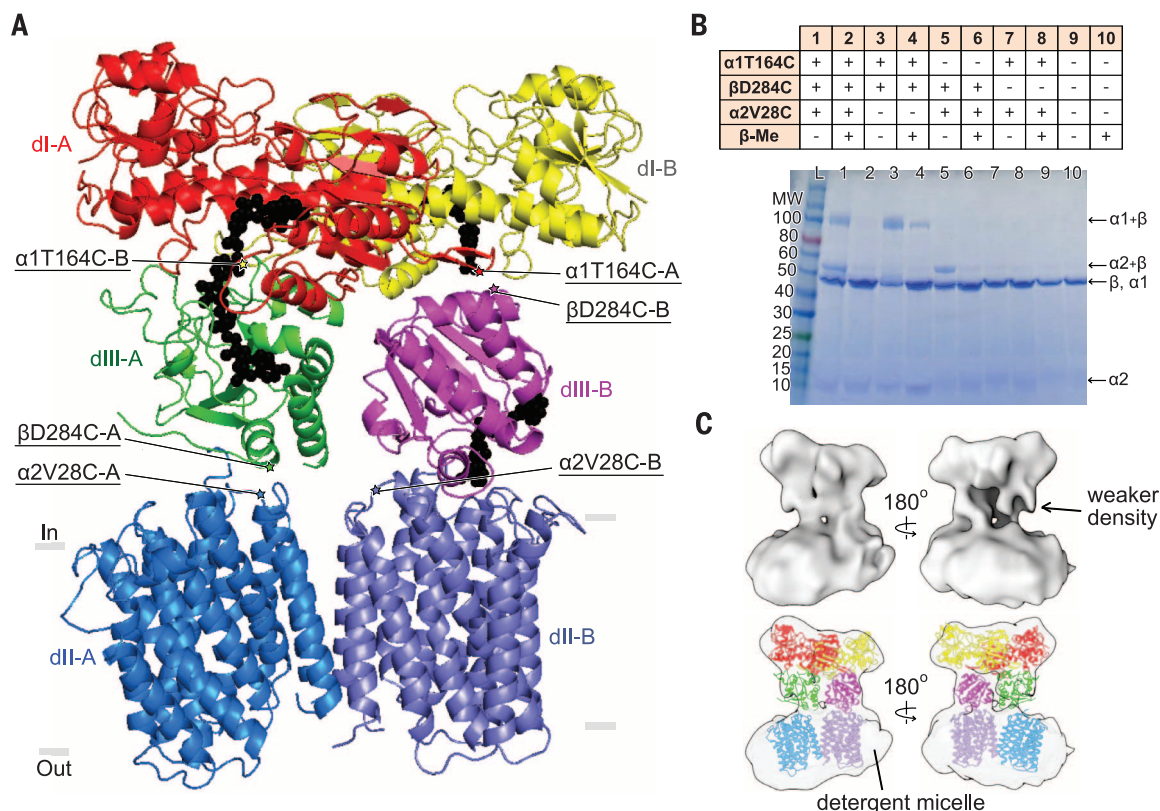


Fig. 3. Structural asymmetry of holo-TH. (A) The crystal structure shows two orientations of dIII: face-up dIII-A (green) and face-down dIII-B (magenta) with respect to their NAD(P)H-binding sites. Nucleotides, NAD(H) in dI, and NADP(H) in dIII, are modeled as black spheres based on the heterotrimer structure (11, 12). Subunits sandwiching dIII-A and dIII-B are respectively labeled as A and B. Underlined labels mark the mutations used for crosslinking experiments. **(B)** SDS-PAGE shows the crosslinking of dIII in two orientations. The table on top describes samples in lanes 1 to

10. For the wild-type enzyme (lane 10), subunits α_1 and β each run with the same apparent molecular weight (MW) of about 45 kD; the α_2 subunit shows a faint band at 10 kD. $\beta D284C$ on dIII can crosslink with either α_1T164C in dI (lanes 1 and 3), forming $\alpha_1+\beta$; or with α_2V28C on dII (lanes 1 and 5), forming $\alpha_2+\beta$. The presence of β -Me largely eliminates the crosslinking (lanes 2, 4, and 6). **(C)** The cryo-EM structure reveals an asymmetric dimer: One copy of dIII exhibits weaker density than the other.

To confirm the existence of the two dIII orientations in holo-TH, pairs of cysteine residues were inserted into holo-TH for crosslinking experiments using the purified enzyme solubilized in detergent. The structure predicts that residue $\beta D284$ (dIII) should be at the interface with dII in the face-up conformation, but at the interface with dI in the face-down conformation. Residue $\beta D284$ was replaced by a cysteine ($\beta D284C$) in combination with a cysteine placed in dI (α_1T164C) and/or dII (α_2V28C). SDS-polyacrylamide gel electrophoresis (PAGE) analysis (Fig. 3B) showed that dIII can crosslink either to dII, forming the $\alpha_2+\beta$ product, or to dI, forming the $\alpha_1+\beta$ product. The crosslinks were largely reversed by β -mercaptoethanol (β -Me). Activity measurements showed that hydride transfer from NADH to NADP⁺ and then back to an NAD⁺ analog (so-called cyclic activity), which is not coupled to proton translocation (23), is minimally influenced by the crosslinking (table S4). In contrast, hydride transfer from NADPH directly to the NAD⁺ analog, which is coupled to proton translocation (24), is decreased by crosslinking and is increased after disrupting the crosslinks. Although the data are not quantitative, it is

clear that the face-down conformation of dIII is present in the active form of holo-TH and is consistent with the importance of domain dynamics for catalytic function (21).

In addition to crystallography, we performed single-particle cryo-electron microscopy (cryo-EM) imaging of detergent-solubilized *Tt* holo-TH, yielding a structure at 18 Å resolution (Fig. 3C and fig. S6). The structure shows that the enzyme is an asymmetric dimer: One copy of dIII is more disordered than the other.

Previous biochemical data have shown that mutations in a conserved Asp residue in the NADP(H)-binding site of dIII, *E. coli* $\beta D392$, abolish both hydride transfer and proton translocation (16); and the rate-limiting step in forward catalysis is the release of the product NADP(H) from dIII (23). The holo-TH structure provides mechanistic implications about how dIII can be involved in proton translocation: The face-down conformation of dIII brings *Tt* $\beta D378$ (equivalent to *E. coli* $\beta D392$) (16) and regions of dIII that regulate NADP(H) binding, including loops D and E (14, 25), close to the surface of the proton channel and the Asp-Arg salt bridge (Fig. 4A). Hence, it is reasonable that the face-down conformation of dIII is

competent for proton translocation, whereas its face-up conformation allows hydride transfer (Fig. 4B). The division-of-labor assignment works into the binding-change model of the catalytic cycle proposed by Jackson and colleagues (26). The model is consistent with previous biochemical determinations: (i) TH exhibits half-of-the-sites reactivity, so that inhibition of one protomer within the dimeric enzyme inhibits the second protomer (23, 24, 27); (ii) There are “open” and “occluded” conformational states of dIII via its loops D and E, summarized in (26). The model assumes that dIII is mobile, which is a reasonable hypothesis because previous cysteine mutations of the Asp-Arg salt bridge (Fig. 2E) lead to crosslinking and inhibition of both proton translocation in dII and NADP(H) binding in dIII (27). The membrane domain is proposed to have a single buried protonatable site (in most cases, a histidine in TM3 or TM9), and this residue can either be (i) deprotonated and occluded, (ii) accessible to protonation by an “outward-facing” conformation, or (iii) accessible to protonation by an “inward-facing” conformation. We speculate that changes in dIII, which include the protonation state of *Tt* $\beta D378$ (*E. coli* $\beta D392$)

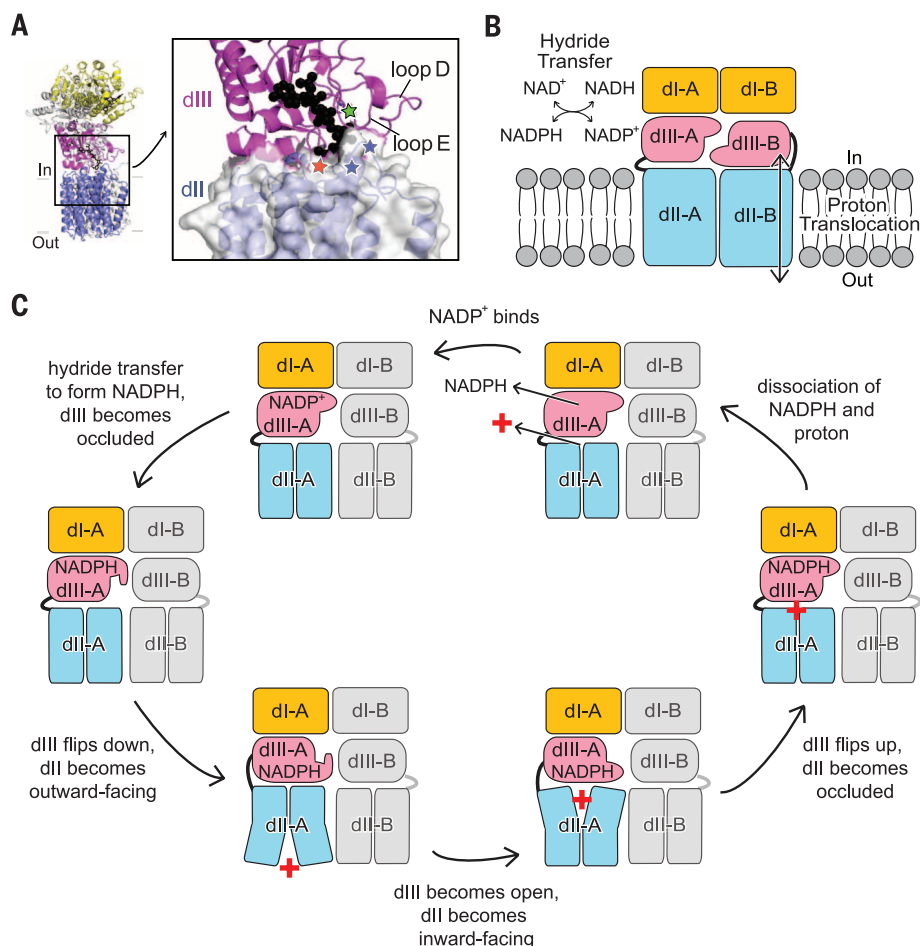


Fig. 4. Possible role of face-down dIII in proton translocation. (A) Regions of dIII that regulate NADP(H) binding, namely loop D, loop E, and Tt β D378 (green star), are close to the proton channel opening (red star) and the Asp-Arg salt bridge (blue stars). The surface area of dII is shown as translucent. NADP(H) is modeled as black spheres. (B) Division of labor of enzymatic activities within a TH dimer: One half of the dimer carries out hydride transfer and the other translocates proton. (C) Coordination between dII and dIII in one half of the TH dimer for the forward reaction. A proton is represented by a red cross. Two halves of the TH dimer cycle out of phase; for simplicity of representation, the other half is shown in gray and remains unchanged.

(28), the conformation of loops D and E (14, 25), and the redox state of NADP(H), are coupled to conformational/protonation changes in the membrane domain coupled to proton translocation (Fig. 4C).

In general terms, we postulate that the two halves of the TH dimer cycle out of phase between the occluded and open states of dIII, each of which is coordinated to the inward-facing or outward-facing conformation of the proton channel. After the hydride transfer reaction, dIII becomes occluded in the face-up orientation, whereupon it flips to the face-down orientation without NADP(H) exchange with the solvent pool of NADP(H). For the forward reaction (NADPH product with a proton translocated inward), the interaction between the occluded dIII and the membrane domain converts dII from the deprotonated occluded state to become outward-facing, followed by the conversion of dIII to the open state, switching dII to inward-

facing, and eventually the flipping up of dIII. Dissociations of both NADPH from dIII and the proton from dII to the solvent are required for the catalytic cycle to proceed. For hydride transfer in the reverse direction, the sequence of events is similar, except that dII proceeds from proton-occluded→inward-facing→outward-facing (fig. S7). The proton motive force is coupled to the dissociation of NADP(H) and therefore to the equilibrium for hydride transfer between NAD(H) and NADP(H).

REFERENCES AND NOTES

- Y. Hatefi, M. Yamaguchi, *FASEB J.* **10**, 444–452 (1996).
- E. L. Arkblad et al., *Free Radic. Biol. Med.* **38**, 1518–1525 (2005).
- E. Meimaridou et al., *Nat. Genet.* **44**, 740–742 (2012).
- H. C. Freeman, A. Hugill, N. T. Dear, F. M. Ashcroft, R. D. Cox, *Diabetes* **55**, 2153–2156 (2006).
- A. A. Toye et al., *Diabetologia* **48**, 675–686 (2005).
- A. Pedersen, G. B. Karlsson, J. Rydström, *J. Bioenerg. Biomembr.* **40**, 463–473 (2008).

- T. Bizouarn, L. A. Sazanov, S. Aubourg, J. B. Jackson, *Biochim. Biophys. Acta* **1273**, 4–12 (1996).
- G. S. Prasad, V. Sridhar, M. Yamaguchi, Y. Hatefi, C. D. Stout, *Nat. Struct. Biol.* **6**, 1126–1131 (1999).
- S. A. White et al., *Structure* **8**, 1–12 (2000).
- G. S. Prasad et al., *Biochemistry* **41**, 12745–12754 (2002).
- T. Johansson et al., *J. Mol. Biol.* **352**, 299–312 (2005).
- N. P. Cotton, S. A. White, S. J. Peake, S. McSweeney, J. B. Jackson, *Structure* **9**, 165–176 (2001).
- V. Sundaresan, J. Chartron, M. Yamaguchi, C. D. Stout, *J. Mol. Biol.* **346**, 617–629 (2005).
- V. Sundaresan, M. Yamaguchi, J. Chartron, C. D. Stout, *Biochemistry* **42**, 12143–12153 (2003).
- J. D. Venning et al., *J. Biol. Chem.* **276**, 30678–30685 (2001).
- J. Meuller, X. Hu, C. Bunthof, T. Olausson, J. Rydström, *Bba-Bioenergetics* **1273**, 191–194 (1996).
- T. Bizouarn, J. Meuller, M. Axelsson, J. Rydström, *Bba-Bioenergetics* **1459**, 284–290 (2000).
- P. D. Bragg, C. Hou, *Arch. Biochem. Biophys.* **388**, 299–307 (2001).
- T. Bizouarn et al., *Biochim. Biophys. Acta* **1457**, 211–228 (2000).
- M. Yamaguchi, C. D. Stout, Y. Hatefi, *J. Biol. Chem.* **277**, 33670–33675 (2002).
- M. Althage, T. Bizouarn, J. Rydström, *Biochemistry* **40**, 9968–9976 (2001).
- A. J. McCoy et al., *J. Appl. Cryst.* **40**, 658–674 (2007).
- M. Hutton, J. M. Day, T. Bizouarn, J. B. Jackson, *Eur. J. Biochem.* **219**, 1041–1051 (1994).
- M. Yamaguchi, Y. Hatefi, *J. Biol. Chem.* **270**, 16653–16659 (1995).
- C. Johansson, A. Pedersen, B. G. Karlsson, J. Rydström, *Eur. J. Biochem.* **269**, 4505–4515 (2002).
- J. B. Jackson, *Biochim. Biophys. Acta* **1817**, 1839–1846 (2012).
- J. B. Jackson, S. A. White, P. G. Quirk, J. D. Venning, *Biochemistry* **41**, 4173–4185 (2002).
- A. Pedersen, T. Johansson, J. Rydström, B. Göran Karlsson, *Bba-Bioenergetics* **1707**, 254–258 (2005).

ACKNOWLEDGMENTS

We thank Y. Hatefi for commitment and inspiration on TH; M. Yeager, H. Heaslet, J. Chartron, and R. Akhouri for their work on *E. coli* holo-TH; M. Saier and Z. Zhang for providing the bacterial strain; M. Soltis and D. Terrell for the Gryphon robot; V. Cherezov and M. Caffrey for helpful comments and suggestions; and W. Liu for help with using the RockImager. We thank the staff of the Stanford Synchrotron Radiation Lightsource and the staff of the Northeastern Collaborative Access Team at the Advanced Photon Source for assistance with data collection. This research was funded by National Institutes of Health (NIH) grant 5R01GM061545 2004 – 2008 and by National Institute of General Medical Sciences (NIGMS) grant 1R01GM103838 - 01A1, GM095600 (to R.B.G.) PA is the Program Announcement number of NIH Research Project Grant. "Structural Biology of Membrane Proteins" is the title of the program. It was a mistake to include it in acknowledgements. The work was performed at the National Resource for Automated Molecular Microscopy, which is supported by a grant from the NIH NIGMS (P41GM103310). A. Moeller is supported by NIH grant GM073197. Atomic coordinates and diffraction data for the structures reported here are deposited in the RCSB Protein Data Bank under accession codes 4093 and 409U. The authors declare no competing financial interests. For the crystallography research, J.H.L. and C.D.S. designed experiments; J.H.L., M.Y., and C.D.S. performed experiments; and J.H.L. and C.D.S. analyzed the data. For the cryo-EM research, A.M. and J.A.S. designed and performed experiments and analyzed data. L.A.S. and R.B.G. contributed the Tt TH operon for expression and initial purification. L.A.S., J.H.L., and R.B.G. created holo-TH constructs and expressed and assayed mutants. J.H.L., R.B.G., and C.D.S. wrote the manuscript.

SUPPLEMENTARY MATERIALS

www.sciencemag.org/content/347/6218/178/suppl/DC1
Materials and Methods
Supplementary Text
Figs. S1 to S12
Tables S1 to S4
References (29–55)

26 August 2014; accepted 25 November 2014
10.1126/science.1260451

EARTH HISTORY

U-Pb geochronology of the Deccan Traps and relation to the end-Cretaceous mass extinction

Blair Schoene,^{1*} Kyle M. Samperton,¹ Michael P. Eddy,² Gerta Keller,¹ Thierry Adatte,³ Samuel A. Bowring,² Syed F. R. Khadri,⁴ Brian Gertsch³

The Chicxulub asteroid impact (Mexico) and the eruption of the massive Deccan volcanic province (India) are two proposed causes of the end-Cretaceous mass extinction, which includes the demise of nonavian dinosaurs. Despite widespread acceptance of the impact hypothesis, the lack of a high-resolution eruption timeline for the Deccan basalts has prevented full assessment of their relationship to the mass extinction. Here we apply uranium-lead (U-Pb) zircon geochronology to Deccan rocks and show that the main phase of eruptions initiated ~250,000 years before the Cretaceous-Paleogene boundary and that >1.1 million cubic kilometers of basalt erupted in ~750,000 years. Our results are consistent with the hypothesis that the Deccan Traps contributed to the latest Cretaceous environmental change and biologic turnover that culminated in the marine and terrestrial mass extinctions.

The Deccan Traps are a continental flood basalt province that comprise >1.3 million km³ of erupted lavas and associated rocks (1) that reach a total thickness of ~3000 m near the eruptive center in Western India (2, 3). Paleomagnetic data (4–7) combined with K-Ar and ⁴⁰Ar/³⁹Ar geochronology of Deccan basalts (8, 9) have been interpreted to indicate that >90% of the eruptive volume was emplaced rapidly (<1 million years), coincident with the Cretaceous-Paleogene boundary (KPB). This temporal relationship has long led to speculation that Deccan volcanism had a major role in the end-Cretaceous mass extinction (10, 11), which saw the disappearance of nonavian dinosaurs and ammonoids, as well as major biotic turnovers in foraminifera, corals, land plants, reptiles, and mammals (12–15). However, age uncertainties from existing geochronology of the Deccan Traps (6, 8, 9) are larger than their estimated total duration, and thus the onset and duration of volcanism cannot be precisely compared to geologic, extinction, or environmental records from sedimentary sections spanning the KPB worldwide.

To better establish a high-resolution eruptive history of the main phase of Deccan volcanism, we sampled volcanic rocks from throughout the 10 formations that make up the Western Ghats (2, 3, 16) and dated them by U-Pb zircon geochronology using chemical abrasion–isotope dilution–thermal ionization mass spectrometry (CA-ID-TIMS) (17). Because zircon is rare in basaltic rocks, our sampling strategy targeted volcanic airfall deposits between basalt flows and high-silica and/or coarse-grained segregations within individual flows (fig. S1). The latter have been described previously in the lower half of the Deccan sequence (18), and we successfully extracted zircon from one such sample in the Jawhar Formation (Fm) (DEC13-30; Fig. 1). Zircon was also separated from three paleosol, or “redbole,” horizons within the Ambenali and Mahabaleshwar Fms (samples RBP, RBE, and RBF; Fig. 1). These distinctive red horizons are interpreted to result from weathering of basalt during periods of volcanic quiescence (5). However, many also contain an evolved, high-SiO₂ volcanoclastic component (19), and we sampled these horizons to search for zircon-bearing volcanic ash that may have accumulated between basalt flows. Three additional zircon-bearing samples were collected from different intervals within a ~40-cm-thick green volcanoclastic bed in the Mahabaleshwar Fm. (DEC13-08, -09, and -10).

Each sample yielded a small number (typically <50) of euhedral zircon crystals with morphologies and internal zonation indicative of an igneous origin (fig. S3). Single grains were selected for analysis, photographed, pretreated, dissolved, and analyzed using CA-ID-TIMS (17). A subset of samples with an adequate number of grains was analyzed at both Princeton University (PU) and the Massachusetts Institute of Technology (MIT) to assess interlaboratory bias. Resulting ²⁰⁶Pb/²³⁸U dates from individual zircons from each sample scatter outside of analytical uncertainty (all uncertainties reported at the 2σ level; data shown in Fig. 2 and figs. S2 and S4 and reported in table S1) but show a similar spread in dates for samples analyzed at both MIT and PU. Given the excellent analytical reproducibility between laboratories (fig. S2), we discuss our results as a single data set below.

The spread in ²⁰⁶Pb/²³⁸U dates from our individual samples cannot be attributed to analytical uncertainties alone (fig. S2), and we interpret this dispersion to result from either prolonged growth of zircon before eruption and/or incorporation of zircon from slightly older eruptions at the same vent. This phenomenon is due to the ability of zircon to retain radiogenic Pb at magmatic temperatures (>700° to 900°C) and can result in zircon dates within volcanic deposits that predate eruption by 10³ to 10⁶ years (20, 21). Given that our goal is to date the deposition of the volcanic ash, taking a weighted mean of all data from single samples is inappropriate and could bias our dates too old (21). Alternatively, the youngest zircon from each deposit may serve as a maximum age for deposition (16). However, this approach assumes that chemical abrasion has completely mitigated Pb loss (17) and could bias our dates too young if this assumption is not true.

To address these potential biases, we analyzed the trace element geochemistry of the dissolved zircon after routine ion exchange separation of U and Pb (17). By asserting that cogenetic zircons from an ashfall should have the same age and the same trace element signature, we identified the population of zircon from our data set that is amenable to statistical grouping (Fig. 2) while alleviating the concern that older, inherited zircon may bias weighted mean dates too old. We find that two or more zircons from each sample meet these criteria, and we calculate weighted means from those grains. Additionally, zircons from different samples have very different trace element signatures, supporting our interpretation that each dated horizon contains a distinct population of zircon with independent age information.

As a further means of refining our age model for the middle Ambenali–lower Mahabaleshwar Fms, we employed a Markov chain Monte Carlo analysis that imposes the law of superposition as a boundary condition (17). Given that stratigraphic horizons young upward, this Bayesian approach uses the ²⁰⁶Pb/²³⁸U dates for each horizon derived above as priors and calculates new uncertainty distributions for each sample that maximize and evaluate the probability that stratigraphically higher beds are younger. Two of three samples from the composite ashbed fail this test (DEC13-08 and -09), and thus the date arising from the third sample (DEC13-10) is used as our best estimate for the deposition of that composite ashbed. Dates derived from the redbole horizons pass the superposition test, consistent with our interpretation based on grain morphology and geochemistry that zircon from these horizons derive from primary volcanic ashfall rather than, for example, eolian transport. The depositional ages presented in Fig. 2 are those from the Monte Carlo analysis, whereas several different interpretations of the geochronological data are presented in table S3.

Regardless of the method used for U-Pb age interpretation, our main conclusions remain unaffected. The U-Pb dates reported here have corresponding uncertainties that are one to two orders of magnitude smaller than previously

¹Department of Geosciences, Princeton University, Princeton, NJ 08540, USA. ²Department of Earth, Atmospheric, and Planetary Sciences, Massachusetts Institute of Technology, Cambridge, MA 02139, USA. ³Institut des Sciences de la Terre (ISTE), Université de Lausanne, GEOPOLIS, CH-1015 Lausanne, Switzerland. ⁴Department of Geology, Amravati University, Amravati, India.

*Corresponding author. E-mail: bschoene@princeton.edu

published geochronology from the Deccan Traps and can thus resolve age differences between the base and top of the main eruptive phase. Using the dates from the lower- and upper-most samples (Fig. 1), we calculate a duration of 753 ± 38 thousand years (ky) for an estimated 80 to 90% of the total eruptive volume of the Deccan Traps.

These data also calibrate the timing of magnetic polarity Chron 29r, which serves as a basis for global correlation of KPB sections. The C29r/C29n reversal was previously identified within the lower Mahabaleshwar Fm (5), from which we collected samples RBP, RBE, and RBF. We use the $^{206}\text{Pb}/^{238}\text{U}$ date of sample RBE of $65.552 \pm 0.026/0.049/0.086$ million years ago (Ma) (2σ uncertainties given here as internal only/with tracer calibration/with ^{238}U decay constant) as our best estimate for the age of C29r/C29n reversal because it was sampled from between two basalts with transitional polarity (Fig. 1) (5). The basal age of C29r is constrained by sample DEC13-30, which was collected from a basaltic segregation vein within the Jawhar Fm near the base of the main Deccan phase and yielded a $^{206}\text{Pb}/^{238}\text{U}$ date of $66.288 \pm 0.027/0.047/0.085$ Ma. From the same outcrop, Chenet *et al.* (9) reported transitional magnetic polarity just tens of meters beneath lavas containing reverse polarity (C29r); from this transitional horizon they reported a K-Ar date of 67.4 ± 2.0 Ma. Though their date was interpreted to represent the C30n/C30r or C31n/C30r transition, with a long hiatus in eruptions represented in that section (9), our U-Pb date from DEC13-30 is not consistent with a hiatus of that magnitude. A simpler interpretation is that the transitional polarity basalts represent the C30n/C29r transition. Thus, the age difference between DEC13-30 and RBE of 736 ± 37 ky is also the length of C29r. An independent estimate for the length of C29r from cyclostratigraphic analysis of marine Ocean Drilling Program (ODP) cores and the Zumaia section, Spain, yields durations of 713 to 725 ky (22), in good agreement with our calibration based on U-Pb geochronology.

Our results also have implications for the age of the KPB and associated mass extinction event, as several estimates for the duration of the Cretaceous portion of C29r of 300 to 340 ky have recently been published based on cyclostratigraphy of magnetically and biostratigraphically calibrated ODP sections (23). Using our date for the C30n/C29r reversal and the average cyclostratigraphic estimate yields an age for the KPB of 65.968 ± 0.085 Ma (including systematic uncertainties), which agrees well with a recently reported KPB age of 66.043 ± 0.086 Ma (also including full systematic uncertainties) from $^{40}\text{Ar}/^{39}\text{Ar}$ geochronology on tephra that bracket the terrestrial KPB near Hells Creek, Montana (24). Determining an age for the KPB by back-calculation from our estimate for the C29r/C29n reversal is more problematic in that estimates for the Paleogene portion of C29r based on cyclostratigraphy of the Zumaia KPB section range from 206 to 398 ky (22, 25). Regardless, the combination of our geochronologic data with cy-

clostratigraphic estimates effectively rules out any age for the KPB younger than 65.740 ± 0.086 Ma.

Although the temporal relationship between large igneous provinces and mass extinctions is

well established (26), the potential kill mechanisms remain a subject of debate. Models of proposed drivers focus on volcanically sourced CO_2 , SO_2 , and halogens, which can cause global warming and/or cooling on different time scales (27); acid

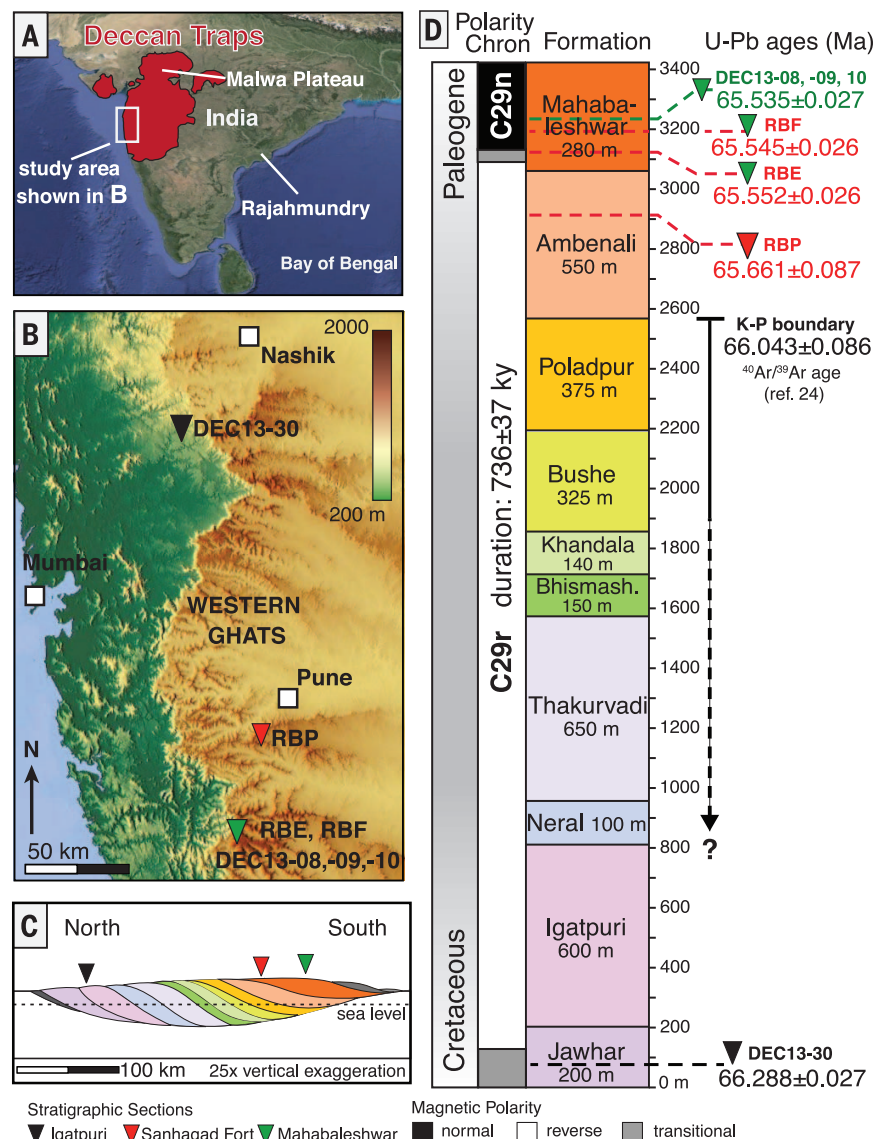


Fig. 1. Geography and stratigraphy of the Deccan Traps. (A) Aerial extent of the Deccan Traps colored in red. (B) Shaded relief map of study area in the Western Ghats. Major cities are indicated by white squares. Approximate locations of sampling transects and samples are indicated by colored triangles; transects are named at the bottom of the figure. The color bar (top right) shows elevation in meters, highlighting the escarpment where the best exposures of Deccan lavas occur. (C) Schematic cross section of Deccan lavas, from Chenet *et al.* (4), showing general southerly dip and younging to the south. Sampling transects are indicated by colored triangles. Colors correspond to the formations named in (D). (D) Composite stratigraphic section of the Deccan Traps in the Western Ghats, with approximate formation thicknesses shown. The geologic time scale is on the left, with the gray area corresponding to the unknown location of the KPB within the Deccan Traps. The geomagnetic polarity time scale is shown, with relevant chrons labeled and polarity indicated by black, white, or gray. The duration of C29r is the difference between the ages of DEC13-30 and RBE. U-Pb ages are shown on the right and are color-coded for sample type: black, segregation vein in basalt; red, volcanic material from paleosol; green, volcanic ashbed. Colored triangles correspond to sampling transects shown in (B) and (C). The date for KPB from Renne *et al.* (24) includes full systematic uncertainties. U-Pb age uncertainties are 2σ and include internal uncertainties only; ages with full systematic uncertainties are $\sim \pm 0.085$ Ma. See text and table S3 for full uncertainty budget and Fig. 2 and table S1 for data.

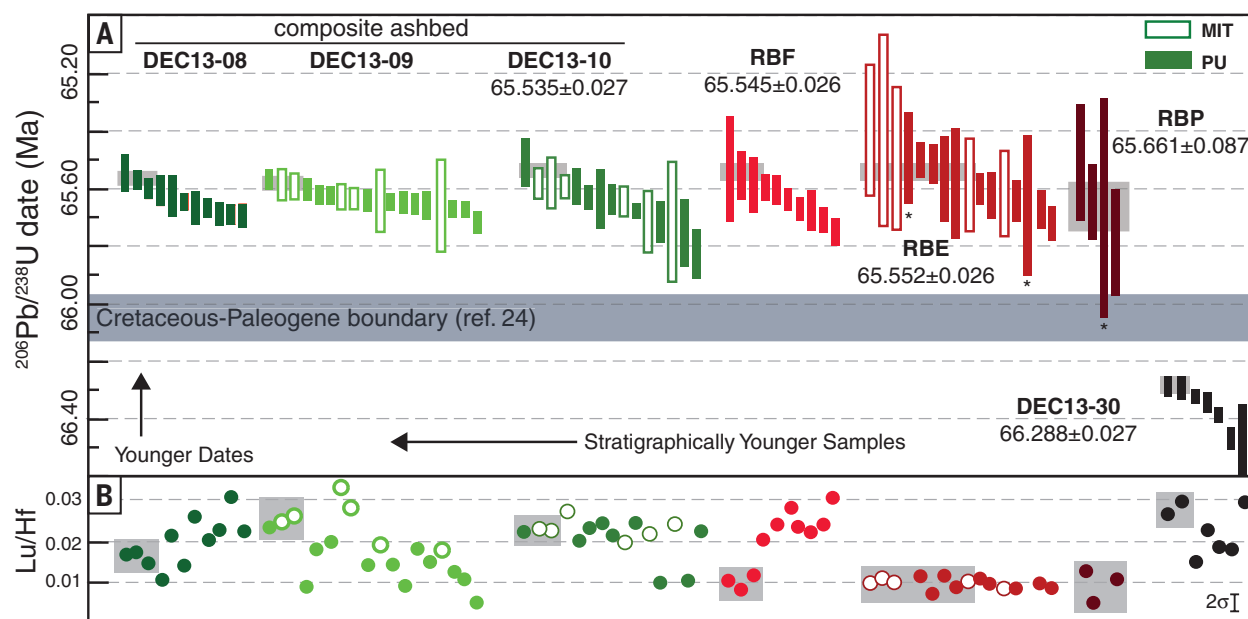


Fig. 2. U-Pb zircon CA-ID-TIMS geochronological data. (A) Rank order plot of U-Pb data presented in this study, color-coded by sample type in Fig. 1 and with sample name next to data. Sample locations are shown in Fig. 1. The vertical axis indicates $^{206}\text{Pb}/^{238}\text{U}$ date, and rectangle height corresponds to 2σ uncertainties for single-crystal zircon analyses, with internal uncertainties only. MIT and PU indicate the laboratory used. Stratigraphic younging is shown from right to left. The horizontal gray band shows the date for KPB from Renne *et al.* (24). Small gray rectangles behind the data indicate the youngest zircons that were indicated to be cogenetic by comparing dates and geochemistry in (B),

from which weighted means were calculated. Dates indicated beneath sample names result from the Monte Carlo Markov chain simulation that uses weighted mean dates and imposes the law of superposition to arrive at our best estimates for the time of deposition of the dated horizons (17). Asterisks indicate zircon without trace element geochemistry. U-Pb data are given in table S1. (B) Lutetium/hafnium (Lu/Hf) ratios of the same volume of dated zircon, younging from right to left as in (A). Gray boxes indicate zircons determined to be cogenetic due to same age and geochemistry. The full geochemical data set is presented in table S2 and plotted in fig. S5.

rain and ozone reduction (28); and ocean acidification (29). Late Cretaceous records beginning near the C30n/C29r transition, and therefore near the onset of the main phase of Deccan volcanism, show a decrease in $\delta^{18}\text{O}$ values of foraminifera (30) and morphological changes in fossil leaves (31) that are consistent with instabilities in global temperature. A two-stage decline in seawater $^{187}\text{Os}/^{188}\text{Os}$ values initiating at the C30n/C29r reversal was interpreted to record weathering of the Deccan Traps, predating a second decline in $^{187}\text{Os}/^{188}\text{Os}$ and a synchronous Ir spike that were attributed to the Chicxulub impact (32). Furthermore, biostratigraphic records show increased rates of biotic turnover in mammals, amphibians, land plants, and foraminifera through the Cretaceous portion of C29r preceding the peak extinction interval (12, 13, 15, 31, 33). Additional testing of the influence of the Deccan Traps on these records will require further determination of eruption tempos and hiatuses coupled with realistic estimates of volatile release from individual eruptive phases (34) that can be temporally linked to paleoenvironmental proxies. Our results are a critical part of this discussion as they are consistent with the hypothesis that environmental and ecological deterioration began with eruption of the Deccan Traps before the Chicxulub impact and the end-Cretaceous mass extinction. Therefore, both the Chicxulub impact and eruption of the Deccan Traps should be considered in any model for the extinction.

REFERENCES AND NOTES

- A. E. Jay, M. Widdowson, *J. Geol. Soc. London* **165**, 177–188 (2008).
- S. Khadri, K. Subbarao, P. Hooper, J. Walsh, *Geol. Soc. India Mem.* **10**, 281 (1988).
- J. E. Beane, C. A. Turner, P. R. Hooper, K. V. Subbarao, J. N. Walsh, *Bull. Volcanol.* **48**, 61–83 (1986).
- A.-L. Chenet *et al.*, *J. Geophys. Res.* **114**, B06103 (2009).
- A.-L. Chenet, F. Fluteau, V. Courtillot, M. Gérard, K. V. Subbarao, *J. Geophys. Res.* **113**, B04101 (2008).
- V. Courtillot *et al.*, *Earth Planet. Sci. Lett.* **182**, 137–156 (2000).
- D. Vandamme, V. Courtillot, *Phys. Earth Planet. Inter.* **74**, 241–261 (1992).
- C. Hofmann, G. Féraud, V. Courtillot, *Earth Planet. Sci. Lett.* **180**, 13–27 (2000).
- A. Chenet, X. Quidelleur, F. Fluteau, V. Courtillot, S. Bajpai, *Earth Planet. Sci. Lett.* **263**, 1–15 (2007).
- V. Courtillot *et al.*, *Earth Planet. Sci. Lett.* **80**, 361–374 (1986).
- G. Keller *et al.*, *Earth Planet. Sci. Lett.* **341–344**, 211–221 (2012).
- G. P. Wilson, *Geol. Soc. Am. Spec. Pap.* **503**, 365 (2014).
- N. Macleod *et al.*, *J. Geol. Soc. London* **154**, 265–292 (1997).
- P. Schulte *et al.*, *Science* **327**, 1214–1218 (2010).
- J. Punekar, P. Mateo, G. Keller, *Geol. Soc. Am. Spec. Pap.* **505**, 91 (2014).
- K. G. Cox, C. J. Hawkesworth, *J. Petrol.* **26**, 355–377 (1985).
- Materials and methods are available on Science Online.
- N. R. Bondre, R. A. Duraiswami, G. Dole, *Bull. Volcanol.* **66**, 29–45 (2004).
- M. Widdowson, J. N. Walsh, K. V. Subbarao, *Geol. Soc. London Spec. Publ.* **120**, 269–281 (1997).
- J. I. Simon, P. R. Renne, R. Mundil, *Earth Planet. Sci. Lett.* **266**, 182–194 (2008).
- B. Schoene, J. Guex, A. Bartolini, U. Schaltegger, T. J. Blackburn, *Geology* **38**, 387–390 (2010).
- T. Westerhold *et al.*, *Palaeogeogr. Palaeoclimatol. Palaeoecol.* **257**, 377–403 (2008).
- S. J. Batenburg *et al.*, *J. Geol. Soc. London* **171**, 165–180 (2014).
- P. R. Renne *et al.*, *Science* **339**, 684–687 (2013).
- F. J. Hilgen, K. F. Kuiper, L. J. Lourens, *Earth Planet. Sci. Lett.* **300**, 139–151 (2010).
- V. E. Courtillot, P. R. Renne, *C. R. Geosci.* **335**, 113–140 (2003).
- M. Mussard, G. Le Hir, F. Fluteau, V. Lefebvre, Y. Goddérès, *Geol. Soc. Am. Spec. Pap.* **505**, 339 (2014).
- B. A. Black, J.-F. Lamarque, C. A. Shields, L. T. Elkins-Tanton, J. T. Kiehl, *Geology* **42**, 67–70 (2014).
- R. A. Feely *et al.*, *Science* **305**, 362–366 (2004).
- L. Li, G. Keller, *Geology* **26**, 995–998 (1998).
- P. Wilf, K. R. Johnson, B. T. Huber, *Proc. Natl. Acad. Sci. U.S.A.* **100**, 599–604 (2003).
- N. Robinson, G. Ravizza, R. Coccioni, B. Peucker-Ehrenbrink, R. Norris, *Earth Planet. Sci. Lett.* **281**, 159–168 (2009).
- G. P. Wilson, D. G. DeMar, G. Carter, *Geol. Soc. Am. Spec. Pap.* **503**, 271 (2014).
- S. Self, S. Blake, K. Sharma, M. Widdowson, S. Septon, *Science* **319**, 1654–1657 (2008).

ACKNOWLEDGMENTS

This work was supported by the Department of Geosciences Scott Fund at Princeton University and the U.S. NSF through the Continental Dynamics Program, Sedimentary Geology and Paleobiology Program, and the Office of International Science and Engineering's India Program under grants EAR-0447171 and EAR-1026271 to G.K.P. Kemery assisted with fieldwork and sample collection; A. Chen assisted with sample processing. MIT's analytical work was supported by the Robert Shrock chair. All data associated with this work can be found in the supplementary materials (17).

SUPPLEMENTARY MATERIALS

www.sciencemag.org/content/347/6218/182/suppl/DC1
Materials and Methods
Figs. S1 to S5
Tables S1 to S3
References (35–108)

9 October 2014; accepted 26 November 2014
Published online 11 December 2014;
10.1126/science.aaa0118

DNA REPAIR

PAXX, a paralog of XRCC4 and XLF, interacts with Ku to promote DNA double-strand break repair

Takashi Ochi,^{1*} Andrew N. Blackford,^{2*} Julia Coates,² Satpal Jhujh,² Shahid Mehmood,³ Naoka Tamura,⁴ Jon Travers,² Qian Wu,¹ Viji M. Draviam,⁴ Carol V. Robinson,³ Tom L. Blundell,^{1†} Stephen P. Jackson^{1,2,5†}

XRCC4 and XLF are two structurally related proteins that function in DNA double-strand break (DSB) repair. Here, we identify human PAXX (PARalog of XRCC4 and XLF, also called C9orf142) as a new XRCC4 superfamily member and show that its crystal structure resembles that of XRCC4. PAXX interacts directly with the DSB-repair protein Ku and is recruited to DNA-damage sites in cells. Using RNA interference and CRISPR-Cas9 to generate PAXX^{-/-} cells, we demonstrate that PAXX functions with XRCC4 and XLF to mediate DSB repair and cell survival in response to DSB-inducing agents. Finally, we reveal that PAXX promotes Ku-dependent DNA ligation in vitro and assembly of core nonhomologous end-joining (NHEJ) factors on damaged chromatin in cells. These findings identify PAXX as a new component of the NHEJ machinery.

DNA double-strand breaks (DSBs) are toxic lesions that arise in cells exposed to agents such as ionizing radiation (IR) and are also generated as intermediates during V(D)J (variable, diversity, joining) and class-switch recombination at immune-receptor gene loci (1). If unrepaired or repaired incorrectly, DSBs cause cell death or genome instability, and defects in DSB repair components cause he-

reditary disorders with symptoms including immunodeficiency, neurodegeneration, infertility, and/or increased cancer predisposition (2). A key DNA repair pathway is nonhomologous end-joining (NHEJ), which involves initial recognition of a DSB by the Ku70-Ku80 heterodimer, followed by the assembly of additional factors including the DNA-dependent protein kinase catalytic subunit (DNA-PKcs), x-ray cross-complementing pro-

tein 4 (XRCC4), and XRCC4-like factor (XLF; also called Cernunnos), with XRCC4 playing a prime role in recruiting DNA ligase IV (LIG4) to carry out the DSB-joining reaction (3).

XRCC4 and XLF, together with spindle-assembly abnormal protein 6 (SAS6), comprise a homologous superfamily of structurally related proteins (4). To identify other members of this protein superfamily, we used a bioinformatics approach, which suggested that the 22-kD human protein, C9orf142, could be an XRCC4 paralog (tables S1 and S2). Although little overall primary sequence similarity is seen, sequence alignments indicated that the N-terminal portion of C9orf142 contains the present-in-SAS6 (PISA) motif that is conserved throughout the XRCC4 superfamily (5) and shares a conserved tryptophan in this motif with XRCC4 and XLF (Fig. 1A and fig. S1A). We have therefore named this previously uncharacterized protein PAXX (PARalog of XRCC4 and XLF). Although PAXX has a wide evolutionary distribution (fig. S1B), we could not identify PAXX orthologs in insects or fungi.

¹Department of Biochemistry, University of Cambridge, 80 Tennis Court Road, Cambridge CB2 1QA, UK. ²Wellcome Trust/Cancer Research UK Gurdon Institute, University of Cambridge, Tennis Court Road, Cambridge CB2 1QN, UK. ³Physical and Theoretical Chemistry Laboratory, University of Oxford, South Parks Road, Oxford OX1 3QZ, UK. ⁴Department of Genetics, University of Cambridge, Cambridge CB2 3EH, UK. ⁵Wellcome Trust Sanger Institute, Hinxton, Cambridge CB10 1SA, UK. *These authors contributed equally to this work. †Corresponding author. E-mail: s.jackson@gurdon.cam.ac.uk (S.P.J.); tlb20@cam.ac.uk (T.L.B.).

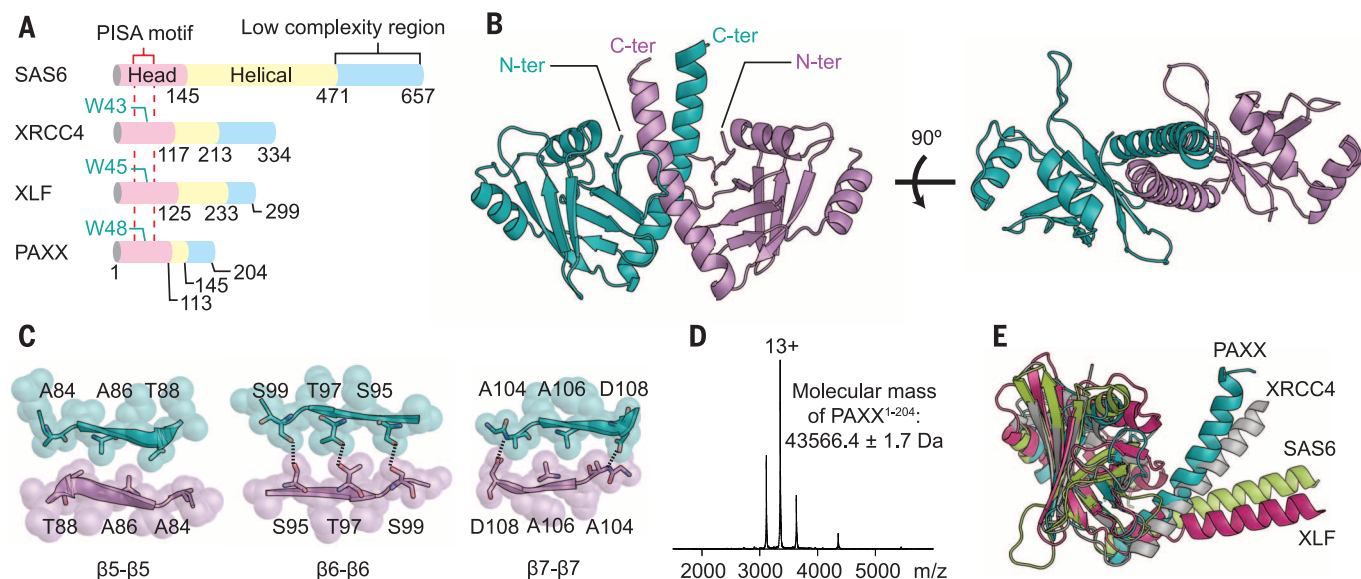


Fig. 1. Crystal structure of PAXX. (A) Domain architecture of human PAXX and other XRCC4 superfamily members. Sequence identities between human PAXX and XRCC4, XLF, and SAS6 are 10.9%, 11.2%, and 10.1%, respectively. (B) Structure of a PAXX dimer with the two polypeptide chains shown in cyan and lavender. The N and C termini of the structure are indicated as N-ter and C-ter, respectively. (C) Residues mediating the PAXX dimerization interface, with β -sheet sandwichlike packing between protomers in adjacent asymmetric units. The packing of each strand from different protomers is shown in surface

and stick representations. Black dotted lines are hydrogen bonds between side-chain pairs (S99 and S95, T97 and T97, S95 and S99) and between the side chain of D108 of each protomer with the main chain of A104 of the adjacent protomer in the crystals. (D) ES-MS profile showing that PAXX¹⁻²⁰⁴ is a dimer. Three charge states are observed for the dimer. The main charge state 13+ is labeled in the mass spectrum. (E) Comparison of XRCC4 superfamily members. The head domains of PAXX (cyan), XRCC4 (silver), XLF (magenta), and SAS6 (green) are superimposed.

We solved crystal structures of PAXX residues 1 to 145, 1 to 166, and the full-length protein (PAXX¹⁻¹⁴⁵, PAXX¹⁻¹⁶⁶, and PAXX¹⁻²⁰⁴) at resolutions of 2.46, 2.35, and 3.45 Å respectively (table S3). PAXX residues 1 to 113 form a head domain that is structurally closely related to those of XRCC4, XLF, and SAS6 (6-11) (Fig. 1, A and B). This is followed by a 31-amino acid α helix, forming a coiled-coil with the other protomer to make a PAXX homodimer (in the asymmetric unit) in a manner similar to the formation of dimeric interfaces formed by XRCC4, XLF, and SAS6. Contacts within the PAXX crystal indicate that the protein has potential to form higher-order protein filaments with similarities to those of its paralogs (fig. S2A), in which two β sheets, each made up of strands β 5 to β 7 from different PAXX dimers, form a β sandwich around a dyad axis running between the sheets and orthogonally to the strands (Fig. 1C). However, small-angle x-ray scattering (SAXS) data of PAXX¹⁻¹⁴⁵ in solution are well explained by the scattering curve

calculated from the structure of the dimer of the construct (fig. S2B), and electrospray mass spectroscopy (ES-MS) confirmed that PAXX predominantly forms dimers in solution under the conditions used (Fig. 1D and table S4). These data thus suggest that the preferred native state for PAXX is a dimer. Although our analyses indicate that the conformation of PAXX is distinct from those of other XRCC4 superfamily members, its overall structural properties most resemble those of XRCC4 (Fig. 1E and fig. S2C).

To gain insights into PAXX function, we expressed green fluorescent protein (GFP), GFP-tagged wild-type (WT) PAXX (GFP-PAXX^{WT}), and GFP-tagged C-terminally truncated PAXX¹⁻¹⁴⁵ in human embryonic kidney HEK293FT cells, purified these, and identified potential binding partners by mass spectrometry. This revealed that the only proteins that bound GFP-PAXX^{WT}, but not GFP-PAXX¹⁻¹⁴⁵ or GFP, corresponded to Ku70 and Ku80. Immunoprecipitation and Western blot analyses confirmed this interaction and es-

tablished that endogenous PAXX and Ku interact (Fig. 2, A and B). Also, in reciprocal experiments, Ku70 (GFP-tagged at its endogenous gene locus) interacted with PAXX (fig. S3A). Given that GFP-PAXX¹⁻¹⁴⁵ did not interact with Ku and because the extreme C terminus of PAXX has been highly conserved through evolution (Fig. 2C), we speculated that PAXX C-terminal residues might mediate Ku binding. To test this, we synthesized a biotinylated peptide encompassing PAXX residues 177 to 204 and found that it specifically retrieved two major proteins that were identified by mass spectrometry to be Ku70 and Ku80 (Fig. 2D); this was confirmed by Western blotting (fig. S3B). Furthermore, mutating two of the most highly conserved residues in the PAXX C terminus (V199 and F201) to alanine in GFP-PAXX^{WT} or biotinylated PAXX¹⁷⁷⁻²⁰⁴ abolished interaction with Ku (Fig. 2E and fig. S3B). In line with these findings, addition of PAXX¹⁷⁷⁻²⁰⁴ peptide to cell lysates inhibited the interaction of PAXX with Ku (fig. S3C), and surface plasmon resonance (SPR) studies with purified proteins established that DNA-bound Ku and PAXX^{WT} interacted directly, whereas PAXX^{V199A/F201A} did not bind to Ku-DNA detectably (fig. S3, D and E). Thus, PAXX binding to Ku-DNA is direct and is mediated by the PAXX C terminus.

In vivo, PAXX was predominantly nuclear (fig. S4, A and B), and GFP-PAXX localized to DNA damage generated by laser microirradiation of live cells (Fig. 3A). To test if PAXX might be involved in DSB repair by NHEJ, we depleted human U2OS cells (a human osteosarcoma cell line) of PAXX, using multiple small-interfering RNAs (siRNAs) (fig. S4C), then performed clonogenic survival assays after exposing the cells to IR. Cells in which PAXX was depleted were significantly more radiosensitive than control cells and displayed sensitivities similar to those of cells depleted of XRCC4 (Fig. 3B and fig. S4D). Furthermore, expression of PAXX^{WT}, but not PAXX^{V199A/F201A}, restored IR resistance in PAXX-depleted cells (Fig. 3B). As PAXX^{V199A/F201A} is impaired for Ku binding, these data support a model in which the PAXX-Ku interaction is crucial for PAXX function in DNA repair.

To verify and extend the above conclusions, we used CRISPR-Cas9 gene editing (12) in non-transformed human retinal pigmented epithelial (RPE-1) cells to generate PAXX^{-/-} clones (fig. S5). Like siRNA-treated U2OS cells, PAXX^{-/-} cells were hypersensitive to IR and the radio-mimetic drug phleomycin (Fig. 3C and fig. S6B). Furthermore, by depleting XRCC4 or XLF in PAXX^{+/+} or PAXX^{-/-} cells (fig. S6C), we established that combined loss of PAXX and XRCC4, or PAXX and XLF, did not cause IR sensitivity greater than that of PAXX^{-/-} cells or cells depleted of XRCC4 or XLF alone (Fig. 3C and fig. S6D), which implies that PAXX functions epistatically with XRCC4 and XLF to promote IR resistance via classical NHEJ. Given that NHEJ-deficient cells display defective resolution of IR-induced γ H2AX foci, we compared the appearance and disappearance of these foci by immunofluorescence microscopy in PAXX^{+/+}

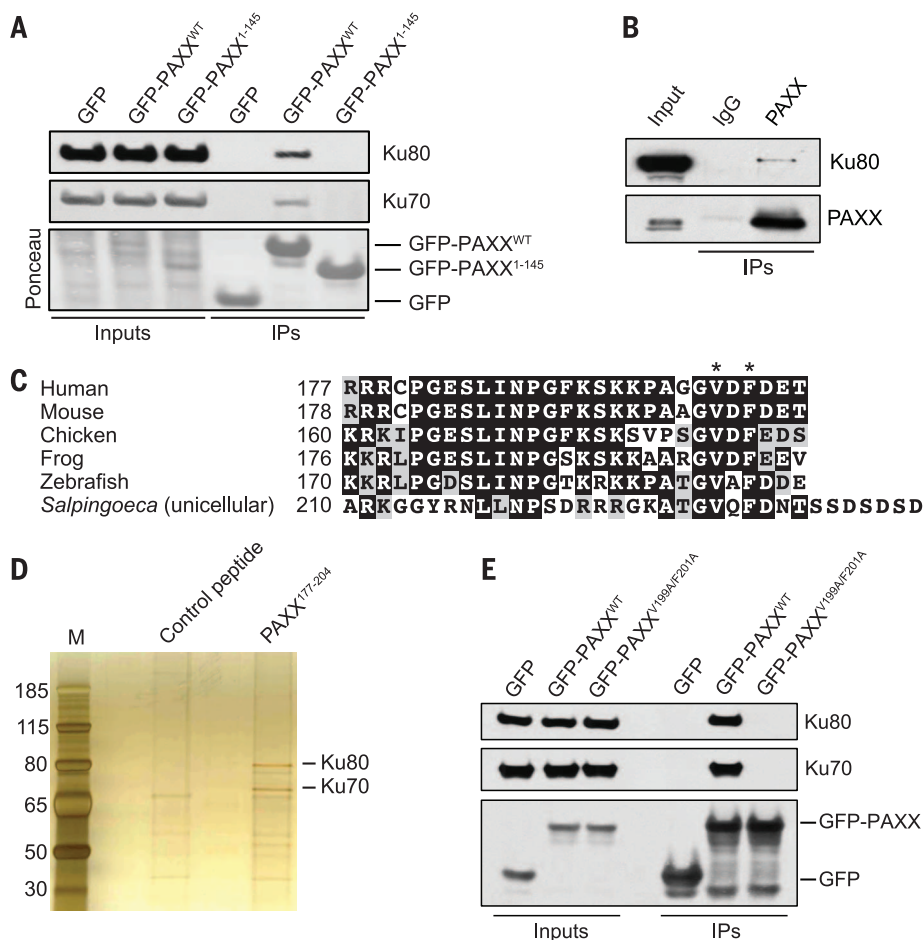
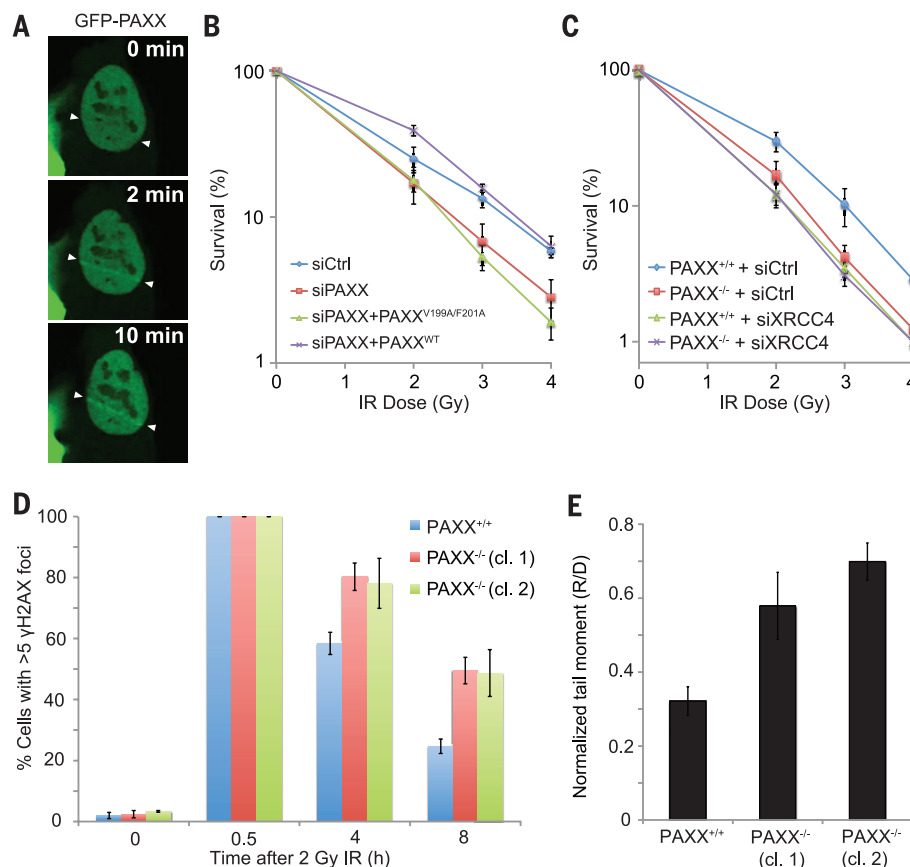


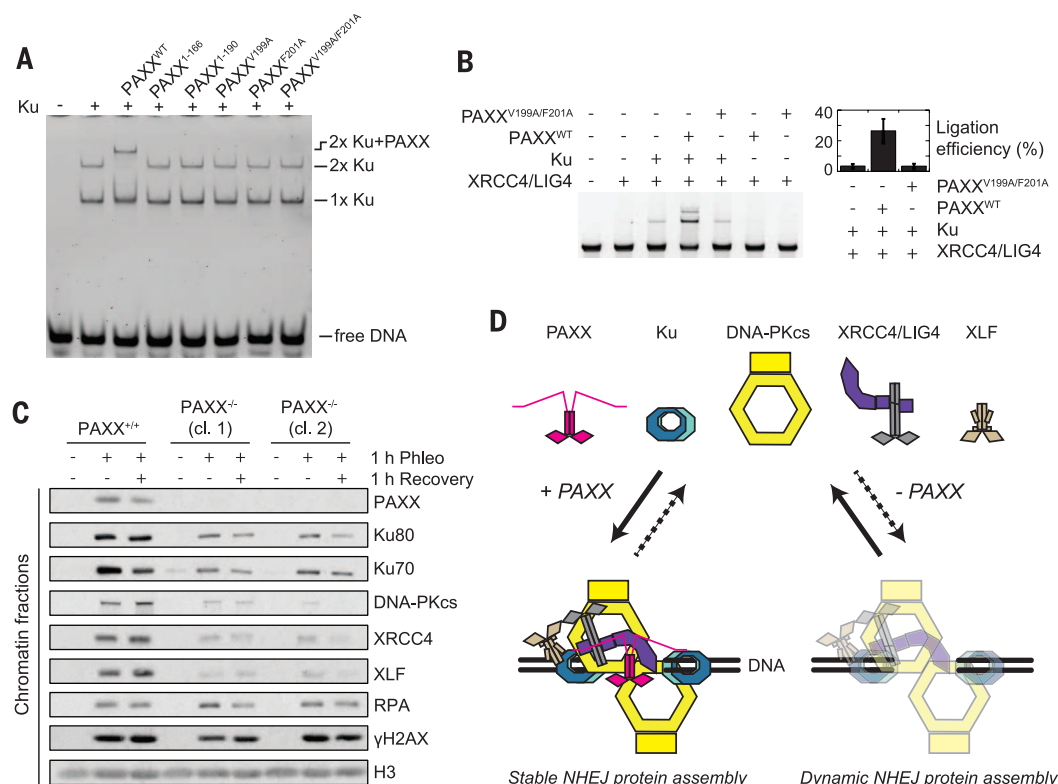
Fig. 2. The PAXX C terminus interacts with Ku. (A) GFP pull-down assays showing that GFP-PAXX^{WT}, but not GFP-PAXX¹⁻¹⁴⁵, transiently overexpressed in HEK293FT cells interacts with Ku. (B) Coimmunoprecipitation (IP) from HeLa nuclear extracts showing that endogenous PAXX and Ku interact. (C) Sequence alignment of the C termini of PAXX orthologs. Conserved residues are indicated with reverse shading, and similar residues are highlighted in gray. (D) Peptide pull-down assays from HeLa nuclear extracts using control (H2AX) or PAXX¹⁷⁷⁻²⁰⁴ peptides analyzed by silver staining. "M" represents protein markers, and numbers represent molecular masses in kilodaltons. (E) GFP pull-down assays showing that PAXX residues V199 and F201 are required for Ku binding in the context of full-length PAXX.

Fig. 3. PAXX is required for DSB repair in human cells.

(A) GFP-tagged PAXX accumulates at sites of laser microirradiation in U2OS cells. White arrowheads indicate the path of the laser used to induce DSBs. **(B)** Clonogenic survival assay showing that PAXX depletion in U2OS cells causes radiosensitivity and that this is rescued by exogenous expression of PAXX^{WT} but not PAXX^{V199A/F201A}. In this experiment and those below, error bars represent the standard error of the mean (SEM) from three independent experiments. **(C)** Clonogenic survival assay showing that PAXX^{-/-} cells are radiosensitive and that PAXX loss is epistatic with XRCC4 depletion. **(D)** PAXX^{-/-} cells display persistent γ -H2AX foci after IR. Cells with >5 foci were scored as positive and were costained with cyclin A to eliminate S and G₂ cells from analysis. At least 100 cells were scored per condition. "cl." indicates clone number. **(E)** PAXX is required for cellular DSB repair as measured by neutral comet assay. R/D ratios represent mean tail length of cells treated with 40 μ g/ml phleomycin for 2 hours and allowed to recover (R) for 2 hours over mean tail length of cells damaged (D) for 2 hours without recovery.

**Fig. 4. PAXX promotes NHEJ in vitro and stabilizes NHEJ proteins on damaged chromatin.**

(A) Electrophoretic mobility shift analysis of Ku and PAXX derivatives with 50 base pairs of 6-FAM(6-carboxyfluorescein)-labeled DNA. PAXX (200 nM) and Ku (20 nM) were added where indicated. **(B)** Stimulation of DNA end ligation by PAXX. pcDNA3.1(-) (50 ng) digested by Eco RV was incubated with PAXX^{V199A/F201A} (250 nM), PAXX (250 nM), Ku (25 nM), and XRCC4/LIG4 (25 nM) as indicated (left). Ligation efficiency (right) was calculated as a percentage of ligated plasmid from four independent assays. **(C)** Chromatin fractionation of PAXX^{+/+} and PAXX^{-/-} cells treated with phleomycin as indicated. Note that DNA damage-dependent chromatin recruitment of proteins, such as RPA, that function in DNA repair pathways other than NHEJ, were unaffected by PAXX loss. H3, histone 3. **(D)** Model of PAXX in NHEJ. Two Ku-bound DNA ends are bound by a PAXX dimer at its C termini, which stabilizes the NHEJ machinery to promote DNA end ligation.



and PAXX^{-/-} cells. Although PAXX loss did not impair γ H2AX focus formation, we observed a substantial defect in γ H2AX focus resolution in multiple PAXX^{-/-} clones (Fig. 3D). Furthermore, both PAXX^{-/-} RPE-1 and PAXX-depleted U2OS cells were impaired in repairing DSBs, as measured by neutral comet assays (Fig. 3E and fig. S6E), and PAXX-depleted U2OS cells were also defective in random-plasmid integration, which occurs through NHEJ events (fig. S6F) (13). As with other NHEJ factors, such as XRCC4, PAXX loss did not impair checkpoint signaling (fig. S7, A and B).

Subsequent biochemical investigations established that, although PAXX does not bind DNA detectably on its own, PAXX retarded the electrophoretic mobilities of DNA complexes containing two Ku molecules (Fig. 4A and fig. S8, A to C). Furthermore, such binding was abrogated in the presence of a large excess of PAXX¹⁷⁷⁻²⁰⁴ peptide or when the extreme PAXX C-terminal region was absent or contained alanine substitutions for V199 and F201 (Fig. 4A and fig. S8D). We next tested whether PAXX affected DNA ligation by LIG4 *in vitro* in a manner dependent on its ability to bind Ku. Indeed, PAXX^{WT}, but not PAXX^{V199A/F201A}, markedly stimulated double-stranded DNA ligation in reactions containing the XRCC4/LIG4 complex—but only in the presence of Ku (Fig. 4B). We speculated that PAXX might act as a scaffold to stabilize two Ku heterodimers at DNA ends and thus promote assembly and/or stability of the NHEJ machinery at DSB sites. To test this, we treated PAXX^{+/+} and PAXX^{-/-} cells with phleomycin and examined the association of NHEJ proteins with chromatin by Western blotting. This revealed that PAXX deficiency produced substantial defects in the ability of Ku, DNA-PKcs, XRCC4, and XLF to assemble on chromatin in response to DNA damage, without affecting the overall levels of these proteins (Fig. 4C and fig. S8E).

In conclusion, we have identified and characterized an XRCC4 superfamily member, PAXX. We have shown that PAXX binds Ku and promotes DSB repair at the biochemical and cellular levels and stabilizes NHEJ-protein assembly at DSB sites (Fig. 4D), which establishes PAXX as a hitherto uncharacterized NHEJ factor.

REFERENCES AND NOTES

1. S. P. Jackson, J. Bartek, *Nature* **461**, 1071–1078 (2009).
2. L. Woodbine, A. R. Gennery, P. A. Jeggo, *DNA Repair (Amst.)* **16**, 84–96 (2014).
3. G. J. Williams *et al.*, *DNA Repair (Amst.)* **17**, 110–120 (2014).
4. T. Ochi, Q. Wu, T. L. Blundell, *DNA Repair (Amst.)* **17**, 98–109 (2014).
5. S. Leidel, M. Delattre, L. Cerutti, K. Baumer, P. Gönczy, *Nat. Cell Biol.* **7**, 115–125 (2005).
6. M. S. Junop *et al.*, *EMBO J.* **19**, 5962–5970 (2000).
7. B. L. Sibanda *et al.*, *Nat. Struct. Biol.* **8**, 1015–1019 (2001).
8. S. N. Andres, M. Modesti, C. J. Tsai, G. Chu, M. S. Junop, *Mol. Cell* **28**, 1093–1101 (2007).
9. Y. Li *et al.*, *EMBO J.* **27**, 290–300 (2008).
10. M. van Bruegel *et al.*, *Science* **331**, 1196–1199 (2011).
11. D. Kitagawa *et al.*, *Cell* **144**, 364–375 (2011).
12. P. D. Hsu, E. S. Lander, F. Zhang, *Cell* **157**, 1262–1278 (2014).
13. P. Ahnesorg, P. Smith, S. P. Jackson, *Cell* **124**, 301–313 (2006).

ACKNOWLEDGMENTS

T.O., Q.W. and T.L.B. are supported by the Wellcome Trust (WT 093167). The Jackson laboratory is funded by Cancer Research UK (CRUK) program grant C6/A11224, the European Research Council, and the European Community Seventh Framework Programme grant agreement HEALTH-F2-2010-259893 (DDRresponse). Core infrastructure funding to the Jackson lab is provided by CRUK (C6946/A14492) and the Wellcome Trust (WT092096). S.P.J. receives his salary from the University of Cambridge, supplemented by CRUK. V.M.D. is a CRUK Career Development Fellow. The Draviam lab is funded by a CRUK Career Development Fellowship (C28598/A9787). We thank M. Hyvönen, V. Bolanos-Garcia, and L. Hanakahi for reagents; K. Scott for assistance with SPR; beamline scientists at I03 and I22 for their help at the Diamond Light Source; and J. Brown, K. Inoue, Y. Kimata, M. Lammers, B. Luisi, N. Lukashchuk, R. Nishi, C. le Sage, C. Schmidt, and P. Wijnhoven for useful discussions and technical

assistance. Crystallization and initial x-ray diffraction experiments were performed in the x-ray crystallographic facility at the Department of Biochemistry, University of Cambridge, with help from the Facility Manager, D. Chirgadze. Protein Data Bank accession numbers of PAXX¹⁻¹⁶⁶ and PAXX¹⁻²⁰⁴ are 3WTD and 3WTF, respectively.

SUPPLEMENTARY MATERIALS

www.sciencemag.org/content/347/6218/185/suppl/DC1
Materials and Methods
Figs. S1 to S9
Tables S1 to S4
References (14–39)

1 October 2014; accepted 1 December 2014
10.1126/science.1261971

METABOLISM

Lysosomal amino acid transporter SLC38A9 signals arginine sufficiency to mTORC1

Shuyu Wang,^{1,2,3,4,*} Zhi-Yang Tsun,^{1,2,3,4,*} Rachel L. Wolfson,^{1,2,3,4} Kuang Shen,^{1,2,3,4} Gregory A. Wyant,^{1,2,3,4} Molly E. Plovianich,⁵ Elizabeth D. Yuan,^{1,2,3,4} Tony D. Jones,^{1,2,3,4} Lynne Chantranupong,^{1,2,3,4} William Comb,^{1,2,3,4} Tim Wang,^{1,2,3,4} Liron Bar-Peled,^{1,2,3,4,†} Roberto Zoncu,^{1,2,3,4,†} Christoph Straub,⁶ Choah Kim,^{1,2,3,4} Jiwon Park,^{1,2,3,4} Bernardo L. Sabatini,⁶ David M. Sabatini^{1,2,3,4,§}

The mechanistic target of rapamycin complex 1 (mTORC1) protein kinase is a master growth regulator that responds to multiple environmental cues. Amino acids stimulate, in a Rag-, Regulator-, and vacuolar adenosine triphosphatase-dependent fashion, the translocation of mTORC1 to the lysosomal surface, where it interacts with its activator Rheb. Here, we identify SLC38A9, an uncharacterized protein with sequence similarity to amino acid transporters, as a lysosomal transmembrane protein that interacts with the Rag guanosine triphosphatases (GTPases) and Regulator in an amino acid-sensitive fashion. SLC38A9 transports arginine with a high Michaelis constant, and loss of SLC38A9 represses mTORC1 activation by amino acids, particularly arginine. Overexpression of SLC38A9 or just its Regulator-binding domain makes mTORC1 signaling insensitive to amino acid starvation but not to Rag activity. Thus, SLC38A9 functions upstream of the Rag GTPases and is an excellent candidate for being an arginine sensor for the mTORC1 pathway.

The mechanistic target of rapamycin complex 1 (mTORC1) protein kinase is a central controller of growth that responds to the nutritional status of the organism and is deregulated in several diseases, including

cancer (1–3). Upon activation, mTORC1 promotes anabolic processes, including protein and lipid synthesis, and inhibits catabolic ones, such as autophagy (4). Environmental cues such as nutrients and growth factors regulate mTORC1, but how it senses and integrates these diverse inputs is unclear.

The Rag and Rheb guanosine triphosphatases (GTPases) have essential but distinct roles in mTORC1 pathway activation, with the Rags controlling the subcellular localization of mTORC1 and Rheb stimulating its kinase activity (5). Nutrients, particularly amino acids, activate the Rag GTPases, which then recruit mTORC1 to the lysosomal surface, where they are concentrated (6, 7). Rheb also localizes to the lysosomal surface (6, 8–10) and, upon growth factor withdrawal, the tuberous sclerosis complex (TSC) tumor suppressor translocates there and inhibits mTORC1 by promoting guanosine 5'-triphosphate (GTP) hydrolysis by Rheb (10). Thus, the Rag and Rheb inputs converge at the lysosome, forming two

¹Whitehead Institute for Biomedical Research and Massachusetts Institute of Technology, Department of Biology, 9 Cambridge Center, Cambridge, MA 02142, USA.

²Howard Hughes Medical Institute, Department of Biology, Massachusetts Institute of Technology, Cambridge, MA 02139, USA. ³Koch Institute for Integrative Cancer Research, 77 Massachusetts Avenue, Cambridge, MA 02139, USA.

⁴Broad Institute of Harvard and Massachusetts Institute of Technology, 7 Cambridge Center, Cambridge, MA 02142, USA. ⁵Harvard Medical School, 260 Longwood Avenue, Boston, MA 02115, USA. ⁶Department of Neurobiology, Howard Hughes Medical Institute, Harvard Medical School, 220 Longwood Avenue, Boston, MA 02115, USA.

*These authors contributed equally to this work. †Present address: Department of Chemical Physiology, The Scripps Research Institute, La Jolla, CA 92037, USA. ‡Present address: Department of Molecular and Cell Biology, University of California Berkeley, Berkeley, CA 94720, USA. §Corresponding author. E-mail: sabatini@wi.mit.edu

halves of a coincidence detector that ensures that mTORC1 activation occurs only when both are active.

There are four Rag GTPases in mammals and they form stable, obligate heterodimers consisting of RagA or RagB with RagC or RagD. RagA and RagB are highly similar and functionally redundant, as are RagC and RagD (1, 6). The function of each Rag within the heterodimer is poorly understood, and their regulation is likely complex, as many distinct factors play important roles. A lysosome-associated molecular machine containing the multisubunit Regulator and vacuolar adenosine triphosphatase (v-ATPase) complexes regulates the Rag GTPases and is necessary for mTORC1 activation by amino acids (11). Regulator anchors the Rag GTPases to the lysosome and also has nucleotide exchange activity for RagA/B

(12, 13), but the molecular function of the v-ATPase in the pathway is unknown. Two GTPase-activating protein (GAP) complexes, which are both tumor suppressors, promote GTP hydrolysis by the Rag GTPases, with GATOR1 acting on RagA/B (14) and Folliculin-FNIP1/2 on RagC/D (15). Last, a distinct complex called GATOR2 negatively regulates GATOR1 through an unknown mechanism (14). Despite the identification of many proteins involved in signaling amino acid sufficiency to mTORC1, the actual amino acid sensors remain unknown.

We have proposed that amino acid sensing initiates at the lysosome and requires the presence of amino acids in the lysosomal lumen (11). Thus, we sought to identify, as candidate sensors, proteins that interact with known components of the pathway and also have transmembrane domains. Mass spectrometric analyses of non-

heated immunoprecipitates of several Regulator components and, to a lesser extent, RagB revealed the presence of isoform 1 of SLC38A9 (SLC38A9.1), a previously unstudied protein with sequence similarity to the SLC38 class of sodium-coupled amino acid transporters (16) (Fig. 1A). SLC38A9.1 is predicted to have 11 transmembrane domains, a cytosolic N-terminal region of 119 amino acids, and three N-linked glycosylation sites in the luminal loop between transmembrane domains 3 and 4 (Fig. 1B and fig. S1, A and B). When stably expressed in human embryonic kidney–293T (HEK-293T) cells, SLC38A9.1 migrated on SDS–polyacrylamide gel electrophoresis as a smear that collapsed to near its predicted molecular mass of 63.8 kD after treatment with peptide *N*-glycosidase F (PNGase F) (Fig. 1C). Isoforms 2 (SLC38A9.2) and 4 (SLC38A9.4) lack the

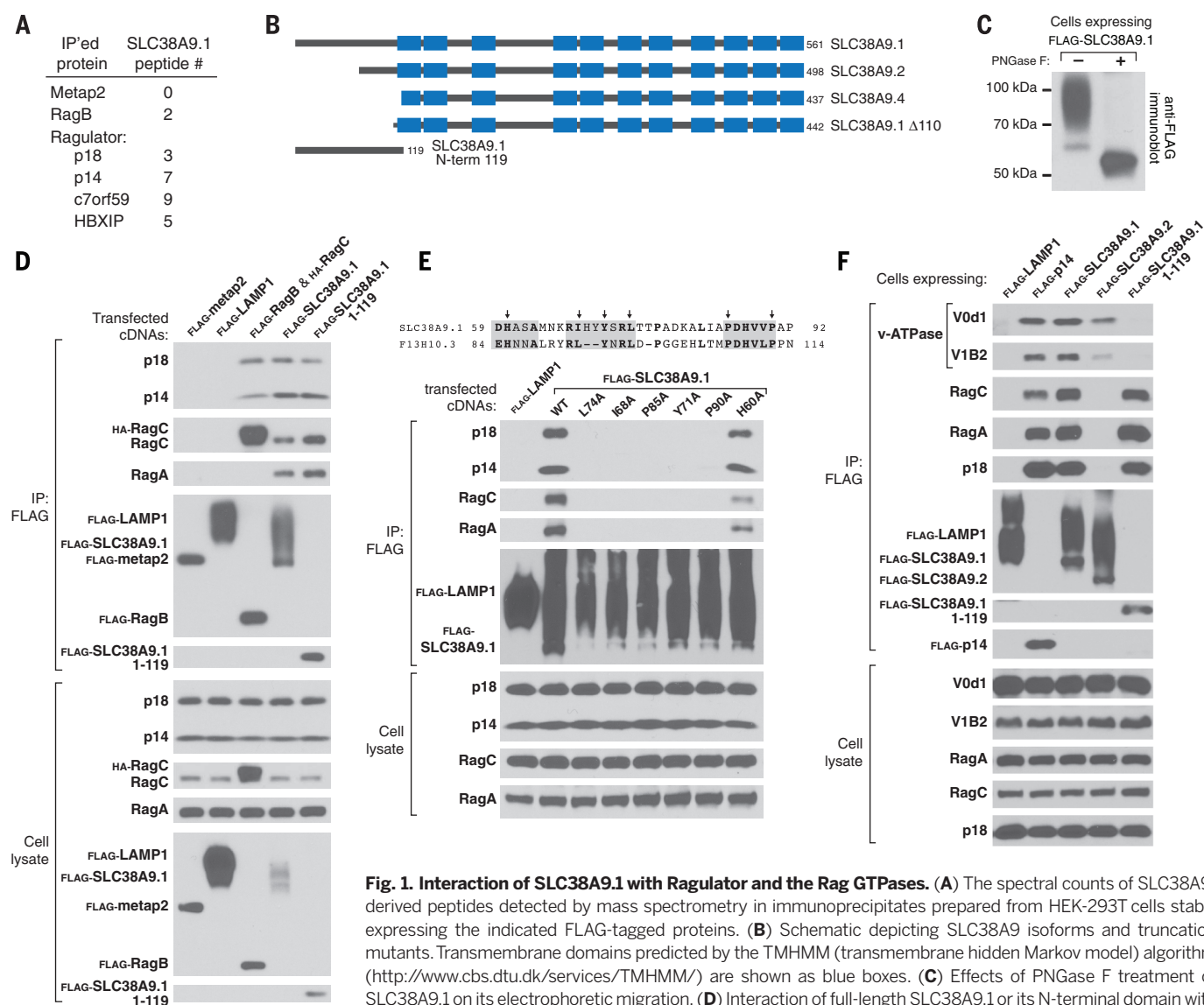


Fig. 1. Interaction of SLC38A9.1 with Regulator and the Rag GTPases. (A) The spectral counts of SLC38A9-derived peptides detected by mass spectrometry in immunoprecipitates prepared from HEK-293T cells stably expressing the indicated FLAG-tagged proteins. (B) Schematic depicting SLC38A9 isoforms and truncation mutants. Transmembrane domains predicted by the TMHMM (transmembrane hidden Markov model) algorithm (<http://www.cbs.dtu.dk/services/TMHMM/>) are shown as blue boxes. (C) Effects of PNGase F treatment of SLC38A9.1 on its electrophoretic migration. (D) Interaction of full-length SLC38A9.1 or its N-terminal domain with endogenous Regulator (p18 and p14) and RagA and RagC GTPases. HEK-293T cells were transfected with the indicated cDNAs in expression vectors, and lysates were prepared and subjected to FLAG immunoprecipitation followed by immunoblotting for the indicated proteins. (E) Identification of key residues in the N-terminal domain of SLC38A9.1 required for it to interact with Regulator and the Rag GTPases. Experiment was performed as in (D) using indicated SLC38A9.1 mutants. (F) Interaction of SLC38A9.1 with v-ATPase components V0d1 and V1B2. HEK-293T cells stably expressing the indicated FLAG-tagged proteins were lysed and processed as in (D).

indicated cDNAs in expression vectors, and lysates were prepared and subjected to FLAG immunoprecipitation followed by immunoblotting for the indicated proteins. (E) Identification of key residues in the N-terminal domain of SLC38A9.1 required for it to interact with Regulator and the Rag GTPases. Experiment was performed as in (D) using indicated SLC38A9.1 mutants. (F) Interaction of SLC38A9.1 with v-ATPase components V0d1 and V1B2. HEK-293T cells stably expressing the indicated FLAG-tagged proteins were lysed and processed as in (D).

first 63 or 124 amino acids of SLC38A9.1, respectively (Fig. 1B).

As expected from the mass spectrometry results, immunoprecipitates of stably expressed FLAG-tagged SLC38A9.1, but not of three other lysosomal membrane proteins—LAMP1 (17), SLC36A1 (18), and SLC38A7 (19)—contained Ragulator (as detected by its p14 and p18 components), RagA, and RagC (Fig. 1D and fig. S2A). Indicative of the strength of the Ragulator-SLC38A9.1 interaction, the amounts of endogenous Ragulator that coimmunoprecipitated with SLC38A9.1 were similar to those associated with the RagB-RagC heterodimer (Fig. 1D). In contrast, SLC38A9.2, SLC38A9.4, or a mutant of SLC38A9.1 lacking its first 110 amino acids (SLC38A9.1 Δ 110) did not associate with Ragulator (fig. S2, B and C). The N-terminal region of SLC38A9.1 is sufficient for it to interact with Ragulator-Rag because on its own, the first 119 amino acids of SLC38A9.1 coimmunoprecipitated similar amounts of Ragulator and Rag GTPases, as did the full-length protein (Fig. 1D and fig. S2C). Using alanine scanning mutagenesis of residues in the N-terminal region conserved to the SLC38A9.1 homolog in *Caenorhabditis elegans* (F13H10.3), we identified I68, Y71, L74, P85, and P90 as required for the Ragulator-SLC38A9.1 interaction (Fig. 1E).

The v-ATPase and its activity are necessary for amino acid sensing by the mTORC1 pathway, and, like SLC38A9.1, it coimmunoprecipitated with stably expressed FLAG-tagged Ragulator (12, 20, 21). Indicating the existence of a supercomplex, stably expressed SLC38A9.1, but not LAMP1, associated with endogenous components of the v-ATPase in addition to Ragulator and the Rag GTPases (Fig. 1F). Although SLC38A9.2 does not interact with Ragulator, it did coimmunoprecipitate the v-ATPase, albeit at lesser amounts than SLC38A9.1 (Fig. 1F). This suggests that the interaction between SLC38A9.1 and the v-ATPase is mediated not through Ragulator but directly or indirectly through the region of SLC38A9.1 that contains its transmembrane domains. Concordant with this interpretation, the N-terminal domain of SLC38A9.1, which interacts strongly with Ragulator, did not coimmunoprecipitate the v-ATPase (Fig. 1F).

Well-characterized members of the SLC38 family of amino acid transporters (SLC38A1-5) localize to the plasma membrane (22), but at least one member, SLC38A7, is a lysosomal membrane protein (19). This is also the case for SLC38A9.1, SLC38A9.2, and SLC38A9.4 because in HEK-293T cells, all three isoforms colocalized with LAMP2, an established lysosomal membrane protein (Fig. 2A and fig. S3, A and B). Amino acids did not affect the lysosomal localization of SLC38A9.1 (Fig. 2A). As would be expected if SLC38A9.1 binds to Ragulator at the lysosome, a Ragulator mutant that does not localize to the lysosomal surface, because its p18 component lacks lipidation sites (23), did not interact with SLC38A9.1 (fig. S3C).

Short hairpin RNA (shRNA)—or small interfering RNA (siRNA)—mediated depletion of SLC38A9 in HEK-293T cells suppressed activation of mTORC1 by amino acids, as detected by the phosphorylation of its established substrate ribosomal protein S6 kinase 1 (S6K1) (Fig. 2B and fig. S3D). Thus, like the five known subunits of Ragulator (12, 13), SLC38A9.1 is a positive component of the mTORC1 pathway. We conclude that SLC38A9.1 is a lysosomal membrane protein that interacts with Ragulator and the Rag GTPases through its N-terminal 119 amino acids (“Ragulator-binding domain”) and is required for mTORC1 activation.

Given the similarity of SLC38A9.1 to amino acid transporters, we reasoned that it might act in conveying amino acid sufficiency to Ragulator and the Rag GTPases. Indeed, stable or transient overexpression in HEK-293T cells of SLC38A9.1, but not of several control proteins, rendered mTORC1 signaling resistant to total amino acid starvation or to just that of leucine or arginine, two amino acids that regulate mTORC1 activity in many cell types (24–26) (Fig. 3A and fig. S4A). Overexpression of SLC38A9.1 did not affect the regulation of mTORC1 by growth factor signaling (fig. S4, D and E). Commensurate with its effects on mTORC1, SLC38A9.1 overexpression suppressed the induction of autophagy caused by amino acid starvation (fig. S4C), a phenotype shared with activated alleles of RagA and RagB (6, 7, 27). Overexpression of variants of SLC38A9 that do

not interact with Ragulator and the Rag GTPases, including SLC38A9.2, SLC38A9.4, and the SLC38A9.1 Δ 110 and SLC38A9.1 I68A mutants, failed to maintain mTORC1 signaling after amino acid withdrawal (Fig. 3, B and C, and fig. S4A). Thus, even in cells deprived of amino acids, some of the overexpressed SLC38A9.1 protein appears to be in an active conformation that confers amino acid insensitivity on mTORC1 signaling in a manner dependent on its capacity to bind Ragulator and Rags. SLC38A9.1 overexpression also activated mTORC1 in the absence of amino acids in HEK-293E, HeLa, and LN229 cells, as well as in mouse embryonic fibroblasts (MEFs), with the degree of activation proportionate to the amount of SLC38A9.1 expressed (fig. S4B). Overexpression of just the Ragulator-binding domain of SLC38A9.1 mimicked the effects of the full-length protein on mTORC1 signaling (Fig. 3D), which indicated that it can adopt an active state when separated from the transmembrane portion of SLC38A9.1.

The gain-of-function phenotype caused by SLC38A9.1 overexpression offered an opportunity to test its relation to the Rag GTPases, mTORC1, and the v-ATPase. The Rag GTPases and mTORC1 both function downstream of SLC38A9.1, as expression of the dominant-negative Rag heterodimer (RagB^{T54N}-RagC^{Q120L}) or treatment with the mTOR inhibitor Torin1 (28) completely inhibited mTORC1 activity, whether SLC38A9.1 was overexpressed or not (Fig. 3, E and F). In contrast, the v-ATPase has a more complex relationship with SLC38A9.1. Its inhibition with concanamycin A eliminated mTORC1 signaling in the control cells but only partially blocked it in cells overexpressing SLC38A9.1 (Fig. 3F). These results suggest a model in which SLC38A9.1 and the v-ATPase represent parallel pathways that converge upon the Ragulator-Rag GTPase complex.

Amino acids modulate the interactions between many of the established components of the amino acid sensing pathway, so we tested if this was also the case for the SLC38A9.1-Ragulator-Rag complex. Indeed, amino acid starvation strengthened the interaction between stably expressed or endogenous Ragulator and endogenous

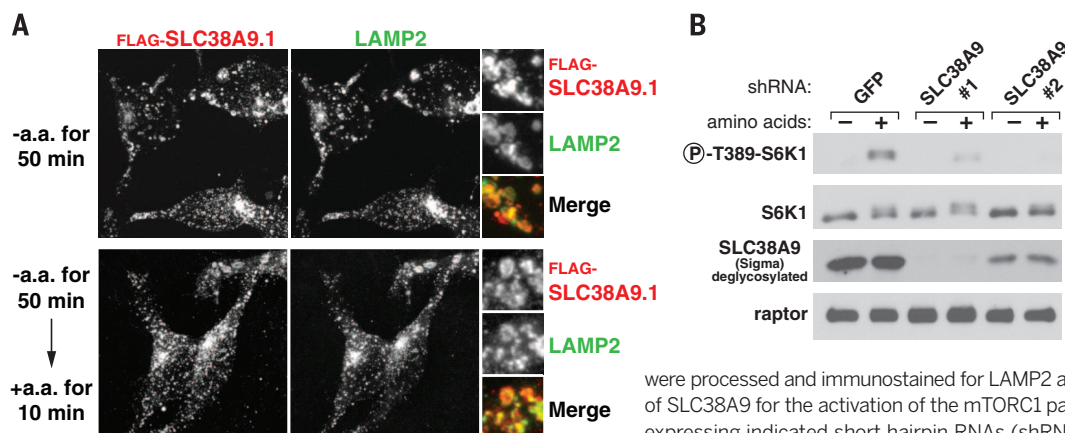


Fig. 2. Localization of SLC38A9.1 to the lysosomal membrane in an amino acid-independent fashion and requirement of SLC38A9 for mTORC1 pathway activation by amino acids. (A) SLC38A9.1 localization in cells deprived of or replete with amino acids. HEK-293T cells stably expressing FLAG-SLC38A9.1 were starved and stimulated with amino acids for the indicated times. Cells

were processed and immunostained for LAMP2 and FLAG-SLC38A9.1. (B) Requirement of SLC38A9 for the activation of the mTORC1 pathway by amino acids. HEK-293T cells expressing indicated short hairpin RNAs (shRNAs) were deprived of amino acids for 50 min or deprived of and then restimulated with amino acids for 10 min. Cell lysates were analyzed for the levels of indicated proteins and the S6K1 phosphorylation state.

SLC38A9 (Fig. 4A and fig. S5), as well as between stably expressed SLC38A9.1 and endogenous Ragulator and Rags (Fig. 4B). We obtained similar results when cells were deprived of and stimulated with just leucine or arginine (Fig. 4A). Curiously, although the N-terminal domain of SLC38A9.1 readily bound Ragulator, the interaction was insensitive to amino acids (Fig. 4B), which suggested that the transmembrane region is required to confer amino acid responsiveness.

As amino acid starvation alters the nucleotide state of the Rag GTPases (6, 7), we tested whether SLC38A9 interacted differentially with mutants

of the Rags that lock their nucleotide state. Heterodimers of epitope-tagged RagB-RagC containing RagB^{T54N}, which mimics the GDP-bound state (6, 7), were associated with more endogenous SLC38A9 than were heterodimers containing wild-type RagB (Fig. 4C). In contrast, heterodimers containing RagB^{Q99L}, which lacks GTPase activity and so is bound to GTP (6, 7, 15), interacted very weakly with SLC38A9 (Fig. 4C). Thus, like Ragulator, SLC38A9 interacts most readily with Rag heterodimers in which RagA/B is GDP-loaded, which is consistent with SLC38A9 binding to Ragulator and with Ragulator being

a guanine nucleotide exchange factor (GEF) for RagA/B. These results suggest that amino acid modulation of the interaction of SLC38A9.1 with Rag-Ragulator largely reflects amino acid-induced changes in the nucleotide state of the Rag GTPases. Because the RagB mutations had greater effects on the interaction of the Rag GTPases with SLC38A9 than with Ragulator (in Fig. 4C, compare the SLC38A9 blots with those for p14 and p18), it is very likely that the Rag heterodimers make Ragulator-independent contacts with SLC38A9 that affect the stability of Rag-SLC38A9 interaction.

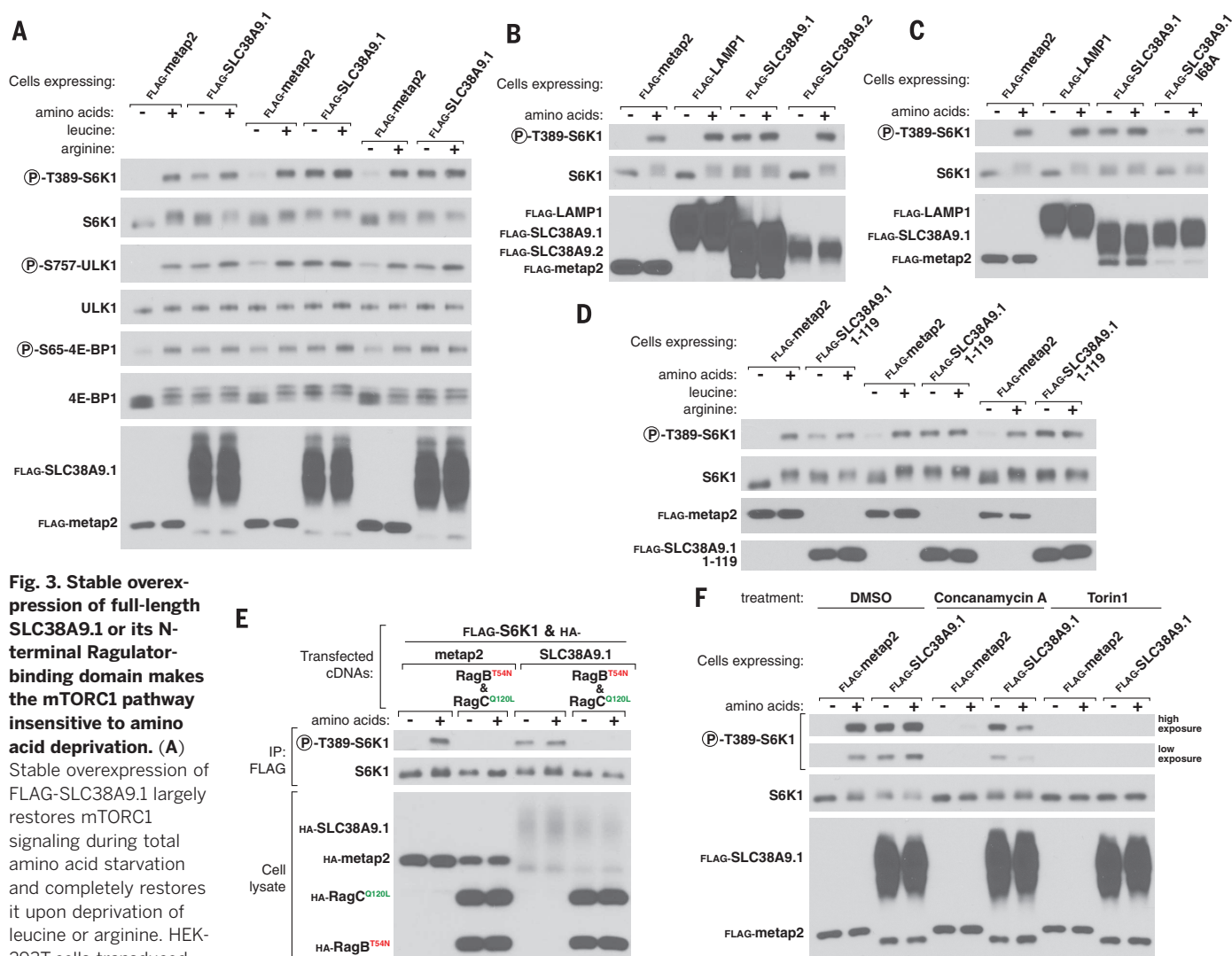


Fig. 3. Stable overexpression of full-length SLC38A9.1 or its N-terminal Ragulator-binding domain makes the mTORC1 pathway insensitive to amino acid deprivation. (A)

Stable overexpression of FLAG-SLC38A9.1 largely restores mTORC1 signaling during total amino acid starvation and completely restores it upon deprivation of leucine or arginine. HEK-293T cells transduced with lentiviruses encoding

the specified proteins were deprived for 50 min of all amino acids, leucine, or arginine and, where indicated, restimulated for 10 min with the missing amino acid(s). Cell lysates were analyzed for the levels of the specified proteins and the phosphorylation states of S6K1, ULK1, and 4E-BP1. **(B and C)** Overexpression of neither SLC38A9.2 nor a point mutant of SLC38A9.1 that fails to bind Ragulator rescues mTORC1 signaling during amino acid starvation. Experiment was performed as in **(A)** except that cells were stably expressing SLC38A9.2 **(B)** or SLC38A9.1 I68A **(C)**. **(D)** Stable overexpression of the Ragulator-binding domain of SLC38A9.1 largely restores mTORC1 signaling during total amino acid starvation and completely rescues it upon deprivation of leucine or arginine. Experiment was performed as in **(A)** except that cells

were stably expressing FLAG-SLC38A9.1 1-119. **(E)** The ability of SLC38A9.1 overexpression to rescue mTORC1 signaling during amino acid starvation is eliminated by coexpression of RagB^{T54N}-RagC^{Q120L}, a Rag heterodimer locked in the nucleotide configuration associated with amino acid deprivation. Effects of expressing the indicated proteins on mTORC1 signaling were monitored by the phosphorylation state of coexpressed FLAG-S6K1. **(F)** Effects of concanamycin A and Torin1 on mTORC1 signaling in cells stably expressing SLC38A9.1. HEK-293T cells stably expressing the indicated FLAG-tagged proteins were treated with the dimethyl sulfoxide (DMSO) vehicle or the specified small-molecule inhibitor during the 50-min starvation for and, where indicated, the 10-min stimulation with amino acids.

We failed to detect SLC38A9.1-mediated amino acid transport or amino acid-induced sodium currents in live cells in which SLC38A9.1 was so highly overexpressed that some reached the plasma membrane (fig. S6, A to E). Because these experiments were confounded by the presence of endogenous transporters or relied on indirect measurements of transport, respectively, we reconstituted SLC38A9.1 into liposomes to directly assay the transport of radiolabeled amino acids. Affinity-purified SLC38A9.1 inserted unidirectionally into liposomes so that its N terminus faced outward in an orientation analogous to that of the native protein in lysosomes (fig. S6, F to H).

We could not use radiolabeled L-leucine in transport assays because it bound nonspecifically to liposomes, so we focused on the transport of L-arginine, which had low background binding (fig. S6I). The SLC38A9.1-containing proteoliposomes exhibited time-dependent uptake of radiolabeled arginine, whereas those containing LAMP1 interacted with similar amounts of arginine as liposomes (Fig. 5A and fig. S6I). Steady-state kinetic experiments revealed that SLC38A9.1 has a Michaelis constant (K_m) of ~39 mM and a catalytic rate constant (k_{cat}) of ~1.8 min⁻¹ (Fig. 5B), indicating that SLC38A9.1 is a low-affinity amino acid transporter. SLC38A9.1

can also efflux arginine from the proteoliposomes (Fig. 5C), but its orientation in liposomes makes it impossible to obtain accurate K_m and k_{cat} measurements for this activity. It is likely that by having to assay the transporter in the “backward” direction we are underestimating its affinity for amino acids during their export from lysosomes.

To assess the substrate specificity of SLC38A9.1, we performed competition experiments using unlabeled amino acids (Fig. 5D). The positively charged amino acids histidine and lysine competed radiolabeled arginine transport to similar degrees as arginine, while leucine had a modest effect and

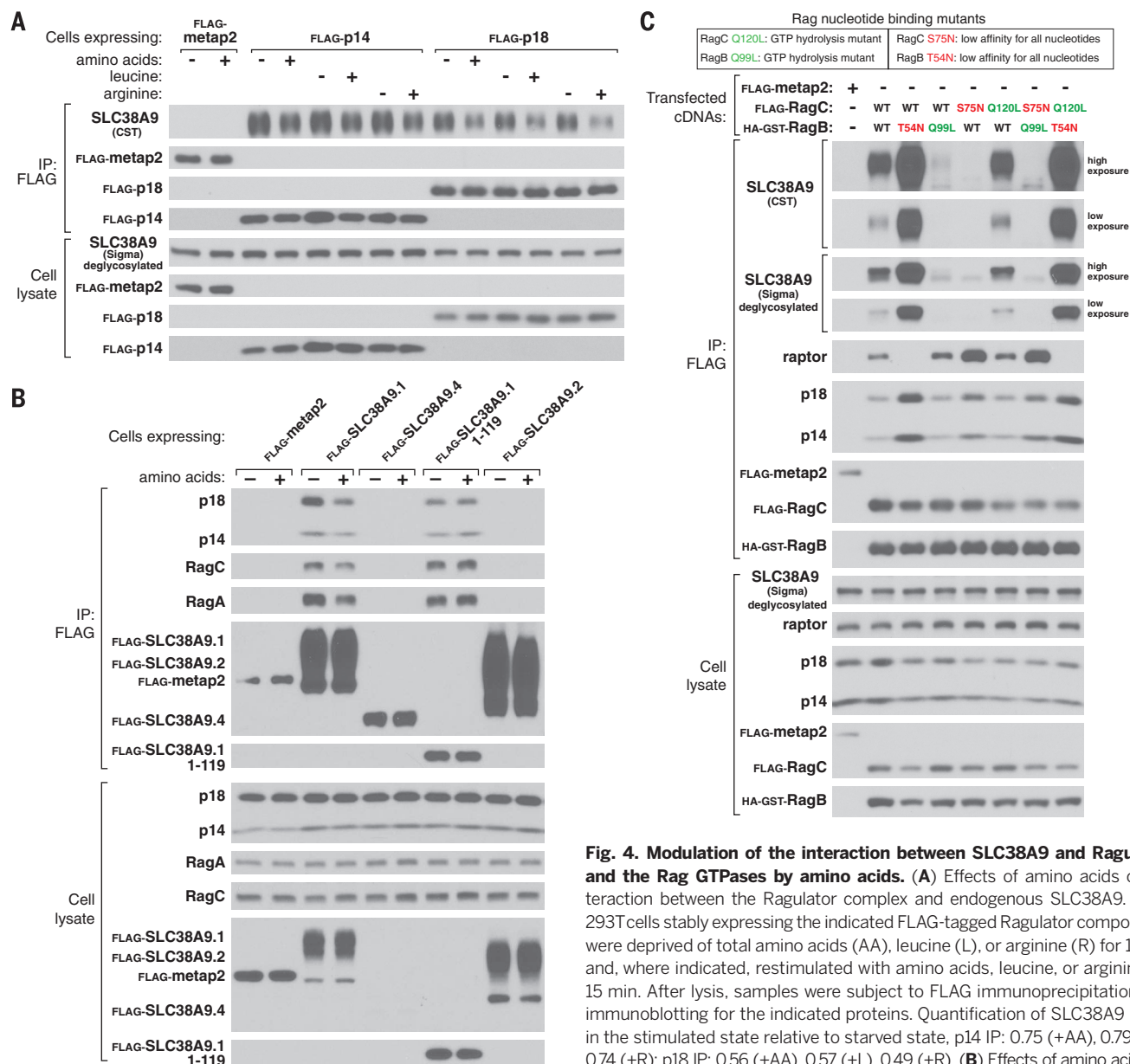


Fig. 4. Modulation of the interaction between SLC38A9 and Ragulator and the Rag GTPases by amino acids. (A) Effects of amino acids on interaction between the Ragulator complex and endogenous SLC38A9. HEK-293T cells stably expressing the indicated FLAG-tagged Ragulator components were deprived of total amino acids (AA), leucine (L), or arginine (R) for 1 hour and, where indicated, restimulated with amino acids, leucine, or arginine for 15 min. After lysis, samples were subject to FLAG immunoprecipitation and immunoblotting for the indicated proteins. Quantification of SLC38A9 levels in the stimulated state relative to starved state, p14 IP: 0.75 (+AA), 0.79 (+L), 0.74 (+R); p18 IP: 0.56 (+AA), 0.57 (+L), 0.49 (+R). (B) Effects of amino acids on the interaction between full-length or truncated SLC38A9.1 and endogenous

Ragulator and the Rag GTPases. Experiment was performed as in (A) except that cells stably expressed the indicated SLC38A9 isoforms or its N-terminal domain (SLC38A9.1 1-119). Quantification of indicated protein levels in the stimulated state relative to starved state, SLC38A9.1 IP: 0.43 (p18), 0.51 (p14), 0.61 (RagC), 0.58 (RagA); SLC38A9.1 1-119 IP: 0.99 (p18), 1.05 (p14), 1.04 (RagC), 1.09 (RagA). (C) Effects of nucleotide-binding mutations in the Rag GTPases on association with endogenous SLC38A9. HEK-293T cells were transfected with the indicated cDNAs in expression vectors, and lysates were prepared and subjected to FLAG immunoprecipitation followed by immunoblotting for the indicated proteins. Two different antibodies were used to detect endogenous SLC38A9.

glycine was the least effective competitor. Thus, it appears that SLC38A9.1 has a relatively nonspecific substrate profile with a preference for polar amino acids.

Given the preference of SLC38A9.1 for the transport of arginine and that arginine is highly concentrated in rat liver lysosomes (29) and yeast vacuoles (30), we asked whether SLC38A9.1

may have an important role in transmitting arginine levels to mTORC1. To this end, we examined how mTORC1 signaling responded to a range of arginine or leucine concentrations in HEK-293T cells in which we knocked out SLC38A9 using CRISPR-Cas9 genome editing (Fig. 5E). Activation of mTORC1 by arginine was strongly repressed at all arginine concentrations, whereas

the response to leucine was only blunted, so that high leucine concentrations activated mTORC1 equally well in null and control cells (Fig. 5F).

Several properties of SLC38A9.1 are consistent with its functioning as an amino acid sensor for the mTORC1 pathway. Purified SLC38A9.1 transports and therefore directly interacts with amino acids. Overexpression of SLC38A9.1 or just its

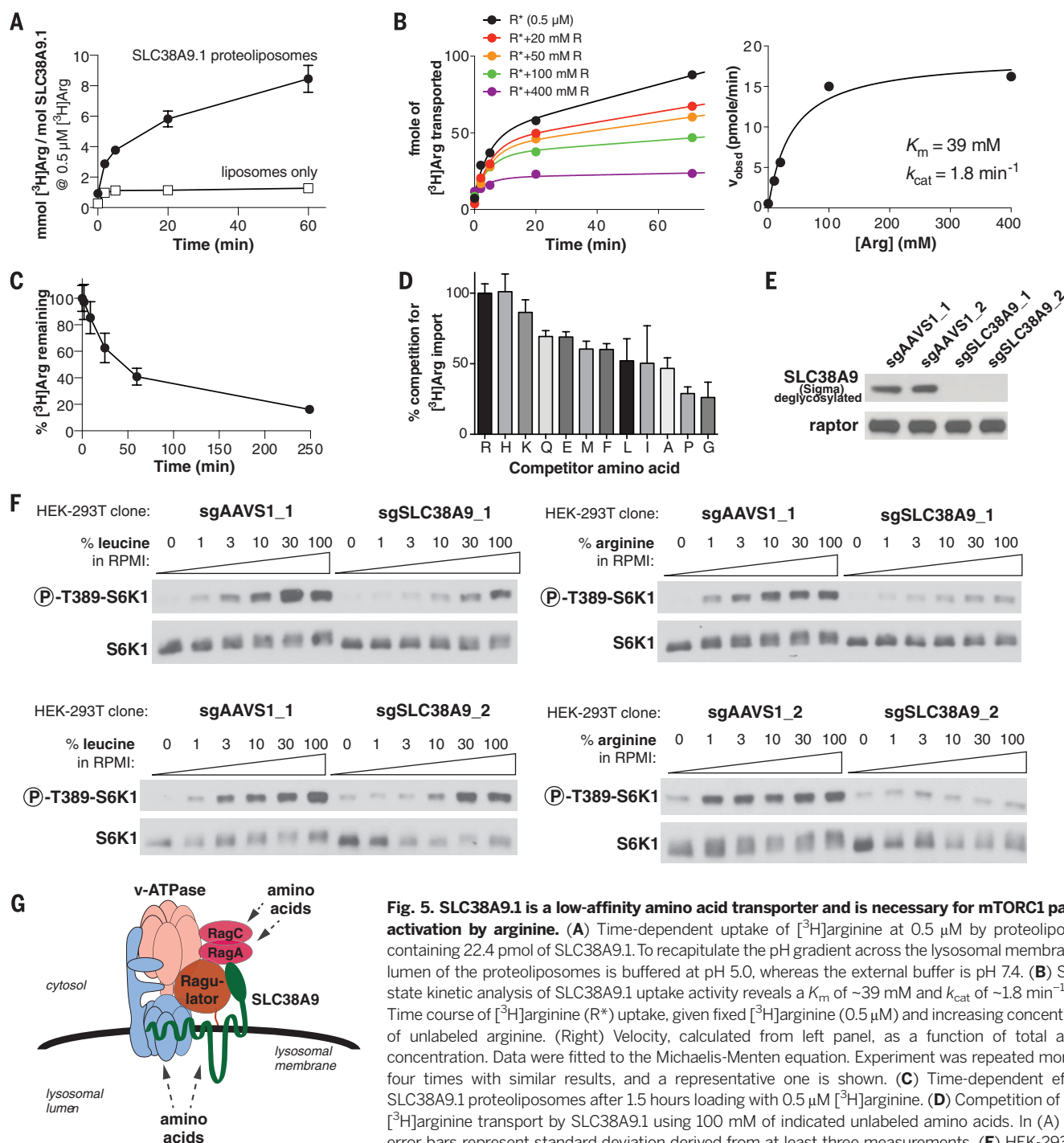


Fig. 5. SLC38A9.1 is a low-affinity amino acid transporter and is necessary for mTORC1 pathway activation by arginine.

(A) Time-dependent uptake of ^3H arginine at 0.5 μM by proteoliposomes containing 22.4 pmol of SLC38A9.1. To recapitulate the pH gradient across the lysosomal membrane, the lumen of the proteoliposomes is buffered at pH 5.0, whereas the external buffer is pH 7.4. (B) Steady-state kinetic analysis of SLC38A9.1 uptake activity reveals a K_m of $\sim 39 \text{ mM}$ and k_{cat} of $\sim 1.8 \text{ min}^{-1}$. (Left) Time course of ^3H arginine (R^*) uptake, given fixed ^3H arginine (0.5 μM) and increasing concentrations of unlabeled arginine. (Right) Velocity, calculated from left panel, as a function of total arginine concentration. Data were fitted to the Michaelis-Menten equation. Experiment was repeated more than four times with similar results, and a representative one is shown. (C) Time-dependent efflux of SLC38A9.1 proteoliposomes after 1.5 hours loading with 0.5 μM ^3H arginine. (D) Competition of 0.5 μM ^3H arginine transport by SLC38A9.1 using 100 mM of indicated unlabeled amino acids. In (A) to (D), error bars represent standard deviation derived from at least three measurements. (E) HEK-293T cells null for SLC38A9 were generated by CRISPR-Cas9 genome editing with two different guide sequences

and isolated by single-cell cloning. The AAVS1 locus was targeted as a negative control. (F) Impairment of arginine-induced activation of the mTORC1 pathway in SLC38A9-null HEK-293T cells. Cells were starved of the indicated amino acid for 50 min and stimulated for 10 min with the indicated amino acid concentrations. The leucine and arginine concentrations in RPMI are, respectively, 381 μM and 1.14 mM. (G) Model for distinct amino acid inputs to the Rag GTPases in signaling amino acid sufficiency to mTORC1.

Ragulator-binding domain activates mTORC1 signaling even in the absence of amino acids. The activation of mTORC1 by amino acids, particularly arginine, is defective in cells lacking SLC38A9. Given these results and that arginine is highly enriched in lysosomes from at least one mammalian tissue (29), we propose that SLC38A9.1 is a strong candidate for being a lysosome-based arginine sensor for the mTORC1 pathway. To substantiate this possibility, it will be necessary to determine the actual concentrations of arginine and other amino acids in the lysosomal lumen and cytosol and compare them to the affinity of SLC38A9.1 for amino acids. If high arginine levels are a general feature of mammalian lysosomes, it could explain why SLC38A9.1 appears to have a relatively broad amino acid specificity; perhaps no other amino acid besides arginine is in the lysosomal lumen at levels that approach its K_m .

The notion that proteins with sequence similarity to transporters function as both transporters and receptors (transceptors) is not unprecedented (31, 32). The transmembrane region of SLC38A9.1 might undergo a conformational change upon amino acid binding that is then transmitted to Ragulator through its N-terminal domain. What this domain does is unknown, but it could regulate Ragulator nucleotide exchange activity or access to the Rag GTPases by other components of the pathway. To support a role as a sensor, it will be necessary to show that amino acid binding regulates the biochemical function of SLC38A9.1.

Even if SLC38A9.1 is an amino acid sensor, additional sensors, even for arginine, are almost certain to exist, as we already know that amino acid-sensitive events exist upstream of Folliculin (15, 33) and GATOR1 (34), which, like Ragulator, also regulate the Rag GTPases. An attractive model is that distinct amino acid inputs to mTORC1 converge at the level of the Rag GTPases, with some initiating at the lysosome through proteins like SLC38A9.1 and others from cytosolic sensors that remain to be defined (Fig. 5G). Indeed, such a model would explain why the loss of SLC38A9.1 specifically affects arginine sensing but its overexpression makes mTORC1 signaling resistant to arginine or leucine starvation: Hyperactivation of the Rag GTPases through the deregulation of a single upstream regulator is likely sufficient to overcome the lack of other positive inputs. A similar situation may occur upon loss of GATOR1, which, like SLC38A9.1 overexpression, causes mTORC1 signaling to be resistant to total amino acid starvation (14).

Modulators of mTORC1 have clinical utility in disease states associated with or caused by mTORC1 deregulation. The allosteric mTOR inhibitor rapamycin is used in cancer treatment (35) and transplantation medicine (36). However, to date, there have been few reports on small molecules that activate mTORC1 by engaging known components of the pathway. The identification of SLC38A9.1—a protein that is a positive regulator of the mTORC1 pathway and has an amino acid binding site—provides an opportunity to develop small-molecule agonists of mTORC1 signaling. Such molecules should promote mTORC1-

mediated protein synthesis and could have utility in combatting muscle atrophy secondary to disuse or injury. Lastly, a selective mTORC1 pathway inhibitor may have better clinical benefits than rapamycin, which in long-term use inhibits both mTORC1 and mTORC2 (37). SLC38A9.1 may be an appropriate target to achieve this.

REFERENCES AND NOTES

- J. L. Jewell, R. C. Russell, K. L. Guan, *Nat. Rev. Mol. Cell Biol.* **14**, 133–139 (2013).
- J. J. Howell, B. D. Manning, *Trends Endocrinol. Metab.* **22**, 94–102 (2011).
- R. Zoncu, A. Efeyan, D. M. Sabatini, *Nat. Rev. Mol. Cell Biol.* **12**, 21–35 (2011).
- S. Sengupta, T. R. Peterson, D. M. Sabatini, *Mol. Cell* **40**, 310–322 (2010).
- M. Laplante, D. M. Sabatini, *Cell* **149**, 274–293 (2012).
- Y. Sancak et al., *Science* **320**, 1496–1501 (2008).
- E. Kim, P. Goraksha-Hicks, L. Li, T. P. Neufeld, K. L. Guan, *Nat. Cell Biol.* **10**, 935–945 (2008).
- K. Saito, Y. Araki, K. Kontani, H. Nishina, T. Katada, *J. Biochem.* **137**, 423–430 (2005).
- C. Buerger, B. DeVries, V. Stambolic, *Biochem. Biophys. Res. Commun.* **344**, 869–880 (2006).
- S. Menon et al., *Cell* **156**, 771–785 (2014).
- R. Zoncu et al., *Science* **334**, 678–683 (2011).
- L. Bar-Peled, L. D. Schweitzer, R. Zoncu, D. M. Sabatini, *Cell* **150**, 1196–1208 (2012).
- Y. Sancak et al., *Cell* **141**, 290–303 (2010).
- L. Bar-Peled et al., *Science* **340**, 1100–1106 (2013).
- Z. Y. Tsun et al., *Mol. Cell* **52**, 495–505 (2013).
- B. E. Sundberg et al., *J. Mol. Neurosci.* **35**, 179–193 (2008).
- S. R. Carlsson, J. Roth, F. Piller, M. Fukuda, *J. Biol. Chem.* **263**, 18911–18919 (1988).
- C. Sagné et al., *Proc. Natl. Acad. Sci. U.S.A.* **98**, 7206–7211 (2001).
- A. Chapel et al., *Mol. Cell Proteomics* **12**, 1572–1588 (2013).
- M. Li et al., *J. Biol. Chem.* **288**, 35769–35780 (2013).
- Y. Xu et al., *J. Biol. Chem.* **287**, 26409–26422 (2012).
- B. Mackenzie, J. D. Erickson, *Pflügers Arch.* **447**, 784–795 (2004).
- S. Nada et al., *EMBO J.* **28**, 477–489 (2009).
- H. Ban et al., *Int. J. Mol. Med.* **13**, 537–543 (2004).
- K. Hara et al., *J. Biol. Chem.* **273**, 14484–14494 (1998).
- K. Yao et al., *J. Nutr.* **138**, 867–872 (2008).
- A. Efeyan et al., *Nature* **493**, 679–683 (2013).
- C. C. Thoreen et al., *J. Biol. Chem.* **284**, 8023–8032 (2009).
- E. Harms, N. Gochman, J. A. Schneider, *Biochem. Biophys. Res. Commun.* **99**, 830–836 (1981).
- K. Kitamoto, K. Yoshizawa, Y. Ohsumi, Y. Anraku, *J. Bacteriol.* **170**, 2683–2686 (1988).
- I. Holsbeek, O. Lagatie, A. Van Nuland, S. Van de Velde, J. M. Thevelein, *Trends Biochem. Sci.* **29**, 556–564 (2004).
- R. Hyde, E. L. Cwiklinski, K. MacAulay, P. M. Taylor, H. S. Hundal, *J. Biol. Chem.* **282**, 19788–19798 (2007).
- C. S. Petit, A. Roczniak-Ferguson, S. M. Ferguson, *J. Cell Biol.* **202**, 1107–1122 (2013).
- L. Chantranupong et al., *Cell Reports* **9**, 1–8 (2014).
- D. Benjamin, M. Colombi, C. Moroni, M. N. Hall, *Nat. Rev. Drug Discov.* **10**, 868–880 (2011).
- B. D. Kahn, J. S. Camardo, *Transplantation* **72**, 1181–1193 (2001).
- D. W. Lammig, L. Ye, D. M. Sabatini, J. A. Baur, *J. Clin. Invest.* **123**, 980–989 (2013).

ACKNOWLEDGMENTS

We thank all members of the Sabatini Lab for helpful insights, E. Spooner for the mass spectrometric analyses, and G. Superti-Furga and M. Rebsamen for suggesting the use of the Sigma antibody to detect SLC38A9. This work was supported by grants from the NIH (R01 CA103866 and AI47389) and Department of Defense (W81XWH-07-0448) to D.M.S. and fellowship support from the NIH to Z.-Y.T. (F30 CA180754), to S.W. (T32 GM007753 and F31 AG044064), to L.C. (F31 CA180271), and to R.L.W. (T32 GM007753); a National Defense Science and Engineering Graduate Fellowship to G.A.W.; an NSF Graduate Research Fellowship to T.W.; an American Cancer Society–Ellison Foundation Postdoctoral Fellowship to W.C. (PF-13-356-01-TBE); a German Academic Exchange Service (DAAD) Fellowship to C.S.; and support from the Howard Hughes Medical Institute to T.D.J., C.K., and J.P. D.M.S. and B.L.S. are investigators of the Howard Hughes Medical Institute.

SUPPLEMENTARY MATERIALS

www.sciencemag.org/content/347/6218/188/suppl/DC1
Materials and Methods
Figs. S1 to S6
References

9 June 2014; accepted 25 November 2014
Published online 7 January 2015;
10.1126/science.1257132

METABOLISM

Differential regulation of mTORC1 by leucine and glutamine

Jenna L. Jewell,¹ Young Chul Kim,^{1,*} Ryan C. Russell,^{1,*} Fa-Xing Yu,² Hyun Woo Park,¹ Steven W. Plouffe,¹ Vincent S. Tagliabracchi,¹ Kun-Liang Guan^{1,†}

The mechanistic target of rapamycin (mTOR) complex 1 (mTORC1) integrates environmental and intracellular signals to regulate cell growth. Amino acids stimulate mTORC1 activation at the lysosome in a manner thought to be dependent on the Rag small guanosine triphosphatases (GTPases), the Ragulator complex, and the vacuolar H⁺-adenosine triphosphatase (v-ATPase). We report that leucine and glutamine stimulate mTORC1 by Rag GTPase-dependent and -independent mechanisms, respectively. Glutamine promoted mTORC1 translocation to the lysosome in RagA and RagB knockout cells and required the v-ATPase but not the Ragulator. Furthermore, we identified the adenosine diphosphate ribosylation factor-1 GTPase to be required for mTORC1 activation and lysosomal localization by glutamine. Our results uncover a signaling cascade to mTORC1 activation independent of the Rag GTPases and suggest that mTORC1 is differentially regulated by specific amino acids.

Cells sense environmental nutrient flux and respond by tightly controlling anabolic and catabolic processes to best coordinate cell growth with nutritional status. The mechanistic target of rapamycin (mTOR), a conserved serine-threonine kinase, is part of the mTOR complex 1 (mTORC1), which helps coordinate

cell growth with nutritional status. Dysregulation of mTORC1 is common in human diseases, including cancer and diabetes (1). Amino acids are essential for mTORC1 activation (2, 3); however, it remains unclear how specific amino acids are sensed. Leucine (Leu) (2, 4, 5), glutamine (Gln) (5–7), and arginine (Arg) (2) have been implicated in

mTORC1 activation. In one model, mTORC1 indirectly senses amino acids within the lysosomal lumen that requires the Rag guanine triphosphatases (GTPases), which are regulated by the pentameric Ragulator complex, the vacuolar H⁺-adenosine triphosphatase (v-ATPase), and the Gator complex (8, 9). When activated, the Rag GTPases bind to and recruit mTORC1 to the lysosome, where the Rheb GTPase activates mTORC1 (4). In mammals, there are four Rag proteins: RagA and RagB, which are functionally redundant; and RagC and RagD, which are also functionally equivalent. The formation of a heterodimer between RagA or RagB with RagC or RagD, and the guanine nucleotide state of the Rag proteins determines mTORC1 recruitment to the lysosome and subsequent activation (4, 10, 11). Under amino acid sufficiency, RagA and RagB complexes are guanosine triphosphate (GTP)-loaded and capable of binding Raptor. Somehow the v-ATPase detects the build-up of lysosomal amino acids (12), stimulates

Regulator guanine nucleotide exchange factor (GEF) activity, and inhibits Gator GTPase-activating protein (GAP) activity (9, 13). This loads RagA-RagB complexes with GTP and recruits mTORC1 to the lysosome, where it encounters Rheb, a potent mTORC1 activator that mediates growth factor signals. The tuberous sclerosis complex (TSC) tumor suppressor is also localized at the lysosome, and it negatively regulates mTORC1 by acting as a GAP for Rheb (14).

We generated mouse embryonic fibroblasts that lack both RagA and RagB [RagA/B knock-out (KO) MEFs] (Fig. 1A and fig. S1). RagA-RagB complexes bind directly to mTORC1 (15), and overexpression of a constitutively active version of one of the two proteins renders mTORC1 insensitive to amino acid starvation (fig. S2) (4, 10). Deletion of RagA/B diminished the abundance of RagC, consistent with RagA and RagB stabilizing RagC and RagD by forming heterodimers (Fig. 1A) (4, 16). Unexpectedly, deletion of RagA and RagB reduced (~30%), but did not abolish, mTORC1 activity, as judged by the phosphorylation state of its substrates ribosomal S6 kinase 1 (S6K1) and eukaryotic translation initiation factor 4E-binding protein 1 (4EBP1). Phosphorylation of S6K1 and 4EBP1 was abolished when the RagA/B KO cells were treated with the mTOR inhibitors Torin1 and Rapamycin or were depleted of the

mTORC1 subunit Raptor with short hairpin RNA (shRNA) (fig. S3). Thus, mTORC1 is active in the absence of RagA and RagB.

To investigate the amino acid response of the RagA/B KO MEFs, we stimulated cells with amino acids and analyzed the kinetics of mTORC1 activation. Both the magnitude and rate at which mTORC1 was activated by amino acids were reduced in cells lacking RagA and RagB (Fig. 1B and fig. S4). Likewise, mTORC1 activity was reduced in RagA/B KO MEFs upon amino acid withdrawal (fig. S5). To exclude the possibility that some cells lacking RagA and RagB spontaneously mutated to compensate for decreased mTORC1 activity, we analyzed individual clones derived from the RagA/B KO MEF population. Single clones displayed an increase in mTORC1 activity in response to amino acids (fig. S6). To determine which amino acids activate mTORC1 in the absence of RagA and RagB, we individually stimulated RagA/B KO MEFs with each of the 20 standard amino acids (fig. S7). Leu and Arg stimulated mTORC1 activation in control, but not RagA/B KO cells (Fig. 1C and figs. S7 and S8). Gln-stimulated activation of mTORC1 in RagA/B KO cells displayed kinetics similar to that of control cells and when RagA/B KO cells were stimulated with the 20 standard amino acids (Fig. 1, B and C, and fig. S4). Stable reexpression

¹Department of Pharmacology and Moores Cancer Center, University of California, San Diego, La Jolla, CA 92093, USA.

²Children's Hospital and Institute of Biomedical Sciences, Fudan University, Shanghai 200032, China.

*These authors contributed equally to this work. †Corresponding author. E-mail: kuguan@ucsd.edu

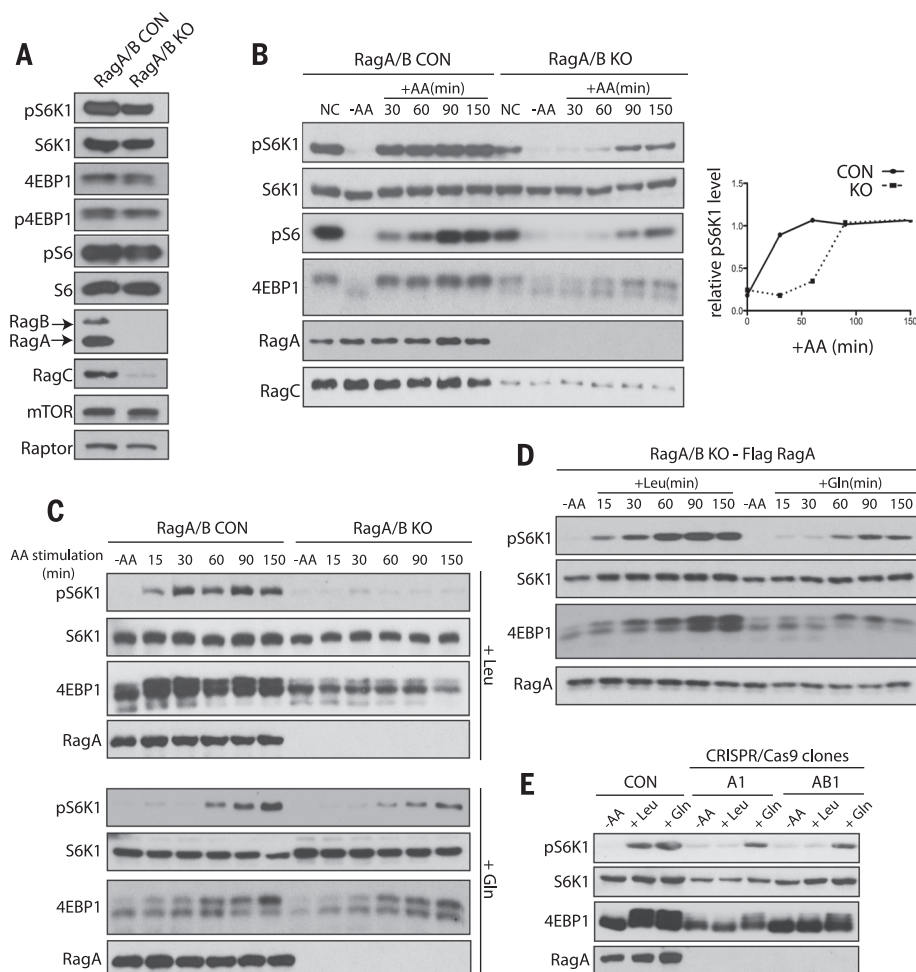


Fig. 1. Gln, but not Leu, activates mTORC1 independently of RagA and RagB.

mTORC1 activity was analyzed by the phosphorylation of S6K1 (pS6K1), S6 (pS6), and 4EBP1 (p4EBP1) and the mobility shift of 4EBP1. AA, amino acids. (A) mTORC1 activity was analyzed in control (CON) and RagA/B KO MEFs under normal conditions (NC). mTOR, Raptor, RagA, RagB, and RagC protein were also analyzed. (B) mTORC1 activity was analyzed in CON and RagA/B KO MEFs under NC, in the absence of amino acids (-AA) and at the indicated times after the addition of amino acids (+AA) (left). Relative abundance of pS6K1 is plotted (right). (C) mTORC1 activity after stimulation with Leu (top) or Gln (bottom) in CON and RagA/B KO MEFs. (D) mTORC1 activity was analyzed after stimulation with Leu or Gln in RagA/B KO MEFs stably expressing Flag-tagged RagA at the indicated times. (E) mTORC1 activity was analyzed in CON, RagA KO (A1) and RagA/B KO (AB1) HEK293A cells that were starved of amino acids or stimulated with Leu or Gln for 150 min.

of Flag-tagged RagA in the RagA/B KO MEFs restored mTORC1 activation in response to Leu (Fig. 1D), which confirmed that RagA and RagB are required for mTORC1 activation by Leu but not Gln.

We performed genome editing by means of clustered regularly interspaced short palindromic repeats (CRISPR/Cas9) to inactivate the RagA and RagB genes in human embryonic kidney 293A (HEK293A) cells (17, 18) (fig. S9). In HEK293A cells and in MEFs, RagA is more abundant than RagB (Fig. 1A and fig. S9E). Loss of RagA alone or both RagA and RagB in these cells prevented Leu-, but not Gln-induced, activation of mTORC1

(Fig. 1E and fig. S9F). Thus, Gln can stimulate mTORC1 activation independently of RagA and RagB or cell type.

The lysosome is essential in the amino acid-sensing pathway to mTORC1 and is thought to be a platform for optimal mTORC1 activation that integrates effects of growth factors, such as insulin, through Rheb and those of amino acids through the Rags (19). Because Gln can activate mTORC1 in the absence of RagA and RagB (Fig. 1, C and E, fig. S7, and fig. S9F), we investigated whether lysosomal localization of mTORC1 was required for Gln-induced activation of mTORC1 in cells lacking RagA and RagB. In control cells,

mTOR translocated to lysosomal membranes identified by the presence of the marker protein lysosome-associated membrane protein 2 (LAMP2) as early as 50 min and remained at the lysosome 150 min after amino acid stimulation (fig. S10A) (4, 11). In contrast, mTOR did not localize to lysosomal membranes in RagA/B KO cells after 50 min of amino acid stimulation (fig. S10B). However, by 150 min, we observed lysosomal localization of mTOR in a subset of cells that also showed activation of mTORC1 (Fig. 2A and fig. S10B). Gln, but not Leu, induced lysosomal localization of mTOR in RagA/B KO MEFs (Fig. 2, B and C). Furthermore, synergistic activation of

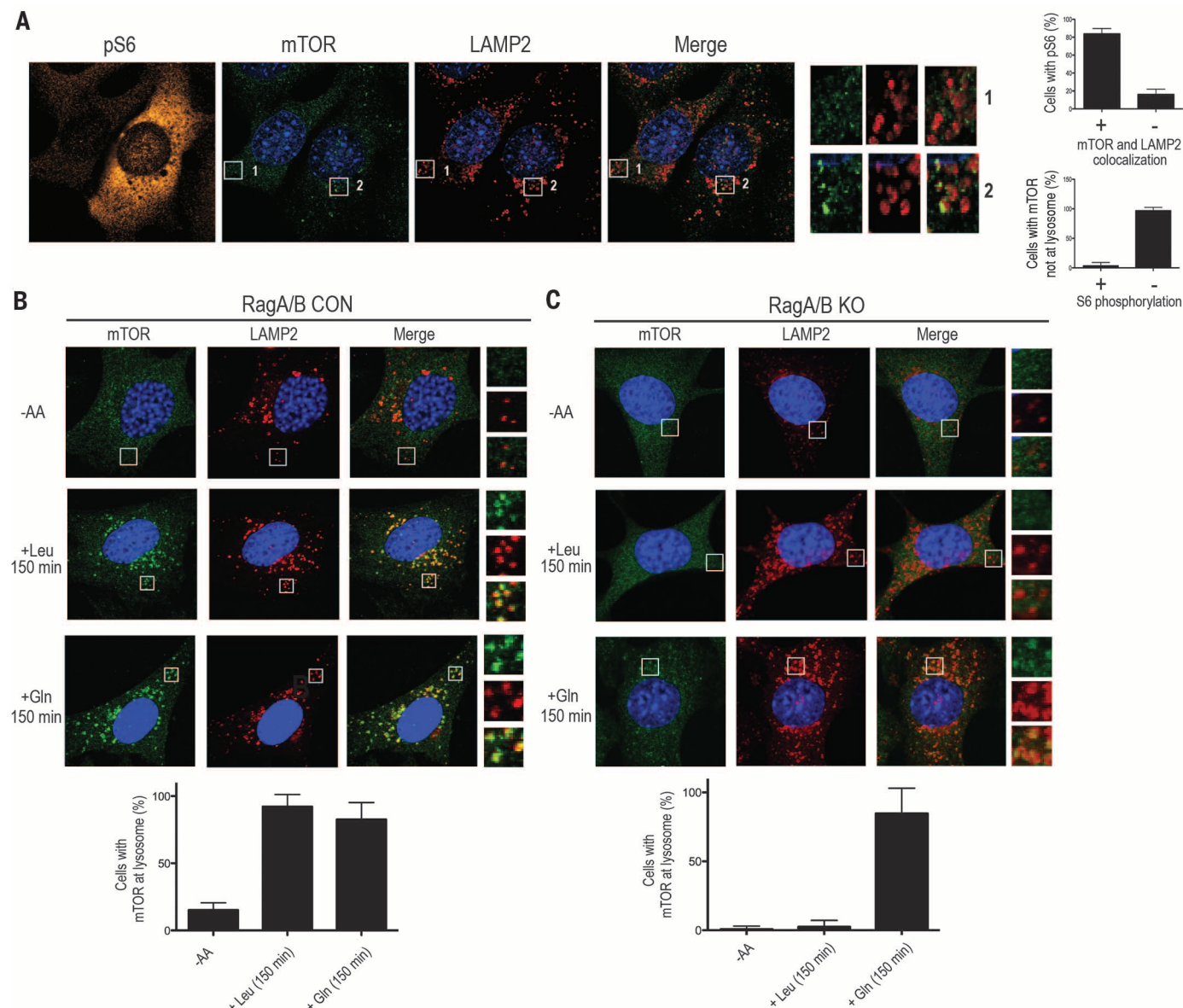


Fig. 2. Gln-induced mTORC1 lysosomal localization in the absence of RagA and RagB. (A) Immunofluorescence (IF) analysis depicting mTORC1 activation by phosphorylation of S6 (pS6; orange) in RagA/B KO MEFs. mTOR (green) and LAMP2 (red) are also shown. Quantification of the percentage of pS6 cells with mTOR and LAMP2 colocalization (top right) and the percentage of cells with mTOR not at lysosome that also contain S6 phos-

phorylation (bottom right). (B and C) IF analysis depicting mTOR and LAMP2 in CON (B) or RagA/B KO MEFs (C), without amino acids or stimulated with Leu or Gln for 150 min (top). Quantification of the percent of cells with mTOR at the lysosome without amino acids or stimulated with Leu or Gln (bottom). Higher-magnification images (A) to (C) of the area depicted by the inset and their overlays are shown on the right.

mTOR by amino acids and insulin was observed in RagA/B KO cells (fig. S11). Thus, Gln appears to induce mTORC1 activation through translocation to the lysosome in a manner independent of RagA and RagB.

Amino acid transporters (5, 12) and the Ragulator complex (11, 13) have been implicated in mTORC1 activation. We analyzed mTORC1 activity in cells depleted of several amino acid transporters and in MEFs lacking p14 (p14 KO MEFs), an essential subunit of the Ragulator complex. Gln activated mTORC1 in cells depleted of some amino acid transporters and in p14 KO MEFs, which indicated that these transporters and the Ragulator are not required for Gln-induced activation of mTORC1 (fig. S12 and fig. 3A).

The v-ATPase is essential for the acidification of the lysosome and interacts with the Rags and Ragulator to stimulate mTORC1 activation in response to amino acids (12). We treated control and RagA/B KO cells with the v-ATPase inhibitor bafilomycin A (Baf A) (20). Baf A inhibited mTORC1 activation in both control and RagA/B KO cells when the cells were stimulated either with all amino acids (Fig. 3B and fig. S13A) or with Leu or Gln individually (Fig. 3C). Baf A also inhibited lysosomal localization of mTORC1 in RagA/B KO cells (fig. S13, B and C). Furthermore, inhibition of the v-ATPase by concanamycin A or inhibition of the lysosomal pH gradient by chloroquine also blocked Gln-induced lysosomal localization and activation of mTORC1 in RagA/B KO cells (fig. S13, D to H). Moreover, depletion of the v-ATPase V0c subunit, which interacts with the Ragulator and controls mTORC1 activity (12), largely prevented amino acid-induced activation of mTORC1 in control and RagA/B KO MEFs (Fig. 3D and fig. S13I). Furthermore, depletion of several lysosomal proteins had no effect on Gln-induced activation of mTORC1 and localization in the absence of RagA and RagB, which indicated that

modification of the v-ATPase was not secondary to a general disruption in lysosomal structure and function (fig. S13, K and L). Taken together, Gln-induced activation of mTORC1 appears to require the v-ATPase and lysosomal function.

In *Drosophila* S2 cells, TORC1 activity is inhibited in cells depleted of the *Drosophila* ADP ribosylation factor–Arf1 (dArf1) (21), and we observed a further decrease in amino acid-induced TORC1 activation when both dRagA and dArf1 were depleted (Fig. 4A). We used small interfering RNA (siRNA) to deplete Arf1 from HEK293A RagA/B KO cells. Gln stimulated mTORC1 activation in RagA/B KO cells treated with a control siRNA; however, it failed to induce mTORC1 activation in RagA/B KO cells depleted of Arf1 (Fig. 4B). Depletion of other Arf family members failed to inhibit Gln-induced activation of mTORC1 in RagA/B KO cells (fig. S14A). Treatment of RagA/B KO cells with brefeldin A (BFA), an Arf1 GEF inhibitor (22), at high doses blocked amino acid signaling to mTORC1, whereas BFA caused only a small decrease in mTORC1 activation in response to amino acids in control cells (Fig. 4C and fig. S14, B and C). Consistently, BFA blocked Gln-induced activation of mTORC1 in RagA/B KO cells (Fig. 4D and fig. S14D). In addition, depletion of Arf1 or BFA treatment did not inhibit Leu-induced activation of mTORC1 in control cells, nor did they affect lysosomal pH (fig. S14, E to G).

Leu or Gln stimulation did not appear to affect the guanine nucleotide state of Arf1 (fig. S14H). Overexpression of a constitutively active Arf1-GTP failed to restore mTORC1 activation under amino acid deficiency (fig. S14I). Further, green fluorescent protein–tagged Arf1 (Arf1-GFP) localization was unaffected by amino acid starvation or stimulation (fig. S15). These results indicate that GTP hydrolysis or nucleotide

cycling of Arf1, or both, is required for mTORC1 activation.

Arf1 regulates vesicular trafficking, so we tested whether bidirectional inhibition of trafficking between the endoplasmic reticulum (ER) and Golgi would affect Gln-induced activation of mTORC1 (23). We depleted proteins involved in anterograde trafficking and treated RagA/B KO cells with Golgicide A (24), yet did not observe an effect on Gln-induced activation of mTORC1 (fig. S16). These results support that Arf1 signaling to mTORC1 is specific and independent of ER-Golgi vesicular transport.

RagA/B KO MEFs treated with BFA were analyzed for mTOR localization in response to Gln stimulation. Gln-induced mTOR localization to the lysosome (Fig. 4E and Fig. 2C); however, pretreatment of cells with BFA inhibited the effect of Gln (Fig. 4E). Artificially targeting mTORC1 to the lysosomal surface by adding the C-terminal lysosomal targeting motif of Rheb to Raptor (11) activated mTORC1 in RagA/B KO cells, even in the presence of BFA (Fig. 4F). Thus, BFA inhibits mTORC1 by interfering with its lysosomal localization, which implicates Arf1 in the signaling pathway that links Gln to mTORC1 localization and activation at the lysosome.

In conclusion, we show that mTORC1 is differentially regulated by Gln and Leu (fig. S17). Our results demonstrate that RagA and RagB are essential for mTORC1 activation by Leu, but not by Gln, and this appears to be evolutionarily conserved in *Saccharomyces cerevisiae* (25). We identified the Arf1 GTPase to be involved in a signaling pathway that connects Gln to mTORC1 activation at the lysosome in the absence of the Rag GTPases. Many cancer cell lines have increased mTORC1 activity and show a high dependence on Gln for growth. Therefore, Gln-induced mTORC1 activation may be important for the growth of both normal and tumor cells.

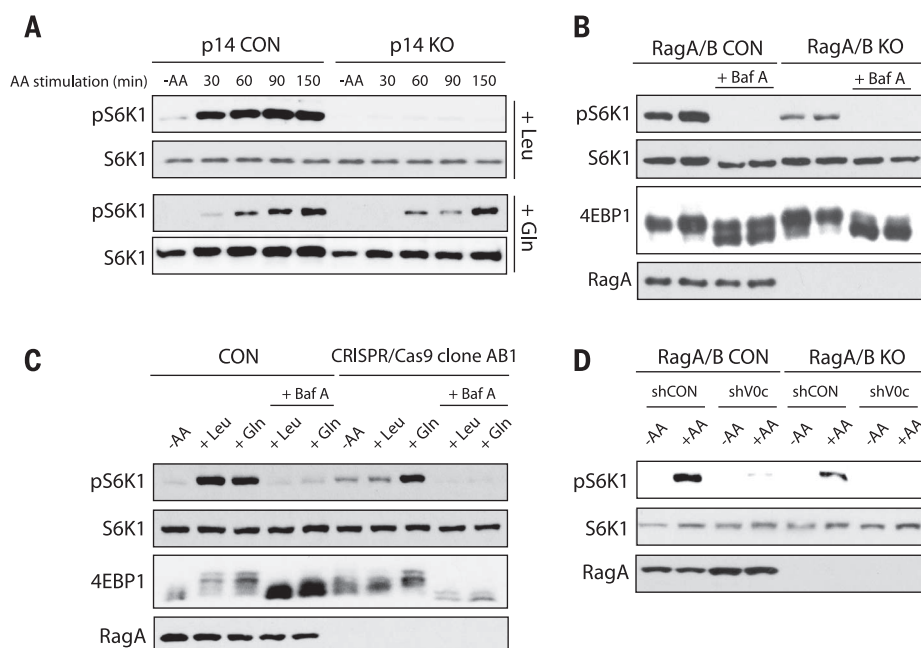


Fig. 3. Gln-induced mTORC1 activation requires the v-ATPase but not the Ragulator. mTORC1

activity was analyzed by the phosphorylation of S6K1 (pS6K) and the mobility shift of 4EBP1. (A) mTORC1 activity was analyzed in CON and p14 KO MEFs that were starved of amino acids, then stimulated with Leu (top) or Gln (bottom) at the indicated times. (B and C) Analysis of mTORC1 activity in CON and RagA/B KO cells that were starved of amino acids; pretreated with or without 1 μ M Baf A; followed by amino acid, Leu, or Gln stimulation for 150 min. (D) CON and RagA/B KO MEFs were treated with shRNA CON (shCON) or shRNA targeting the v-ATPase V0c subunit (shV0c). CON and RagA/B KO MEFs were starved of amino acids, followed by amino acid stimulation, and mTORC1 activity was assessed.

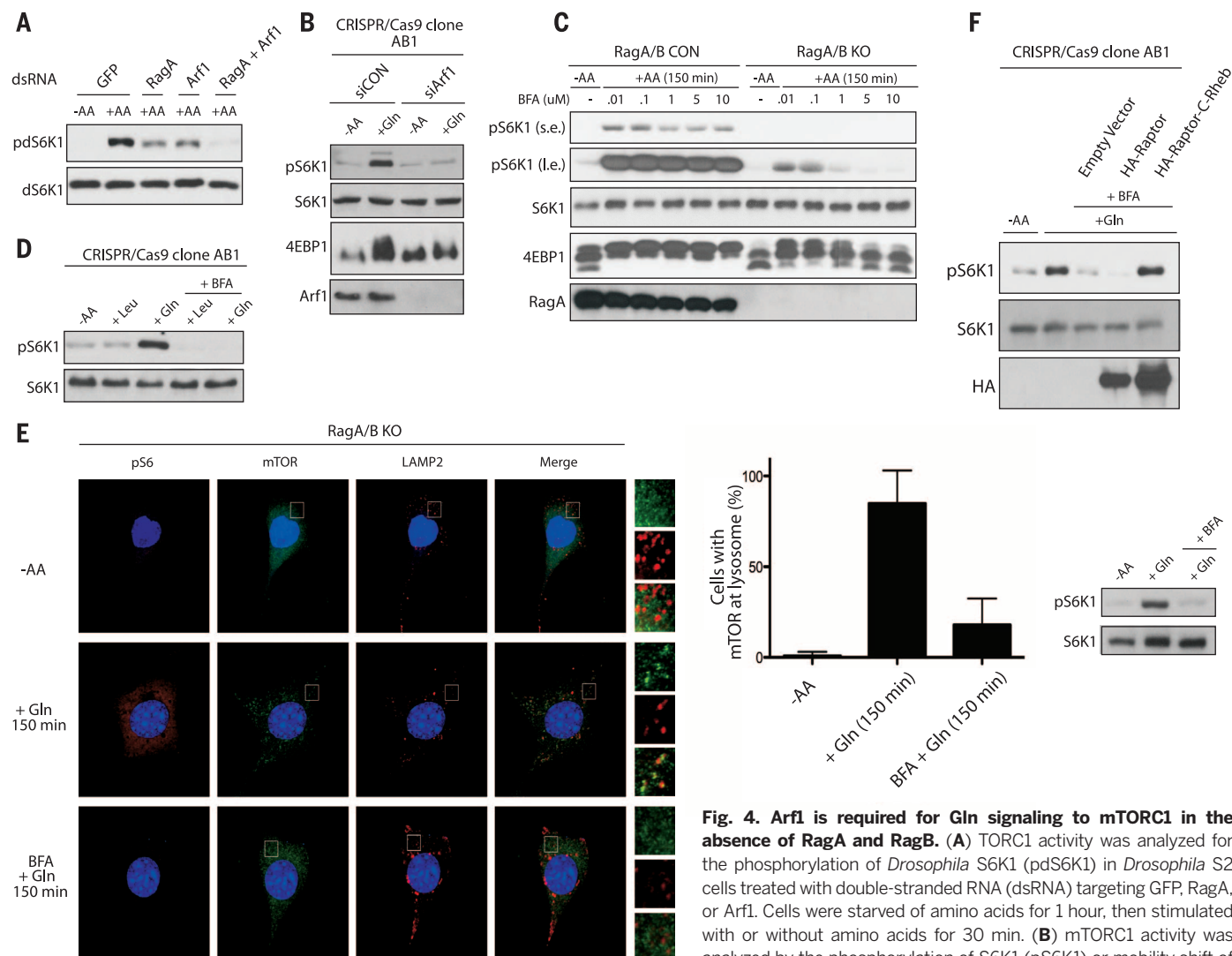


Fig. 4. Arf1 is required for Gln signaling to mTORC1 in the absence of RagA and RagB. (A) TORC1 activity was analyzed for the phosphorylation of *Drosophila* S6K1 (pdS6K1) in *Drosophila* S2 cells treated with double-stranded RNA (dsRNA) targeting GFP, RagA, or Arf1. Cells were starved of amino acids for 1 hour, then stimulated with or without amino acids for 30 min. (B) mTORC1 activity was analyzed by the phosphorylation of S6K1 (pS6K1) or mobility shift of

4EBP1 in RagA/B KO HEK293A cells treated with control (siCON) or Arf1 siRNA (siArf1). Cells were starved of amino acids then stimulated with Gln for 150 min. (C) mTORC1 activity was analyzed as in (B) in CON and RagA/B KO MEFs starved of amino acids, then pretreated with the indicated concentrations of BFA, and stimulated with amino acids for 150 min. Labels s.e. and l.e. denote shorter exposure and longer exposure, respectively. (D) mTORC1 activity was analyzed as in (B) in RagA/B KO HEK293A cells starved of amino acids, then pretreated with or without 1 μ M BFA, and stimulated with Leu or Gln for 150 min. (E) IF analysis depicting mTORC1 activation (pS6; orange) and lysosomal localization (LAMP2; red; mTOR; green) in RagA/B KO MEFs. Cells were starved of amino acids, pretreated with or without 1 μ M BFA, followed by stimulation with Gln for 150 min. Higher magnification images of the area depicted by the inset and their overlays are shown on the right of the images. Quantification of the percentage of cells with mTOR at the lysosome under different conditions and corresponding Western blot (right). (F) mTORC1 activity was analyzed as in (B) in RagA/B KO HEK293A cells transfected with HA-Raptor or HA-Raptor containing the C-terminal CAAX motif of Rheb (HA-Raptor-C-Rheb). Cells were starved of amino acids, pretreated with or without 1 μ M BFA, and stimulated with Gln for 150 min.

REFERENCES AND NOTES

- M. Laplante, D. M. Sabatini, *Cell* **149**, 274–293 (2012).
- K. Hara et al., *J. Biol. Chem.* **273**, 14484–14494 (1998).
- X. Wang, L. E. Campbell, C. M. Miller, C. G. Proud, *Biochem. J.* **334**, 261–267 (1998).
- Y. Sancak et al., *Science* **320**, 1496–1501 (2008).
- P. Nicklin et al., *Cell* **136**, 521–534 (2009).
- S. G. Kim et al., *Mol. Cell* **49**, 172–185 (2013).
- R. V. Durán et al., *Mol. Cell* **47**, 349–358 (2012).
- J. L. Jewell, R. C. Russell, K. L. Guan, *Nat. Rev. Mol. Cell Biol.* **14**, 133–139 (2013).
- L. Bar-Peled et al., *Science* **340**, 1100–1106 (2013).
- E. Kim, P. Goraksha-Hicks, L. Li, T. P. Neufeld, K. L. Guan, *Nat. Cell Biol.* **10**, 935–945 (2008).
- Y. Sancak et al., *Cell* **141**, 290–303 (2010).
- R. Zoncu et al., *Science* **334**, 678–683 (2011).
- L. Bar-Peled, L. D. Schweitzer, R. Zoncu, D. M. Sabatini, *Cell* **150**, 1196–1208 (2012).
- S. Menon et al., *Cell* **156**, 771–785 (2014).
- R. Gong et al., *Genes Dev.* **25**, 1668–1673 (2011).
- T. Sekiguchi, E. Hirose, N. Nakashima, M. Ii, T. Nishimoto, *J. Biol. Chem.* **276**, 7246–7257 (2001).
- L. Cong et al., *Science* **339**, 819–823 (2013).
- P. Mali et al., *Science* **339**, 823–826 (2013).
- J. L. Jewell, K. L. Guan, *Trends Biochem. Sci.* **38**, 233–242 (2013).
- M. Forgac, *Nat. Rev. Mol. Cell Biol.* **8**, 917–929 (2007).
- L. Li et al., *J. Biol. Chem.* **285**, 19705–19709 (2010).
- J. B. Helms, J. E. Rothman, *Nature* **360**, 352–354 (1992).
- C. D'Souza-Schorey, P. Chavrier, *Nat. Rev. Mol. Cell Biol.* **7**, 347–358 (2006).
- J. B. Sænz et al., *Nat. Chem. Biol.* **5**, 157–165 (2009).
- D. Stracka, S. Jozefczuk, F. Rudroff, U. Sauer, M. N. Hall, *J. Biol. Chem.* **289**, 25010–25020 (2014).

ACKNOWLEDGMENTS

We thank members of the Guan laboratory for critical comments; L. Huber for p14 null cells; and F. Flores, J. Zhou, and C. Worby for technical help. Supported by grants from NIH (R01GM051586 and R01CA108941 to K.-L.G.; T32CA121938 to J.L.J.; T32GM007752 to S.W.P.; and K99DK099254 to V.S.T.), Department of Defense (W81XWH-13-1-055) to K.-L.G., The Hartwell Foundation to J.L.J., and a Canadian Institutes of Health Research grant to R.C.R.

SUPPLEMENTARY MATERIALS

www.sciencemag.org/content/347/6218/194/suppl/DC1
Materials and Methods
Figs. S1 to S17
References (26–35)

31 July 2014; accepted 25 November 2014
Published online 7 January 2015;
10.1126/science.1259472



The Transfection Experts

X2




siRNA

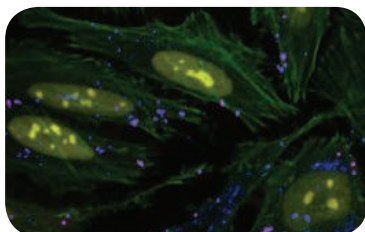
DNA

A Transfection Breakthrough **NEW! *TransIT*-X2[®] Dynamic Delivery System**

Achieve superior transfections with an advanced non-liposomal, polymeric system that efficiently delivers DNA *and/or* RNA out of the endosome and into the cytoplasm, overcoming a critical barrier to nucleic acid delivery.

The *TransIT*-X2[®] Dynamic Delivery System gives researchers:

-  **Efficiency**—superior broad spectrum transfection
-  **Delivery**—independent *or* simultaneous delivery of plasmid DNA and siRNA
-  **Technology**—novel, non-liposomal, polymeric technology



Functional Co-delivery of Plasmid DNA and siRNA. *TransIT*-X2[®] Dynamic Delivery System was used to *simultaneously* transfect CyTM5-labeled plasmid DNA (blue) encoding nuclear YFP (yellow) and CyTM3-labeled siRNA (red) into HeLa cells. Actin cytoskeleton is stained green.

Visit www.mirusbio.com for full experimental details.

ADVANCE YOUR TRANSFECTIONS.

Request a **FREE SAMPLE** of *TransIT*-X2[®] Dynamic Delivery System.

Visit www.mirusbio.com,
call 888.530.0801 (U.S. only) or +1.608.441.2852 (outside the U.S.)

www.mirusbio.com

Two decades of gene delivery expertise





Webinar

Now Available for On-Demand Viewing!

Recorded Live On: November 19, 2014

Improving Characterization of Monoclonal Antibodies

Making a Better Biotherapeutic

During the webinar, viewers will:

- Gain a deeper understanding of the factors important in biotherapeutic protein production and characterization
- Learn the fundamentals of microfluidics-based capillary electrophoresis
- Hear how microchip-CE can speed protein analysis, particularly in the drug development pipeline.

Characterization of therapeutic proteins remains labor-intensive and time consuming due to their often complex and heterogeneous structure. This has led to a concerted effort within the biotechnology and biopharmaceutical industry to address these bottlenecks as a means to boost the development of more biotherapeutics. Studies in this vein, such as testing the effect of various cell culture conditions on posttranslational modifications or monitoring the purification process of recombinant proteins, produce large numbers of samples that can easily exceed the capacity of modern analytical laboratories. High throughput analytical platforms with high precision, automation, and ease-of-use are therefore in great demand. To this end, the use of microfluidic analytical platforms such as microchip capillary electrophoresis (CE) have greatly increased the efficiency and reproducibility needed for analyzing proteins intended for therapeutic use. In this webinar, our expert panelists will discuss posttranslational modifications and quality assessment of biotherapeutic proteins for biopharmaceutical development using microfluidic-CE characterization.

Speakers



Niomi Peckham
Alexion Pharmaceuticals
Cheshire, Connecticut



I-Jane Chen, Ph.D.
PerkinElmer
Hopkinton, MA

View Now! webinar.sciencemag.org

Webinar sponsored by



Brought to you by the
Science/AAAS Custom
Publishing Office



 @SciMagWebinars



Protease Enzymes

The IdeS Protease enables fast, easy, high-performance digestion of immunoglobulin, while the human and yeast protein extracts provide a test material for optimizing mass spec sample preparation. IdeS Protease is a recombinant, engineered version of the immunoglobulin-degrading enzyme from *Streptococcus pyogenes*. It is a highly specific protease that slices Immunoglobulin G at a single, targeted site, offering 100% digestion in 30 minutes with no optimization. IdeS can be used to characterize therapeutic antibody candidates using liquid chromatography/mass spectrometry (LC/MS), and contains a histidine tag for easy removal. The versatile IdeS enzyme cuts IgGs from a range of species, as well as Fc-fusion proteins. Available in either predigested, cleaned form for immediate use in LC/MS analysis or intact, undigested form to provide a test material for optimizing mass spec protein sample preparation, the extracts provide clean, consistent, quantified, model system samples for LC/MS method development and instrument monitoring.

Promega

For info: 608-274-4330
www.promega.com/extracts

Phospho-Specific Polyclonal Antibodies

A custom phospho-specific antibody production service that is both reliable and produces high-quality product. This service includes synthesis of phosphorylated and nonphosphorylated peptides, conjugation to a carrier protein, immunization, serum production, and a two-step affinity purification of the antibodies. To ensure absolute specificity for each phosphorylated amino acid a stringent dot blot testing regime is carried out guaranteeing that for all projects the phospho peptide is preferentially recognized. A complete package of nonphosphorylated and phosphorylated peptides, preimmune sera, and antisera as well as affinity purified phospho-specific and nonphospho antibodies are supplied with each customer order.

AMS Biotechnology

For info: +44-(0)-1235-828200
www.amsbio.com/customservices.aspx



RNA-Binding Protein Immunoprecipitation Kits

Magna Nuclear RNA-binding Protein Immunoprecipitation (RIP) kits are specially designed to allow the discovery and analysis of both coding and noncoding chromatin-associated RNAs. Two versions of the kit are available, enabling users to analyze RNA both strongly and weakly associated with chromatin; one version uses cross-linked chromatin while the other uses native chromatin. Native RIP allows recovery of high-affinity, more direct interactions while the cross-linked method is designed to capture higher molecular weight complexes and more readily trap weaker interacting RNAs. Compared with other kits available to researchers, the Magna Nuclear RIP kits deliver much lower background signals, high signal-to-noise ratios and have been demonstrated to work in RNA-seq to enable NGS-based discovery and profiling. The kits offer flexible and scalable input requirements; RNA can be recovered from as few as 5,000 cells (cross-linked) or 100,000 cells (native).

EMD Millipore

For info: 800-645-5476
www.emdmillipore.com/epigenetics

HPLC Columns

Kinetex EVO C18 columns incorporate a patented organo-silica grafting process that utilizes uniform stabilizing ethane cross-linking to create a unique selectivity and ultimately, pH stability from 1 to 12. Kinetex EVO C18 has the performance advantages of Core-Shell Technology even at extreme low and high pH. This new advancement adds alkaline pH ruggedness and a highly versatile selectivity to the Kinetex core-shell family of high-performance liquid chromatography (HPLC), UHPLC, and preparative LC products. The wide pH 1 to 12 stability and improved peak shape for bases make the Kinetex 5 μ m EVO C18 especially ideal for analytical and preparative HPLC methods at a variety of challenging pH levels such as those in open access labs. With the introduction of the 5 μ m Kinetex EVO C18 particle, HPLC and preparative HPLC users can utilize 3 μ m or better efficiencies and low backpressures to easily replace traditional hybrid materials and run at higher linear flow rates to compress long run times.

Phenomenex

For info: 310-212-0555
www.phenomenex.com

Chromatographic Isolation

Accelerated Chromatographic Isolation (ACI) is a new advance converting simple flash purification into a faster and more economical way to isolate pure compounds. Traditional purification taking more than 15 minutes is reduced to 5 minutes; a 250 mg scale laboratory experiment can now be purified in less than 3 minutes on a 10 g column with an ACI-enabled Biotage Isolera flash purification system. It is fully automated, reliable, and lightning fast, able to completely purify 250 mg of sample in less than three minutes; this is quicker than most people take to run the TLC.

Biotage Isolera systems already recom-

mend cartridges based on the sample size and programmed TLC data; they work out the best solvent gradient based on compound, and provide real time indication of eluting compounds, using ultraviolet, ELSD, or Mass Detection. They subtract signal baselines automatically, so chemists can be confident that the correct fractions are collected.

Biotage

For info: 800-446-4752
www.biotage.com

Electronically submit your new product description or product literature information! Go to www.sciencemag.org/products/newproducts.dtl for more information.

Newly offered instrumentation, apparatus, and laboratory materials of interest to researchers in all disciplines in academic, industrial, and governmental organizations are featured in this space. Emphasis is given to purpose, chief characteristics, and availability of products and materials. Endorsement by *Science* or AAAS of any products or materials mentioned is not implied. Additional information may be obtained from the manufacturer or supplier.

AAAS | 2015 ANNUAL MEETING

12–16 FEBRUARY • SAN JOSE, CA

INNOVATIONS, INFORMATION, AND IMAGING



AAAS, publisher of *Science*, thanks the sponsors and supporters of the 2015 Annual Meeting



Johnson & Johnson



Genentech
A Member of the Roche Group



the Lemelson foundation
improving lives through invention



for its generous support of
the Science Journalism Awards

Advance registration ends on 22 January 2015

www.aaas.org/meetings

Introducing

bio-technne®

HIGHEST QUALITY PRODUCT PORTFOLIO



TRUSTED GLOBAL BRANDS

R&D systems

NOVUS™
BIOLOGICALS

TOCRIS

bio-technne®		LEARN MORE		bio-technne.com/launch		
	Building Innovation Opportunities	bio-technne.com info@bio-technne.com techsupport@bio-technne.com	North America TEL 800 343 7475	Europe • Middle East • Africa TEL +44 (0)1235 529449	China info.cn@bio-technne.com TEL +86 (21) 52380373	Rest of World bio-technne.com/find-us/distributors TEL +1 612 379 2956

Bio-Techne is a trading name for R&D Systems



There's only one **Science**

Science Careers Advertising

For full advertising details, go to ScienceCareers.org and click For Employers, or call one of our representatives.

Tracy Holmes

Worldwide Associate Director
Science Careers
Phone: +44 (0) 1223 326525

THE AMERICAS

E-mail: advertise@sciencecareers.org
Fax: 202 289 6742

Tina Burks

Phone: 202 326 6577

Nancy Toema

Phone: 202 326 6578

Marci Gallun

Sales Administrator
Phone: 202 326 6582

Online Job Posting Questions

Phone: 202 312 6375

EUROPE / INDIA / AUSTRALIA / NEW ZEALAND / REST OF WORLD

E-mail: ads@science-int.co.uk
Fax: +44 (0) 1223 326532

Axel Gesatzki

Phone: +44 (0) 1223 326529

Sarah Lelarge

Phone: +44 (0) 1223 326527

Kelly Grace

Phone: +44 (0) 1223 326528

JAPAN

Katsuyoshi Fukamizu (Tokyo)

E-mail: kfukamizu@aaas.org
Phone: +81 3 3219 5777

Hiroyuki Mashiki (Kyoto)

E-mail: hmashiki@aaas.org
Phone: +81 75 823 1109

CHINA / KOREA / SINGAPORE / TAIWAN / THAILAND

Ruolei Wu

Phone: +86 186 0082 9345
E-mail: rwu@aaas.org

All ads submitted for publication must comply with applicable U.S. and non-U.S. laws. Science reserves the right to refuse any advertisement at its sole discretion for any reason, including without limitation for offensive language or inappropriate content, and all advertising is subject to publisher approval. Science encourages our readers to alert us to any ads that they feel may be discriminatory or offensive.

Science Careers

FROM THE JOURNAL SCIENCE ■ AAAS

ScienceCareers.org

Prince Albert II de Monaco - Institut Pasteur Award 2015

The Institut Pasteur, the Monaco Scientific Center and the Prince Albert II of Monaco Foundation are pleased to invite applications for the "Prince Albert II of Monaco - Institut Pasteur" Award 2015.

This award will be given to an investigator in the field of:

"Environmental and climatic changes: impacts on Human Health"

The Award will honor an investigator under fifty years old who has made outstanding contributions to the field. The honoree will receive a 40,000 Euros award for his team. Candidates from all relevant disciplines (ecological, biomedical, and social sciences) are invited to submit their applications, which will be evaluated by a Jury of renowned scientific experts.

The dossier should include:

- a one-page letter written by the nominee describing the importance of his/her contribution to the field of "Environmental and climatic changes and their impacts on Human Health"
- a curriculum vitae
- a list of scientific publications and/or books
- a one-page outline of her/his plans for future research
- two letters of support

All applications files must be submitted in english.

The deadline for submitting nominations is **March 30th, 2015**. All files should only be sent in electronic format, as a single pdf file to: award@ec2h-monaco.org and award-monaco-pasteur@pasteur.fr

To learn more please visit : <http://www.ec2h-monaco.org/en> and www.pasteur-international.org



EMPIRE SCHOLAR in NEUROSCIENCE

SUNY Upstate Medical University seeks a neuroscientist at the Associate/Full Professor level to fill a tenured position as part of the New York State Empire Innovator Program, which aims to expand the ranks of world-class faculty in the SUNY system. Research should focus on studying the mechanisms of neurological function, disease, and dysfunction at the cellular, molecular or systems levels. Areas of particular interest that would synergize with existing strengths include, but are not limited to vision, addiction biology, psychiatric genetics, neurological disorders, neurodegenerative diseases, neuro-oncology, and neurodevelopmental disorders. Candidates using stem cell biology, biomarker development, cross-disciplinary translational research, behavioral methods or cutting-edge optical approaches are especially encouraged to apply.

The successful candidate will join a growing team of collaborative and interdisciplinary neuroscientists in Central New York at Upstate Medical University, neighboring Syracuse University, the Syracuse Veterans Hospital, and nearby Cornell and Binghamton Universities. The position is open to individual applicants or to established research teams. Significant current external research funding is required. Successful candidates will hold joint appointments in a basic science and one of several clinical departments, and will be expected to maintain a vigorous and independently funded research program. SUNY Upstate offers a highly competitive hard-money state-line salary, a generous start-up package supplemented by contributions from the New York State Empire Innovation fund and access to a unique, integrated clinical-basic science research environment. Neuroscientists at Upstate benefit from a new research building containing 100,000 sq.ft. of laboratory space equipped with state-of-the-art research facilities and research cores that support sophisticated imaging capabilities including deep brain imaging, super-resolution microscopy, and whole genome sequencing and analysis to name a few.

Applicants should submit a curriculum vitae, statement of research interests and three letters of reference by April 30, 2015 to www.upstate.edu/hr/jobs to Posting #036887. Applications will be evaluated as they are received and until the position is filled.

UPSTATE
MEDICAL UNIVERSITY

We are an Equal Opportunity Employer. All qualified applicants will receive consideration for employment without regard to race, color, religion, sex, national origin, protected veteran status or disability.

The BBVA Foundation Frontiers of Knowledge Awards recognize and encourage fundamental advances in basic and applied research, as materialized in models and theories for understanding the natural and social worlds, technological innovations of broad impact and salient contributions to the creation, performance and conducting of the classical music of our time. Honors also go to outstanding contributions that advance understanding or deliver material progress with regard to two key challenges of the global society of the 21st century, climate change and development cooperation.

The BBVA Foundation Frontiers of Knowledge Awards are undertaken in collaboration with the Spanish National Research Council (CSIC).

Fundación BBVA

Plaza de San Nicolás, 4
48005 Bilbao, Spain

Paseo de Recoletos, 10
28001 Madrid, Spain

www.fbbva.es

With the collaboration of



Categories

- Basic Sciences (Physics, Chemistry, Mathematics)
- Biomedicine
- Ecology and Conservation Biology
- Climate Change
- Information and Communication Technologies
- Economics, Finance and Management
- Development Cooperation
- Contemporary Music

Nominations

Nominations are invited from scientific and artistic societies, R&D centers, university and hospital departments, conservatories of music, orchestras, public agencies, and organizations working in the climate change and development areas, as well as other organizations and natural persons specified in the award conditions.

Deadline for submission

Nominations are open from January 1 through to June 30, 2015 at 23:00 GMT.

For more details and full entry conditions: www.fbbva.es/awards · awards-info@fbbva.es



Avoid driving your job search around in circles.

- Search thousands of job postings
- Create job alerts based on your criteria
- Get career advice from our Career Forum experts
- Download career advice articles and webinars
- Complete an individual development plan at "myIDP"

Target your job search using relevant resources on **ScienceCareers.org**.

ScienceCareers
FROM THE JOURNAL SCIENCE



The Department of Cellular and Molecular Biology at UT Health Northeast invites applications from outstanding scientists for state funded faculty positions at all levels to conduct independent research. The research of the applicant should be in various research areas of biochemistry or cell biology with an emphasis of cell motility and cytoskeletal regulation. Investigators working on cell motility using electron microscopy are encouraged to apply.

The mission of the research program at UT Health Northeast is to create an outstanding research community that links basic science and clinical science. UT Health Northeast has established research programs in lung injury/repair and pulmonary infectious diseases and the successful candidate is encouraged to interact with researchers in these areas. A strong track record and current extramural funding is required. Teaching in the biotechnology graduate program is encouraged and voluntary.

Our institution is growing rapidly and substantive resources have been allocated to build its basic and translational research portfolio. The Department has recently set up a state-of-the-art cellular and molecular imaging facility including a custom made single molecule total internal reflection fluorescence (TIRF) microscope, ultrafast super-resolution microscope which can visualize dynamic movement of the molecules in living cells, and a confocal microscope with a white light laser system. The successful candidate will be provided with competitive start-up packages and new laboratory facilities.

Applicants should submit their CV, a statement of future research plans and the names of three references to: **Dr. Mitsuo Ikebe, Chair of Department of Cellular and Molecular Biology, The University of Texas Health Science Center at Tyler, 11937 US Highway 271, Tyler TX 75708-3154**

Review of application will continue until the position is filled.

UT Health is an Equal Opportunity and Affirmative Action Employer and seeks to build a diverse employee community. It is the policy of The University to promote and ensure equal employment opportunity for all individuals without regard to race, color, religion, sex, national origin, age, sexual orientation, disability, or veteran status. Women and minorities are encouraged to apply.

Science Careers

Cernet

“《科学》职业” 已经与
Cernet/赛尔互联开展合
作。中国大陆的高校可以
直接联系Cernet/赛尔互联
进行国际人才招聘。



请访问
Sciencecareers.org/CER
点得联系信息。

招募学术精英,《科学》是您的不二之选

Science



UNIVERSITY OF MIAMI
MILLER SCHOOL
of MEDICINE

FACULTY POSITION MOLECULAR AND CELLULAR PHARMACOLOGY Miller School of Medicine University of Miami

The Department of Molecular and Cellular Pharmacology at the University of Miami Miller School of Medicine is seeking applications for a **TENURE-TRACK FACULTY POSITION** (rank open). Candidates must have a Ph.D. and/or M.D. degree and have an established record of research excellence. Applicants from all areas of molecular/cellular biology and biomedical research are welcome. Rank and salary will be commensurate with experience. Competitive laboratory space and start-up funds will be offered.

Applicants should send electronic copies of their CV, statement of current and future research interests and the names and addresses of three references to ELalor@med.miami.edu and hard copies to Ms. Elba M. Lalor, Senior Manager, Business Operations, Department of Molecular and Cellular Pharmacology, University of Miami Miller School of Medicine, P.O. Box 016189, Miami, FL 33101.

An Equal Opportunity/Affirmative Action Employer.

Assistant Professor of Freshwater Ecology Department of Ecology Montana State University

The Department of Ecology at Montana State University invites applications for a tenure-track Assistant Professor of Freshwater Ecology. The department seeks candidates who combine theory, observations, and experiments to tackle important contemporary issues in freshwater ecology, and who will bridge basic and applied science to answer questions that are both regionally important and relevant to society. Candidates with research interests and skills that complement the current faculty are particularly encouraged to apply. The successful candidate is expected to maintain a vibrant research program and laboratory group funded by extramural grants. The teaching assignment is comprised of three classes: Freshwater Ecology, General Ecology, and an additional course in Aquatic Ecology taught every other year. The Department of Ecology is committed to faculty diversity, and women and minority candidates are especially encouraged to apply. Applicants should submit all materials electronically, including a letter of interest addressing the required and preferred qualifications (see full ad), a CV, a statement of research accomplishments and future directions, a statement of teaching experience and interests, copies of up to three publications, and names and full contact information of three references. For the complete job announcement and application procedures, go to: <https://jobs.montana.edu/postings/1210>

MSU is an AA/ADA/EEO/Vet Pref Employer.



**Joint Faculty Positions at
the Center for Quantitative Biology and
Peking-Tsinghua Center for Life Sciences**

JOINT FACULTY POSITIONS

The Center for Quantitative Biology (CQB) and Peking-Tsinghua Center for Life Sciences (CLS) at Peking University jointly open for applications for faculty positions at all ranks.

We seek for creative individuals in all areas of quantitative biology, with emphases on (but not limited to):

- (1) Systems biology;
- (2) Synthetic biology;
- (3) Computational biology/Bioinformatics;
- (4) Disease mechanism and drug design from system biology perspective;
- (5) Development of quantitative methods and technology.

CQB (<http://cqb.pku.edu.cn/>) is dedicated to research and education at the interface between the traditionally more quantitative disciplines (such as mathematics, physical sciences, engineering, computer science) and the biological sciences. CLS (<http://www.cls.edu.cn/>) is a center of excellence to support and nurture creative research of long lasting impact.

Application materials (with cover letter, summary of research interests, CV and less than 5 representative publications, all in a single PDF file) should be sent to Ms. Wei Xiao (gsmkyb@pku.edu.cn), to whom you should also ask your references to send in their recommendation letters.



西南交通大学
Southwest Jiaotong University

**Southwest Jiaotong University, P.R.China
Anticipates Your Working Application**

Southwest Jiaotong University (SWJTU), founded in 1896, situates itself in Chengdu, the provincial capital of Sichuan. It is a national key multidisciplinary "211" and "985 Feature" Projects university directly under the jurisdiction of the Ministry of Education, featuring engineering and a comprehensive range of study programs and research disciplines spreading across more than 20 faculties and institutes/centers. Boasting a complete Bachelor-Master-Doctor education system with more than 2,500 members of academic staff, our school also owns 2 first-level national key disciplines, 2 supplementary first-level national key disciplines (in their establishment), 15 first-level doctoral programs, 43 first-level master programs, 75 key undergraduate programs, 10 post-doctoral stations and more than 40 key laboratories at national and provincial levels.

Our university is currently implementing the strategy of "developing and strengthening the university by introducing and cultivating talents". Therefore, we sincerely look forward to your working application.

More information available at <http://www.swjtu.edu.cn/>

I. Positions and Requirements

A. High-level Leading Talents

It is required that candidates be listed in national top talents programs such as *Program of Global Experts*, *Top Talents of National Special Support Program*, "*Chang Jiang Scholars*", *China National Funds for Distinguished Young Scientists* and *National Award for Distinguished Teacher*.

Candidates are supposed to be no more than 50 years old. The limitation could be extended in the most-needed areas of disciplinary development.

Candidates who work in high-level universities/institutes and reach the above requirements are supposed to be no more than 45 years old.

B. Young Leading Scholars

Candidates are supposed to be listed in or qualified to apply for the following programs:

• *National Thousand Young Talents Program*

• *The Top Young Talents of National Special Support Program (Program for Supporting Top Young Talents)*

• *Science Foundation for the Excellent Youth Scholars*

Candidates should have good team spirit and leadership, outstanding academic achievements, broad academic vision and international cooperation experience and have the potential of being a leading academic researcher.

C. Excellent Young Academic Backbones

Candidates under 40 years old are expected to graduate from high-level universities/institutes either in China or other countries. Those who are professors, associate professors and other equal talents from high-level universities/institutes overseas could be employed as professors and associate professors as well.

D. Excellent Doctors and Post Doctoral Fellows

Candidates under 35 years old are supposed to be excellent academic researchers from high-level universities either in China or other countries.

II. Treatments

The candidates will be provided with competitive salaries and welfares that include settling-in allowance, subsidy of rental residence, start-up funds of scientific research, assistance in establishing scientific platform and research group as well as international-level training and promotion. As for outstanding returnees, we can offer further or specific treatments that can be discussed personally.

III. Contact us:

Contacts: Ye ZENG & Yinchuan LI Telephone number: 86-28-66366202 Email: talent@swjtu.edu.cn
Address: Human Resources Department of SWJTU, the western park of high-tech zone, Chengdu, Sichuan, P.R.China, 611756

<http://www.swjtu.edu.cn/>

Max Planck Institute for Intelligent Systems



MAX-PLANCK-GESELLSCHAFT

Scientist or Research Engineer for Central Scientific Facility

We study intelligent systems, focusing on what computations allow synthetic and natural intelligent systems to do in perception, action, and learning. Our site in Tübingen, Germany is part of a campus with three Max Planck institutes and scientists from around the world. Three research departments collaborate on topics in machine learning, perception, and robotics to understand intelligent systems. Such systems rely on light to obtain information from the world.

We already work with a variety of systems including cameras (ranging from off-the-shelf SLRs to cooled emCCDs and sCMOS), sophisticated optical hardware (telescopes, wavefront sensors, tracking mounts), and computational photographic systems (Vicon, Kinect, motion capture technology, 3D scanners).

Your responsibilities

You will join a team that will take part in building a central scientific facility as part of „Optics and Sensing Laboratory“. You will work closely with researchers across the institute's departments and research groups to investigate, develop and implement technologies in the above fields. 50% of your time is devoted to basic research, involving other scientists and PhD students. You will also be involved in the development of institute infrastructure e.g. e-Learning system, providing system instructions and guidance for students, testing new promising technologies.

Requirements

- PhD or extensive experience in physics, engineering, or computer science
- Comprehensive hands-on experience with optical experimentation, optical design and system implementation, telescopes and astronomical camera systems plus an open mind to get involved in other areas that the central scientific facility will work on, including: low level processing and acquisition in computer vision systems, camera synchronization and calibration, multi-camera capture, motion capture systems, scanners, stereo imaging.
- Excellent programming skills in a hardware-near programming language like C, C++, and high-level scientific programming language like Matlab, Python. Familiarity with Linux environment is highly desirable, GPGPU programming skills are a plus.
- In-depth knowledge of an optical design software like Zemax, OSLO, or CodeV.
- Strong project management skills.
- Experience of work in research teams, preferably multi-disciplinary teams.
- Proficient communication skills.
- German language skills are not required, but a plus. Good written/spoken English is mandatory.
- A desire to get your hands dirty, and an affinity to computers and systems.
- A desire to create the future.

Our offer

Salaries will be based on previous experience according to TVöD guidelines (E9 to E15). An initial contract will be offered for 2 years but subsequent tenure is possible. This is a full-time position. The Max Planck Society is committed to employing more handicapped individuals and especially encourages them to apply. The Max Planck Society seeks to increase the number of women in areas where they are underrepresented and therefore explicitly encourages women to apply. The position will be open until filled or no longer needed. Preference will be given to applications received by 31 January, 2014.

In case of questions on the technical aspects of the position, please contact Prof. Dr. Bernhard Schölkopf at bs@tuebingen.mpg.de. For administrative questions, please contact Sabrina Jung at sabrina.jung@tuebingen.mpg.de. More information about the Tübingen site of our institute can be found at <http://is.tue.mpg.de/>.

Contact

Candidates should send their application quoting the reference number 57.14. In English via e-mail to Ms. Ballmann at personal@vw.mpi-stuttgart.mpg.de. The application should include 4 PDF documents: 1) your CV, 2) publication list, 3) certificates and references, 4) a 2-page of motivation, relevant previous experience, and statement of research interests. A Microsoft Word template can be downloaded from <http://tinyurl.com/na5vwx2>, which can also be edited by free libre office (<http://www.libreoffice.org/>). Please carefully read and follow the instructions on how to fill in the form.

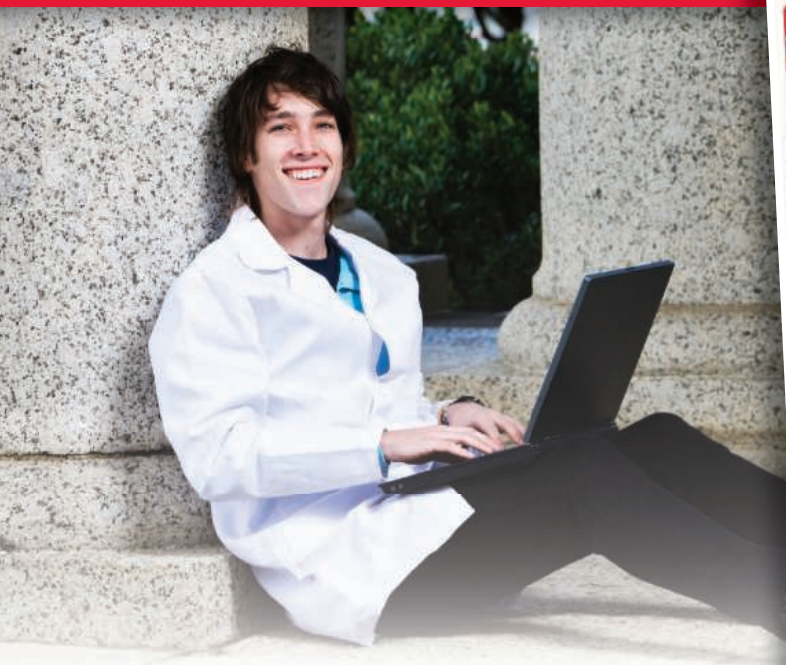
If you prefer to send a hardcopy application, you may do so. Please address it to:

Max Planck Institute for Intelligent Systems
Gemeinsame Verwaltung
Heisenbergstr. 1
70569 Stuttgart
Germany



For your career in science, there's only one **Science**

A career plan customized
for you, by you.



myIDP.sciencecareers.org



Recommended by leading professional societies and endorsed by the National Institutes of Health, an individual development plan will help you prepare for a successful and satisfying scientific career.



In collaboration with FASEB, UCSF, and the Medical College of Wisconsin and with support from the Burroughs Wellcome Fund, AAAS and *Science* Careers present the first and only online app that helps scientists prepare their very own individual development plan.

Visit the website and
start planning today!
myIDP.sciencecareers.org

In partnership with:



Faculty Careers

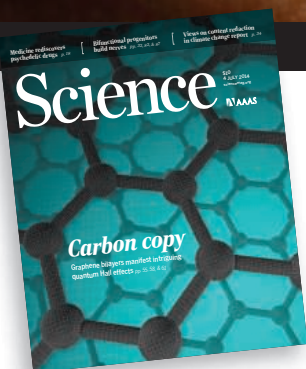
January 30, 2015

Reserve ads by January 13 to guarantee space

— THERE'S A SCIENCE TO REACHING SCIENTISTS. —

For recruitment in science, there's only one **Science**

ScienceCareers
online @sciencecareers.org



Managing an academic research group means keeping an eye on long-term goals, funding agency priorities, and publication plans. Faculty members also train students and postdoctoral fellows. PIs must match people to projects in a way that gets the group to its goals while encouraging its members to mature as scientists. This feature discusses strategies and tips for research program management.

Why you should advertise in these issues of *Science*:

Reach: Your job ad is seen by 570,400 readers around the globe from varied backgrounds and it sits on special bannered pages promoting faculty positions. 60% of our weekly readers work in academia and 67% are Ph.D.s. *Science* connects you with more scientists win academia than any other publication.

Results: If you are looking to hire faculty, *Science* offers a simple formula: relevant content that spotlights your ad + a large qualified audience = hiring success.

Limited budget?
Ask about banner ads
or 3rd party e-mails

To book your ad, contact:

advertise@sciencecareers.org

THE AMERICAS

202 326 6582

EUROPE/ROW

+44 (0) 1223 326500

JAPAN

+81 3 3219 5777

CHINA/ KOREA/ SINGAPORE/ TAIWAN

+86 186 0082 9345

ScienceCareers.org

By Elizabeth A. Marchio

My metamorphosis

I grew up in the 1980s and 1990s, in a lower-middle-class suburban neighborhood on the outskirts of Columbus. Our home didn't have air conditioning or cable television, so there was little reason to ever be inside. At 10 years old, I was allowed to roam the neighborhood unsupervised. I bicycled everywhere, climbed trees to catch tree frogs, and searched for aquatic life in the local creeks, among other clothes-ruining endeavors. One formative experience occurred at a housing development a mile from my home, when I came across a pool of water in the massive tire tracks of a dump truck. It was 2 feet deep and muddy. I peered into the pool, holding my small, green net in one hand and a bucket in the other, searching for movement. I spotted my quarry in the warm, shallow edges: dime-sized black spots zooming to the depths as my shadow passed. Tadpoles!

I stalked through the pool, my shoes squeaking and sliding in the mud. After much splashing and several failed attempts, I caught one—but this was not the leopard frog tadpole I expected. It had a remarkable red tail. I couldn't believe it! I had something I had never seen before!

After collecting a couple of dozen of them in my greatly excited state, I hung the bucket on my handlebars and sloshed home. I kept them in the garage, with my zoo of neighborhood creatures I had gathered. Two weeks later, the bucket clamored with metamorphosed froglets, which I identified by a field book as Cope's gray tree frogs (*Hyla chrysocelis*). When they started scaling the sides of the bucket, I realized it was time to return them to the collection site. I pedaled out to their natal pool to find it had been bulldozed. I released them in my backyard instead. My path into science started here.

Many years later, during a 5-year college hiatus, I worked for almost every aquarium store in the Columbus area. I joined the local aquarium club—the Columbus Area Fish Enthusiasts—and kept fish from all over the world. While working at the first aquarium store, I met my husband, Dan, and during our premarried life we propagated fish, plants, and coral and sold them over the Internet. We became self-taught experts in ornamental fish and aquarium keeping.

As I progressed from novice to advanced aquarist, I yearned for more. With the help of two inspirational mentors, Meg Daly and John Wenzel, I went back to school at Ohio State University (where they both worked), finished my Bachelor of Science degree in zoology, and was accepted to



"I came to realize that my passion isn't just for fish; it's also for people interested in fish."

Southeastern Louisiana University as a master's degree student, studying the phylogeography and taxonomy of fish.

I began to see my aquarium experience as a common life history element among higher level ichthyologists. This science-oriented leisure activity has a habit of turning fish into a lifelong passion.

That passion landed both Dan and me in fish-related Ph.D. programs at Texas A&M University. During my first year, as I counted fish bones in a developmental study of *Gambusia* species, I came to realize that my passion isn't just for fish; it's also for people interested in fish—and for those poor millennials who never had the opportunity to go outside and chase tadpoles. Will my generation be the last to have such experiences and, through them, come to love the natural world,

natural history, and conservation?

Today, I'm a social scientist studying how science-related leisure activities, such as playing outdoors and keeping aquariums, can mold people into ichthyologists, natural scientists, and scientifically literate citizens. As I look back and consider how I got here from the creek and the mud, I realize that I never left. I entered science on the tail of a tadpole. My passion led to my own metamorphosis, and now I'm studying the metamorphoses of others. ■

Elizabeth A. Marchio is a Ph.D. student in the Department of Recreation, Park, and Tourism Sciences at Texas A&M University, College Station. For more on life and careers, visit www.sciencecareers.org. Send your story to SciCareerEditor@aaas.org.

ILLUSTRATION: ROBERT NEUBECKER